NMR-Spectroscopic Investigations in Brønsted Acid Catalysis.

Dissertation

zur Erlangung des Doktorgrades
der Naturwissenschaften (Dr. rer. nat.)
der Fakultät für Chemie und Pharmazie
der Universität Regensburg

vorgelegt von

Julian Greindl
aus Regensburg

im Jahr 2017

Die vorliegende Dissertation beruht auf Arbeiten, die zwischen Februar 2014 und Dezember 2017 im Arbeitskreis von Professor Dr. Ruth M. Gschwind am Institut für organische Chemie der Universität Regensburg durchgeführt wurden.

Promotionsgesuch eingereicht am:

Die Arbeit wurde angeleitet von: Prof. Dr. Ruth M. Gschwind

Prüfungsausschuss:

Vorsitzender:	Prof. Dr. Rainer Müller
1. Gutachter:	Prof. Dr. Ruth M. Gschwind
2. Gutachter:	Prof. Dr. Werner Kremer
3. Prüfer:	Prof. Dr. Julia Rehbein

Meiner Frau

NMR-Spectroscopic Investigations in Brønsted Acid Catalysis.

Julian Greindl

Contents

1 Introduction and Outline

1.1 Brønsted acids as catalysts

The use of acids as catalysts is a long standing success story in the area of enantioselective synthesis. Most prominently, the field of Lewis-acid catalysis features an ever growing number of asymmetric catalysts, which enable the activation of an C-X double bond by decreasing the LUMO energy, thereby enabling the nucleophilic addition to the activated bond.[1,2] Excellent enantioselectivity has been achieved by combining chiral ligands with metal centered Lewis-acids to form chiral catalysts. The enantioselectivity is generally induced by strong, directional interactions such as coordinate covalent bonds.[3] Phosphoramidites for example have been labelled as a privileged class of ligands in asymmetric catalysis, due to their high versatility and accessibility.[4] In addition to the directional coordinate bonds, the contribution of CH-π and π-π interligand interactions for this catalyst class was reported in our working group in 2013.[5] In addition to organometallic compounds, Brønsted acids have emerged as a prominent class of enantioselective catalysts.[6,7] In Brønsted acid catalysis, hydrogen bonding provides a similar but weaker and less directional activation than coordinate covalent bonds, but without the need for transition metals. In recent years, a variety of highly selective chiral Brønsted acid catalyzed reactions have been reported, including Mannich reactions,[8,9] Strecker reactions,[10] Biginelli reactions[11] and transfer hydrogenations.[12,13]

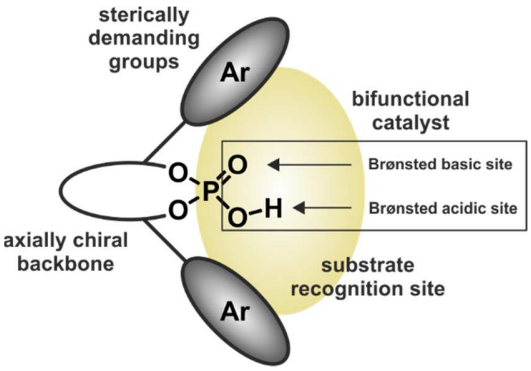

Figure 1. Model of a Brønsted acid catalyst. The backbone of the catalyst induces the chirality, while sterically demanding groups create a chiral binding pocket for the substrate. The activation takes place at the acidic or basic site of the bifunctional catalyst.

In these reactions, mainly 1,1'-bi-2-naphthol (BINOL) derived phosphoric acids with sterically demanding aromatic groups at the 3,3' position are used as catalysts.[8,14] The BINOL backbone introduces the chirality into the catalyst, whereas the phosphoric acid offers an

acidic, as well as a basic binding site and enables the formation of a hydrogen bond to the substrate (Figure 1). The directionality of the hydrogen bond in combination with the sterically demanding aromatic groups at the 3 and 3' position is supposed to provide the molecular organization that is needed to favor one of the formed transition states.[3] The used 3,3'-substituents vary from reaction to reaction and range from functionalized phenyl groups, such as 2,4,6-triisopropylphenyl[12] or 3,5-bis(trifluoromethyl)phenyl,[13] to extended aromatic systems, such as naphthyl or phenantryl[15] groups, to even more complex moieties, such as adamanthyl or triphenylsilyl[16] groups (see Figure 2 for a selection of BINOL derived chiral phosphoric acids).[17]

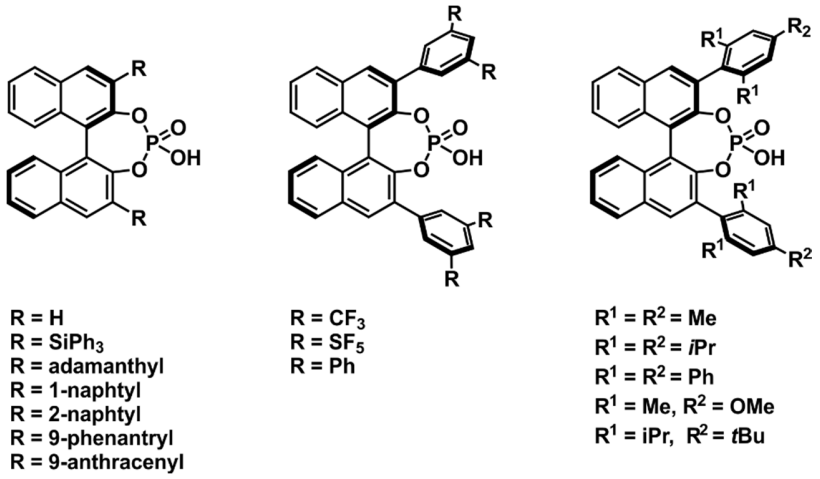

Figure 2. Selection of BINOL derived chiral phosphoric acids used in Brønsted acid catalysis. A large variety of 3,3'-substituents is utilized in synthesis, mainly consisting of functionalized or extended aromatic systems.

Despite the growing number of reactions and catalysts in Brønsted acid catalysis, the structures, catalyst/substrate complexes and mechanisms are relatively unexplored. Reasons therefore lie in the relatively large molecular size of the catalyst class, the high flexibility and consequential large number of conformations and the high amount of intermediate states. All of this makes theoretical studies computationally expensive and often require downsized model systems. Experimental access to these systems is even more difficult, due to chemical exchange of the hydrogen bonded substrates and the often poor solubility of the reactants.

1.2 Structural investigations in Brønsted acid catalysis

In computational studies by Goodman and Himo on the mechanism of the transfer hydrogenation of imines with the BINOL derived phosphoric acids in 2008, a variety of different transition states were identified by using model systems of the involved molecules.[18,19] In a continuative study, a detailed guide to predicting the enantioselectivity of phosphoric acid catalyzed reactions of imines was published by Goodman in 2016.[20] Despite the growing interest in the reason for the enantioselectivity of Brønsted acid catalyzed reactions, experimental data is relatively rare. Two crystal structures of different chiral phosphoric acid/imine complexes were reported by MacMillan and Schneider.[21,22] These structures both feature a hydrogen bond between the acid and the *E*-isomer of the imine but show a different orientation of the substrate. In 2013, Tang published a paper on the transfer hydrogenation of an imine.[23] In this organometallic cooperative catalysis, a Brønsted acid catalyst, an iridium complex and an imine form a ternary transition state complex, which was shown through a range of techniques, including NMR spectroscopy. By identifying two NOEs, they could experimentally proof the existence of the ternary complex in solution and further predict a plausible transition state through NOE restricted calculations (Figure 3).

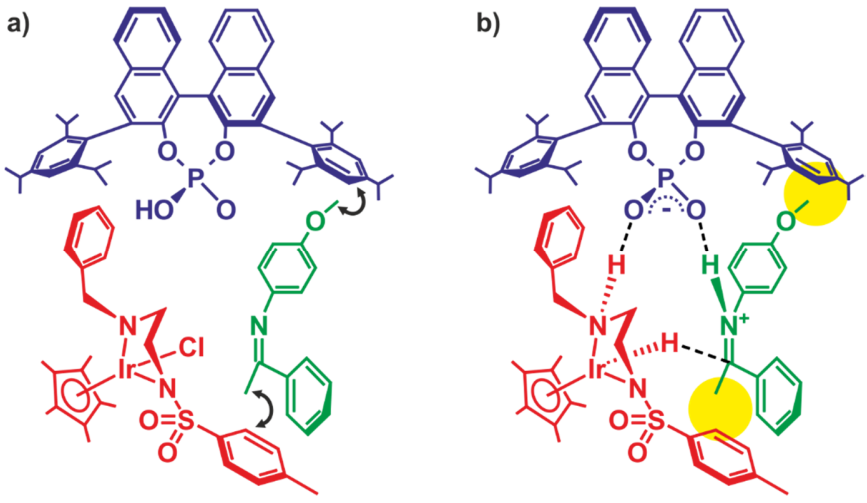

Figure 3. a) Black arrows mark the NOEs that were identified by Tang et al. The interactions indicate the presence of a ternary complex of Brønsted acid catalyst (blue), iridium complex (red) and imine (green); **b)** Yellow circles show the NOE constrains that enabled the calculation of the ternary transition state of the hydride transfer.

One NOE shows the proximity of the methoxy group of the imine to the Brønsted acid, whereas the second NOE shows an interaction between the methyl group of the imine and the iridium complex (Figure 3a). A variety of transition state structures were calculated by utilizing the obtained NOE restrictions. The resulting transition state shows not only hydrogen bonding, but also a range of CH- π interactions, which are likely to dictate the activity and selectivity of the catalytic system (Figure 3b).

In chapter two of this thesis, a combination of 2D and selective 1D NOESY techniques was used to determine the actual structure of a phosphoric acid catalyst/imine complex in solution, without the use of model systems. The investigated binary complex was predicted as a precursor for the transition state in the enantioselective transfer hydrogenation by Rueping in 2005. As phosphoric acid catalyst, the BINOL derived Brønsted acid (*R*)-3,3′-bis(2,4,6-triisopropylphenyl)-1,1′-binaphthyl-2,2′-diyl hydrogenphosphate (TRIP) was used due to its good solubility and signal dispersion in dichloromethane at low temperatures. NMR spectroscopic measurements at down to 180 K are needed in order to reach the slow exchange regime on the NMR time scale, which makes the identification of interactions via NOE analysis possible. But even at temperatures as low as 130 K, a steady exchange of different structures inside the binary complexes was found. Four core complex structures and their conformational exchange were identified and compared to theoretical calculations. For the very first time, experimental data was obtained for the structure of catalyst/*Z*-imine complexes, which are predicted to be the precursor for the reactive species in the asymmetric transfer hydrogenation reaction.

The hydrogen bond that is formed in TRIP/imine complexes is the focus of chapter three of this thesis. By labelling the investigated imines with ^{15}N, a number of different parameters become accessible by NMR spectroscopic methods. In addition to the ^{1}H chemical shift of the hydrogen bond proton and the ^{31}P chemical shift of the phosphoric acid catalyst, the ^{15}N chemical shift of the imine can be measured and correlated to the ^{1}H chemical shift. This correlation is plotted in a Steiner-Limbach plot to analyze hydrogen bond strength and character and to derive the bond distances. Furthermore, three coupling constants that are involved in the hydrogen bond can be determined: 1) The $^{1}J_{HN}$ coupling of the hydrogen bond proton to the imine nitrogen. 2) The $^{2h}J_{PH}$ coupling of the H-bond proton to the phosphorous of the catalyst. 3) The $^{3h}J_{PN}$ coupling of the phosphoric acid and the imine across the hydrogen bond. With the help of these parameters in combination with theoretical calculations, an in depth analysis of the hydrogen bonds of several TRIP/imine complexes was performed.

Chapters two and three have been published in the Journal of the American Chemical Society.

The fourth chapter of the thesis expands the analysis of Brønsted acid catalyst/imine complexes by combining structural investigations and hydrogen bond analysis in a study on the varying 3,3'-substituents of BINOL derived phosphoric acid catalysts used in synthesis. Identifying a suitable phosphoric acid from the plethora of catalysts available is mostly done by trial and error. By investigating the structural discrepancies of binary catalyst/imine complexes with different 3,3'-substituents, an experimental approach to an identification of crucial interaction points between Brønsted acid catalysts and imine substrate is taken. Comparing the structural differences of the investigated catalyst/imine complexes revealed only minor deviations of the imine position, depending on the catalyst. The hydrogen bond analyses revealed, that the biggest difference lies in the PON angle of the hydrogen bridge in the catalyst/*Z*-imine complexes. Here, noticeably flatter angles are found for catalyst TRIP and TiPSY (~120°) when compared to TRIFP (~110°), which also shows significantly lower enantioselectivity under identical reaction conditions. The presented approach is intended to help with a more focused way of selecting one of the available catalysts and aid the development of new chiral phosphoric acids.

1.3 Summary

A combination of NMR spectroscopic methods and theoretical calculations was used in chapters two to four give a detailed look into the activation modes in Brønsted acid catalysis. Different substrates and catalysts were combined and the structures of the binary complexes, as well as the hydrogen bonds that are formed, were intensely studied. NMR spectroscopic investigations revealed not only the structure of binary catalyst/*E*-imine complexes, but also enabled the experimental analysis of *Z*-imine complex structures for the very first time. The hydrogen bond analyses revealed a remarkable independence of the Brønsted acid/imine hydrogen bridge on the used substrates and catalyst, with the PON angle being the most significant difference.

1.4 Mechanistic investigations in solvothermal synthesis

A variety of nanochemical compounds can be prepared by solvothermal synthesis, due to the improved control over physical properties of products through variation of reaction conditions.[24–26] The solvothermal synthesis of quinoline derivatives is the focus of the fifth chapter of this thesis. These quinoline derivatives were identified as an organic product in the preparation of copper catena by Max Vilsmeier. NMR spectroscopic methods in combination with crystallographic analyses were used to identify the quinoline derivatives and the side-products of the solvothermal reaction in order to confirm a proposed mechanism. The mechanism is based on a similar reaction that was reported by Vaughan in 1948 and shows the elimination of a methyl group in the form of methane gas as the final reaction step.[27]

1.5 References

[1] D. Schinzer, *Selectivities in Lewis Acid Promoted Reactions*, Kluwer Academic: Dordrecht, **1989**.

[2] H. Yamamoto, *Lewis Acids in Organic Synthesis*, Wiley–VCH, Weinheim, **2000**.

[3] K. Brak, E. N. Jacobsen, *Angew. Chem. Int. Ed.* **2013**, *54*, 534–561.

[4] J. F. Teichert, B. L. Feringa, *Angew. Chem. Int. Ed. Engl.* **2010**, *49*, 2486–2528.

[5] E. Hartmann, M. M. Hammer, R. M. Gschwind, *Chemistry* **2013**, *19*, 10551–10562.

[6] M. S. Taylor, E. N. Jacobsen, *Angew. Chemie* **2006**, *118*, 1550–1573.

[7] M. Terada, *Synthesis (Stuttg).* **2010**, *12*, 1929–1982.

[8] T. Akiyama, J. Itoh, K. Yokota, K. Fuchibe, *Angew. Chemie Int. Ed.* **2004**, *43*, 1566–1568.

[9] M. Yamanaka, J. Itoh, K. Fuchibe, T. Akiyama, *J. Am. Chem. Soc.* **2007**, *129*, 6756–64.

[10] M. Rueping, E. Sugiono, C. Azap, *Angew. Chemie Int. Ed.* **2006**, *45*, 2617–2619.

[11] X. Chen, X. Xu, H. Liu, L. Cun, L. Gong, *J. Am. Chem. Soc.* **2006**, *128*, 14802–14803.

[12] S. Hoffmann, A. M. Seayad, B. List, *Angew. Chemie Int. Ed.* **2005**, *44*, 7424–7427.

[13] M. Rueping, E. Sugiono, C. Azap, T. Theissmann, *Org. Lett.* **2005**, *7*, 3781–3783.

[14] D. Uraguchi, M. Terada, *J. Am. Chem. Soc.* **2004**, *126*, 5356–5357.

[15] M. Rueping, A. P. Antonchick, T. Theissmann, *Angew. Chemie Int. Ed.* **2006**, *45*, 6751–6755.

[16] S. G. Ouellet, A. M. Walji, D. W. C. Macmillan, *Acc. Chem. Res.* **2007**, *40*, 1327–1339.

[17] D. Parmar, E. Sugiono, S. Raja, M. Rueping, *Chem. Rev.* **2014**, *114*, 9047–9153.

[18] L. Simón, J. M. Goodman, *J. Am. Chem. Soc.* **2008**, *130*, 8741–8747.

[19] T. Marcelli, P. Hammar, F. Himo, *Chem. - A Eur. J.* **2008**.

[20] J. P. Reid, L. Simón, J. M. Goodman, *Acc. Chem. Res.* **2016**, *49*, 1029–1041.

[21] R. I. Storer, D. E. Carrera, Y. Ni, D. W. C. MacMillan, *J. Am. Chem. Soc.* **2006**, *128*, 84–86.

[22] M. Sickert, F. Abels, M. Lang, J. Sieler, C. Birkemeyer, C. Schneider, *Chem. – A Eur. J.* **2010**, *16*, 2806–2818.

[23] W. Tang, S. Johnston, J. a Iggo, N. G. Berry, M. Phelan, L. Lian, J. Bacsa, J. Xiao, *Angew. Chem. Int. Ed. Engl.* **2013**, *52*, 1668–1672.

[24] D. Banerjee, S. J. Kim, L. A. Borkowski, W. Xu, J. B. Parise, *Cryst. Growth Des.* **2010**, *10*, 709–715.

[25] R. X. Æ. Jian, K. Shang, *J. Mater. Sci.* **2007**, *42*, 6583–6589.

[26] M. Choucair, P. Thordarson, J. A. Stride, *Nat. Nanotechnol.* **2009**, *4*, 30–33.

[27] W. R. Vaughan, *Org. Synth.* **1948**, *28*, 49–51.

2 Brønsted Acid Catalysis – Structural Preferences and Mobility in Imine/Phosphoric Acid Complexes

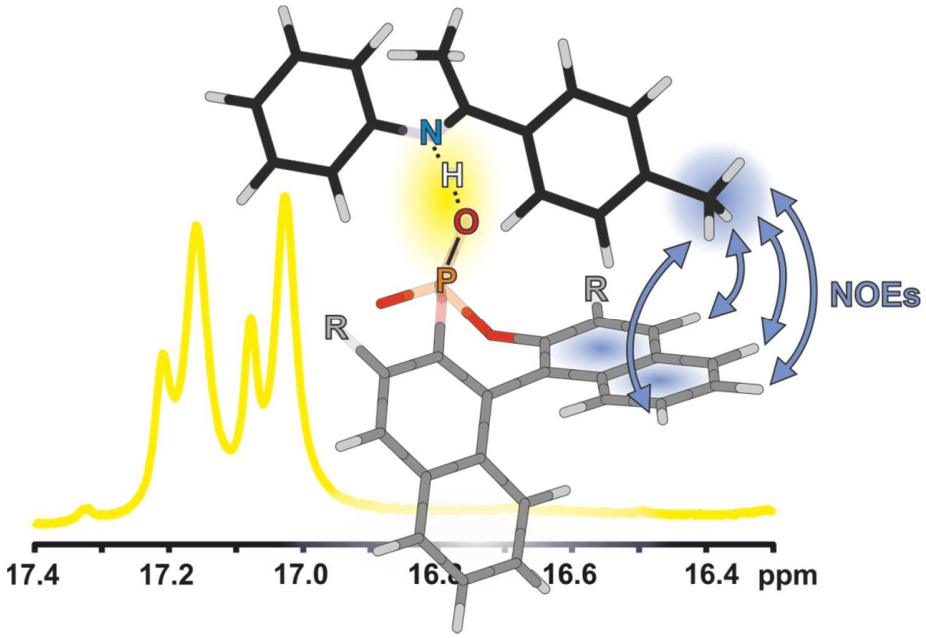

Julian Greindl, Johnny Hioe, Nils Sorgenfrei, Fabio Morana and Ruth M. Gschwind*

J. Am. Chem. Soc. **2016**, *138*, 15965–15971

DOI: 10.1021/jacs.6b09244

a) The major part of the NMR measurements and assignments was performed by Julian Greindl. b) All computational studies were performed by Johnny Hioe. c) Solvent studies and initial NMR and NOE experiments on the binary complexes **2a-c**/**1c** were conducted by Nils Sorgenfrei. d) Fabio Morana contributed in the optimization of the sample preparation and by synthesis of the catalyst (*R*)-TRIP f) Imine substrates were synthesized by all authors except Johnny Hioe.

2.1 Abstract

Despite the huge success of enantioselective Brønsted acid catalysis, experimental data about structures and activation modes of substrate/catalyst complexes in solution are very rare. Here, for the first time, detailed insights into the structures of imine/Brønsted acid catalyst complexes are presented on the basis of NMR data and underpinned by theoretical calculations. The chiral Brønsted acid catalyst *R*-TRIP (3,3′-bis(2,4,6-triisopropylphenyl)-1,1′-binaphthyl-2,2′-diyl hydrogen phosphate) was investigated together with six aromatic imines. For each investigated system, an *E*-imine/*R*-TRIP complex and a *Z*-imine/*R*-TRIP complex were observed. Each of these complexes consists of two structures, which are in fast exchange on the NMR time scale; i.e., overall four structures were found. Both identified *E*-imine/*R*-TRIP structures feature a strong hydrogen bond but differ in the orientation of the imine relative to the catalyst. The exchange occurs by tilting the imine inside the complex and thereby switching the oxygen that constitutes the hydrogen bond. A similar situation is observed for all investigated *Z*-imine/*R*-TRIP complexes. Here, an additional exchange pathway is opened via rotation of the imine. For all investigated imine/*R*-TRIP complexes, the four core structures are highly preserved. Thus, these core structures are independent of electron density and substituent modulations of the aromatic imines. Overall, this study reveals that the absolute structural space of binary imine/TRIP complexes is large and the variations of the four core structures are small. The high mobility is supposed to promote reactivity, while the preservation of the core structures in conjunction with extensive π-π and CH-π interactions leads to high enantioselectivities and tolerance of different substrates.

2.2 Introduction

Since the development of the first BINOL-derived phosphoric acids in 2004 by Akiyama and Terada,[1,2] Brønsted acid catalysts have emerged as a viable catalyst class for a variety of enantioselective reactions.[3–7] Due to their excellent yields and *ee* values, these catalysts are able to provide a complementary technique to transition metal catalyzed reactions. For the Brønsted acid catalyzed enantioselective reduction of imines, Rueping *et al.* postulated a catalytic cycle that involves the formation of a binary complex as a precatalytic state consisting of catalyst **1b** and the imine (see Figure 1a).[4] Subsequent addition of a reduction agent, e.g., Hantzsch ester, leads to a ternary complex. However, the reasons for the high enantioselectivity induced by these catalysts have remained unclear, as structural investigations on the key reactive intermediates are very challenging.

A DFT study by Himo on the transfer hydrogenation of imines proposed that the enantioselectivity is dictated by the kinetics of the hydride transfer step in the ternary complex.[8] Using a truncated phosphoric acid as a catalyst model, the transition state involving the *Z*-imine was predicted to react faster than the *E*-imine. Goodman *et al.* could further confirm the *Z*-imine transition state as the reactive pathway by using catalysts **1a** and **1b** (see Figure 1b) in their calculations.[9]

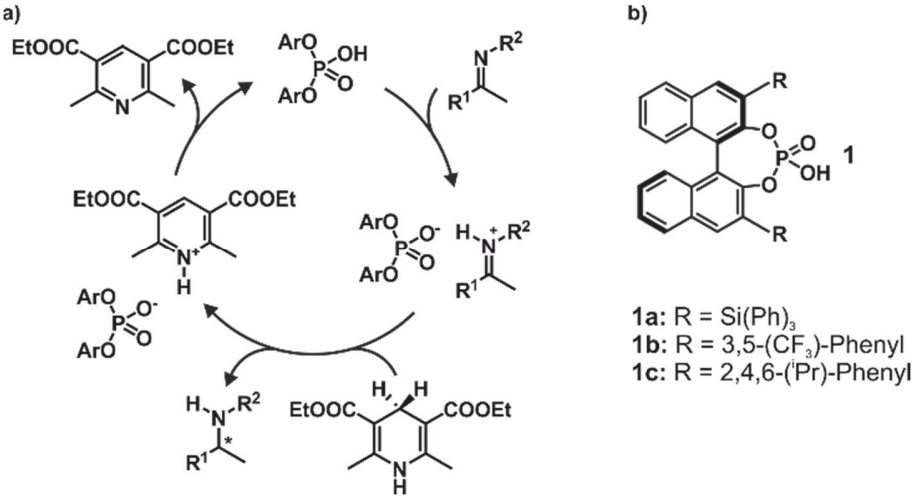

Figure 1. a) Catalytic cycle for the transfer hydrogenation, as proposed by Rueping *et al.*[4] b) Brønsted acid catalysts **1a-c** successfully applied for enantioselective reduction of imines or reductive amination.[3–5]

So far, the only detailed experimental data about the binary complex was reported by MacMillan and co-workers, who were able to identify the structure of the *E*-imine/**1a** complex

by a single crystal X-ray analysis.[3] In 2013, W. Tang *et al.* elucidated the structure of a ternary **1c**/imine/iridium complex with the help of two NOE signals between methyl groups.[10] Additional experimental investigations of solvent and temperature effects on the interaction between catalyst and imine were performed by Rueping *et al.*[11] With a combination of dielectric spectroscopy, quantum chemistry, and ^{1}H NMR, they showed the important role of close-contact ion-pairs in a transfer hydrogenation reaction. With the help of vibrational circular dichroism, Merten *et al.* investigated the influence of different solvents on the transmission of stereochemical information from the chiral Brønsted catalyst anion to a Mn^{III}-salen complex in an asymmetric epoxidation reaction.[12] Our first NMR study about the hydrogen bond properties of achiral imine/diphenylphosphate complexes proposed the coexistence of ion paired and neutral hydrogen bond complexes.[13] However, our recent theoretical and NMR investigations on the hydrogen bond situation in binary complexes containing chiral phosphoric acids revealed the ion paired complexes as the dominating species.[14] A landscape of asymmetric single-well potential surfaces was revealed, composed of ion-paired complexes. However, to the best of our knowledge, no detailed experimental structure analysis of any Brønsted acid catalyst/substrate complex in solution has been presented so far.

In this paper, detailed structural information on chiral Brønsted acid/imine complexes is described on the basis of NMR data and theoretical calculations. A high mobility of the imine inside the substrate/catalyst complex is observed for both *E*- and *Z*-imine. For each isomer, two orientations of the imine in relation to the catalyst can be observed. These two basic structures are in fast exchange on the NMR time scale. Interchanging the orientations is possible by either rotating the imine by 180° or tilting the imine and thereby switching the oxygen that constitutes the hydrogen bond. For *E*-imine/catalyst complexes, only tilting is observed. For the *Z*-imine/catalyst complex, which is postulated to be the reactive species, the reduced steric hindrance of the imine enables both exchange pathways, canceling the asymmetry of the binary complex. These structural characteristics are conserved in all complexes despite varying substrates.

2.3 Results and Discussion

Model Systems and Methods For our structural investigations, six imine/catalyst complexes were selected. Catalyst **1c** was used, because it provided the best combination of solubility, ^{1}H chemical shift dispersion, and performance, compared to **1a,b** (see Figure 1b). Typical aromatic imines used in synthesis **2a-c** and **3a-c** were chosen, to provide different electronic properties (see Figure 2).[4,5] **2a-c** derived from aniline were selected, because this allowed for a simple ^{15}N labeling, which enables the unambiguous assignment of α-methyl groups and NH protons. In addition, **3a,c** derived from anisidine were investigated to show the effect of an inverse relative electron density of the two aromatic substituents. The trifluoromethyl substituents of **2c** and **3a** enable ^{19}F NMR investigations, and imine **3c** allows for the direct comparison with the single crystal structure[5] by means of theory. Toluene, dichloromethane (CD_2Cl_2), and freonic mixtures[15] of $CDCl_2F$ and $CDClF_2$ were tested as solvents. After extensive optimization of sample preparations, NMR parameters, and solvent screening, we were able to improve the line widths tremendously and altogether enable an investigation by means of NMR (for spectra, see the Supporting Information). Due to the better solubility of the imine/**1c** complexes in CD_2Cl_2, all relevant structural investigations were performed in this solvent. Low temperature measurements were used in order to reduce conformational averaging and exchange. The NMR measurements at 180 and 130 K were done in CD_2Cl_2 and freonic mixtures, respectively (see the Supporting Information).

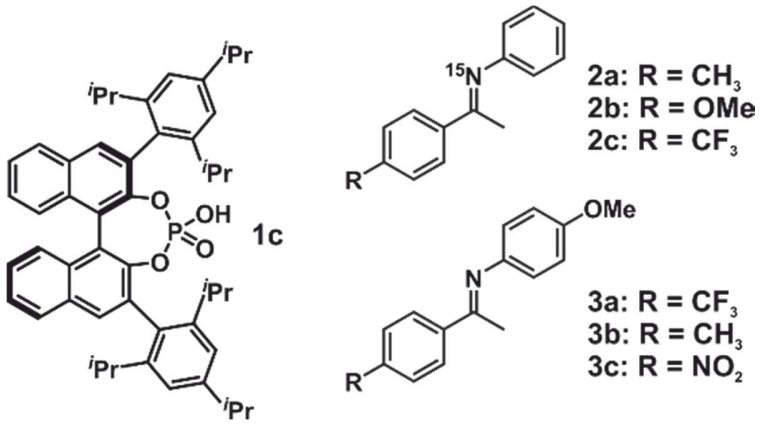

Figure 2. Brønsted acid catalyst **1c** and imines with different functional groups. Imines **2a-c** and **3a-b** were investigated by means of NMR and theory. Imine **3c** was used for theoretical calculations exclusively.

For the complexes **2a**-**c**/**1c** and **3a**-**c**/**1c**, theoretical calculations were performed to identify the energetic minima. All complexes were optimized in the continuum of CD_2Cl_2 (SMD) at the

DFT level of theory using Grimme's D3 empirical dispersion parameter (TPSS-D3/def2-SVP).[16–20] As the experiment was performed at 180 K, the dielectric constant of the continuum medium was raised (from 8.93 at RT to 16.20 at 180 K) to adapt to the experimental condition. In all cases, only ion pair minima were obtained, which is in full agreement with the dominating species found in our recent NMR studies.[14] Vibrational analysis were performed at the TPSS-D3/def2-SVP level of theory. In all cases, no imaginary vibrational mode is obtained. Subsequently, single point calculations (SCS-MP2/CBS//TPSS-D3/def2-SVP)[21] and additional solvent corrections (SMD)[17] on the optimized geometry were performed to determine the energy differences between conformational minima. Softwares used were Gaussian 09, version D.01, for geometry optimization and frequency analysis and ORCA 3.0.3 for single points.[22,23]

Computational Study. Four types of energetic minima with different arrangements of the imines were identified in our theoretical calculations. Two structures *Type I E* and *Type II E* containing *E*-isomers and two structures *Type I Z* and *Type II Z* containing *Z*-isomers of the imine (Figure 3a) are representatively illustrated by ***E,Z*-2a**/**1c**. Each of these four structures has at least three low energy conformations of the isopropyl groups without affecting the core structure composed of the imine and the binaphtyl backbone. Therefore, in Figure 3a and in the further discussion, these isopropyl conformations are Boltzmann averaged but not depicted.

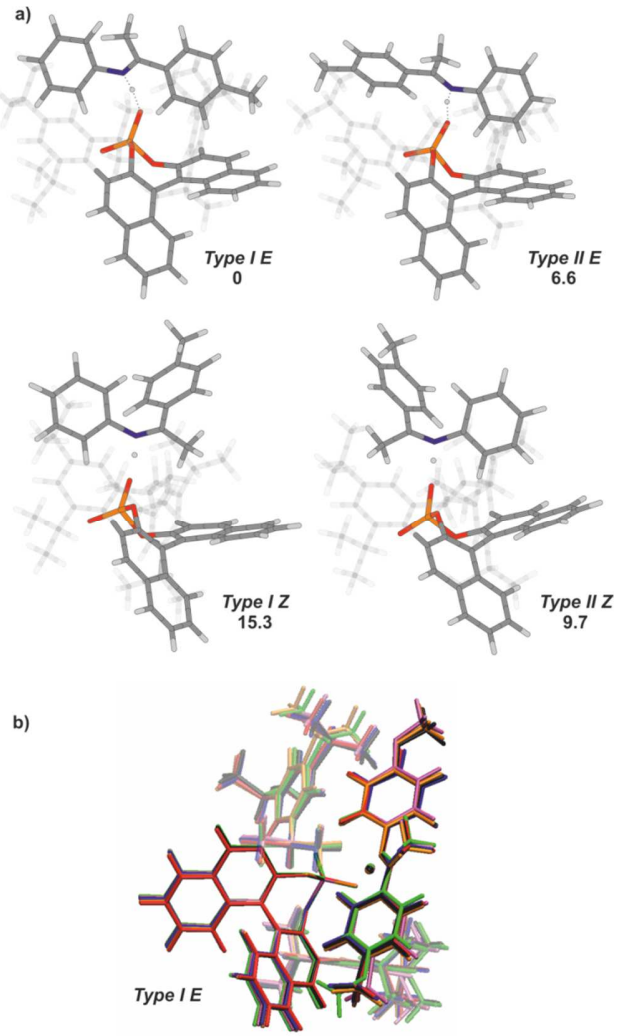

Figure 3. a) Calculated structures of the **2a**/**1c** complexes. Energies are shown in kJ mol^{-1} relative to *Type I E*.[24] The bis(2,4,6-triisopropylphenyl) groups are shown transparent for the sake of clarity. b) Overlay of global minima of investigated ***E*-2a-c**/**1c** and ***E*-3a-c**/**1c** *Type I E* complexes. For the sake of clarity, a different orientation of the catalyst was chosen.

The structural analysis suggests that the methyl substituent in the para-position of the imine is situated above the binaphtyl moiety of the catalyst for conformation *Type I E*, which indicates a CH-π interaction. In contrast to structure *Type I E*, the imine in conformation *Type II E* is rotated by 180°. The aniline part of the imine is now located proximal to the binaphtyl moiety of the catalyst. The conformational analysis of *E*-isomer complexes suggests a preference (ca. 4.5–9.3 kJ/mol) for structure *Type I E* due to the CH-π stabilization rather than *Type II E* (Figure 3; ***E*-2a**/**1c**). This thermodynamic preference is conserved in the series of the investigated *E*-imine/**1c** complexes and seems to be independent of functional group

induced electronic modulations, which is demonstrated by superimposed global minima in Figure 3b. Even the inverted electronic properties of the imine substituents in ***E*-3a**/**1c**, ***E*-3b**/**1c**, and ***E*-3b**/**1c** are not sufficient to alter the relative thermodynamic stability between *Type I E* and *Type II E*. The similar structures of the aromatic imine/catalyst complexes suggest that the electronic properties of the imine have very little influence on the structure of the binary complex.[25]

Structurally, the two complexes involving *Z*-imines exhibit either an interaction between the aniline part of the imine and the binaphthyl backbone of the catalyst (*Type II Z*) or an interaction between the α-methyl group and the catalyst backbone (*Type I Z*) (see Figure 3a). Here the conformation *Type II Z* is always thermodynamically favored (4.9-9.5 kJ/mol) over *Type I Z* in the series of the investigated *Z*-imine/**1c** complexes.

Noncovalent Interaction (NCI) Analysis[26,27] All investigated binary complexes feature a strong hydrogen bond independent of their structural arrangements,[14] which is marked by the critical point ($s(\rho) = 0$) around $\mathrm{sgn}(\lambda_2)\rho$ = -0.06 to -0.07 in the plot of density ρ vs reduced density gradient $s(\rho)$ (Figure 4: NCI analysis of the global minima of complex ***E,Z*-2a**/**1c**). This is in full agreement with our current experimental results, which showed a downfield shifted proton in the ^{1}H spectra around 15-19 ppm. The strong hydrogen bond is also depicted by the blue surface which exists in all investigated complexes (Figure 5; ***E,Z*-2a**/**1c**).

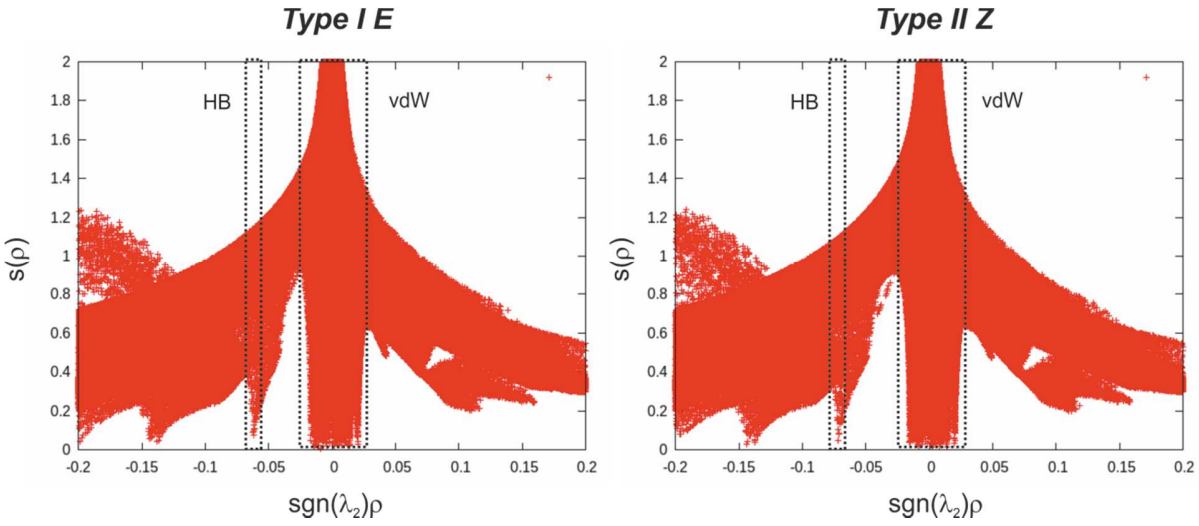

Figure 4. Plot of density ($sgn(\lambda_2)\rho$) vs reduced density gradient ($s(\rho)$) showing a large area of van der Waals interaction and the strong hydrogen bond in the complex *Type I E* and *Type II Z* of ***E,Z*-2a**/**1c**.

Additionally, the plot in Figure 4 exhibits also a large region of many weak interactions characteristically indicated by the critical points around $sgn(\lambda_2)\rho$ = -0.03 to 0.03, which is expected for complexes with many aromatic surfaces. Figure 5a illustrates the NCI analysis of the conformation *Type I E* in the complex ***E*-2a**/**1c**. The existence of the weak interactions, to which the CH-π interaction (red circle) also belongs, is indicated by the green surface. These numerous van der Waals interactions are contributing significantly to the geometry of the complex and conformational distribution. Therefore, the application of the dispersion corrected functional (D3)[18] is indispensable in the simulation. Respectively, the chemical shift calculation of the protons of the methyl group predicted a typical shielding by the aromatic ring as discussed below. Compared to the conformation *Type I E*, the aniline part of the imine in the conformation *Type II E* is expected to interact with the binaphtyl moiety of the catalyst. Accordingly, a weak π-π interaction is predicted by the NCI analysis (Figure 5b). Moreover, the para-methyl group of the imine in the conformation *Type II E* faces outward from the catalyst. Therefore, no particular interaction and shielding is expected.

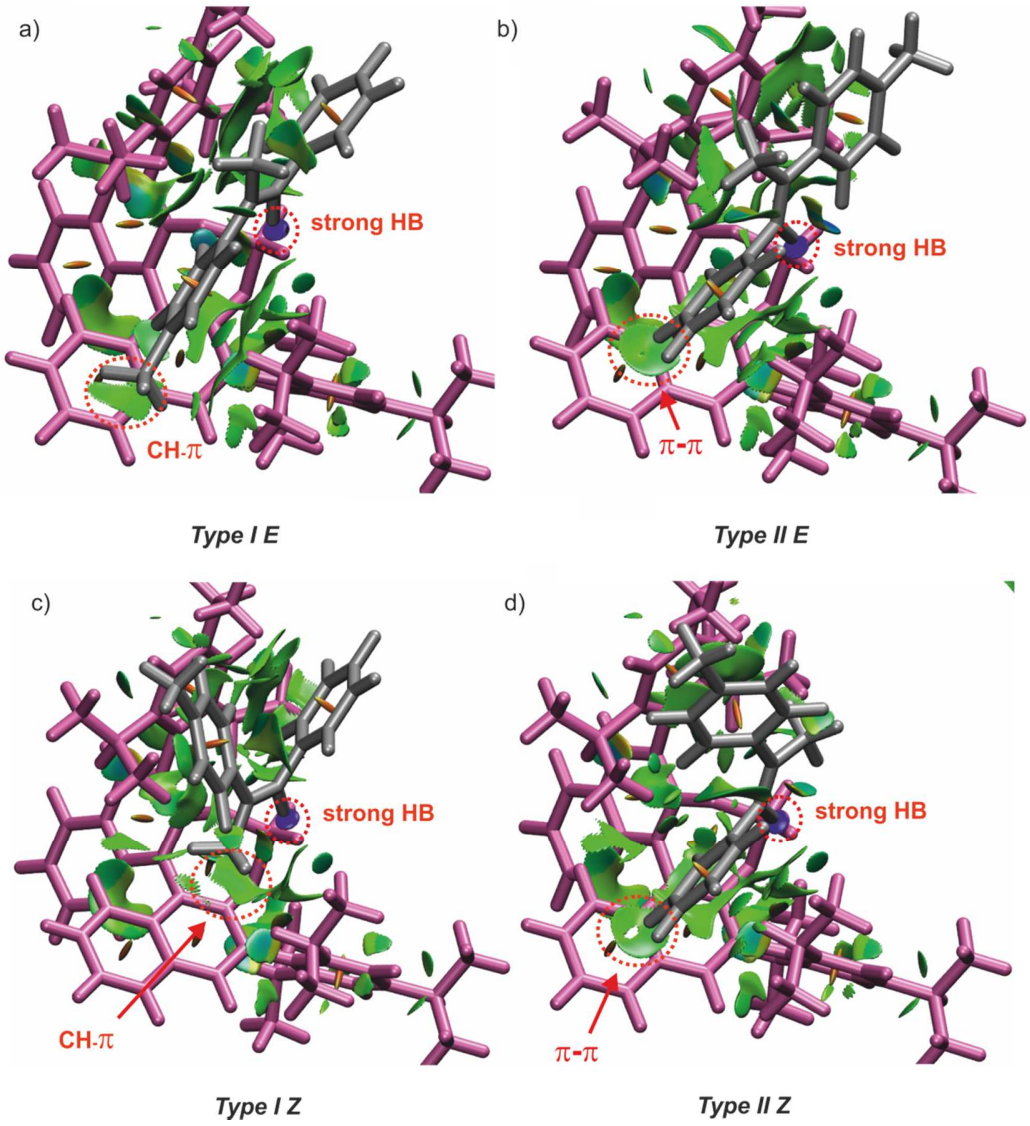

Figure 5. NCI analysis of the **2a**/**1c** complexes (global minima) showing weak dispersive interactions (green surfaces) and an attractive strong hydrogen bridge between imine and catalyst (blue surfaces). a) *Type I E* shows CH-π interaction between the p-methyl substituent of the imine and BINOL of the catalyst. b) The imine is rotated 180° in *Type II E* and shows the aniline moiety lies on top of the BINOL aromatic surface and the p-methyl group faces outward from the catalyst. c) In *Type I Z,* the imine is also rotated and exhibits a CH-π interaction between the α-methyl group and BINOL.. d) Similar to *Type II E*, *Type II Z* shows a π-π interaction between the aniline moiety and BINOL, as well as a CH-π interaction between the α-methyl group with the 2,4,6-triisopropylphenyl group of the catalyst; for comparison and clarity, a similar orientation as in Figure 3b was adopted. Isovalue 0.5 and a color range between -3.0 to 3.0 were chosen.

Similar to the situation in ***E*-2a**/**1c** complexes, several characteristic dispersive interactions can also be identified in ***Z*-2a**/**1c** complexes (Figure 5c,d). While in the conformation *Type I Z* the α–methyl substituent has a CH-π interaction with the binapthyl moiety of the catalyst, the conformation *Type II Z* has a distinctive π-π interaction (T-shape) between the aniline part and the binapthyl moiety of the catalyst. In this case, we expect that some of the protons of the aniline are shielded by the aromatic ring. Furthermore, it is also recognizable that the α-methyl substituent in *Type II Z* interacts weakly with the 2,4,6-triisopropylphenyl group of the catalyst (see the Supporting Information for a rotated picture). Therefore, it is expected that the protons of the α–methyl in both conformations *Type II Z* and *Type I Z* experience similar shielding effects.

In all conformations (*Type I/II E/Z*), the NCI analysis showed also many weak dispersive interactions between the 3,3' substituent of the catalyst and the aniline/ketone part of the substrate. This demonstrates that these interactions, which often serve as a target for modulation to achieve high stereoselectivity in synthetic application, are already preformed and pronounced in the binary complexes. However, the NCI analysis as a whole suggests that modifications both of the 3,3' substituent and of the binaphthyl backbone are important targets for catalyst design.

NMR Studies. At 300 K, the 1:1 mixtures of imine/**1c** complexes show only one averaged set of ^{1}H signals for the Brønsted acid catalyst, whereas two sets of signals are detected for each imine, corresponding to their *E*- and *Z*-isomers with *E*/*Z* ratios ranging from 80:20 to 70:30 (for details, see the Supporting Information). By lowering the temperature to 180 K, two complete sets of signals, one of an *E*-imine/**1c** complex and one of a *Z*-imine/**1c** complex, are observed. Even at 180 K, an exchange between *E*-imine inside the *E*-imine/**1c** complex and *E*-imine outside the complex takes place. This exchange is slow on the NMR time scale and leads to an additional set of signals for the *E*-imine. An in depth investigation of the hydrogen bonds revealed for all imines a mainly ion-paired character for both *E* and *Z* complexes at 180 K and a fixed geometry of the hydrogen bond.[14] Using various homo- and heteronuclear 2D spectra, ^{1}H and ^{13}C chemical shift assignments of the *Z*- and *E*-imines as well as a complete chemical shift assignment of the ^{1}H signals of the imine/binaphthyl core structure were achieved (for details, see the Supporting Information).

The *E* Imine/1c Complexes NOE studies were conducted in order to determine the structure of the complexes present in solution. Considering the experimentally detected high percentage of *E*-imine complexes (70-80%) and the computationally calculated preference for

structure *Type I E*, the NOE between the varying functional groups of imines **2a-c** and **3a-b** and the binaphthyl backbone of **1c** should be most pronounced.

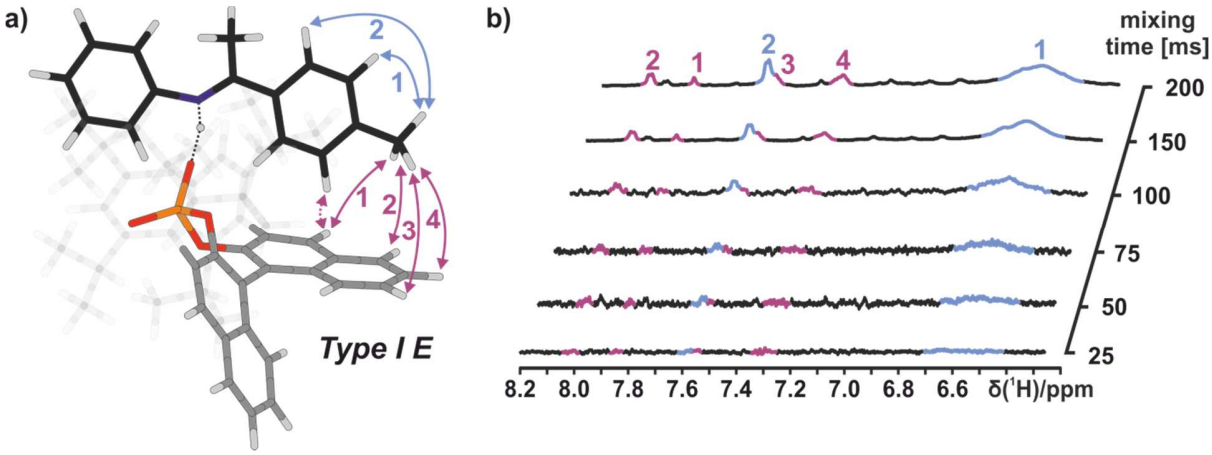

Figure 6. a) Calculated structure *Type I E* of ***E*-2a**/**1c** corroborated by inter- (red arrows) and intramolecular NOEs (blue arrows); b) corresponding experimental data from 1D selective NOESY spectra at 180 K in CD_2Cl_2 (see the Supporting Information for additional data).

Selective 1D ^{1}H,^{1}H-NOESY spectra of the *p*-methyl group of ***E*-2a** were used to identify the predicted NOEs unambiguously (see Figure 6). Selective NOE buildup curves of the ***E*-2a**/**1c** complex show deviations from linearity even below a 100 ms mixing time, similar to small proteins. Therefore, only qualitative analysis of intermolecular distances is possible. Selective 1D ^{1}H,^{1}H NOESY spectra with mixing times of 150 ms were further used for the detection of intermolecular NOEs between the catalyst and the imine, in order to gain NOE intensity with as little chemical exchange as possible. For complexes **2b**/**1c** and **3a**/**1c**, the same NOE pattern was found by exciting the functional groups of the acetophenone parts of the *E*-imines with selective NOESY spectra (for spectra, see the Supporting Information). For imines **2b** and **3a**, ^{1}H,^{19}F HOESY spectra with mixing times of 500 ms were successfully used to identify NOEs between the *p*-trifluoromethyl groups and the binaphthyl backbone of the catalyst. In conclusion, for every investigated *E*-imine/**1c** complex, the same NOE pattern can be observed between the different functional groups of the acetophenone moiety of the imine (*p*-Me, *p*-MeO, and *p*-CF_3) and the binaphtyl backbone of **1c** (for 1D ^{1}H,^{1}H NOESY spectra and 2D ^{1}H,^{19}F HOESY spectra of the other complexes, see the Supporting Information). Thus, independent of the electronic properties of the imines, all complexes show a strong population of structure *Type I E*.

The identification of structure *Type II E* in complex **2a**/**1c**, which showed an imine orientation similar to the crystal structure,[3] is by far more complicated. According to the calculations, *Type II E* is less populated and the aniline signals providing the crucial NOE information show broad line widths. In addition, the expected NOE intensities between the aniline moiety and the binaphtyl backbone of the catalyst are further weakened by rotation. Therefore, imines **3a** and **3b** were used, which enable the measurement of selective 1D ^{1}H,^{1}H NOESY spectra by exciting the methoxy group of the anisidine moiety. The best signal dispersion was found in ***E*-3a**/**1c** (see Figure 7). The identified NOE pattern reveals a proximity of the anisidine moiety of the imine to the binaphtyl backbone of the catalyst (see Figure 7b). Since structures *Type I E* and *Type II E* are observed simultaneously, a fast exchange between both structures must occur, even at 180 K. In principle, the two structures are related by two potential exchange modes. Either the imine rotates by 180° under retention of the hydrogen bond or the imine switches the oxygen that constitutes the hydrogen bond and is thereby tilted inside the complex. Due to the extended shape of the *E*-imine and the steric configuration of the catalyst, the latter is more likely to occur. In comparison to structure *Type I E*, the NOE interaction in *Type II E* takes place on the other naphthyl half of the catalyst backbone (see Figure 7a). This experimentally proves that exchange occurs via the tilting mechanism (an exchange of *Type I E* and *Type II E* by rotation of the imine would lead to an interaction between both the acetophenone and anisidine moiety with the same naphthyl side of the catalyst). For the aniline derived imines **2a-c**, even a weak NOE between the aniline moiety of the imines and the binaphthyl backbone of **1c** was observed with the help of longer mixing times (300 ms) in 2D ^{1}H,^{1}H NOESY spectra. This proves the existence of *Type II E* for all investigated complexes (see the Supporting Information for spectra).[24]

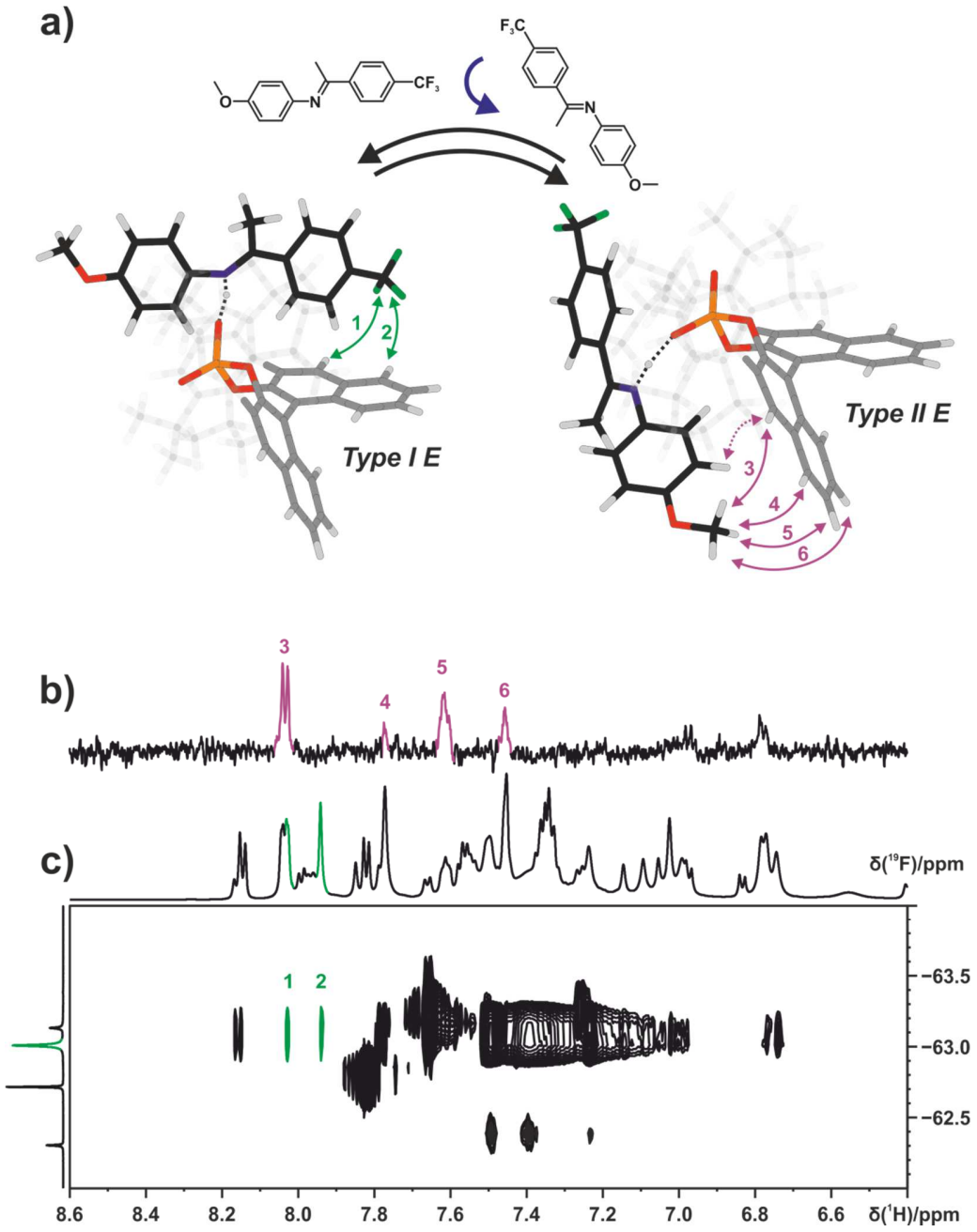

Figure 7. a) Tilting of the imine ***E*-3a** in relation to the catalyst **1c**. The observed NOE pattern (green and purple arrows) reveals the coexistence of complex structures *Type I E* and *Type II E*, which are in fast exchange on the NMR time scale at 180 K in CD_2Cl_2; b) section of a 1D selective NOESY of ***E*-3a**/**1c** at 180 K in CD_2Cl_2 at 600 MHz (excitation on the methoxy group of imine ***E*-3a**) showing intermolecular NOEs 3-6 corresponding to structure *Type II E*; c) section of a $^{1}H,^{19}F$ HOESY spectrum of ***E*-3a**/**1c** at 180 K in CD_2Cl_2 at 600 MHz showing NOEs 1 and 2 corresponding to structure *Type I E*.

In addition to the analysis of the NOE pattern, also the proton chemical shift pattern confirms the tilting process (switching the oxygen that forms the hydrogen bond) as the only exchange mode for *E*-imine/**1c** complexes. The two structures *Type I E* and *Type II E* exchange fast on the NMR time scale and produce only one set of chemical shifts. Within this assignment for any *E*-imine/**1c** combination, separated sets of chemical shifts are observed for the two naphthyl parts (Figure 8, blue and green colored peaks; for assignment and details, see the Supporting Information). In general, this chemical shift pattern can only be observed if one of the two described exchange processes (tilting or rotation) occurs exclusively. For the *E* complexes, tilting takes place (see above and Figure 7a). In cases where both exchange processes (tilting and rotation) are active, the complex would be symmetrized and an averaged set of signals for both halves of the binaphthyl backbone would be observed (see *Z*-imine/**1c** complexes and Figure 10 below).

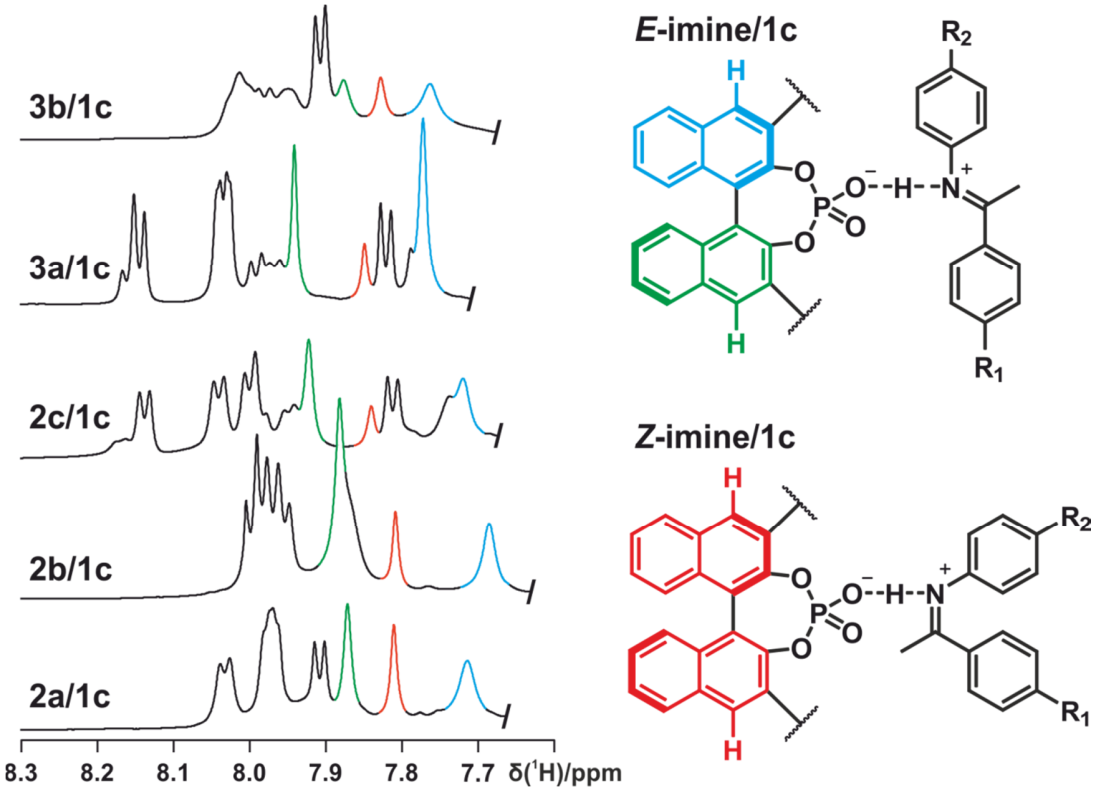

Figure 8. ^{1}H chemical shifts of the protons of the binaphthyl backbone of complexes **2a-c**/**1c** and **3a-b**/**1c** at 180 K in CD_2Cl_2 at 600 MHz. In every investigated sample, the asymmetry of the catalyst is preserved for the *E*-imine/**1c** complexes but broken for the *Z*-imine/**1c** complexes.

Both the experimental and theoretical chemical shift analyses of the *E*-imine/**1c** complexes reveal strong high field shifts of the *p*-methyl group and the nearby aromatic protons again

corroborating *Type I E* (see Figures 5a and 6a for structures and Figure 9 for spectra). In the structure of ***E*-2a**/**1c,** the *p*-methyl group is effectively shielded by the naphthyl backbone of the catalyst, while, with HBF_4 as the noncoordinating protonating agent, no shielding can occur. This results in a high field shift of the *p*-methyl group in ***E*-2a**/**1c** compared to ***E*-2a**/HBF_4 ($\Delta\delta_{exp}$, 0.37 ppm; $\Delta\delta_{calc}$, 0.66 ppm) (see Figure 9 and the Supporting Information). Since the *p*-methyl group in *Type II E* is not shielded (see Figure 5b), the exchange between *Type I E* and *Type II E* leads to a reduction of the shielding effect caused by the binaphthyl moiety in *Type I E*. In the calculation of the chemical shielding analysis, only *Type I E* is considered, resulting in a larger chemical shift difference ($\Delta\delta_{calc}$: 0.66 ppm). Thus, the offset between calculated and experimentally determined Δδ corroborates the coexistence of *Type I E* and *Type II E*.

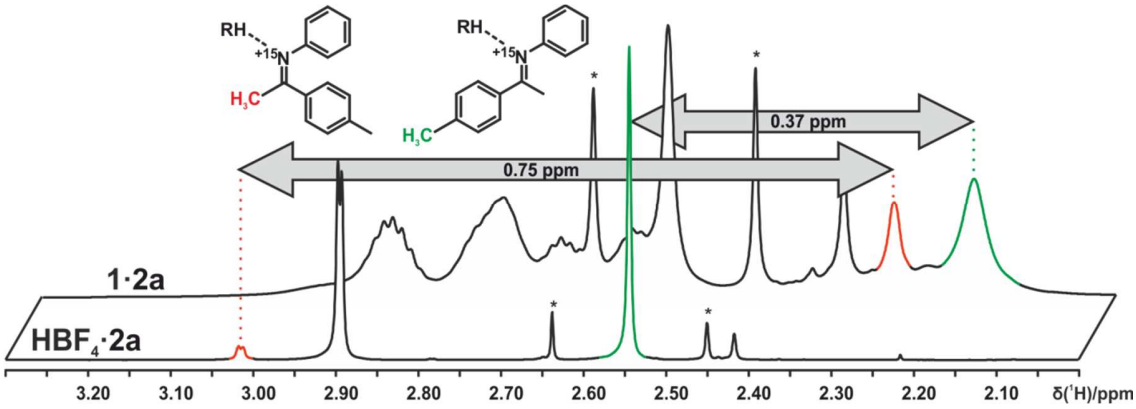

Figure 9. Shielding effects on methyl groups of **2a**/**1c** due to CH-π interactions between the methyl groups and the extended aromatic systems of the catalyst. Free protonated imine was simulated with HBF_4, and the chemical shifts were compared to the imine/**1c** complexes (180 K in CD_2Cl_2, 600 MHz).

The Z Imine/1c Complexes The calculated energy differences between the two structures *Type II Z* and *Type I Z* ranging from 4.9 to 9.5 kJ/mol are similar to those between *Type I E* and *Type II E*. Again, a preference for *Type II Z* is expected. Similar to the *E*-imine/**1c** complex, the two structures *Type II Z* and *Type I Z* are in principle related by rotation of the imine by 180° without breaking the hydrogen bond, or by tilting the imine inside the complex and thereby switching the oxygen that forms the hydrogen bond. In comparison to *Type I E* and *Type II E*, only one averaged set of signals can be observed for both naphthyl halves of the catalyst backbone (see Figure 8). By exciting the α-methyl group of ***Z*-2a** in the **2a**/**1c** complex in a selective 1D $^1H,^1H$ NOESY spectrum, structures *Type II Z* and *Type I Z* were identified simultaneously (see Figure 10b). Due to the reduced steric hindrance of the *Z*-imine compared to the *E*-imine, an exchange between the two complex structures *Type II Z* and *Type I Z* is

possible by rotation, as well as tilting of the imine (see Figure 10a). This explains the broken asymmetry of the catalyst in the *Z*-imine/**1c** complexes (see Figure 8). With the help of selective 1D ^{1}H,^{1}H NOESY spectra, the exact same situation was identified for all investigated *Z*-imine/**1c** complexes (see the Supporting Information for spectra).

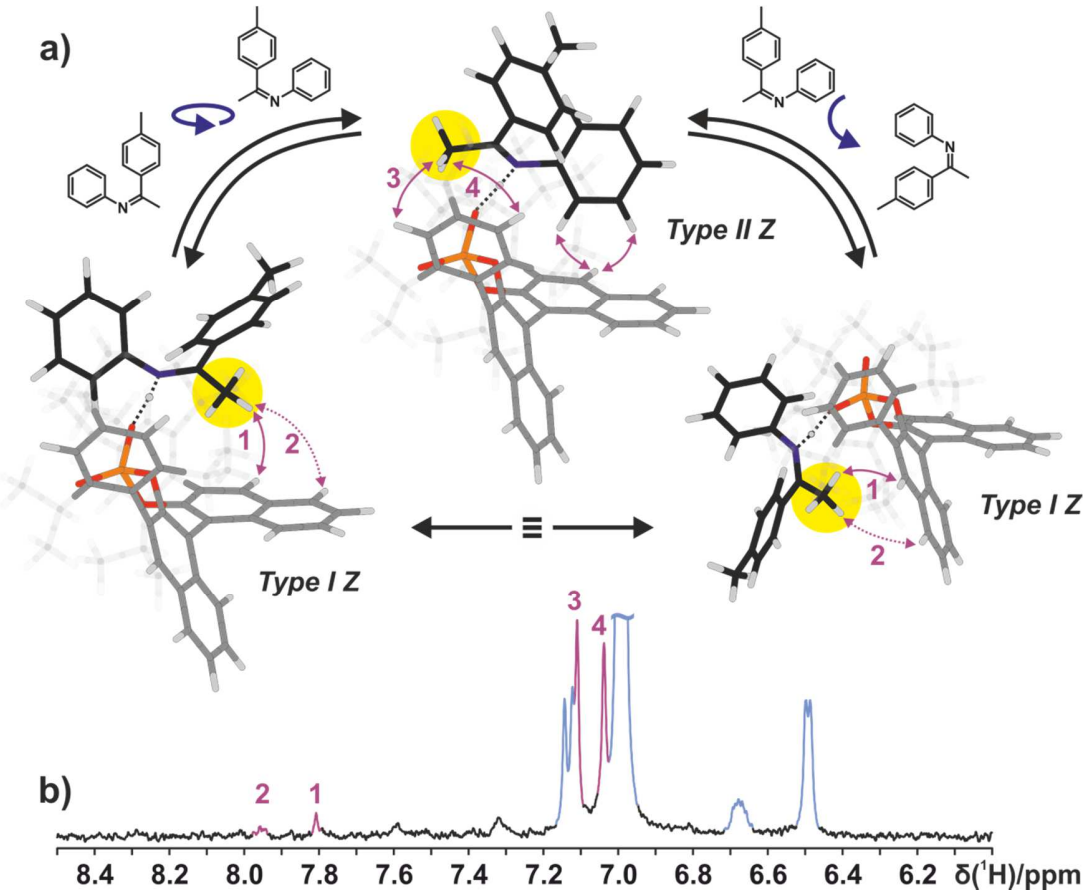

Figure 10. a) NOE pattern (purple arrows) found for the investigated ***Z*-2a**/**1c** complexes. The intramolecular NOEs could not be assigned to a single structure *Type II Z* or *Type I Z*, but instead show that an equilibrium of both structures exists in solution (see the Supporting Information for additional parameters). b) Section of a selective 1D ^{1}H,^{1}H NOESY excited on the α-methyl group (yellow circle in part a) of ***Z*-2a** at 180 K in CD_2Cl_2 at 600 MHz.

Moreover, the comparison of experimental and theoretical chemical shifts of ***Z*-2a**/**1c** fits to the Boltzmann weighted average of *Type II Z* and *Type I Z*. Both structures show a close proximity of the α-methyl group to either the 2,4,6-triisopropylphenyl moiety (*Type II Z*) or the binaphthyl backbone of the catalyst (*Type I Z*), which leads to a strong high field shift for the respective methyl group due to CH-π interactions ($\Delta\delta_{exp}$, 0.75 ppm; $\Delta\delta_{calc}$, 0.74 ppm; see Figure 9).

2.4 Conclusion

By means of NMR and theoretical calculations, we were able to identify the structure of binary complexes, consisting of the chiral phosphoric acid **1c** and *E*-/*Z*-isomers of aromatic imines. All *E*-imine/catalyst complexes possess two structures, which are in fast exchange on the NMR time scale even at 180 K. Due to the extended steric properties of the *E*-imine, this exchange occurs by tilting the imine inside the complex and thereby switching the oxygen that constitutes the hydrogen bond. This preserves the asymmetry of the *E*–imine/catalyst complexes. Additionally, the structure of the *Z*-imine/catalyst complexes was determined for the first time. For all *Z*-imine/catalyst complexes, a similar exchange process between two structures was observed. However, the compact structure of the *Z*-imine enables an additional exchange pathway by rotation, symmetrizing the catalyst. For all investigated imine/*R*-TRIP (3,3′-bis(2,4,6-triisopropylphenyl)-1,1′-binaphthyl-2,2′-diyl hydrogen phosphate) complexes, dispersive interactions between substrate and catalyst were identified not only at the 3,3' substituents of the catalyst but at the binaphthyl backbone as well, revealing the importance of modifications at this moiety for catalyst design. The four presented core structures are highly preserved; i.e., these core structures were found to be independent of electron density and substituent modulations of the aromatic imines. This invariance of the structures across all imine substrates reflects the strength of this class of catalysts. Extended dispersive interactions between catalyst and substrate, which are postulated to provide high stereoselectivities in the transition states, are preformed in the binary complex, while the strong hydrogen bond allows for a high substrate tolerance. For example, for phosphoramidites, it is known that variations in the electron density of the substrate often have to be compensated by changes in the ligand structure.[28] The structural investigations presented here show that in Brønsted acid catalysis the strength of the hydrogen bond overrides the variations in the CH-π and π-π interactions caused by different functional groups of the substrates. Assuming that these structural features of the binary complexes are preserved in the transition states, Brønsted acid catalysis seems to combine both, high stereoinduction due to dispersive interactions and structural invariance caused by the hydrogen bond.

2.5 References

(1) Akiyama, T.; Itoh, J.; Yokota, K.; Fuchibe, K. *Angew. Chem. Int. Ed.* **2004**, *43*, 1566–1568.

(2) Uraguchi, D.; Terada, M. *J. Am. Chem. Soc.* **2004**, *126*, 5356–5357.

(3) Storer, R. I.; Carrera, D. E.; Ni, Y.; MacMillan, D. W. C. *J. Am. Chem. Soc.* **2006**, *128*, 84–86.

(4) Rueping, M.; Sugiono, E.; Azap, C.; Theissmann, T. *Org. Lett.* **2005**, *7*, 3781–3783.

(5) Hoffmann, S.; Seayad, A. M.; List, B. *Angew. Chem. Int. Ed.* **2005,** *44***,** 7424‑7427.

(6) Rueping, M.; Sugiono, E.; Azap, C. *Angew. Chem. Int. Ed.* **2006**, *45*, 2617–2619.

(7) Mahlau, M.; List, B. *Angew. Chem.* **2013**, *125*, 540–556.

(8) Marcelli, T.; Hammar, P.; Himo, F. *Chem. - Eur. J.* **2008**, *14*, 8562–8571.

(9) Simón, L.; Goodman, J. M. *J. Am. Chem. Soc.* **2008**, *130*, 8741–8747.

(10) Tang, W.; Johnston, S.; Iggo, J. a; Berry, N. G.; Phelan, M.; Lian, L.; Bacsa, J.; Xiao, J. *Angew. Chem. Int. Ed.* **2013**, *52*, 1668–1672.

(11) Kim, H.; Sugiono, E.; Nagata, Y.; Wagner, M.; Bonn, M.; Rueping, M.; Hunger, J. *ACS Catal.* **2015**, *5*, 6630–6633.

(12) Merten, C.; Pollok, C. H.; Liao, S.; List, B. *Angew. Chem. Int. Ed.* **2015**, *54*, 8841–8845.

(13) Fleischmann, M.; Drettwan, D.; Sugiono, E.; Rueping, M.; Gschwind, R. M. *Angew. Chem.* **2011**, *123*, 6488–6493.

(14) Sorgenfrei, N.; Hioe, J.; Greindl, J.; Rothermel, K.; Morana, F.; Lokesh, N.; Gschwind, R. M. *J. Am. Chem. Soc.* **2016**, *138,* 16345–16354

(15) Siegel, J. S.; Anet, F. A. L. *J. Org. Chem.* **1988**, *53*, 2629–2630.

(16) Tao, J.; Perdew, J. P.; Staroverov, V. N.; Scuseria, G. E. *Phys. Rev. Lett.* **2003**, *91*, 146401.

(17) Marenich, A. V; Cramer, C. J.; Truhlar, D. G. *J. Phys. Chem B.* **2009**, *113*, 6378–6396.

(18) Grimme, S.; Antony, J.; Ehrlich, S.; Krieg, H. *J. Chem. Phys.* **2010**, *132*, 154104.

(19) Weigend, F.; Furche, F.; Ahlrichs, R. *J. Chem. Phys.* **2003**, *119*, 12753–12762.

(20) Weigend, F.; Ahlrichs, R. *Phys. Chem. Chem. Phys.***2005**, *7*, 3297–3305.

(21) Grimme, S. *J. Chem. Phys.* **2003**, *118*, 9095–9102.

(22) Neese, F. *Wiley Interdiscip. Rev. Comput. Mol. Sci.* **2012**, *2*, 73–78.

(23) Frisch, M. J.; Trucks, G. W.; Schlegel, H. B.; Scuseria, G. E.; Robb, M. A.; Cheeseman, J. R.; Scalmani, G.; Barone, V.; Mennucci, B.; Petersson, G. A.; Nakatsuji, H.; Caricato, M.; Li, X.; Hratchian, H. P.; Izmaylov, A. F.; Bloino, J.; Zheng, G.; Sonnenberg, J. L.; Hada, M.; Ehara, M.; Toyota, K.; Fukuda, R.; Hasegawa, J.; Ishida, M.; Nakajima, T.; Honda, Y.; Kitao, O.; Nakai, H.; Vreven, T.; Montgomery, J. A., Jr.; Peralta, J. E.; Ogliaro, F.; Bearpark, M.; Heyd, J. J.; Brothers, E.; Kudin, K. N.; Staroverov, V. N.; Kobayashi, R.; Normand, J.; Raghavachari, K.; Rendell, A.; Burant, J. C.; Iyengar, S. S.; Tomasi, J.; Cossi, M.; Rega, N.; Millam, J. M.; Klene, M.; Knox, J. E.; Cross, J. B.; Bakken, V.; Adamo, C.; Jaramillo, J.; Gomperts, R.; Stratmann, R. E.; Yazyev, O.; Austin, A. J.; Cammi, R.; Pomelli, C.; Ochterski, J. W.; Martin, R. L.; Morokuma, K.; Zakrzewski, V. G.; Voth, G. A.; Salvador, P.; Dannenberg, J. J.; Dapprich, S.; Daniels, A. D.; Farkas, Ö.; Foresman, J. B.; Ortiz, J. V.; Cioslowski, J.; Fox, D. J. *Gaussian* 09, revision D.01; Gaussian, Inc., Wallingford CT, 2009

(24) The simulation at 180 K showed a Boltzmann population of Z-imine/catalyst complexes less than 1% relative to the E-imine/catalyst complexes. This is in agreement with the experiment which proved that no *Z*-imine/catalyst complexes were found when the complex was synthesized at 180 K.

(25) A quantitative analysis to determine the experimental ratio between *Type I E* and *Type II E* is currently not possible due to long mixing times and the inaccuracy of the distance measurements.

(26) Johnson, E. R., Keinan S., Mori-Sánchez, P., Contreras-García J., Cohen, A. J., Yang, W. *J. Am. Chem. Soc.* **2010**, *132*, 6498-6506.

(27) Contreras-García J., Johnson, E. R., Keinan S., Chaudret, R., Piquemal J. P., Beratan, D. N., Yang, W. *J. Chem. Theory Comput.* **2011**, *7*, 625-632.

(28) Hartmann, E.; Hammer, M. M.; Gschwind, R. M. *Chem. –Eur. J.* **2013**, *19*, 10551–10562.

2.6 Supporting Information

Deuterated solvents were purchased from Deutero or Sigma Aldrich Where dry solvents were essential, CD_2Cl_2 was freshly distilled over CaH_2 and Toluene-d8 was refluxed over Na/Benzophenone under Argon atmosphere. Freon mixtures were prepared from $CDCl_3$ and $SbCl_5/SbF_3$ according to literature procedures and stored in small lecture bottles. The catalysts were purchased from Sigma Aldrich or synthesized from the bisphenols according the procedure of Klussmann et al.

High resolution mass spectra were measured by the central analytics division in the Institute of Organic Chemistry. Gas chromatography coupled with a mass selective detector was performed on an Agilent 6890N Network GC-System.

2.6.1 Synthesis of Ketimines

Imines were synthesized by refluxing aniline and the corresponding ketone over activated molecular sieves 4 Å in toluene. The toluene was used either in p.A. quality or was dried by refluxing over sodium.

(E)-1-(4-methylphenly)-N-phenylethan1-imine [2a]

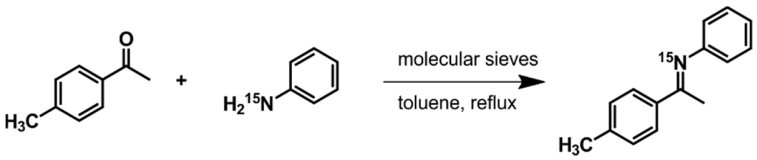

Molecular sieves 4 Å (1.6 g) were weighed in to a 25 ml Schlenk flask equipped with a reflux condenser. The setup dried at 350°C under reduced pressure. 4-Methylacetophenone (0.403 g, 3.00 mmol, 0.40 ml) and Aniline (98% ^{15}N, 0.30 ml, 0.310 g, 3.30 mmol) were dissolved in 5 ml anhydrous Toluene under argon atmosphere. A drying tube filled with $CaCl_2$ was added to the setup and the solution was refluxed for 20 h. After cooling down to r.t., the yellow solution was filtered and the solvent was removed under reduced pressure. The obtained yellow solid was recrystallized in methanol and yielded as a yellow solid (0.123 g, 0.58 mmol, 20 %) predominantly as *E*-Isomer (>99 % via ^{1}H-NMR analysis).

^{1}H-NMR (400.1 MHz, CD_2Cl_2) δ_H = 7.86 (m, 2H), 7.34 (m, 2H), 7.25 (m, 2H), 7.06 (m, 1H), 6.76 (m, 2H), 2.40 (s, 3H) 2.18 ppm (d, $^{3}J_{HN}$ = 1.76 Hz, 3H)

^{13}C-NMR {^{1}H} (100.6 MHz): δ_C = 165.3 (d, $^{1}J_{NC}$ = 7.0 Hz), 152.4 (d, $^{1}J_{NC}$ = 1.6 Hz), 137.3 ($^{2}J_{NC}$ = 8.3 Hz), 129.34, 129.29 (d, $^{3}J_{NC}$ = 3.2 Hz), 127.5 (J_{NC} = 3.2), 123.3, 123.9, 119.7 ($^{2}J_{NC}$ = 2.3 Hz), 21.5, 17.4 ppm (d, $^{2}J_{NC}$ = 2.8 Hz)

^{15}N-NMR (40.5 MHz): δ_N = 328.9 ppm

HR-MS (ESI, *m/z*): found 211.1248 (M+H)+ (calculated for 211.1248 for $C_{15}H_{16}[^{15}N]O$); Diff(ppm) = -0.37

(E)-1-(4-methoxyphenyl)-N-phenylethan-1-imine (98% 15N) [2b]

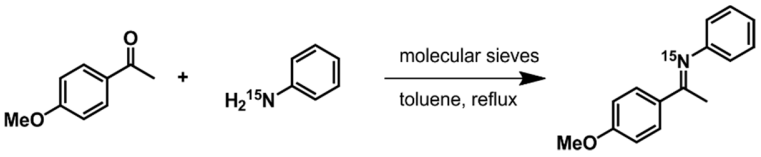

Molecular sieves 4 Å (1.6 g) were weighed in to a 25 ml Schlenk flask equipped with a reflux condenser. The setup dried at 350°C under reduced pressure. 4-Methoxyacetophenone (0.450 g, 3.00 mmol) and Aniline (98% ^{15}N, 0.30 ml, 0.310 g, 3.30 mmol) were dissolved in 5 ml anhydrous Toluene under argon atmosphere. A drying tube filled with $CaCl_2$ was added to the setup and the solution was refluxed for 20 h. After cooling down to r.t., the yellow solution was filtered and the solvent was removed under reduced pressure. The obtained yellow solid was recrystallized in methanol and yielded as a yellow solid (0.223 g, 0.986 mmol, 33 %) predominantly as E-Isomer (>99 % via ^1H-NMR analysis).

^{1}H-NMR (400.1 MHz, CD_2Cl_2) δ_H = 7.95 (m, 2H), 7.35 (m, 2H), 7.07 (m, 1H), 6.96 (m, 2H), 6.77 (m, 2H), 2.18 ppm (d, $^3J_{HN}$ = 1.76 Hz)

^{13}C-NMR {^{1}H} (100.6 MHz, CD_2Cl_2): δ_C = 164.5 (d, $^1J_{NC}$ = 7.1 Hz), 161.9, 152.5 (d, $^2J_{NC}$ = 1.7 Hz), 132.5 (d, $^1J_{NC}$) = 8.4 Hz), 129.2, 129.1 (d, $^3J_{NC}$ = 3.3 Hz), 123.2, 119.8 (d, $^2J_{NC}$ = 2.3 Hz), 113.8, 55.7, 17.2 ppm (d, $^2J_{NC}$ = 2.7 Hz)

^{15}N-NMR (40.5 MHz, CD2Cl2): δ_N = 325.5 ppm

HR-MS (ESI, *m/z*): found 227.1198 (M+H)+ (calculated 227.1197 for $C_{15}H_{16}[^{15}N]O$); Diff(ppm) = 0.49

(E)-N-phenyl-1-(4-(trifluoromethyl)phenyl)ethan-1-imine (98% 15N**) [2c]**

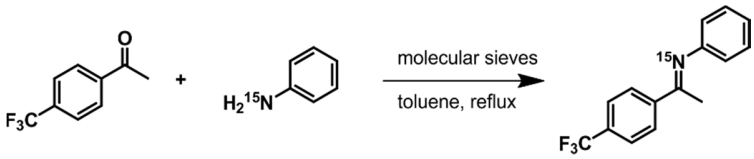

Molecular sieves 4 Å (1.6 g) were weighed in to a 25 ml Schlenk flask equipped with a reflux condenser. The setup dried at 350°C under reduced pressure. 4-Trifluoromethylacetophenone (0.376 g, 2.00 mmol) and Aniline (98% ^{15}N, 0.20 ml, 0.207 g, 2.20 mmol) were dissolved in 5 ml anhydrous Toluene under argon atmosphere. A drying tube filled with $CaCl_2$ was added to the setup and the solution was refluxed for 20 h. After cooling down to r.t., the yellow solution was filtered and the solvent was removed under reduced pressure. The obtained yellow solid was recrystallized in methanol and yielded as a yellow solid (0.340 g, 1.29 mmol, 64 %) predominantly as E-Isomer (>99 % via ^{1}H-NMR analysis).

^{1}H-NMR (400.1 MHz, CD_2Cl_2): δ_H = 8.11 (m, 2H), 7.73 (m, 2H), 7.38 (m, 2H), 7.12 (m, 1H), 6.80 (m, 2H), 2.25 ppm (d, $^{3}J_{NH}$ = 1.8 Hz, 3H)

^{13}C-NMR {^{1}H} (100.6 MHz): δ_C = 164.5 (d, $^{1}J_{NC}$ = 7.1 Hz), 151.7 (d, ^{1}JNC = 1.5 Hz), 143.2 ($^{2}J_{NC}$ = 7.3 Hz), 132.1 (q, $^{2}J_{FC}$ = 32.4 Hz) 129.4, 128.0 (d, $^{3}J_{NC}$ = 3.2 Hz),125.6 (q, $^{4}J_{FC}$ = 3.8 Hz), 124.6 (q, $^{1}J_{FC}$ = 272.0 Hz), 123.9, 119.5 ($^{2}J_{NC}$ = 2.3 Hz), 17.5 ppm (d, $^{2}J_{NC}$ = 2.8 Hz)

^{19}F-NMR {^{1}H} (376 MHz, CD_2Cl_2): δ_F = - 63.1 ppm

^{15}N-NMR (60.8 MHz, CD_2Cl_2, 300 K): δ_N = 338.2 ppm

GC-MS (EI, 70 EV): *m/z* (RT) = 264.1 [M+] (8.794 min)

HR-MS (ESI, *m/z*): found 265.097 (M+H)+ (calculated 265.0965 for $C_{15}H_{13}F_3[^{15}N]$); Diff(ppm) = 1.89

(E)-N-(4-methoxyphenyl)-1-(4-(trifluoromethyl)phenyl)ethan-1-imine **[3a]**

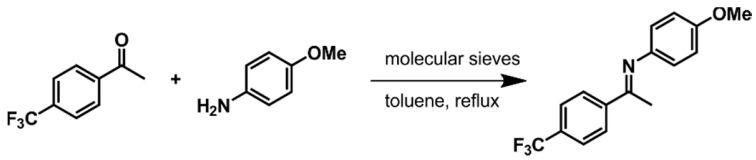

Molecular sieves 4 Å (1.6 g) were weighed in to a 25 ml Schlenk flask equipped with a reflux condenser. The setup dried at 350°C under reduced pressure. 4-Trifluoromethylacetophenone (0.565 g, 3.00 mmol) and Anisidine (0.406 g, 3.30 mmol) were dissolved in 5 ml anhydrous Toluene under argon atmosphere. A drying tube filled with $CaCl_2$ was added to the setup and the solution was refluxed for 20 h. After cooling down to r.t., the yellow solution was filtered and the solvent was removed under reduced pressure. The obtained yellow solid was recrystallized in methanol and yielded as a yellow solid (0.612 g, 2.09 mmol, 70 %) predominantly as E-Isomer (>99 % via ^{1}H-NMR analysis).

^{1}H-NMR (400.1 MHz, $CDCl_3$): δ_H = 8.00 (d, $^3J_{HH}$ = 8.2 Hz, 2H), 7.63 (d, $^3J_{HH}$ = 8.2 Hz, 2H), 6.86 (d, $^3J_{HH}$ = 8.2 Hz, 2H), 6.70 (d, $^3J_{HH}$ = 8.1 Hz, 2H), 3.76 (s, 3H), 2.22 ppm (s, 3H)

^{13}C-NMR {^{1}H} (100.6 MHz): δ_C = 127.5, 125.3, 120.8, 114.3, 55.5, 17.4 ppm

2.6.2 Sample preparation

Preparation of binary complexes in CD_2Cl_2

Catalyst **1c** was dried for 30 min at 150°C under reduced pressure. Ketimine and **1c** were directly weighed into a 5 mm NMR tube under an inert argon atmosphere. CD_2Cl_2 (0.6 ml) and 1.0 ml of tetramethylsilane atmosphere were added to the tube. The sample was stored in an -80°C freezer. A 1:1 ratio of catalyst/ketamine was used for all samples. A concentration 50 mmol/L was used for samples **2a**/**1c** and **2b**/**1c**. For samples **2c**/**1c** and **3a**/**1c** a concentration of 25 mmol/L was used, due to the limited solubility at low temperatures.

Preparation of binary complexes in freonic solvent mixtures

Catalyst **1c** was dried for 30 min at 150°C under reduced pressure. Ketimine and **1c** were directly weighed into a heavy wall NMR tube equipped with a J. Young valve under an inert argon atmosphere. 1.0 ml of tetramethylsilane atmosphere were added and the sample was connected to a vacuum line. The NMR tube was evacuated and cooled down to 77 K. The freonic solvent mixture was condensed through column filled with P_2O_5 and KOH into the NMR-tube.

2.6.3 Solvent screening

Toluene, dichloromethane, and a freonic solvent mixture of CDF_2Cl and $CDFCl_2$ were chosen as solvents, because of their low melting points (toluene: 178 K, CD_2Cl_2: 176.5 K, $CDF_2Cl/CDFCl_2$: <110 K). Vastly superior linewidths and signal dispersion was observed in CD_2Cl_2 and the freonic solvent mixture (see figure 1). The investigated reaction is reported to work in toluene, as well as dichloromethane, with toluene having superior yields.

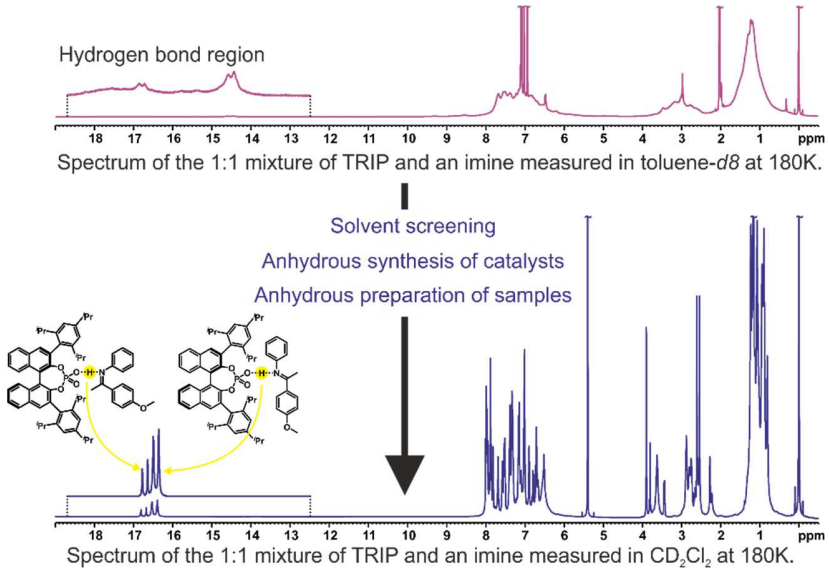

Figure S1: Comparison of ^1H spectra of an imine/catalyst complex at 180 K

The observed signal pattern in the freonic solvent mixture is similar to that observed in dichloromethane. Dichloromethane was used as a solvent for most NMR investigations, due to its better solubility.

2.6.4 Identification of the *E*- and *Z*-imines inside the complex

To identify the *E*- and the *Z*-imine inside the complex, standard 2D ^{1}H,^{1}H-NOESY experiments were performed at 180 K.

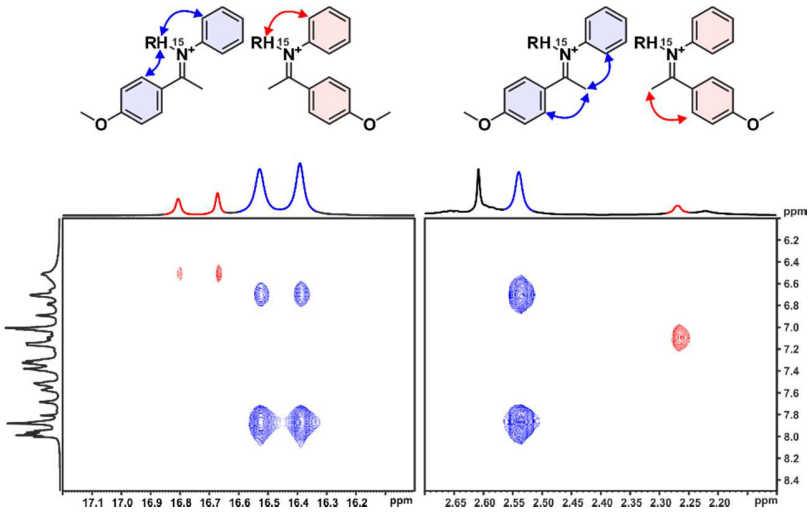

Figure S2: Details of the 2D ^{1}H,^{1}H-NOESY spectrum at 180 K *in dichloromethane*, that was used to identify the E- and the Z-imine inside the imine/catalyst complex. The same pattern was found for every investigated imine.

For the *Z*-imine, the proton inside the hydrogen bond shows only one strong NOE to the aniline part of the imine, whereas for the *E*-imine, an NOE to the aniline part of the imine, as well as an NOE to the acetophenone part of the imine can be found. The methyl group of the *Z*-imine shows only one strong NOE to the acetophenone part of the imine, whereas for the *E*-imine, NOEs to the aniline part and the acetophenone part can be observed (see figure 2). For every investigated imine, the same NOE pattern can be observed.

2.6.5 Assignment of the ^{1}H and ^{13}C chemical shifts

The ^{1}H (black) and ^{13}C (green) chemical shifts of all investigated complexes were assigned with standard 2D NMR experiments ($^{1}H,^{1}H$ COSY, $^{1}H,^{1}H$ TOCSY, $^{1}H,^{1}H$ NOESY, $^{1}H,^{13}C$ HSQC, $^{1}H,^{13}C$ HMBC) at 180 K. Due to signal overlap, the 2,4,6-triisopropylphenyl groups could not be assigned in most cases. The ^{19}F (orange) and ^{15}N (blue) chemical shifts were assigned with $^{1}H,^{19}F$ HMBC and $^{1}H,^{15}N$ HMBC spectra respectively.

Complex 2a/1c

E-2a/1c

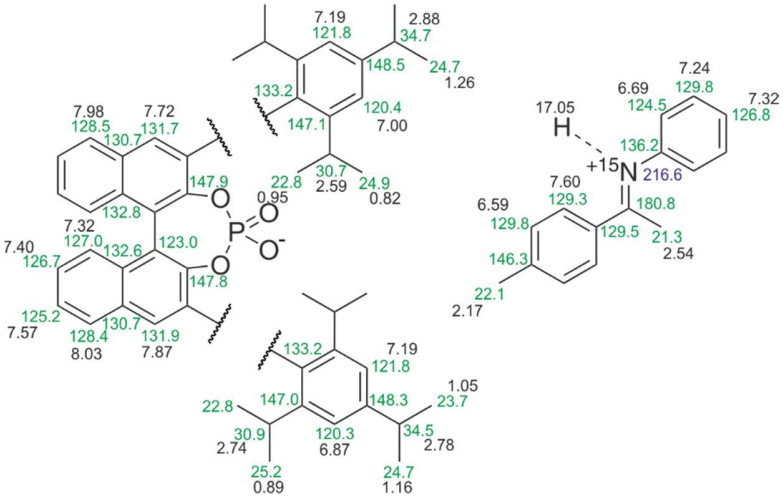

Z-2a/1c

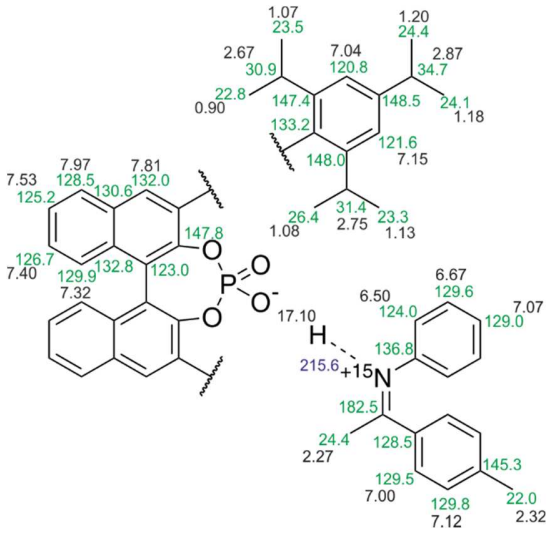

Complex 2b/1c

E-2b/1c

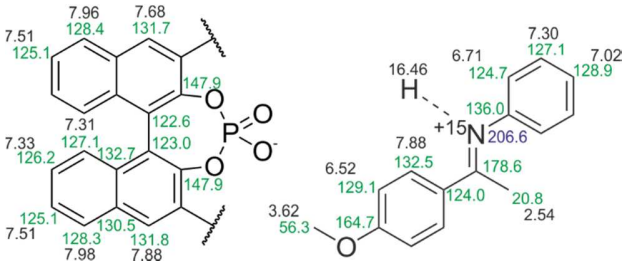

E-2b/1c

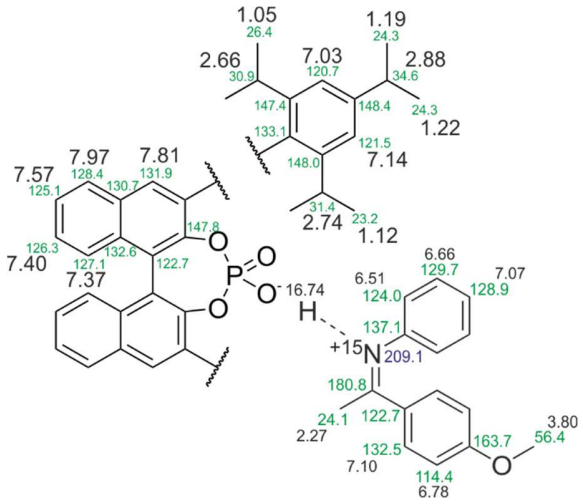

Complex 2c/1c

E-2c/1c

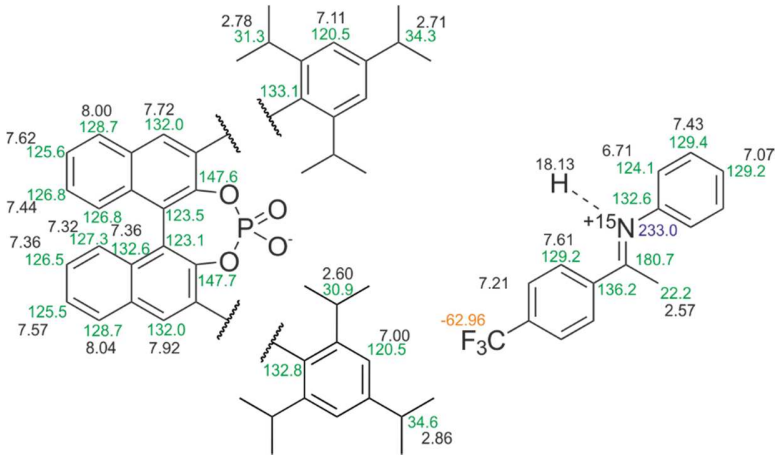

Z-2c/1c

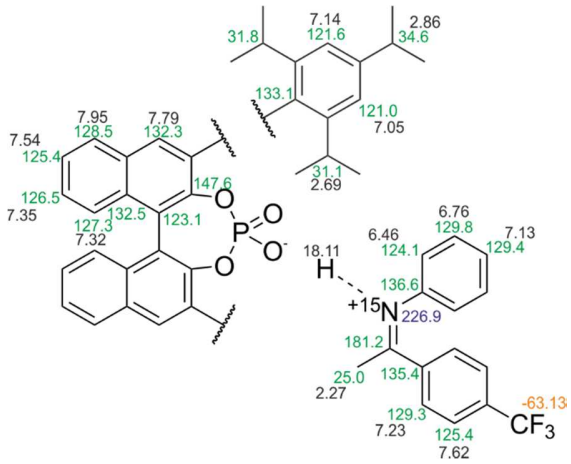

Complex 3a/1c

E-3a/1c

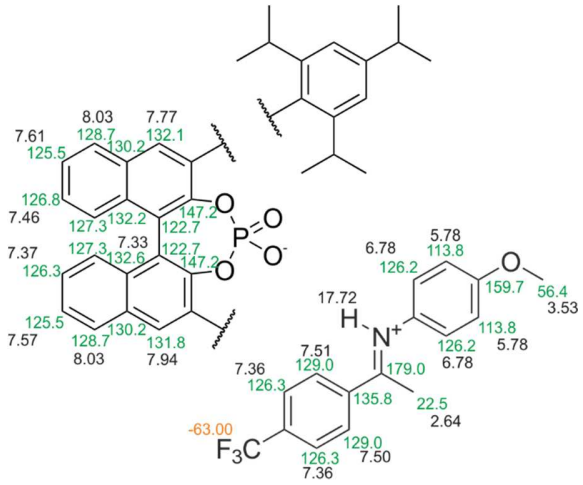

Z-3a/1c

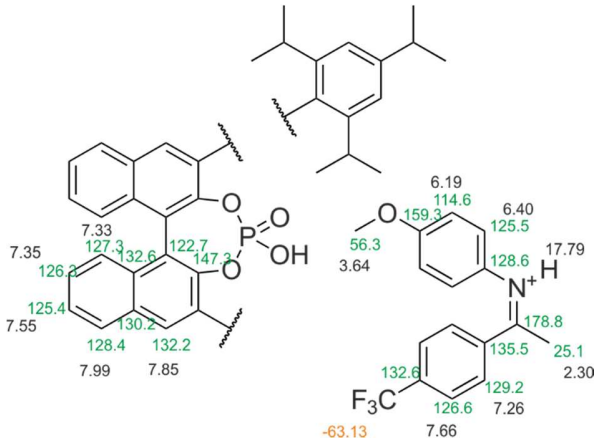

Complex 3b/1c

E-3b/1c

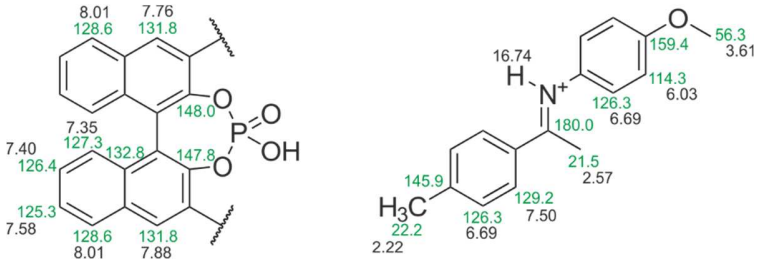

Z-3b/1c

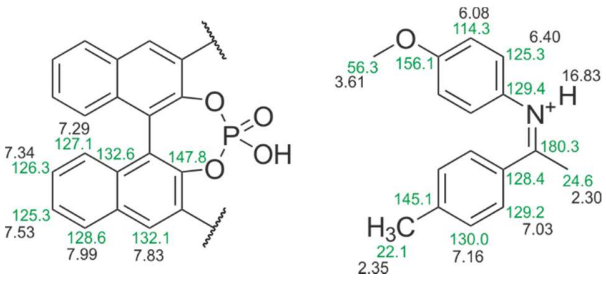

2.6.6 Low temperature measurements in the freonic solvent mixture

The NOE pattern for the investigated *Z*-imine/**1c** complexes showed that a fast exchange on the NMR time scale between two structures takes place, even at 180 K. Therefore we carried out measurements at as low as 130 K, in order to reach the slow exchange regime. For these measurements a freonic solvent mixture of CDF_2Cl and $CDFCl_2$ was used.

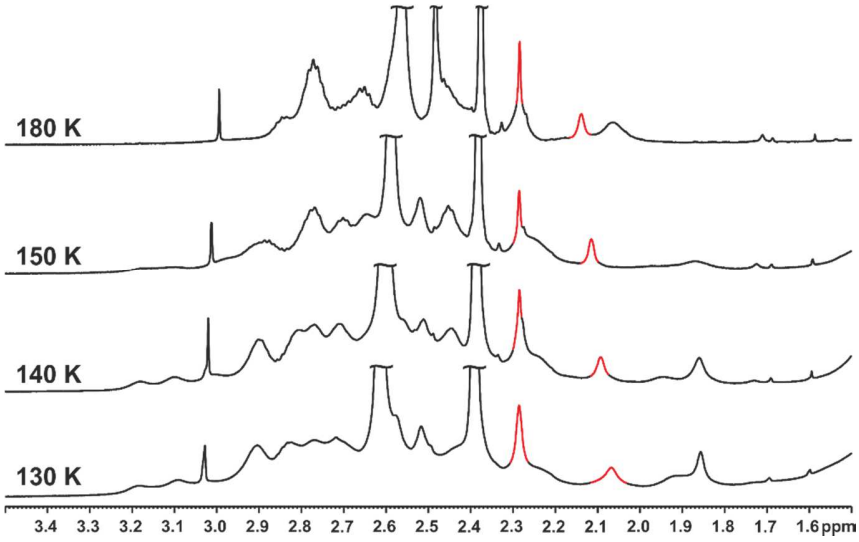

Figure S3: 1H spectra of the 2a/TRIP complex in a mixture of CDFCl2 and CDF2Cl at different temperatures. The signals labeled in red arise from the 4-methyl group and the methyl group of the imine. Compared to the other signal, no substantial line broadening was observed, even at 130 K.

By lowering the temperature, natural line broadening occurs. Even at 130 K, no substantial line broadening was observed for the *Z*-imine, when compared to the other signals.

2.6.7 Structure identification of all *E*-imine/TRIP complexes.

Selective ^{1}H NOESY spectra were used to identify the structures of complexes ***E*-2a-b/1c** in solution. For ***E*-2c/1c** and ***E*-3a/1c**, $^{1}H,^{19}F$ HOESY spectra was used. The spectra were measured in CD_2Cl_2 at 180 K. In every investigated complex, the same orientations of the imine were observed. One orientation (***TYPE I E***)was identified by the NOE pattern between the varying functional groups on the ketone part of the imines and parts of the BINOL backbone of **1c**. In the complexes ***E*-2a-b/1c**, the functional groups, as well as signals of the BINOL backbone were excited in selective ^{1}H NOESY spectra. The other orientation (***TYPE II E***) was identified by 2D $^{1}H,^{1}H$ NOESY spectra with a mixing time if 300 ms for imines **2a-c** and with selective 1D $^{1}H,^{1}H$ NOESY spectra for imines **3a,b**. The methoxy group of the anisidine moiety of the imines was selectively excited in this case. In every investigated sample an exchange between the *E*-Isomer of the imine substrate inside the imine/**1c** complex and the free imine in solution was observed at 180 K. This chemical exchange leads to a variety of exchange peaks between the observed forms of the imine in the selective NOESY spectra. Additional signals are produced by spin diffusion effects inside the extended aromatic system. The exchange peaks and spin diffusion effects can be reduced by shortening the mixing time of the NOESY experiments, which also leads to a tremendous loss of signal intensity.

Additional 1D selective NOESY spectra where measured by exciting the ^{1}H signals of the BINOL backbone of the catalyst. Due to the large signal overlap in the aromatic region, these signals could not be excited selectively and therefor produced ambiguous NOEs. Nevertheless, these NOEs are in full agreement with the identified structure.

E-2a/1c complex

Structure of ***TYPE I E***

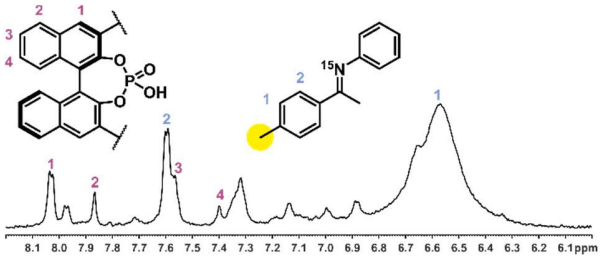

Selective NOESY spectrum of complex ***E*-2a/1c**. The excited methyl group of imine **2a** is labeled yellow. Additional signals are observed, due to chemical exchange and spin diffusion effects.

Structure of ***TYPE II E***

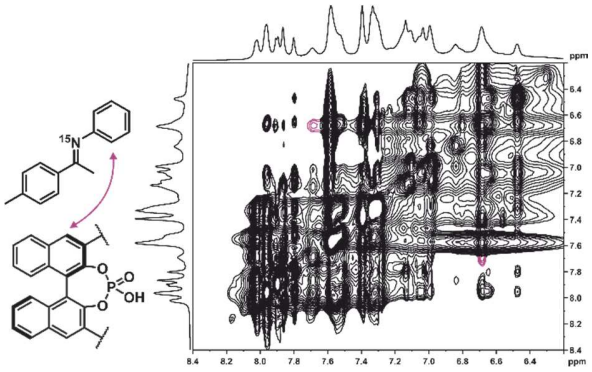

2D ^{1}H,^{1}H NOESY spectrum of complex ***E*-2a/1c**. The NOE that reveals structure ***TYPE II E*** is labeled in purple.

E-2b/1c complex

Structure of ***TYPE I E***

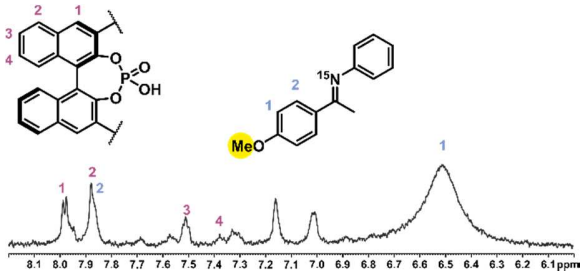

Selective NOESY spectrum of complex ***E*-2b/1c**. The excited methoxy group of imine **2b** is labeled yellow. Additional signals are observed, due to chemical exchange and spin diffusion effects.

Structure of ***TYPE II E***

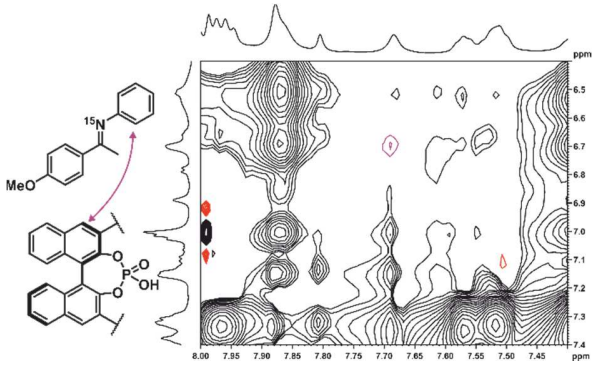

2D ^{1}H,^{1}H NOESY spectrum of complex ***E*-2b/1c**. The NOE that reveals structure ***TYPE II E*** is labeled in purple.

E-2c/1c complex

Structure of ***TYPE I E***

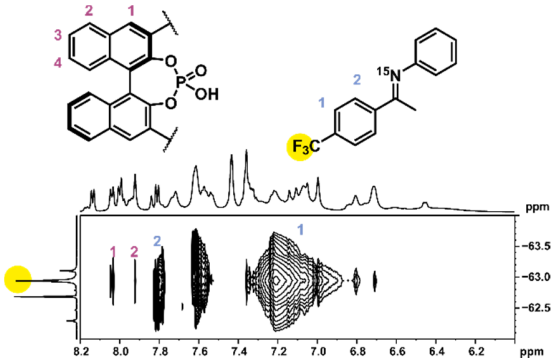

$^{1}H,^{19}F$ HOESY spectrum of complex ***E*-2c/1c**. The trifluoromethyl group of ***E*-2c** inside the complex is labeled yellow. Additional signals are observed, due to chemical exchange and spin diffusion effects.

Structure of ***TYPE II E***

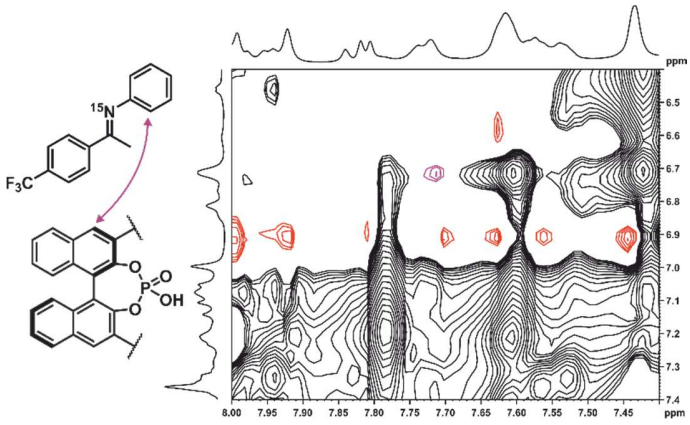

2D $^{1}H,^{1}H$ NOESY spectrum of complex ***E*-2c/1c**. The NOE that reveals structure ***TYPE II E*** is labeled in purple.

E-3a/1c complex

Structure of ***TYPE I E***

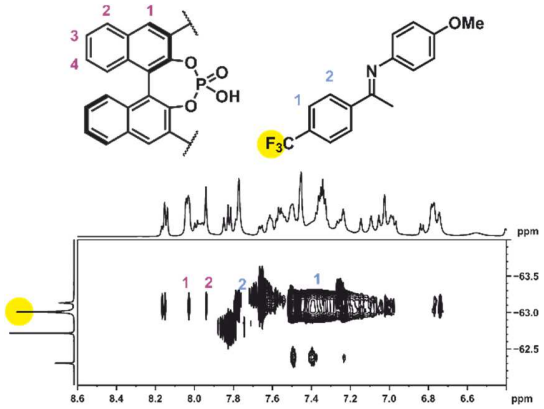

^{1}H,^{19}F HOESY spectrum of complex ***E*-3a/1c**. The trifluoromethyl group of ***E*-3a** inside the complex is labeled yellow. Additional signals are observed, due to chemical exchange and spin diffusion effects.

Structure of ***TYPE II E***

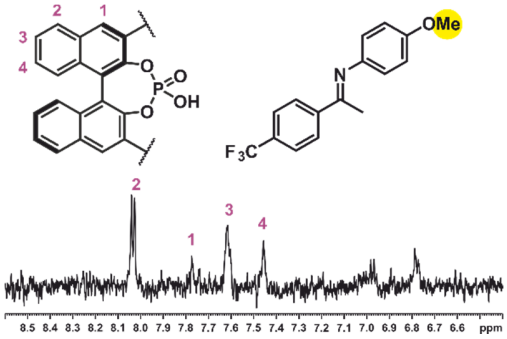

Selective NOESY spectrum of complex ***E*-3a/1c**. The excited methoxy group of imine **3a** is labeled yellow. Additional signals are observed, due to chemical exchange and spin diffusion effects.

E-3b/1c complex

Structure of ***TYPE I E***

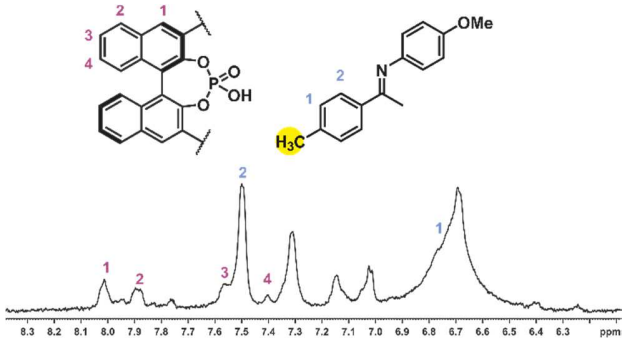

Selective NOESY spectrum of complex ***E*-3b/1c**. The excited methyl group of imine 3**b** is labeled yellow. Additional signals are observed, due to chemical exchange and spin diffusion effects.

Structure of ***TYPE II E***

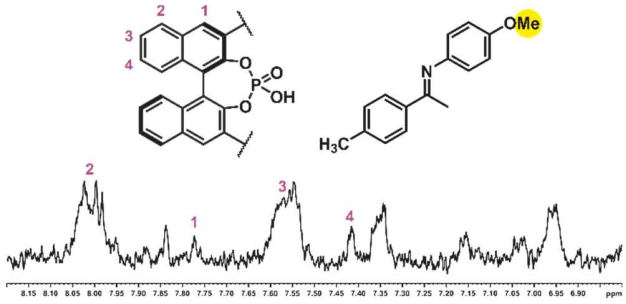

Selective NOESY spectrum of complex ***E*-3b/1c**. The excited methoxy group of imine **3b** is labeled yellow. Additional signals are observed, due to chemical exchange, chemical shift overlap and spin diffusion effects. Especially the overlap of the chemical shifts of the methoxy groups of both *E*- and *Z*-imine in complex **3b**/**1c** leads to many additional peaks in the selective NOESY.

2.6.8 Build-up curve

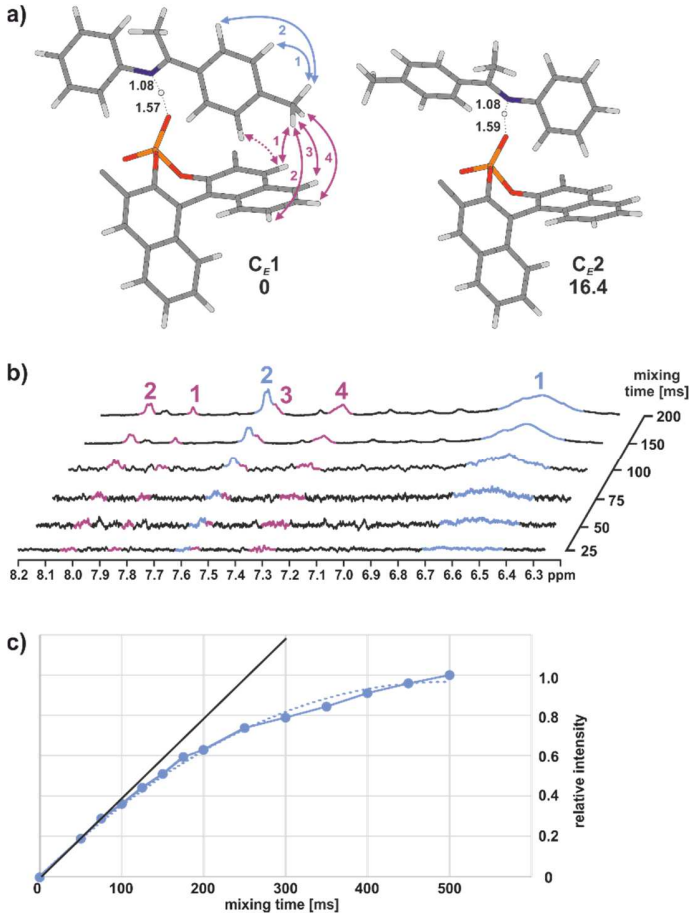

Figure S4; a) Complex structures ***TYPE I E*** and ***TYPE II E*** of complex ***E*-2a**/**1c**; b) Selective 1D NOESY build up curve; the α-methyl group of the imine was excited; c) Build-up of the intensity of intramolecular NOE 1 (blue arrow in a)), a deviation from a linear build is visible even at 100 ms mixing time, due to spin diffusion effects.

2.6.9 Structure identification of all *Z*-imine/TRIP complexes.

Selective ^{1}H NOESY spectra were used to identify the structures of complexes ***Z*-2a-c**/**1c** and ***Z*-3a**/**1c** in solution. In every investigated complex, the same NOE pattern was observed. The spectra were measured in CD_2Cl_2 at 180 K.

Z-2a/1c complex

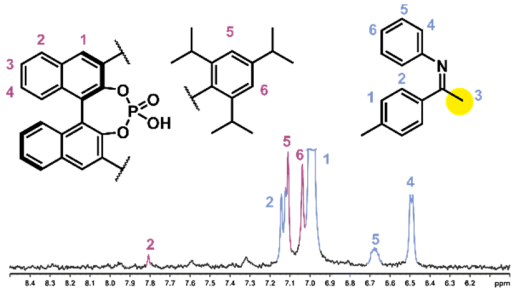

Selective NOESY spectrum of complex ***Z*-2a**/**1c**. The excited methyl group of imine **2a** is labeled yellow.

Z-2b/1c complex

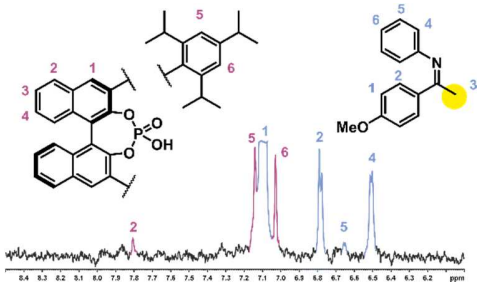

Selective NOESY spectrum of complex ***Z*-2b**/**1c**. The excited methyl group of imine **2b** is labeled yellow.

Z-2c/1c complex

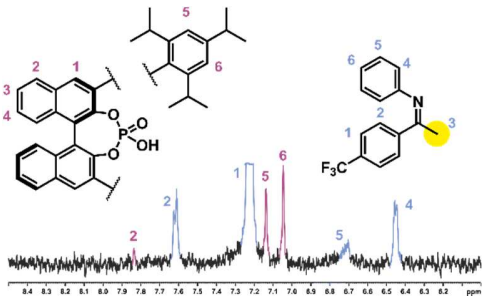

Selective NOESY spectrum of complex ***Z*-2c**/**1c**. The excited methyl group of imine **2c** is labeled yellow.

Z-3a/1c complex

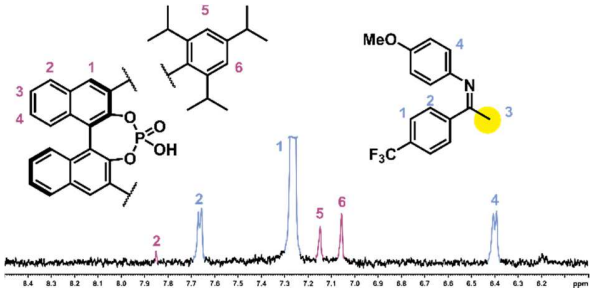

Selective NOESY spectrum of complex ***Z*-3a**/**1c**. The excited methyl group of imine **3a** is labeled yellow.

Z-3b/1c complex

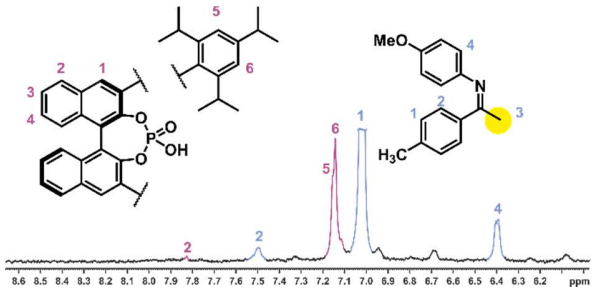

Selective NOESY spectrum of complex ***Z*-3b**/**1c**. The excited methyl group of imine **3b** is labeled yellow.

2.6.10 Chemical shift analysis of the 2a/1c complexes

The measured ^{1}H chemical shifts of the imine inside the complex are compared to the calculated chemical shifts.

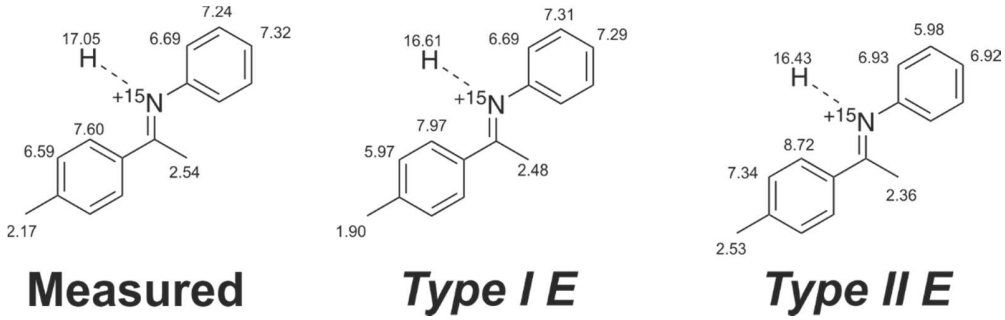

The calculated chemical shifts of complex ***TYPE I E*** show the same trend as the measured chemical shifts of the complex ***E*-2a/1c** in dichloromethane at 180 K. The strong high field shift of the *p*-methyl group and the nearby aromatic proton are a result of the strong deshielding due to the CH/π interaction of these protons and the BINOL backbone of the catalyst.

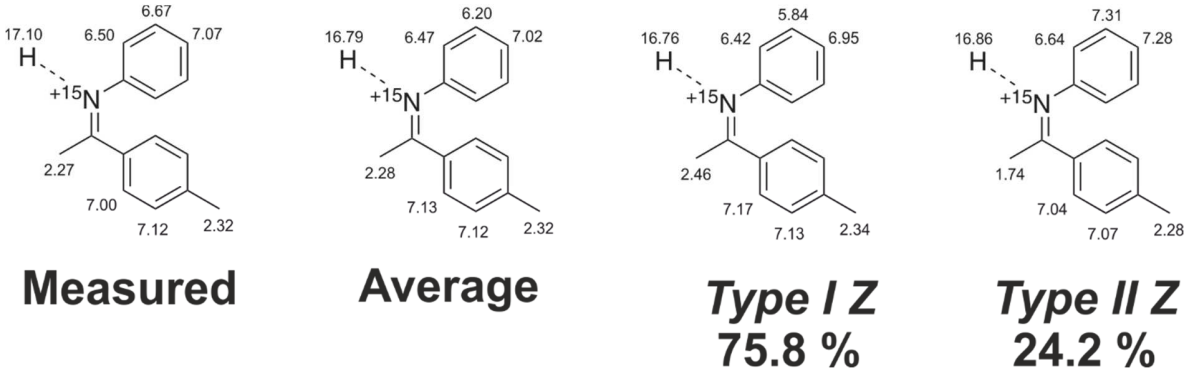

The weighted and averaged chemical shifts of the calculated structures *TYPE II Z* and *TYPE I Z* are in good agreement with the measured shifts of complex ***E*-2a/1c** in dichloromethane at 180 K.

2.6.11 Spectrometer data

NMR experiments were performed on Bruker Avance III HD 400 MHz spectrometer, equipped with 5 mm BBO BB-1H/D probe head with Z-Gradients and a Bruker Avance III HD 600 MHz spectrometer, equipped with a 5 mm TBI 1H/19. Temperature was controlled in the VT-experiments by BVT 3000 and BVTE 3900. For NMR measurements employing standard NMR solvents 5 mm NMR tubes were used, if not other noted. For samples in freonic mixtures as solvents, 5 mm heavy wall (1.4 mm wall thickness) NMR tubes equipped with J. Young valves from Wilmad were used. NMR Data were processed, evaluated and plotted with TopSpin 3.2 software. Further plotting of the spectra was performed with Corel Draw X14 – X17 software. ^{1}H,^{13}C chemical shifts were referenced to TMS or the respective solvent signals. The heteronuclei ^{15}N,^{19}F and were referenced, employing $\nu(X) = \nu(TMS) \times \Xi_{reference} / 100$ % according to Harris et al. The following frequency ratios and reference compounds were used: $\Xi(^{15}N) = 10.132912$ (lq. NH_3) and $\Xi(^{19}F) = 94.094011$ (CCl_3F)

Pulse programs

All pulse programs used are standard Bruker NMR pulse programs.

Acquisition Parameters

^{1}H NMR: Pulse program: zg; Relaxation delay = 2 – 3 s, Acquisition time = 2.48 s, SW = 22.0 ppm, TD = 64k, NS = 8 – 64; zg30; Relaxation delay = 2 s, Acquisition time = 2.48 s, SW = 22.0 ppm, TD = 64k, NS = 8 – 64;

2D-^{1}H,^{1}H NOESY: Pulse program: noesygpph; Relaxation delay = 5 - 8 s, NS = 8-32, mixing time (D8) = 300.00 ms; TD = 4096; increments = 512 - 1k;

2D-^{1}H,^{1}H COSY: Pulse program: cosygpqf; Relaxation delay = 5 - 8 s, NS = 8-32, TD = 4096; increments = 512 - 1k;

^{13}C NMR: Pulse program: zgpg30; Relaxation delay = 2.00 s, Acquisition time = 0.80 s, SW = 270.0 ppm, TD = 64k, NS = 1k – 2k;

2D-^{1}H,^{13}C HSQC: Pulse program: hsqcedetgpsisp2.3; Relaxation delay = 4 - 8 s, NS = 8-32, $^{1}J_{XH}$ = 145 Hz; TD = 4096; increments = 512 - 1k;

2D-^{1}H,^{13}C HMBC: Pulse program: hmbcgplpndqf; Relaxation delay = 4 - 8 s, NS = 8-32, $^{1}J_{XH}$ = 145 Hz, J_{XH}(long range) = 10 Hz; TD = 4096; increments = 512 - 1k;

^{15}N NMR: Pulse program: zg; Relaxation delay = 10.00 s, Acquisition time = 0.54 s, SW = 502.8 ppm, TD = 32k, NS = 256 – 2048;

2D-^{1}H,^{15}N HMBC: Pulse program: inv4gplrndqf; Relaxation delay = 5 - 8 s, NS = 16-32, delay for evolution of long range couplings (D6) = 20.00 ms; TD = 4096; increments = 128 - 512;

^{19}F-NMR: Pulse program: zg30; Relaxation delay = 2 – 3 s, Acquisition time = 11.60 s, SW = 10.0 ppm, TD = 128k, NS = 8 – 64;

2D-^{1}H,^{19}F HOESY: Pulse program: hoesyph; Relaxation delay = 5 - 8 s, NS = 16-32, mixing time (D8) = 500.00 ms; TD = 4096; increments = 1k;

Selective 1D-^{1}H,^{1}H NOESY: Pulse program: selnogp; Relaxation delay = 5 - 8 s, NS = 128-2k, mixing time (D8) = 25 – 1000 ms (150 – 200 ms and NS = 1k-2k for structure identification); TD = 64k; 180° shaped pulse = 50 – 150 ms, shape = Gauss 180;

2.6.12 Data of the theoretical calculations

The CBS basis set extrapolation proceeds under the two point extrapolation procedure (eq.1 – 3) as in implemented in ORCA3.0.3 with the basis set Def2-SVP and Def2-TZVP.

$$E_{\mathrm{SCF}}^{X} = E_{\mathrm{SCF}}^{\infty} + Ae^{-\alpha\sqrt{X}} \qquad \text{eq. 1}$$

$$E_{\mathrm{corr,MP2}}^{\infty} = \frac{X^{\beta}E_{\mathrm{corr,MP2}}^{X} - (X-1)^{\beta}E_{\mathrm{corr,MP2}}^{X-1}}{X^{\beta} - (X-1)^{\beta}} \qquad \text{eq.2}$$

$$E_{\mathrm{MP2}}^{\infty} = E_{\mathrm{corr,MP2}}^{\infty} + E_{\mathrm{SCF}}^{\infty} \qquad \text{eq. 3}$$

Since low vibrations can cause significant error in the calculation of entropy, the harmonic approximation is corrected using the procedure by Grimme, which employs a weighted partition function between harmonic and free rotor approximations.

NCI analysis

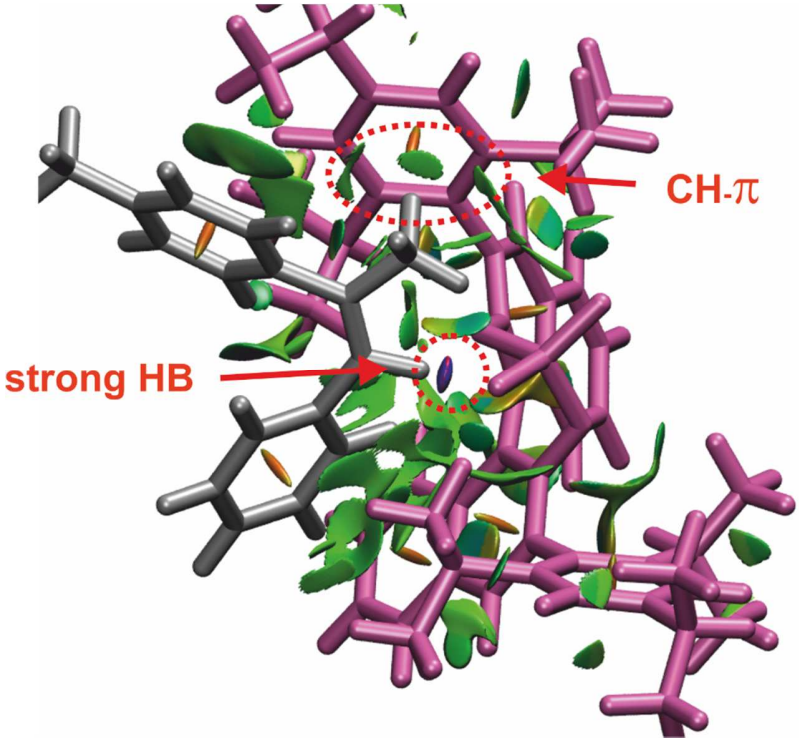

Figure S5. NCI analysis of Z-2a/1c *Type II*. Rotated view to highlight CH-π interaction between α-methyl group of the imine and 2,4,6-triisopropylphenyl group of the catalyst.

Table S1. Calculated energies of the (*R*)-TRIP imine complexes the solution phase

	Etot TPSS-D3	G180 TPSS-D3	Nimag	G180,solv. SCS-MP2
	Def2-SVP	Def2-SVP		CBS
me-ketimine/TRIP				
E-2a/1c conf0 (Type I)	-3216.1293034	-3214.9779909	0	-3210.8402178
E-2a/1c conf1 (Type I)	-3216.1292922	-3214.9783768	0	-3210.8405949
E-2a/1c conf2 (Type I)	-3216.1281091	-3214.9776036	0	-3210.8404332
E-2a/1c conf0 (Type II)	-3216.1288254	-3214.9770885	0	-3210.8379438
E-2a/1c conf1 (Type II)	-3216.1288923	-3214.9771949	0	-3210.8380750
E-2a/1c conf2 (Type II)	-3216.1281937	-3214.9763154	0	-3210.8371123
Z-2a/1c conf0 (Type II)	-3216.1239436	-3214.9742384	0	-3210.8370365
Z-2a/1c conf1 (Type II)	-3216.1239479	-3214.9737243	0	-3210.8365321
Z-2a/1c conf2 (Type II)	-3216.1230459	-3214.9719391	0	-3210.8358809
Z-2a/1c conf3 (Type II)	-3216.1243248	-3214.9733132	0	-3210.8352594
Z-2a/1c conf0 (Type I)	-3216.1216601	-3214.9718608	0	-3210.8346718
Z-2a/1c conf1 (Type I)	-3216.1216456	-3214.9716979	0	-3210.8346181
Z-2a/1c conf2 (Type I)	-3216.1212309	-3214.9701984	0	-3210.8321087

ome-ketimine/TRIP				
E-2b/1c conf0 (Type I)	-3291.2958062	-3290.143671	0	-3285.9698539
E-2b/1c conf1 (Type I)	-3291.2957223	-3290.143170	0	-3285.9693529
E-2b/1c conf2 (Type I)	-3291.2947169	-3290.142961	0	-3285.9689460
E-2b/1c conf0 (Type II)	-3291.2952666	-3290.143039	0	-3285.9678192
E-2b/1c conf1 (Type II)	-3291.2940632	-3290.142076	0	-3285.9676053
E-2b/1c conf2 (Type II)	-3291.2955281	-3290.141910	0	-3285.9676420
E-2b/1c conf3 (Type II)	-3291.2942653	-3290.141420	0	-3285.9668046
E-2b/1c conf4 (Type II)	-3291.2942222	-3290.141566	0	-3285.9673435
E-2b/1c conf5 (Type II)	-3291.2953907	-3290.142301	0	-3285.9680170
Z-2b/1c conf0 (Type II)	-3291.2881317	-3290.138687	0	-3285.9654871
Z-2b/1c conf1 (Type II)	-3291.2880073	-3290.138259	0	-3285.9657424
Z-2b/1c conf2 (Type II)	-3291.2873514	-3290.136991	0	-3285.9656882
Z-2b/1c conf3 (Type II)	-3291.2887209	-3290.139127	0	-3285.9655835
Z-2b/1c conf4 (Type II)	-3291.2881877	-3290.137369	0	-3285.9655633
Z-2b/1c conf5 (Type II)	-3291.2881191	-3290.138095	0	-3285.9654841
Z-2b/1c conf6 (Type II)	-3291.2873533	-3290.136156	0	-3285.9647129

Z-2b/1c conf7 (Type II)	-3291.2887316	-3290.138912	0	-3285.9650782
Z-2b/1c conf0 (Type I)	-3291.2861415	-3290.135660	0	-3285.9628199
Z-2b/1c conf1 (Type I)	-3291.2861924	-3290.135523	0	-3285.9628561
Z-2b/1c conf2 (Type I)	-3291.2858786	-3290.134948	0	-3285.9615452
Z-2b/1c conf3 (Type I)	-3291.2863205	-3290.137066	0	-3285.9639722
Z-2b/1c conf4 (Type I)	-3291.2864156	-3290.136289	0	-3285.9632361
Z-2b/1c conf5 (Type I)	-3291.2860152	-3290.137701	0	-3285.9634013
cf3-ketimine/TRIP				
E-2c/1c conf0 (Type I)	-3513.6465830	-3512.5205064	0	-3508.3958759
E-2c/1c conf1 (Type I)	-3513.6465235	-3512.5207007	0	-3508.3960729
E-2c/1c conf2 (Type I)	-3513.6457328	-3512.5204823	0	-3508.3959762
E-2c/1c conf0 (Type II)	-3513.6375353	-3512.5171876	0	-3508.3919597
E-2c/1c conf1 (Type II)	-3513.6375690	-3512.5187441	0	-3508.3936257
E-2c/1c conf2 (Type II)	-3513.6372055	-3512.5172824	0	-3508.3923135
Z-2c/1c conf0 (Type II)	-3513.6411194	-3512.5141016	0	-3508.3916784
Z-2c/1c conf1 (Type II)	-3513.6411936	-3512.5140964	0	-3508.3917285

Z-2c/1c conf2 (Type II)	-3513.6399301	-3512.5135202	0	-3508.3919537
Z-2c/1c conf3 (Type II)	-3513.6416873	-3512.5142537	0	-3508.3903968
Z-2c/1c conf0 (Type I)	-3513.6375353	-3512.5110397	0	-3508.3897986
Z-2c/1c conf1 (Type I)	-3513.6375690	-3512.5114201	0	-3508.3900476
Z-2c/1c conf2 (Type I)	-3513.6372055	-3512.5104673	0	-3508.3876702
ome-cf3-ketimine/TRIP				
E-3a/1c conf0 (Type I)	-3628.111866	-3626.9518503	0	-3622.7355951
E-3a/1c conf1 (Type I)	-3628.111719	-3626.9517008	0	-3622.7359474
E-3a/1c conf2 (Type I)	-3628.110813	-3626.9529548	0	-3622.7367638
E-3a/1c conf3 (Type I)	-3628.112400	-3626.9534522	0	-3622.7374813
E-3a/1c conf4 (Type I)	-3628.112112	-3626.9539513	0	-3622.7383783
E-3a/1c conf5 (Type I)	-3628.111580	-3626.9526340	0	-3622.7359897
E-3a/1c conf0 (Type II)	-3628.111930	-3626.9529648	0	-3622.7347878
E-3a/1c conf1 (Type II)	-3628.112139	-3626.9524390	0	-3622.7341516
E-3a/1c conf2 (Type II)	-3628.111372	-3626.9519985	0	-3622.7342329

Z-3a/1c conf0 (Type II)	-3628.106399	-3626.9475052	0	-3622.7332675
Z-3a/1c conf1 (Type II)	-3628.106393	-3626.9473794	0	-3622.7330704
Z-3a/1c conf2 (Type II)	-3628.104956	-3626.9463497	0	-3622.7331959
Z-3a/1c conf3 (Type II)	-3628.107676	-3626.9492683	0	-3622.7338728
Z-3a/1c conf0 (Type I)	-3628.101010	-3626.9434394	0	-3622.7305094
Z-3a/1c conf1 (Type I)	-3628.101616	-3626.9416407	0	-3622.7262811
Z-3a/1c conf2 (Type I)	-3628.101561	-3626.9436228	0	-3622.7309610
Z-3a/1c conf3 (Type I)	-3628.101626	-3626.9438736	0	-3622.7311135
Z-3a/1c conf4 (Type I)	-3628.101963	-3626.9422244	0	-3622.7264107
ome-ch3-ketimine/TRIP				
E-3b/1c conf0 (Type I)	-3330.592144	-3329.4088051	0	-3325.1805363
E-3b/1c conf1 (Type I)	-3330.592006	-3329.4089581	0	-3325.1810063
E-3b/1c conf2 (Type I)	-3330.591542	-3329.4093499	0	-3325.1804439
E-3b/1c conf3 (Type I)	-3330.593070	-3329.4106280	0	-3325.1822841
E-3b/1c conf4 (Type I)	-3330.592881	-3329.4105133	0	-3325.1823263
E-3b/1c conf0 (Type II)	-3330.594000	-3329.4103556	0	-3325.1787176

E-3b/1c conf1 (Type II)	-3330.593958	-3329.4105325	0	-3325.1790970
E-3b/1c conf2 (Type II)	-3330.593524	-3329.4096527	0	-3325.1785529
Z-3b/1c conf0 (Type II)	-3330.588810	-3329.4073733	0	-3325.1791460
Z-3b/1c conf1 (Type II)	-3330.588676	-3329.4071171	0	-3325.1788328
Z-3b/1c conf2 (Type II)	-3330.587739	-3329.4052449	0	-3325.1780921
Z-3b/1c conf3 (Type II)	-3330.589223	-3329.4070524	0	-3325.1776291
Z-3b/1c conf0 (Type I)	-3330.584634	-3329.4032057	0	-3325.1753078
Z-3b/1c conf1 (Type I)	-3330.584538	-3329.4035100	0	-3325.1754672
Z-3b/1c conf2 (Type I)	-3330.584521	-3329.4023288	0	-3325.1726030
Z-3b/1c conf3 (Type I)	-3330.585319	-3329.4033326	0	-3325.1751190
Z-3b/1c conf4 (Type I)	-3330.585216	-3329.4032161	0	-3325.1751941
Z-3b/1c conf5 (Type I)	-3330.584905	-3329.4038217	0	-3325.1740197
ome-no2-ketimine/TRIP				
E-3c/1c conf0 (Type I)	-3495.681803	-3494.5237310	0	-3490.2561506
E-3c/1c conf1 (Type I)	-3495.681937	-3494.5233009	0	-3490.2559409
E-3c/1c conf2 (Type I)	-3495.681214	-3494.5223690	0	-3490.2543048

E-3c/1c conf0 (Type II)	-3495.683907	-3494.5256113	0	-3490.2545437
E-3c/1c conf1 (Type II)	-3495.683703	-3494.5247775	0	-3490.2537381
E-3c/1c conf2 (Type II)	-3495.682741	-3494.5247566	0	-3490.2541695

AdditionalSupporting Information, especially the computational data are provided free of charge at http://pubs.acs.org/

2.6.13 References

[1] J. Siegel, F. Anet, *J. Org. Chem.* **1988**, *9*, 2629–2630.

[2] I. G. Shenderovich, A. P. Burtsev, G. S. Denisov, N. S. Golubev, H.-H. Limbach, *Magn. Reson. Chem.* **2001**, *39*, 91–99.

[3] M. Klussmann, L. Ratjen, S. Hoffmann, V. Wakchaure, R. Goddard, B. List, *Synlett* **2010**, *2010*, 2189–2192.

[4] M. Rueping, E. Sugiono, C. Azap, T. Theissmann, *Org. Lett.* **2005**, *7*, 3781–3783.

[5] S. Hoffmann, A. M. Seayad, B. List, *Angew. Chemie Int. Ed.* **2005**, *44*, 7424–7427.

[6] R. K. Harris, E. D. Becker, S. M. Cabral de Menezes, R. Goodfellow, P. Granger, *Magn. Reson. Chem.* **2002**, *40*, 489–505.

3 NMR Spectroscopic Characterization of Charge Assisted Strong Hydrogen Bonds in Brønsted Acid Catalysis

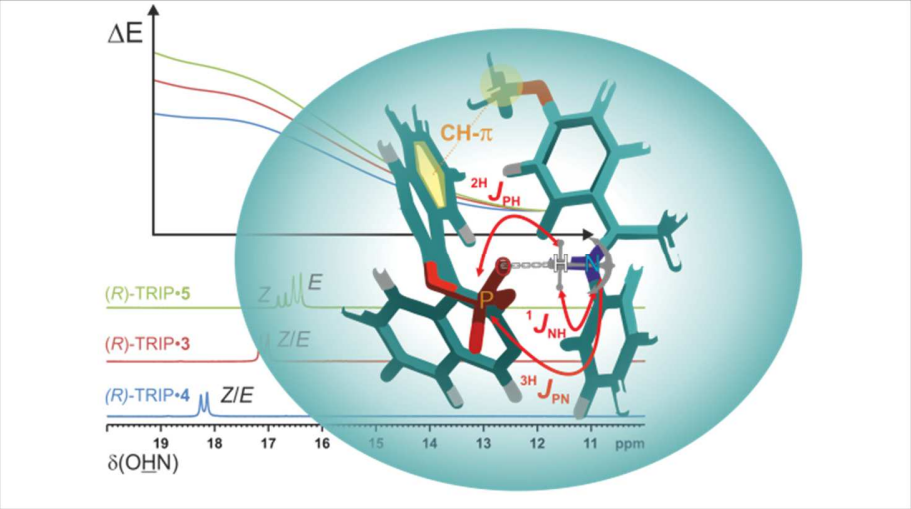

Nils Sorgenfrei, Johnny Hioe, Julian Greindl, Kerstin Rothermel, Fabio Morana, N. Lokesh and Ruth M. Gschwind

J. Am. Chem. Soc., **2016**, *138*, 16345–16354

DOI: 10.1021/jacs.6b09243

a) The major part of the NMR measurements and of the hydrogen bond analytics was performed by Nils Sorgenfrei. b) All theoretical calculations were performed by Dr. Johnny Hioe and he contributed to the evaluation of the Steiner-Limbach correlation. c) Julian Greindl contributed to the measurements of the (*R*)-TRIP•**3-5** complexes (trans-hydrogen bond scalar couplings and additional experiments) and HBF_4•imine complexes d) Kerstin Rothermel conducted the necessary preparations and measurements of the isotope effects and investigated a major part of the phenol/carboxylic acid complexes. Furthermore she contributed to sample preparations. e) Fabio Morana contributed in the optimization of the sample preparation ((*R*)-TRIP•**3-5**) and by synthesis of the catalyst (*R*)-TRIP. f) N. Lokesh assisted in the measurement of the isotope effects. g) Substrates were synthesized from all authors, except N. Lokesh and Johnny Hioe. h) Thomas Hausler and Dr. Polyssena Renzi contributed imine substrates for the isotope effect measurements.

Source of this chapter: ACS Publications http://pubs.acs.org/doi/10.1021/jacs.6b09244

3.1 Abstract

Hydrogen bonding plays a crucial role in Brønsted acid catalysis. However, the hydrogen bond properties responsible for the activation of the substrate are still under debate. Here, we report an in depth study of the properties and geometries of the hydrogen bonds in (*R*)-TRIP imine complexes (TRIP: 3,3′-Bis(2,4,6-triisopropylphenyl)-1,1′-binaphthyl-2,2′-diylhydrogen phosphate). From NMR spectroscopic investigations ^{1}H and ^{15}N chemical shifts, a ,,Steiner-Limbach correlation'', a deuterium isotope effect as well as quantitative values of $^{1}J_{NH}$, $^{2h}J_{PH}$ and $^{3h}J_{PN}$ were used to determine atomic distances (r_{OH}, r_{NH}, r_{NO}) and geometry information. Calculations at SCS-MP2/CBS//TPSS-D3/def2-SVP-level of theory provided potential surfaces, atomic distances and angles. In addition, scalar coupling constants were computed at TPSS-D3/IGLO-III. The combined experimental and theoretical data reveal mainly ion pair complexes providing strong hydrogen bonds with an asymmetric single well potential. The geometries of the hydrogen bonds are not affected by varying the steric or electronic properties of the aromatic imines. Hence, the strong hydrogen bond reduces the degree of freedom of the substrate and acts as a structural anchor in the (*R*)-TRIP imine complex.

3.2 Introduction

Hydrogen bonding impacts the energetics and structures of molecules as well as the reactivity and stereoselectivity of their reactions and is therefore of utmost significance in nature.[1] Nowadays, hydrogen bonding is more and more recognized by chemists as potential activation mode for electrophilic substrates such as carbonyl compounds or imines in the field of asymmetric catalysis.[2-4] A ,,privileged class" of asymmetric Brønsted acid catalysts constitute BINOL (1,1'-binaphtol) derived phosphoric acids, which were introduced by Akiyama and Terada[2,5-7] and found applications in a wide pool of reactions with imines as substrates, including Mannich reactions, cycloadditions, aza-ene-type reactions, hydrocyanations and transfer-hydrogenations.[7,8] Especially, for the asymmetric reductions of imines with Hantzsch 1,4–dihydropyridine ester **1** this class of chiral phosphoric acids provides high stereoselectivities and yields as, e.g. ,published by the groups of Rueping,[9,10] List[11] and MacMillan.[12] The proposed catalytic cycle for this asymmetric reduction is shown in Figure 1a.[3,9,11] The phosphoric acid protonates the imine and forms a chiral hydrogen bond assisted ion pair, which reacts subsequently with the Hantzsch ester **1** to form the chiral amine.

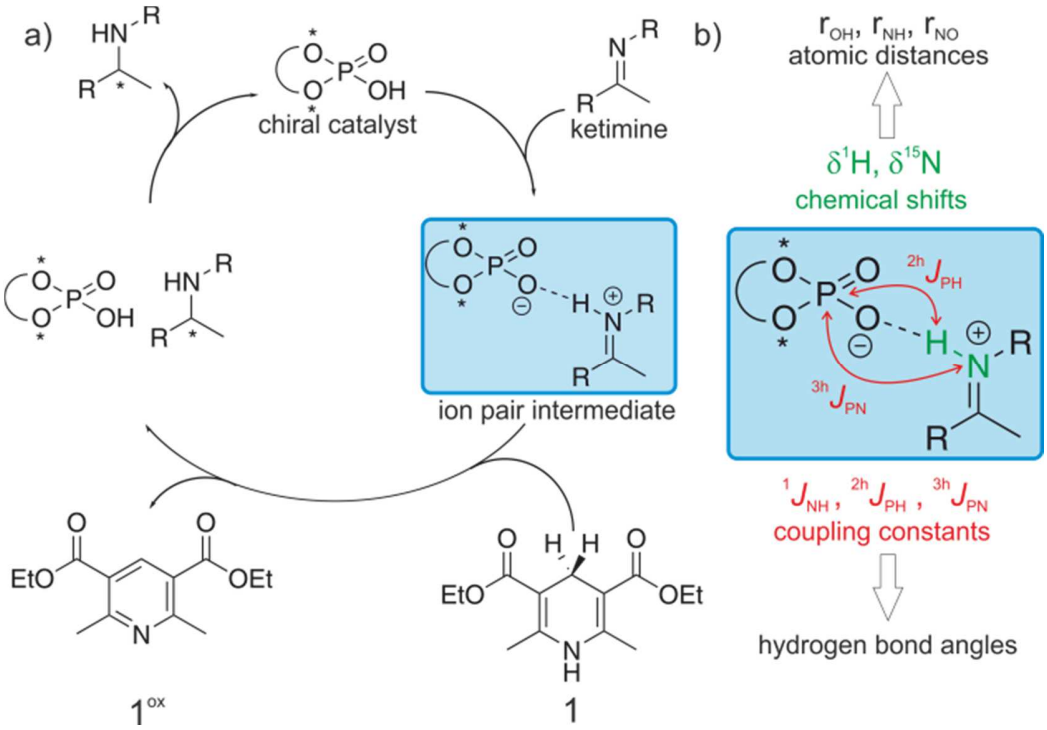

Figure 1. a) Catalytic cycle proposed for the Brønsted acid catalyzed enantioselective reduction of imines with Hantzsch-1,4-dihydropyridine ester **1**;[9,11] b) experimental observables used in this study to characterize the hydrogen bond interaction in (*R*)-TRIP imine complexes.

Several DFT studies of the groups of Himo and Goodman addressed the issue of enantioselectivity in this catalytic reaction.[13-16]

They proposed a fast acid-base equilibrium between imine and catalyst followed by an *E/Z* isomerization of the iminium ion. Next a ternary complex is formed between the ion pair and the Hantzsch ester, which is stabilized by an additional hydrogen bond between the NH of the Hantzsch ester and the phosphoric acid. The absolute stereochemistry of the product and the enantiomeric excess (*ee*) is then determined by the relative energy of the ternary transitions states of the *E* and *Z* iminium ion, respectively.[13-17]

Furthermore, a detailed experimental study was published by Tang *et al*., regarding the basis of enantioselectivity in the Brønsted acid catalyzed reduction of imines with gaseous H_2 as reduction agent and an achiral iridium complex as cocatalyst.[8] Again, a ternary complex and the corresponding transition states were proposed to be responsible for the stereodiscrimination.

However, in the whole field of Brønsted acid catalysis detailed experimental data providing structural insights are extremely rare. Thus, so far not even the hydrogen bond situation in the binary ion pair intermediate has been clarified. The concept of full protonation of basic substrates such as imines by acidic catalysts - often proposed by synthetic chemists and theoreticians - is an oversimplification and an extreme point of view as noted by Toste *et al*.[4] For example, purely hydrogen bonded complexes were proposed in a computational and NMR spectroscopic study of the activation of N-Boc protected imines by a chiral phosphoric acid.[18] Furthermore, in a preceding NMR study of our group investigating achiral diphenylphosphoric acid (DPP) imine complexes, both hydrogen bonded complexes and ion pairs were proposed to coexist in solution.[19] There, a typical temperature dependent ratio was observed, high temperatures favor hydrogen bonding, whereas at low temperatures ion pairs are more stabilized.[19] Contrary results were obtained studying complexes of DPP with 2-methylquinoline at elevated temperatures.[20] There, ion-pairing was found to be the dominant interaction motif.[20] However, to our knowledge detailed experimental studies about the hydrogen bond properties in ketimine complexes with the chiral phosphoric acids have not been reported so far.

Therefore, in this work we present the first detailed, NMR based experimental investigations on the hydrogen bond activation of imines by chiral phosphoric acids. The hydrogen bonds in these binary catalyst substrate complexes were experimentally characterized by ^{1}H, ^{15}N chemical shifts and trans-hydrogen bond scalar couplings. From the chemical shifts the individual atomic distances (r_{OH}, r_{NH}, r_{NO}) within the hydrogen bonds were derived and the $^{2h}J_{PH}$ and $^{3h}J_{PN}$ scalar couplings give information about the angles (Figure 1b). These detailed experimental data are compared with high level theoretical calculations about the atomic distances, scalar couplings of the hydrogen bonds and structures of the binary complexes. This reveals not only unprecedented insights into the hydrogen bond activation of Brønsted acid catalysis but also the limitations of both experimental and theoretical models.

3.3 Results and Discussion

Model Systems. (*R*)-TRIP 3,3′-bis(2,4,6-triisopropylphenyl)-1,1′-binaphthyl-2,2′-diylhydrogen phosphate was chosen as catalyst, because structural information based on NOE data was available for some (*R*)-TRIP imine complexes (see below).[21] In addition, imines with different steric and electronic properties were selected (Figure 2) to rationalize the influence of the substrate on the hydrogen bonding properties of the ion pairs. Furthermore, tetrafluoroboric acid, was selected to mimic purely ionic complexes. Acetic acid (AcOH), trimethyl acetic acid (TMA), as well as phenols (4-chlorophenol, 4-nitrophenol, 3,5-dichlorphenol, 3-(trifluoromethyl)phenol) were chosen to form strictly neutral hydrogen bonded complexes. The preparation of ^{15}N-labeled imines and representative methods for sample preparation are described in the Supporting Information. All acid imine and phenol imine complexes were investigated in CD_2Cl_2 and/or freonic mixtures by NMR spectroscopy, because in these solvents the best NMR properties were detected in terms of chemical shift dispersion and line widths (for spectra in toluene see Supporting Information). Extremely low temperatures between 180 and 130 K were used to reach the slow hydrogen bond exchange regime. These low temperatures in combination with the selection of phosphoric acids and up to 98% ^{15}N enriched imines allowed for the detection of $^{2h}J_{PH}$ and $^{3h}J_{PN}$ as sensors for hydrogen bond angles and atomic distances.[22]

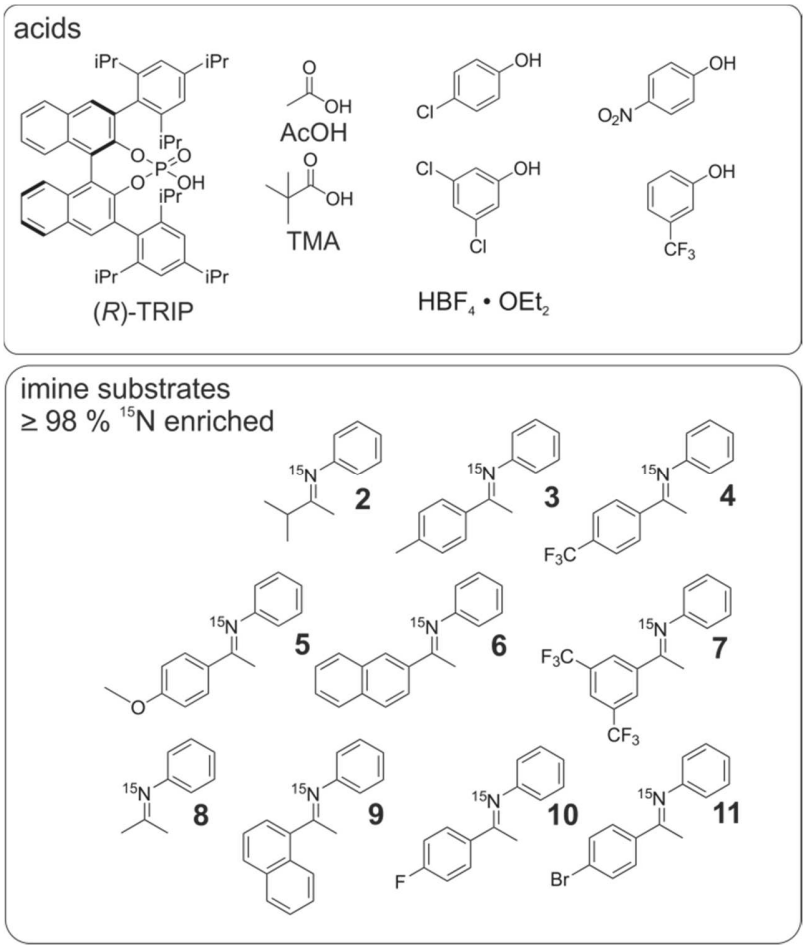

Figure 2. Model systems for hydrogen bond studies; Brønsted acid catalyst (*R*)-TRIP and other acidic compounds were used as donors; all imines **2–11**, tested as acceptors were 98% ^{15}N enriched to enable the detection of $\Delta\delta^{15}$N and $^{3h}J_{PN}$.

Computational Details. The binary complexes consisting of (*R*)-TRIP and imines **3-5** and **8** were chosen as models in the theoretical calculations. The structures are optimized at RI-DFT level of theory using meta-GGA functional TPSS-D3 with def2-SVP basis set in the gas phase and in the continuum of dichloromethane (SMD model).[23-25] A dielectric constant of 16.2 was used to simulate the low temperature measurement at 180 K. Bond parameters (distances and angles) were averaged over large conformational space (due to isopropyl rotation) according Boltzmann distributions at 180 K. The final free energies of the conformations were evaluated at SCS-RI-MP2/CBS level of theory (for extrapolation procedure see Supporting Information).[26] Solvation energies were added subsequently to the Gibbs free energy using SMD solvation model at 180 K in dichloromethane. The ^{1}H and ^{15}N chemical shifts, respectively the scalar coupling constants ($^{1}J_{NH}$, $^{2h}J_{PH}$ and $^{3h}J_{PN}$), were

computed at TPSS with IGLO-III basis set using the complete model, respectively the reduced model.[27] The 2,4,6-triisopropylphenyl groups were replaced with hydrogens, and subsequently subjected to frozen optimization. For the geometry optimization, free energy of solvation and scalar coupling constant calculation Gaussian09 version D.01 was used. For single point calculation ORCA3.0.3 was used.[28,29]

Detection and Characterization of Hydrogen Bonds by NMR. For most of the chiral phosphoric acid imine complexes ((*R*)-TRIP **2**–**11**), two main ion pair species were detected representing hydrogen bridged ion pairs with *E* and *Z* configured imines. Therefore, in the following this general pattern and its assignment is described exemplarily on the hydrogen bonded complex of (*R*)-TRIP and **5** in CD_2Cl_2 at 180 K (Figure 3). For (*R*)-TRIP·**5*E*** and (*R*)-TRIP·**5*Z*** the proton in the hydrogen bond is detected at 16.47 and 16.75 ppm, respectively (Figure 3a). Such chemical shifts larger than 16 ppm are usually observed for hydrogen atoms in ,,strong'' or ,,low-barrier hydrogen bonds''.[1,30,31] Both signals are doublets with $^1J_{NH}$ coupling constants of 79.7 and 81.2 Hz showing the covalent connectivity to ^{15}N and the existence of an ion pair structure (for further support see $^1H,^{15}N$-HMQC spectra in the Supporting Information).[19] The *E* and *Z* configurations of the imines were assigned based on $^3J_{NH}$ couplings constants between ^{15}N of imine and methyl protons and as well as by NOESY measurements (for details see Supporting Information). The ionic character of both isomers is further corroborated by the significant high-field shift of the ^{15}N resonances to 206.7 and 209.2 ppm for *E* and *Z,* respectively (Figure 3b and d), compared to the free base **5** at 321.0 ppm (Figure 3e); $\Delta\delta^{15}N > 110$ ppm), which is a clear indicator for the proton transfer to the lone pair of the nitrogen.[32] Also the ^{13}C low field shifts of the imino groups ($\Delta\delta \sim 13.7$ and $\Delta\delta \sim 16.0$ ppm for *E* and *Z,* respectively; see Figure 3d and e) corroborate this analysis.[33,34]

For (*R*)-TRIP imine complexes the large $^1J_{NH}$ coupling constants, the significant high field shift of the ^{15}N resonances upon complex formation and the refined spectroscopic and theoretical analysis of the data (see below) indicate a strong preference for the ionic hydrogen bond[1,35] (Figure 3d) except for imine **7**, in which the two CF_3-groups significantly reduce the basicity. The hydrogen bonded complex can be involved in association/dissociation equilibria with the isolated molecules or the separated ion pairs.[36-38] In case of imines with low basicity (e.g., **4** or **7**) or in the presence of an excess of imine a separated ^{15}N signal of the free non protonated imine is observed at 180 K, which is in slow exchange with the imine in the complex.

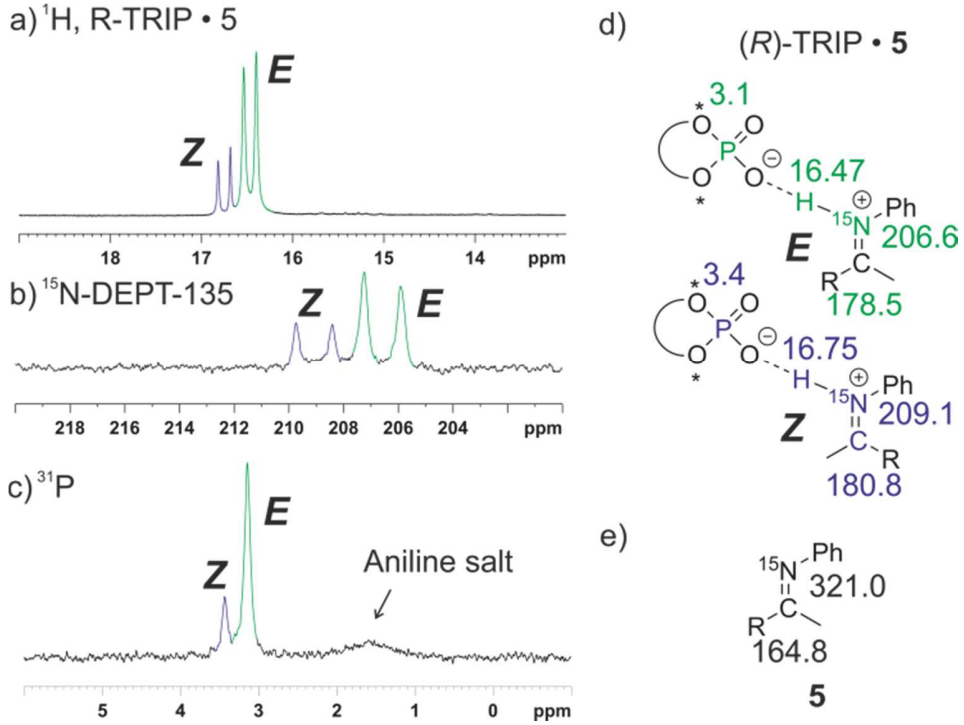

Figure 3. a-c) Sections of the ^{1}H, ^{15}N-DEPT-135 and ^{31}P spectra of a 1:1 complex of (*R*)-TRIP and **5** (CD_2Cl_2, 180 K, 600 MHz), clearly showing the coexistence of both *E* and *Z* complexes; d) chemical shifts of (*R*)-TRIP·5*E/Z*; e) chemical shifts of unbound **5**.

Considering our experimental conditions (e.g., low temperatures and the noncoordinative CD_2Cl_2 as solvent) and the estimated strength of the formed hydrogen bonds (>70 kJ/mol),[1] the formation of solvent separated ion pairs in (*R*)-TRIP complexes is negligible.[39] This is substantiated by detection of large $^{2h}J_{PH}$ and $^{3h}J_{PN}$ coupling constants (see below).[40] Thus, the ^{1}H and ^{15}N chemical shifts observed for the binary substrate complexes of (*R*)-TRIP with the imines at 180 K are the ,,intrinsic'' chemical shifts of the individual hydrogen bonded species and can be used for the analysis of the hydrogen bond situation of these complexes.[35,41]

Hydrogen Bond Analysis Based on δ^{1}H, δ^{15}N and $^{1}J_{NH}$. In ^{1}H-NMR spectra, chemical shifts above 16 ppm are usually observed for hydrogen atoms in ,,strong'' or ,,low-barrier hydrogen bonds''.[1,30,31] According to literature the formation of strong hydrogen bonds is associated with a ,,proton-transfer reaction''[1,38] between hydrogen bond donor and hydrogen bond acceptor. The progress of the proton transfer is dependent on the acidity of the hydrogen bond donor and the basicity of the acceptor, and as well as the polarity of the solvent.[1,36,38,39,42] Therefore, empirical correlations of ^{1}H ,,{δ(O<u>H</u>N)}'' and ^{15}N ,,{δ(OH<u>N</u>)}'' chemical shifts, as well as $^{1}J_{NH}$,,{^{1}J(O<u>H</u>N)}'' coupling constants with the atomic distances can be used to determine

the position of the proton inside the hydrogen bond, as previously developed by Limbach and Denisov in their studies of OHN hydrogen bonds in pyridine acid complexes (Equation 1-5).[35,41,43,44] Using an extended set of complexes with varying acidic and basic properties of their hydrogen bond donors and acceptors, the proton position within the hydrogen bond can be varied stepwise. There, the parabolic dependence of δ(O<u>H</u>N) on δ(OH<u>N</u>) was used to determine the valence bond orders *p*OH^{H} and *p*NH^{H} by employing the empirical correlations presented in Equation 1-2**.**

$$\delta(\mathrm{O\underline{H}N}) = \delta(\mathrm{O\underline{H}})^0 p_{\mathrm{OH}}^{\mathrm{H}} + \delta(\underline{\mathrm{H}}\mathrm{N})^0 p_{\mathrm{HN}}^{\mathrm{H}} + 4\delta(\mathrm{O\underline{H}N}) p_{\mathrm{OH}}^{\mathrm{H}} p_{\mathrm{HN}}^{\mathrm{H}} \quad (1)$$

$$\delta(\mathrm{OH\underline{N}})^{\mathrm{ref}} = \delta(\underline{\mathrm{N}})^0 p_{\mathrm{OH}}^{\mathrm{H}} + \delta(\underline{\mathrm{H}}\mathrm{N})^0 p_{\mathrm{HN}}^{\mathrm{H}} + 4\delta(\mathrm{OH\underline{N}}) p_{\mathrm{OH}}^{\mathrm{H}} p_{\mathrm{HN}}^{\mathrm{H}} \quad (2)$$

Furthermore, they proposed a correlation between ^{1}J(O<u>H</u>N) and the valence bond orders as well.[35,41,43,44]

$$^{1}J(\mathrm{O\underline{H}N}) = {}^{1}J(\underline{\mathrm{H}}\mathrm{N})^0 p_{\mathrm{HN}}^{\mathrm{H}} - 8\,{}^{1}J(\mathrm{O\underline{H}N})(p_{\mathrm{OH}}^{\mathrm{H}})^2 p_{\mathrm{HN}}^{\mathrm{H}} \quad (3)$$

The determined *p*OH^{H} and *p*NH^{H} for a hydrogen bond are then consulted to derive the corresponding atomic distances (r_{OH}, $r_{NH,}$ r_{NO}) according to Equations 4-5.

$$p_{\mathrm{NH}} = \exp\{\tfrac{-(r_{\mathrm{NH}} - r_{\mathrm{NH}}^0)}{b_{\mathrm{NH}}}\} \quad (4)$$

$$p_{\mathrm{OH}} = \exp\{\tfrac{-(r_{\mathrm{OH}} - r_{\mathrm{OH}}^0)}{b_{\mathrm{OH}}}\} \quad (5)$$

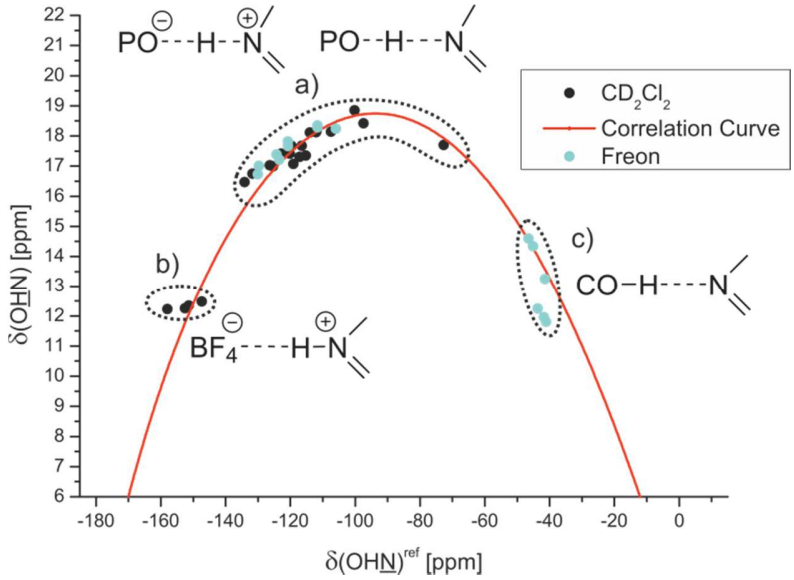

Figure 4. Plot of $\delta(OH\underline{N})^{ref}$ against the $\delta(O\underline{H}N)$ of the hydrogen bonded complexes; a) (*R*)-TRIP with **2**–**11**; b) HBF_4 with **3** and **5**; c) carboxylic acids and phenols with **3** and **5**; the ^{15}N chemical shifts of all complexes are referenced to **7** {$\delta(OH\underline{N})^{ref}$= $\delta(OH\underline{N})$ - 340.8 ppm}; spectra corresponding to the different hydrogen bond types are shown in Figure 5; for details see Supporting Information.

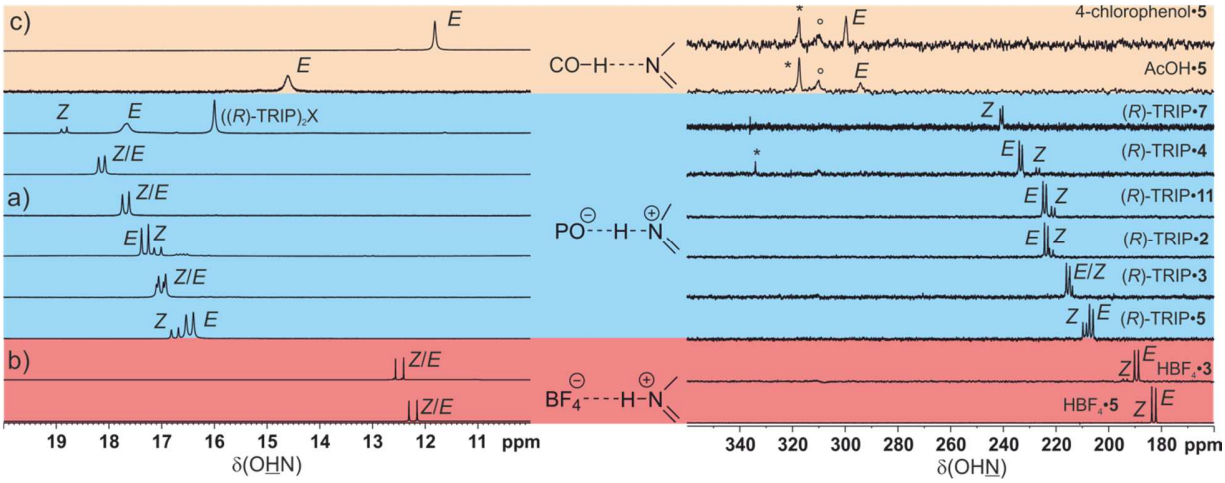

Figure 5. Dependence of $\delta(O\underline{H}N)$ and $\delta(OH\underline{N})$ on the hydrogen bond strength in the *E* and *Z* acid imine complexes shown by selected of ^1H (low field sections) and ^{15}N spectra in CD_2Cl_2 and freonic mixtures between 180 to 130 K; the shown spectra correspond to the hydrogen bond types in Figure 4; a) (*R*)-TRIP imine complexes; b) HBF_4·**3** and HBF_4·**5**; c) AcOH·**5** and 4-chlorophenol·**5**; for the ^{15}N spectra of (*R*)-TRIP·**7**, (*R*)-TRIP·**5** and HBF_4·**5** polarization transfer experiments were used (INEPT and DEPT); (*) signals of free imine; (deg) impurity or artifact; in case of (*R*)-TRIP·**7** signals of $((R)\text{-TRIP})_2X$ complexes are observed[35,55]; a list of $\delta(O\underline{H}N)$ and $\delta(OH\underline{N})$ of the individual complexes is provided in the Supporting Information Table S9-12.

For a detailed explanation of the empirical equations and constants applied in this study for the acid imine complexes see Supporting Information. To enable a reliable parametrization of the constants {δ(O<u>H</u>)°; δ(<u>H</u>N)°; δ(H<u>N</u>)°; δ(<u>N</u>)°; ^1J(<u>HN</u>)°; δ(O<u>H</u>N)*; δ(OH<u>N</u>)*, ^1J(O<u>HN</u>)*} used in Equations 1-3, it was necessary to cover a wide range of the valence bond orders pOH^H and pNH^H. Hence, the database was extended from (*R*)-TRIP imine complexes with ,,strong'' hydrogen bonds to ionic and neutral acid imine complexes with ,,moderate'' hydrogen bond strength.[1,35,41] As mentioned earlier, for the strictly ionic acid imine complexes, tetrafluoroboric acid was selected, which was already used in our previous study.[19]

Acetic acid (AcOH) and trimethylacetic acid (TMA) as well as several substituted phenols were selected for the strictly neutral acid imine complexes. The plot of δ(OH<u>N</u>)^{ref} against δ(O<u>H</u>N) of all acid imine complexes is shown in Figure 4. Representative ^{1}H and ^{15}N spectra related to the different hydrogen bond types are shown in Figure 5. In strictly ionic complexes with ,,moderate'' hydrogen bonds (HBF_4·**3**, HBF_4·**5)** δ(O<u>H</u>N) values between 12 and 13 ppm and high values of $^1J_{NH}$ about 92.6 Hz are observed, indicating a complete proton transfer reaction and therefore short r_{NH} (Figure 4b, Figure 5b).[1] With decreasing acidity of the hydrogen bond donor (*R*)-TRIP and decreasing basicity of the acceptor (**5** > **3** > **2** > **11** > **4** > **7**) the proton is shifted toward the center of the hydrogen bond, which is interpreted as an increase of strength of the hydrogen bond (Figure 4a; Figure 5a).[1,35,41] In the case of (*R*)-TRIP·***7E***, the proton is even shifted beyond the maximum indicating a decrease of the hydrogen bond strength and a considerable population of the neutral hydrogen bonded complex. In the predominant ionic complexes high proton chemical shifts are observed from 16.47 ((*R*)-TRIP·***5E***) to 18.85 ppm ((*R*)-TRIP·***7Z***) in combination with reduced absolute $^1J_{NH}$ coupling constants from 82.2 Hz ((*R*)-TRIP·***5E***) to 60.6 Hz ((*R*)-TRIP·***7Z***). In contrast, for the neutral hydrogen bonded complex (*R*)-TRIP·***7E*** a reduced $^1J_{NH}$ coupling constant (42 Hz at 170 K) was observed, which is in full agreement with the trend in the Steiner-Limbach correlation curve. Continuing to the less acidic donors AcOH and 4–chlorophenol the proton is now shifted further on, toward the oxygen atom (Figure 4c, Figure 5c). This leads again to a weakening of the hydrogen bonds, visible by the high field shift of the proton signal at 11.81 ppm for 4-chlorphenol·**5**. Now with the proton close to the oxygen, the splitting due to the $^1J_{NH}$ coupling vanishes. In contrast, the ^{15}N resonance of the hydrogen bonded complexes is shifted continuously from 182.2 ppm for HBF_4·***5E*** over 230.2 ppm for (*R*)-TRIP·***4Z*** to 299.7 ppm for 4-chlorophenol·**5** (Figure 5 a-c)**.**

A satisfying curve fit of the data points was achieved, employing Equation 1 and Equation 2 (Figure 4, red curve; for details and fitting parameters see Supporting Information). The

observed parabolic dependence of δ(O<u>H</u>N) on δ(OH<u>N</u>) is in good agreement with the previous investigations on pyridine-acid complexes by Limbach and co-workers.[35,41] For (*R*)-TRIP imine complexes the continuous progression of the data points on the correlation curve is indicative for a strong hydrogen bond and excludes a tautomeric equilibrium between two proton positions in a classical double well potential (data points on two intersecting straight lines).[35] Regarding the $^1J_{NH}$ coupling constants of the investigated Brønsted acid imine complexes, a good characterization by the valence bond model is achieved as well, shown by the plots of ^1J(O<u>H</u>N) against δ(O<u>H</u>N) and δ(OH<u>N</u>) (see Supporting Information). The magnitude of the measured coupling constants (60.6 – 82.2 Hz) reflects again the above-described predominant ionic character of the (*R*)-TRIP imine complexes and the significantly reduced value of (*R*)-TRIP·**7*E*** (42 – 46 Hz) corroborates the shift toward neutral hydrogen bonds.

On the basis of the δ(O<u>H</u>N) of the Brønsted acid imine complexes (see Table S9-12 in the Supporting Information) and the fitted correlation curve (Figure 4), the bond orders pOH^H and pNH^H of the individual (*R*)-TRIP imine complexes were obtained (see Supporting Information Table S13). Next equations 4-5 are used to determine the atomic distances r_{OH}, r_{NH} and r_{NO}. These experimentally derived values for r_{NH} and r_{OH}, are depicted in Figure 8 and discussed below together with the results from the theoretical calculations. For all values including r_{NO} see Table S13 in the Supporting Information. All hydrogen bond distances are in the range of strong OHN hydrogen bonds[1] and vary between 111 and136 pm for r_{NH}, 114-146 pm for r_{OH}, and 249–257 pm for r_{NO}. In addition, the obtained average proton donor distances - in the case of (*R*)-TRIP complexes r_{OH} - below 160 pm indicate the partial covalent character of the formed hydrogen bonds.[45,46]

Comparison of NMR Data and Theoretical Calculations.

Ion Pair Structures. Next the results of this study were correlated with our recent NMR spectroscopic and computational study regarding the general structures of (*R*)-TRIP complexes with the aromatic imines (**3-5**) to gain further insight into the hydrogen bond interaction.[21] In general two binding modes of *E*/*Z*-imines and catalyst (*R*)-TRIP are theoretically possible, which are stabilized by dispersive interactions.

For *E*-imines (**3-5**) theoretical calculations showed that the orientation, in which the *para*-substituted ketone moiety reclines on the chiral BINOL aromatic surface is majorly populated for all aromatic imines investigated (Figure 6a). However, initial experimental and theoretical structural studies with short aliphatic imines (**2** and **8**) and doubly substituted imines[21] indicate

the second orientation with a 180° rotated imine (structure not shown) to be also populated. In case of *Z*-imine complexes ((*R*)-TRIP·**3-5**) also, NOESY spectra predict that the two binding modes in the complex to be populated. The most stable one is depicted in Figure 6b.[21] Furthermore, ^{1}H spectra, which showed only one averaged signal set for the protons at the BINOL moiety, suggested that the *Z* isomers of the (*R*)-TRIP imine complexes are extremely dynamic even at very low temperatures. The theoretical calculations predicted that both orientations differ only by 4.5–6 kJ/mol. It is very likely that the compact structure of *Z*-imines allows the rotation and translation of the imines in the binary complex.[21] Fortunately, the actual interpretation of the hydrogen bonds is not affected by this structural diversity, because the geometries of the hydrogen bonds are extremely similar in both conformations. For further discussion of hydrogen bond geometry (atomic distances and angles) and the interpretation of scalar coupling constants ($^{1}J_{NH}$, $^{2h}J_{PH}$, $^{3h}J_{PN}$), only Boltzmann averaged values over two orientations and the isopropyl rotation were considered.

Potential Surface of the Hydrogen Bond Complexes. The theoretical calculations showed that the alteration of hydrogen bond situation strongly depends on the dielectric medium, in which the complex is simulated (Figure 7a-c). In the gas phase, ion pair- and neutral hydrogen bond-complexes are true minima (Figure 7a). Without any solvent correction, the latter is thermally more stable (ca. 8 – 13 kJ/mol) and therefore almost exclusively populated. However, the solvent correction at 180 K (ε = 16.20) to the gas phase structure (nonrelaxed) leads to a significant stabilization of the charge separated contact ion pair minima and inverts the population (Figure 7b).

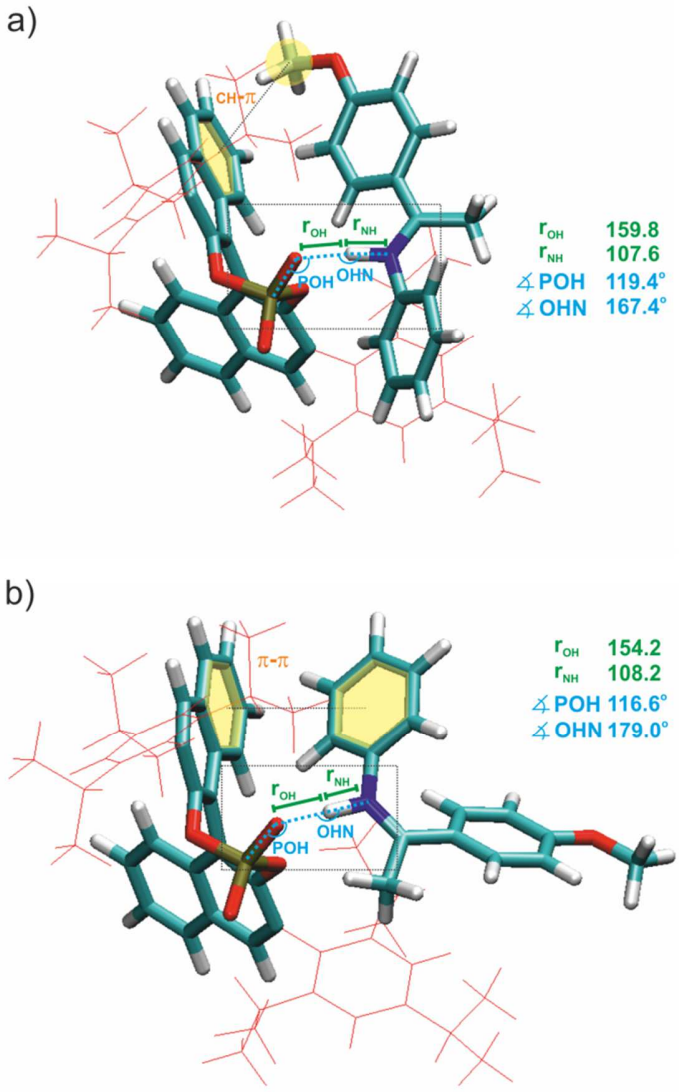

Figure 6. Global minima of (*R*)-TRIP·**5** in CD_2Cl_2 at 180 K (ε = 16.20), optimized at DFT level of theory (for computational details see Supporting Information); a) (*R*)-TRIP·5 *E*; b) (*R*)-TRIP·**5** *Z*.

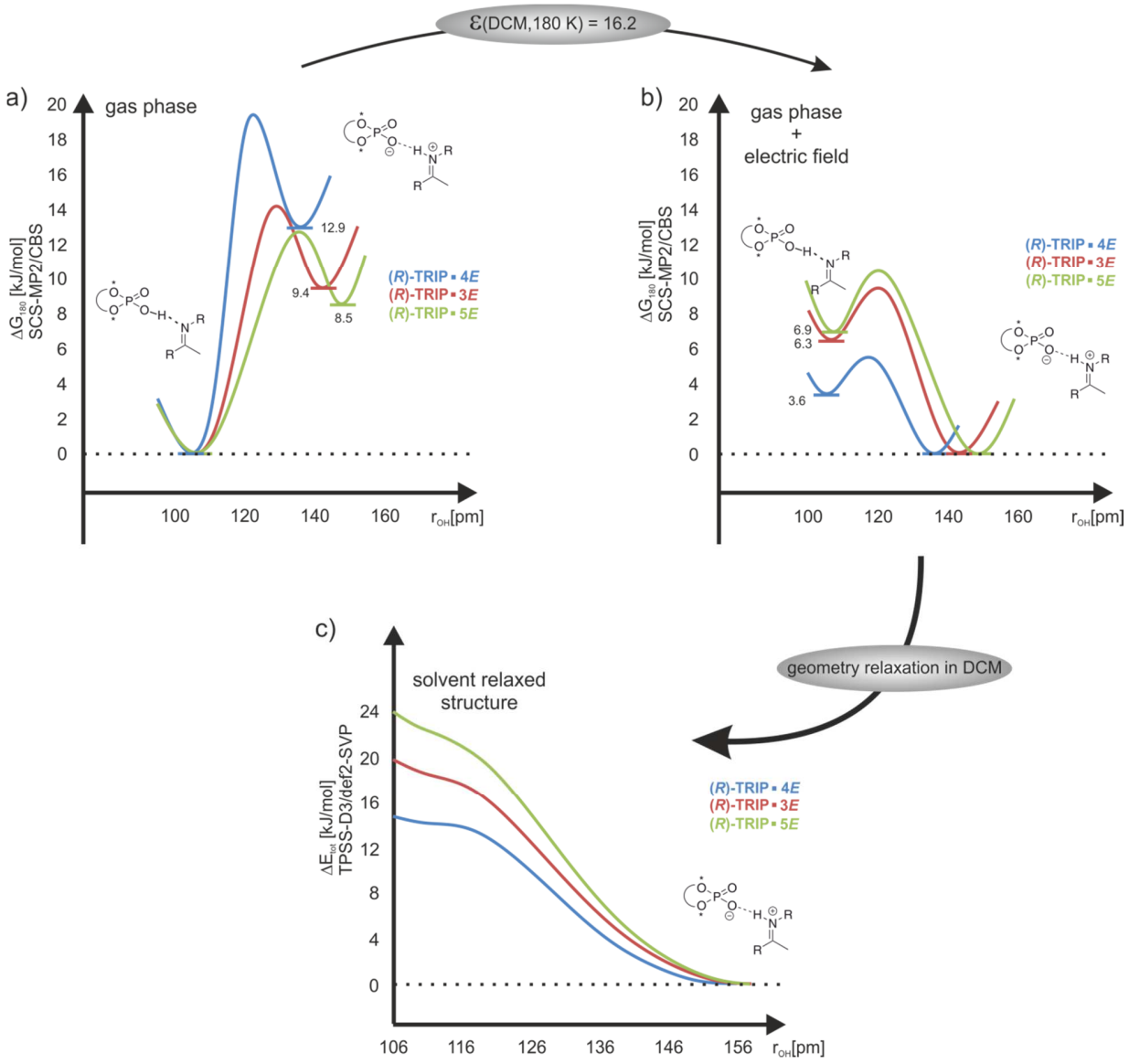

Figure 7. a) Schematic gas phase potential energy profiles of (*R*)-TRIP/imine complexes; b) schematic solvent corrected (in DCM: 180 K, nonrelaxed) potential energy profiles of (*R*)-TRIP/imine complexes; c) relaxed scan over r_{OH} of the complexes in DCM continuum at 180 K (ε = 16.20).

After the relaxation in the continuum, the minimum of the neutral hydrogen bonded complex even disappeared and the potential surface becomes an asymmetric single well potential (Figure 7c).[47] Furthermore, weaker hydrogen bonds are calculated indicated by longer r_{OH} and r_{NO} as well as shorter r_{NH} values (for r_{OH} and r_{NH} see Figure 8). However, the calculated atomic distances of the solvent relaxed structures are still in the range of strong OHN hydrogen bonds ($r_{NO} \leq 265$ pm, for details see Supporting Information).[31]

From the experimental data available, it is difficult to assess whether the second minimum of the neutral hydrogen bond really disappears in solution at 180 K. The most indicative parameter for a single well or double well potential is the deuterium isotope effect.[31,48] For (*R*)-TRIP·**3,5*E*** a small positive isotope effect was measured ((*R*)-TRIP·**3*E*** $\Delta\delta(^1H\text{-}^2H)$, 180 K, CH_2Cl_2) = 0.15 ppm, (*R*)-TRIP·**5*E*** $\Delta\delta(^1H\text{-}^2H)$, 180 K, CH_2Cl_2) = 0.27 ppm, for spectra see Supporting Information), while a slightly larger isotopic effect was obtained for (*R*)-TRIP·**4*E*** ($\Delta\delta(^1H\text{-}^2H)$, 180 K, CH_2Cl_2) ~ 0.36 ppm). The slightly larger value for (*R*)-TRIP·**4*E*** could be caused by a flattened shape of the potential surface along the proton transfer coordinates and a vibrational motion of the proton near to the flattened surface,[30] and is in agreement with its potential energy profile (see Figure 7c). The effects of the flattened surface and the dynamic motion of the proton near to the surface are further supported by the considerable deviation between experimental and theoretical values of $^1J_{NH}$ in (*R*)-TRIP·**4*E*** (see discussion below). Furthermore, complexes with less basic imines and considerable contributions of neutral hydrogen bonds such as (*R*)-TRIP·**7*E*** let expect the existence of double well potentials. Nevertheless, all accessible experimental isotope effects so far are in agreement with an asymmetric single well potential as shown in Figure 7c.[48]

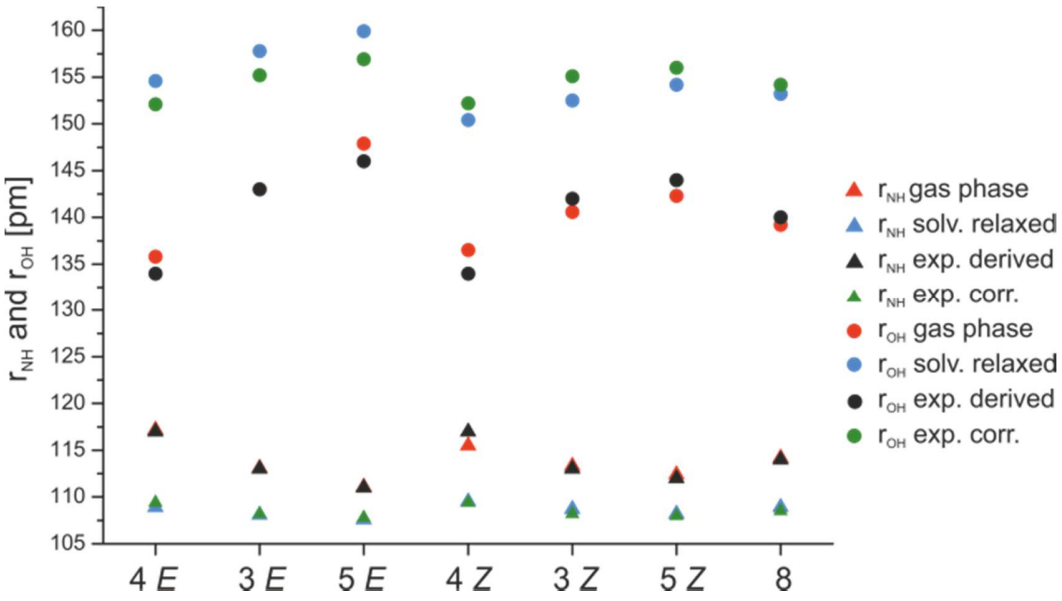

Figure 8. Comparison of the experimentally derived and calculated r_{NH} and r_{OH} distances of (*R*)-TRIP·**3-5** and (*R*)-TRIP·**8**.

Validation of Theoretical Models Based on Atomic Distances, $^1J_{NH}$, and Chemical shifts. To further validate the applicability of the different theoretical models for the interpretation of the experimental data, next the theoretically calculated atomic distances were compared with those derived from the ,,Steiner-Limbach correlation'' (Figure 8) for the normal case, the predominantly ionic complexes. The calculated distances of the contact ion pairs in the gas phase are very close to the values derived from the ,,Steiner-Limbach correlation'', which was at first glance very surprising. However, it is known that in the previous work of Limbach and co-workers[35,41] the parameters and constants (r_{OH}°, r_{NH}°, b_{OH}, b_{NH}) were fitted with a solid state data set[49] and compared to gas phase data.

To circumvent potential systematic offsets connected with indirectly derived NMR parameters, next $^1J_{NH}$ coupling constants as directly measurable values were selected. Experimental $^1J_{NH}$ values between 68.6 Hz – 82.2 Hz indicate the predominant occupation of the ion pair minimum. Therefore, in the following discussion of the theoretical values the limiting case of exclusive population of ion pairs was assumed, i.e., exclusively the values of the contact ion pair minima are considered even in the gas phase. Our results show that using the gas phase structures even for the exclusive interpretation of the ion pairs, the calculated $^1J_{NH}$ values are significant smaller than the directly measured coupling constants (red bars in Figure 9**,** for details see Supporting Information).

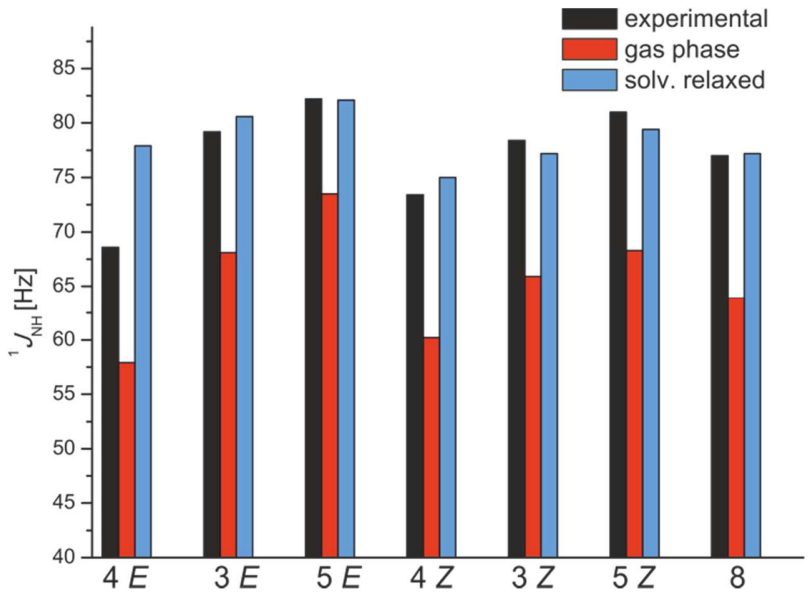

Figure 9. Comparison of experimental (black bars) and calculated (blue and red bars) $^1J_{NH}$ values of (*R*)-TRIP·**3, 4, 5, 8** show an excellent agreement between experimental values and calculated values using solvent relaxed structures, with the exception of (*R*)-TRIP·**4** *E*; only ion pair structures are

considered in the calculations; values of the *E*/*Z* isomers were Boltzmann averaged over the two experimentally observed conformations, see text.

By the application of solvent relaxed structures a significant improvement was achieved in the prediction of the $^1J_{NH}$ coupling constants for *E* and *Z* complexes of (*R*)-TRIP·**3, 5, 8** (blue bars in Figure 9).

In these cases the absolute deviation between experiment and calculation is mostly marginal and amounts to ~2 Hz (Figure 9). Therefore, the relaxed structures in the solvent model are considered to represent the experimental condition/observation more realistically and are used for the further discussion. The only significant deviation (8.8 Hz for *E*) is obtained for (*R*)-TRIP·**4*E***, which provides the strongest/shortest hydrogen bond due to the electron withdrawing CF_3 substituent in the imine **4** (Figure 9). A partial decoupling of the $^1J_{NH}$ due to chemical exchange with the unbound imine would be a potential explanation for the reduced $^1J_{NH}$ values. However, an experiment with 2-fold excess of **4** revealed, that neither the chemical shift nor the observed $^1J_{NH}$ are affected significantly (see Supporting Information). This excludes a significant influence of chemical exchange on the $^1J_{NH}$ under our experimental conditions. (*R*)-TRIP·**4** is the complex with the highest probability of a population of the neutral hydrogen bonded complex (see discussion about the potential above and Figure 7c). Now this reduced $^1J_{NH}$ scalar coupling constant can be an indication for the existence of a second minimum for the neutral hydrogen bonded complexes in solution. The next probable explanation is that the low basicity of **4** leads to a significant delocalization of the proton within the asymmetric single well potential. These dynamic motions of the proton can only be reproduced by dynamic calculation, which would be extremely costly for a system of this size. Both scenarios are in principal possible; however our current interpretation of isotopic effect favors the asymmetric potential picture as depicted in Figure 7c. In summary the application of the ,,Steiner-Limbach correlation'' based on the chemical shifts and $^1J_{NH}$ coupling constants confirm the formation of strong hydrogen bonds in the (*R*)-TRIP imine complexes and the predominance of the contact ion pair structure. For (*R*)-TRIP complexes with highly basic imines theoretical and experimental data indicate an asymmetric single well potential. The comparison of the atomic distances reveals that the classical ,,Steiner-Limbach correlation'' reproduces the distances of the gas phase structures. However, the comparison of the "direct" observables $^1J_{NH}$ with the different theoretical models demonstrates that the solvent relaxed structures resemble the experimental data the most, which was also corroborated by the analysis of the ^1H,^{15}N chemical shifts and NBO[50] (for details see Supporting Information).

Despite of this substantial improvement, the large deviation between the calculated and experimental values for (*R*)-TRIP·**4*E*** demonstrated somewhat the limit of the applied theoretical treatment, which failed to describe either the correct shape of the potential surface or the dynamic motion of the proton in extreme cases.

The described offset in combination with our theoretical data about the solvent relaxed structures can now be used to introduce a solvent correction term (see Equation 6) in the empirical correlation between chemical shifts and atomic distances for phosphoric acid imine complexes.[51]

$$r_{\mathrm{XH}} = r_{\mathrm{XH}}^{\text{Steiner-Limbach}} + f_{\mathrm{solv}}(\Delta p) \quad (6)$$

The solvent correction term depends implicitly on the experimental condition (e.g., solvent, temperature) and explicitly on the bond order difference ($\Delta p = p\mathrm{OH}^{\mathrm{H}} - p\mathrm{OH}^{\mathrm{H}}$) from the Steiner-Limbach model. This difference in bond order indicates the strengths of the hydrogen bond, the position in the Steiner-Limbach curve and the sign of the correction term to be applied. By considering the parabolic form of the Steiner-Limbach curve, the correction term should be larger with stronger hydrogen bond character and approaches a maximum with the strongest hydrogen bond. Therefore, Gauss-functions were applied for the correction term (see Equation 7 and for fitting procedures Supporting Information).

$$f_{\mathrm{solv}}(\Delta p) = A * \mathrm{sign}(p_{\mathrm{OH}} - p_{\mathrm{NH}})\exp(-B * (p_{\mathrm{OH}} - p_{\mathrm{NH}})^2) + C \quad (7)$$

The constants *A*, *B* and *C* were obtained via fitting to the available theoretical data (for data see Supporting Information). Accordingly, the corrected empirical values are now very close to the predicted values in the solution phase (see Figure 8). A first cross validation of this solvent correction term derived from the TRIP complexes on a binary complex using another catalyst ((*R*)-3,3′-Bis(3,5-bis(trifluoromethyl)phenyl)-1,1′-binaphthyl-2,2′-diyl hydrogen phosphate)[9] and **3*E*** provided only marginal offsets (deviation without correction: 2.1 pm for NH bond distance, respectively 6.1 pm for OH bond distance; with correction: 0.7 pm for NH bond distance, respectively 2.1 pm for OH bond distance) between the empirical value and the solvent relaxed structure. This suggests a general applicability to phosphoric acid imine complexes, however the full potential will be subject to further studies.

Analysis of Hydrogen Bond Geometry Based on $^{2h}J_{PH}$ and $^{3h}J_{PN}$ Trans-hydrogen bond scalar couplings can serve as valuable sensors for changes in hydrogen bond geometry.[22] Therefore, next calculated and measured $^{2h}J_{PH}$ and $^{3h}J_{PN}$ scalar couplings[52] (Figure 1b) were interpreted to get insight into the geometrical properties of the hydrogen bonds in (*R*)-TRIP imine complexes. In all calculated (*R*)-TRIP imine structures nearly linear hydrogen bonds were found (see Figure 6 for (*R*)-TRIP·**5**), which is expected for strong hydrogen bonds.[1] The calculated angles (POH, OHN) and dihedral angles (α) vary only insignificantly between gas phase and solvent relaxed structures. Furthermore, there are only minor deviations between the imines **3-5** and **8**, regarding the POH and OHN hydrogen bond angles (for data, see Supporting Information). The $^{2h}J_{PH}$ couplings between the NH protons and ^{31}P were measured qualitatively by 1D/2D ^{1}H,^{31}P-HMBC spectra and 3D HNPO spectra and quantitatively by spin echo difference experiments as reported previously[53] (for spectra and pulse sequences, see Supporting Information). The sign of the $^{2h}J_{PH}$ and $^{3h}J_{PN}$ scalar couplings was not determined and therefore only absolute values are stated. Figure 10 shows a plot of the ^{1}H chemical shift of the hydrogen bonded proton δ(O<u>H</u>N) against the experimental $^{2h}J_{PH}$ coupling constants.

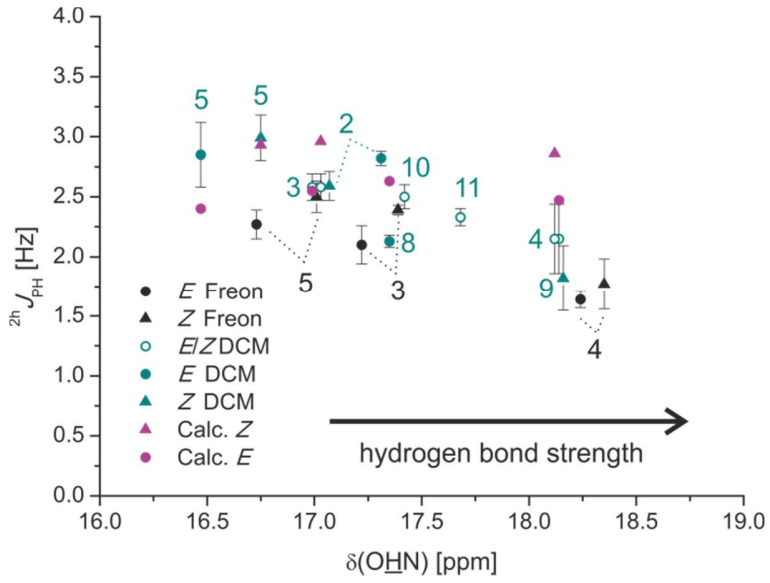

Figure 10. Plot of $^{2h}J_{PH}$ values versus δ(O<u>H</u>N); experimental values black and cyan (180 K, except (*R*)-TRIP·**8** 200 K and (*R*)-TRIP·**4** 170 K); calculated, Boltzmann averaged values of (*R*)-TRIP·**3, 4, 5, 8**: magenta.

With increasing δ(O<u>H</u>N) a continuous decrease of the $^{2h}J_{PH}$ is observed (from 2.99 ± 0.19 Hz for (*R*)-TRIP·**5*Z***, CD_2Cl_2, 180 K to 1.64 ± 0.07 Hz for (*R*)-TRIP·**4*E***, 170 K, Freon). In general,

slightly smaller values were measured for the complexes in Freon mixtures, which is in agreement with the higher ^{1}H chemical shifts indicating a stronger hydrogen bond. From protein nucleotide complexes[54] and their model systems[22] the $^{2h}J_{PH}$ angle coupling constant is known to depend on r_{NO} and the POH angle. Considering the small variance of the POH-angles in our system ((*R*)-TRIP·**3**-**5, 8*E*** 117°-118° and (*R*)-TRIP·**3**-**5, 8*Z*** 115°-117°), the observed decrease of the $^{2h}J_{PH}$ should be connected with the increasing hydrogen bond strength and therefore decreasing r_{OH} (see above) and r_{NO} (see Supporting Information). In the study of Brüschweiler *et al.* increasing $^{2h}J_{PH}$ values are predicted for decreasing r_{NO}. In our (*R*)-TRIP imine systems the opposite trend is observed. Therefore, the $^{2h}J_{PH}$ coupling constants of (*R*)-TRIP·**3**-**5, 8** in CD_2Cl_2 were calculated for the ion pair minima. First of all, the calculated $^{2h}J_{PH}$ values successfully reproduce the order of the magnitude of the experimental data (Figure 10). However, the trend in the experimental data, i.e., decreasing $^{2h}J_{PH}$ with increasing hydrogen bond strength could not be found. Considering the discussion about the $^{1}J_{NH}$ scalar coupling constants of (*R*)-TRIP·**4**, any effect of a population of the neutral hydrogen bond or vibrational effects should also affect the corresponding $^{2h}J_{PH}$ data. The calculations reveal a negative sign for $^{2h}J_{PH}$ coupling constants similar to previous studies of protein nucleotide complexes[22,54] and a positive sign for $^{2h}J_{PH}$ for the neutral hydrogen bonded complex. Thus, both a small population of the neutral hydrogen bonded complex as well as vibrations of the proton toward oxygen should result in reduced scalar coupling values as detected for (*R*)-TRIP·**4**. Next the $^{3h}J_{PN}$ coupling constants were investigated to get insight into the geometric properties regarding the dihedral angles POHN. The experimental $^{3h}J_{PN}$ coupling constants are in the range of ~ 3.25 – 2.50 Hz (see Figure 11).

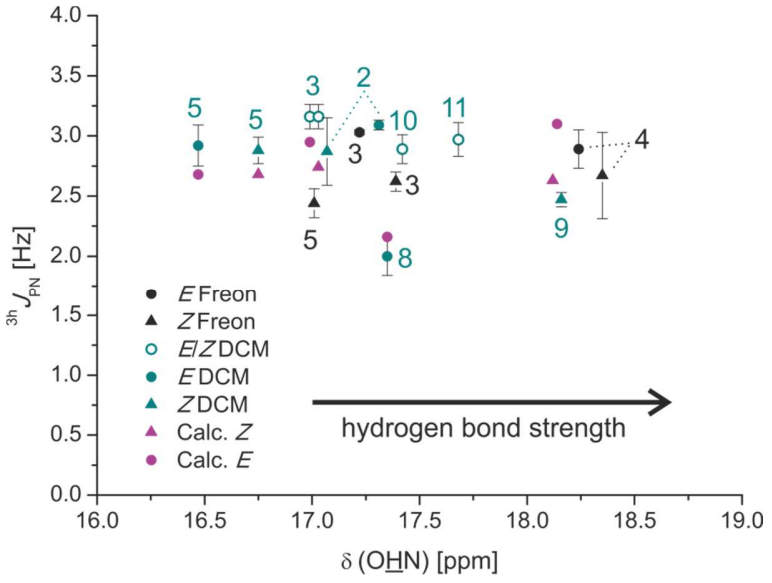

Figure 11. Plot of $^{3h}J_{PN}$ values versus δ(OHN); experimental values black and cyan (180 K, except (*R*)-TRIP·**8** 200 K and (*R*)-TRIP·**4** 170 K); calculated, Boltzmann averaged values of (*R*)-TRIP·**3, 4 ,5 ,8**: magenta.

The absolute magnitude of the $^{2h}J_{PH}$ and $^{3h}J_{PN}$ coupling constants is significantly larger than that reported by Mishima *et al.* for weak hydrogen bonds providing similar POH angles of around 107° to 120°.[53] This can be rationalized by the different electron density distribution due to the strong and partially covalent hydrogen bond character in (*R*)-TRIP imine systems.[1,45,46] Also for $^{3h}J_{PN}$ the calculations were able to reproduce the order of the magnitude and revealed a negative sign for $^{3h}J_{PN}$. However, both experimental and calculated $^{3h}J_{PN}$ values lack a clear dependence on the ^{1}H chemical shifts (Figure 11). Similar independence of the hydrogen bond strength was observed previously for $^{2h}J_{FN}$ in HF collidine complexes.[36] From the calculated structures dihedral angles POHN around 90° ± 15° are predicted (see Supporting Information). Exactly for this range of dihedral angles the smallest absolute values and smallest variations of $^{3h}J_{PN}$ are expected. Additionally, the OHN-angles are very linear (165°-175° for (*R*)-TRIP *E*- imine and 170°-180° for (*R*)-TRIP *Z*-imine; see Supporting Information for the complete data). Thus, the slight decrease of the $^{2h}J_{PH}$ and the stability of $^{3h}J_{PN}$ confirm the marginal variance of the hydrogen bond geometry found in the calculations.

3.4 Conclusion

Thorough NMR and computational investigations of the activation of imine substrates via hydrogen bonding by (*R*)-TRIP, a catalyst with broad applicability in Brønsted acid catalysis, were conducted for the first time. A strong hydrogen bond constitutes the dominant interaction between (*R*)-TRIP and imine. The analysis of its ^{1}H, ^{15}N chemical shifts as well as its $^{1}J_{NH}$ values reveals mostly a predominantly ionic character of the hydrogen bonded complexes. For (*R*)-TRIP·**7*E***, including the imine with the lowest basicity**,** also contributions of neutral hydrogen bonds were found. Individual atomic distances of the hydrogen bonds were elucidated by applying a ,,Steiner-Limbach correlation'' based on ^{1}H, ^{15}N chemical shifts, which are in good agreement with the gas phase structures from the DFT based calculations, therefore a solvent correction term was introduced. Indeed, a comparison with $^{1}J_{NH}$ values as direct experimental data demonstrates the solvent relaxed structures to describe the system more realistic. The continuous shift of the proton by variation of the imine basicity is indicative for a strong hydrogen bond character. Theoretical calculations of the potential surface reveal a major population of the neutral hydrogen bond complex in the gas phase and an inverted population in solution phase. Moreover, in (*R*)-TRIP·**4*E/Z***, the complex with the strongest

hydrogen bond calculated, the comparison between theoretical and experimental coupling constants suggests a potential participation of neutral hydrogen bond complexes or a strongly delocalized hydrogen atom due to vibrational motion, which cannot be described by our theoretical treatment. For the weaker but more neutral (*R*)-TRIP·**7*E*** complex even a double well potential is expected. The magnitude of deuterium isotope effect corroborates an asymmetric single well potential for (*R*)-TRIP·**3-5*E*** complexes. Furthermore, the trans-hydrogen scalar couplings $^{3h}J_{PN}$ and $^{2h}J_{PH}$ were detected via $^{1}H,^{31}P$-HMBC and 3D-HNPO experiments and quantified via spin echo experiments. These experimental values in combination with structure and coupling constant calculations give a detailed insight into the spatial arrangement of the hydrogen bond atoms. Nearly linear hydrogen bonds are formed with minimal variations within one structural type independent of the imine investigated. That means, the variation of the steric and electronic properties of aromatic imines does not affect the structure as well as the hydrogen bond geometry. Thus, in the (*R*)-TRIP imine complexes investigated, the hydrogen bond acts as structural anchor in the precatalytic complex.

Preliminary results showed that the product formation is faster with stronger hydrogen bonds in the precatalytic (*R*)-TRIP imine complex. Further investigations about the formation, stability and the hydrogen bond interaction of ternary complexes are currently conducted.

3.5 References

(1) Steiner, T. *Angew. Chem. Int. Ed.* **2002**, *41*, 48.

(2) Taylor, M. S.; Jacobsen, E. N. *Angew. Chem. Int. Ed.* **2006**, *45*, 1520.

(3) Mahlau, M.; List, B. *Angew. Chem. Int. Ed*. **2013**, 52, 518.

(4) Phipps, R. J.; Hamilton, G. L.; Toste, F. D. *Nat. Chem.* **2012**, *4*, 603.

(5) Uraguchi, D.; Terada, M. *J. Am. Chem. Soc.* **2004**, *126*, 5356.

(6) Akiyama, T.; Itoh, J.; Yokota, K.; Fuchibe, K. *Angew. Chem. Int. Ed.* **2004**, *43*, 1566.

(7) Zamfir, A.; Schenker, S.; Freund, M.; Tsogoeva, S. B. *Org. Biomol. Chem.* **2010**, *8*, 5262.

(8) Tang, W.; Johnston, S.; Iggo, J. a; Berry, N. G.; Phelan, M.; Lian, L.; Bacsa, J.; Xiao, *J. Angew. Chem. Int. Ed.* **2013**, *52*, 1668.

(9) Rueping, M.; Sugiono, E.; Azap, C.; Theissmann, T.; Bolte, M. *Org. Lett.* **2005**, *7*, 3781.

(10) Rueping, M.; Azap, C.; Sugiono, E.; Theissmann, T. *Synlett* **2005**, 2367.

(11) Hoffmann, S.; Seayad, A. M.; List, B. *Angew. Chem.* **2005**, *117*, 7590.

(12) Storer, R. I.; Carrera, D. E.; Ni, Y.; MacMillan, D. W. C. *J. Am. Chem. Soc.* **2006**, *128*, 84.

(13) Simón, L.; Goodman, J. M. *J. Am. Chem. Soc.* **2008**, *130*, 8741.

(14) Marcelli, T.; Hammar, P.; Himo, F. *Chem. - Eur. J.* **2008**, *14*, 8562.

(15) Marcelli, T.; Hammar, P.; Himo, F. *Adv. Synth. Catal.* **2009**, *351*, 525.

(16) Simón, L.; Goodman, J. M. *J. Org. Chem.* **2011**, *76*, 1775.

(17) Reid, J. P.; Simón, L.; Goodman, J. M. *Acc. Chem. Res.* **2016**, *49*, 1029.

(18) Gridnev, I. D.; Kouchi, M.; Sorimachi, K.; Terada, M. *Tetrahedron Lett.* **2007**, *48*, 497.

(19) Fleischmann, M.; Drettwan, D.; Sugiono, E.; Rueping, M.; Gschwind, R. M. *Angew. Chem. Int. Ed.* **2011**, *50*, 6364.

(20) Kim, H.; Sugiono, E.; Nagata, Y.; Wagner, M.; Bonn, M.; Rueping, M.; Hunger, *J. ACS Catal.* **2015**, *5*, 6630.

(21) Greindl, J.; Hioe, J.; Sorgenfrei, N.; Morana, F.; Gschwind, R. M. *J. Am. Chem. Soc.,* **2016**, *138*, 15965.

(22) Czernek, J.; Brüschweiler, R. *J. Am. Chem. Soc.* **2001**, *123*, 11079.

(23) Tao, J.; Perdew, J. P.; Staroverov, V. N.; Scuseria, G. E. *Phys. Rev. Lett.* **2003**, *91*, 146401.

(24) Grimme, S.; Antony, J.; Ehrlich, S.; Krieg, H. *J. Chem. Phys.* **2010**, *132*, 154104.

(25) Marenich, A. V.; Cramer, C. J.; Truhlar, D. G. *J. Phys. Chem. B* **2009**, *113*, 6378.

(26) Grimme, S. *J. Chem. Phys.* **2003**, *118*, 9095.

(27) Kutzelnigg W., Fleischer U., Schindler M., *Interpretation of NMR Chemical Shifts and Magnetic Susceptibilities, Springer-Verlag, Heidelberg*, **1990**, vol. 23.

(28) Frisch, M. J.; Trucks, G. W.; Schlegel, H. B.; Scuseria, G. E.; Robb, M. A.; Cheeseman, J. R.; Scalmani, G.; Barone, V.; Mennucci, B.; Petersson, G. A.; Nakatsuji, H.; Caricato, M.; Li, X.; Hratchian, H. P.; Izmaylov, A. F.; Bloino, J.; Zheng, G.; Sonnenberg, J. L.; Hada, M.; Ehara, M.; Toyota, K.; Fukuda, R.; Hasegawa, J.; Ishida, M.; Nakajima, T.; Honda, Y.; Kitao, O.; Nakai, H.; Vreven, T.; Montgomery, J. A., Jr.; Peralta, J. E.; Ogliaro, F.; Bearpark, M.; Heyd, J. J.; Brothers, E.; Kudin, K. N.;

Staroverov, V. N.; Kobayashi, R.; Normand, J.; Raghavachari, K.; Rendell, A.; Burant, J. C.; Iyengar, S. S.; Tomasi, J.; Cossi, M.; Rega, N.; Millam, J. M.; Klene, M.; Knox, J. E.; Cross, J. B.; Bakken, V.; Adamo, C.; Jaramillo, J.; Gomperts, R.; Stratmann, R. E.; Yazyev, O.; Austin, A. J.; Cammi, R.; Pomelli, C.; Ochterski, J. W.; Martin, R. L.; Morokuma, K.; Zakrzewski, V. G.; Voth, G. A.; Salvador, P.; Dannenberg, J. J.; Dapprich, S.; Daniels, A. D.; Farkas, Ö.; Foresman, J. B.; Ortiz, J. V.; Cioslowski, J.; Fox, D. J. *Gaussian* 09, Revision D.01, Gaussian, Inc., Wallingford CT, 2009.

(29) Neese, F. *Wiley Interdiscip. Rev. Comput. Mol. Sci.* **2012**, *2*, 73.

(30) Frey, P. a. *Magn. Reson. Chem.* **2001**, *39*, 190.

(31) Frey, P. a; Whitt, S. a; Tobin, J. B. *Science* **1994**, *264*, 1927.

(32) Günther, H. NMR *Spectroscopy Basic Principles, Concepts, and Applications in Chemistry*, 3rd ed.; Wily-VCH Verlag GmbH& Co. KGaA: Weinheim, **2013**.

(33) Olah, G. A.; Kreienbuh, P. *J. Am. Chem. Soc.* **1967**, *15*, 4756.

(34) Olah, G. A.; Donovan, D. J. *J. Org. Chem.* **1978**, *43*, 860.

(35) Sharif, S.; Denisov, G. S.; Toney, M. D.; Limbach, H. *J. Am. Chem. Soc.* **2007**, *129*, 6313.

(36) Golubev, N. S.; Shenderovich, I. G.; Smirnov, S. N.; Denisov, G. S.; Limbach, H.-H. *Chem. - Eur. J.* **1999**, *5*, 492.

(37) Shenderovich, I. G.; Burtsev, A. P.; Denisov, G. S.; Golubev, N. S.; Limbach, H.-H. *Magn. Reson. Chem.* **2001**, *39*, 91.

(38) Ishikita, H.; Saito, K. *J. R. Soc. Interface* **2014**, *11*, 20130518.

(39) Reichhardt, C.; Welton, T. In Solvents and Solvent Effects in Organic Chemistry; Wiley-VCH Verlag GmbH & Co. KGaA: Weinheim, **2011**; pp 136–138.

(40) Anderson, K. M.; Esadze, A.; Manoharan, M.; Brüschweiler, R.; Gorenstein, D. G.; Iwahara, J. *J. Am. Chem. Soc.* **2013**, *135*, 3613.

(41) Limbach, H.-H.; Pietrzak, M.; Sharif, S.; Tolstoy, P. M.; Shenderovich, I. G.; Smirnov, S. N.; Golubev, N. S.; Denisov, G. S. *Chem. - Eur. J.* **2004**, *10*, 5195.

(42) Reichhardt, C.; Welton, T. In Solvents and Solvent Effects in Organic Chemistry; Wiley-VCH Verlag GmbH & Co. KGaA: Weinheim, **2011**; pp 417–422.

(43) Benedict, H.; Shenderovich, I. G.; Malkina, O. L.; Malkin, V. G.; Denisov, G. S.; Golubev, N. S.; Limbach, H. *J. Am. Chem. Soc.* **2000**, *122*, 1979.

(44) Limbach, H.-H.; Pietrzak, M.; Benedict, H.; Tolstoy, P. M.; Golubev, N. S.; Denisov, G. S. *J. Mol. Struct.* **2004**, *706*, 115.

(45) Grabowski, S. J. *Chem. Rev.* **2011**, *111*, 2597.

(46) Grabowski, S. J.; Sokalski, W. A.; Dyguda, E.; Leszczyn, J. *J. Phys. Chem. B* **2006**, *110*, 6444.

(47) The y-axis in Figure 7c has a scale in total energy due to the vanishing neutral hydrogen bond minima (no stationary point can be found; hence, no vibrational analysis can be performed)

(48) Smirnov, S. N.; Golubev, N. S.; Denisov, G. S.; Benedict, H.; Schah-Mohammedi, P.; Limbach, H.-H. *J. Am. Chem. Soc.* **1996**, *118*, 4094.

(49) Steiner, T. *J. Phys. Chem. A* **1998**, *102*, 7041.

(50) E. D. Glendening, J, K. Badenhoop, A. E. Reed, J. E. Carpenter, J. A. Bohmann, C. M. Morales, C. R. Landis, and F. Weinhold, NBO 6.0.,Theoretical Chemistry Institute, University of Wisconsin: Madison, WI, **2013**.

(51) The adjustment of the constants employed in equations 4 and 5 (b_{XH}^o and r_{XH}^o) to our theoretical data (see Supporting Information) is not suitable, because it impairs the weak neutral hydrogen bonded systems.

(52) For the description of the trans-hydrogen bond scalar couplings the definition of Dingley *et al*. is used. The abbreviation $^{3h}J_{PN}$ stands for scalar coupling between ^{15}N and ^{31}P over three bonds including a hydrogen bond and $^{2h}J_{PH}$ for scalar coupling between a ^{1}H and ^{31}P over two bonds. For reference see A. J. Dingley, F. Cordier, S. Grzesiek, *Concepts Magn. Reson.*, **2001**, *13*, 103-127.

(53) Federwisch, G.; Kleinmaier, R.; Drettwan, D.; Gschwind, R. M. *J. Am. Chem. Soc.* **2008**, *130*, 16846.

(54) Mishima, M.; Hatanaka, M.; Shigeyuki, Y.; Takahisa, I.; Wälchli, M.; Ito, Y.; Shirakawa, M. *J. Am. Chem. Soc.* **2000**, *122*, 5883.

(55) Detering, C.; Tolstoy, P. M.; Golubev, N. S.; Denisov, G. S.; Limbach, H. *Dokl. Phys. Chem.* **2001**, *3*

4 The influence of 3,3'-substituents of BINOL derived chiral phosphoric acids on the structure and hydrogen bond geometry of catalyst/imine complexes

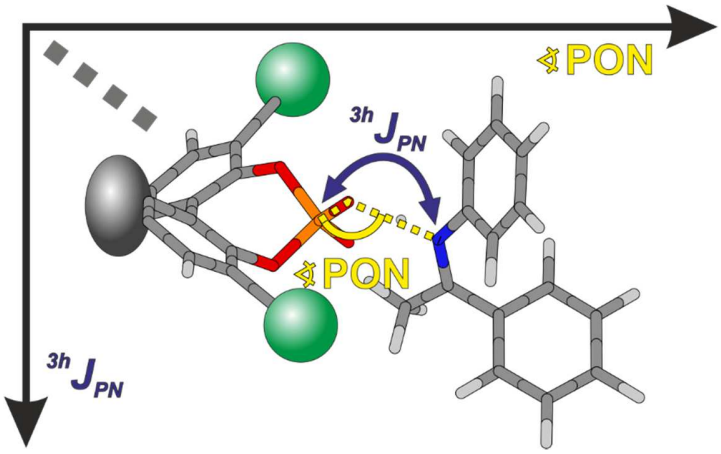

Maxime Melikian, Johnny Hioe, Julian Greindl, Nils Sorgenfrei, Thomas Hausler, Fabio Morana and Ruth M. Gschwind

a) NMR measurements for the structure determination and assignments were performed by Maxime Melikian. b) All computational studies were performed by Johnny Hioe. c) NMR measurements for the hydrogen bond analysis were done by Nils Sorgenfrei, Thomas Hausler, Maxime Melikian and Julian Greindl. d) Fabio Morana contributed in the optimization of the sample preparation and by synthesis of the catalyst (*R*)-TRIP f) Imine substrates were synthesized by all authors except Johnny Hioe. e) The major part of the manuscript was written by Julian Greindl and Johnny Hioe.

4.1 Abstract

BINOL derived chiral phosphoric acids (CPAs) are widely known for their high selectivity and reactivity. Numerous 3,3' substituents are used in synthesis for a variety of organocatalytic reactions. However, experimental investigations on the stereoinducing effect of these 3,3' substituents are scarce. Therefore, in a combined NMR spectroscopic and computational study, we analyzed here the structure and hydrogen bonds of various CPA/imine complexes to reveal the subtle differences, which may affect the enantioselectivity and reactivity. The four core structures of TiPSY ((*R*)-3,3′-bis(triphenylsilyl)-1,1′-binaphthyl-2,2′-diyl hydrogenphosphate)/imine were experimentally determined and compared to TRIP ((*R*)-3,3′-bis(2,4,6-triisopropylphenyl)-1,1′-binaphthyl-2,2′-diyl hydrogenphosphate)/imine complexes, revealing an astounding independence of the general structures on the 3,3'-substituents. Hydrogen bond strengths, distances and angles of TRIFP ((*R*)-3,3′-bis(3,5–bis (trifluoromethyl) phenyl)-1,1′-binaphthyl-2,2′-diyl hydrogenphosphate), TiPSY and TRIP/imine complexes were compared, by analyzing $^{1}J_{NH}$, $^{2h}J_{PH}$, $^{3h}J_{PN}$ coupling constants and chemical shifts of ^{1}H and ^{15}N via a Steiner-Limbach plot. The resulting internal acidity of the different CPAs showed no correlation with the reactivity in transfer hydrogenation reactions. The $^{3h}J_{PN}$ scalar coupling and their correlated PON-angles are the only experimetal parameters, which are connected to the established theoretical steric descriptors (AREA and rotational barrier of the 3,3'-substituent).

4.2 Introduction

In the field of Brønsted acid catalysis a variety of different catalyst classes have emerged in recent years, one of them being BINOL (1,1'-bi-2-naphthol) derived chiral phosphoric acids (CPAs).[1,2] CPAs have been successfully applied in several enantioselective syntheses such as transfer hydrogenations,[3–5] reductive aminations,[6,7] Mannich type reactions,[8–10] Strecker reactions,[11] and enantioselective additions.[12,13] The main difference between these BINOL derived CPAs are the 3,3' substituents, which greatly influence not only yields, but especially the selectivity of named reactions. Thus, CPAs with varying 3,3' substituents such as the 2,4,6-triisopropylphenyl groups of the Brønsted acid catalyst TRIP, the 3,5-bis(trifluoromethyl) groups of TRIFP, or the triphenylsilyl groups of catalyst TiPSY have been successfully employed (Figure 1b).[14–16] The cited transfer hydrogenations and the reductive amination generally show an increase in enantiomeric excess when the bulkiness of the substituents is increased, but also a sudden drop in yield and enantioselectivity when using extended aromatic systems such as naphthyl, or 4-biphenyl groups. The reason for these differences is still largely unexplored and vary from reaction to reaction.[17] To our knowledge, there is no experimental method for determining a suitable BINOL derived CPA other than trial and error, which can be explained by a lack of understanding of the underlying interactions and involved structures. Recent major efforts in determining the effect of 3,3'-substituents on the stereoinducing capabilities of CPA catalysts were conducted by Reid and Goodman using a combination of DFT and force field calculations.[18,19] The distal parameter, AREA (A Remote Environment Angle), and two proximal parameters, the rotational barrier of the 3,3'-substituents and A-values, were surveyed. Ground state parameters depending exclusively on the catalyst were determined by theoretical calculations and taken to predict the property of the transition state, and thus may be used for the selection and the development of the optimal catalyst for a specific reaction. Finding a straightforward trend between the properties of a substituent and reaction outcome (*ee* and yield) is a difficult task, due to the large amount of different reactions that can be catalyzed by CPAs. The steric descriptors AREA and A-values seem to be promising parameters that connect structural changes of the catalyst with selectivity of the reaction, but due to the lack of mechanistic investigations, only a correlation was established. In contrast to the detailed theoretical calculations, experimental investigations are rare, which is partially explained by the difficult accessibility of the predicted structures.

In a combined study of theoretical calculations and NMR spectroscopic investigations, Tang et al. showed the possibility to gain direct experimental insight into complex structures featuring CPAs with the help of an NOE analysis.[20] For the enantioselective transfer hydrogenation of imines, a catalytic cycle was proposed by Rueping et al.,[15] which suggests the formation of a binary complex between catalyst and substrate, directly followed by the enantioselective hydrogenation step (Figure 1a). Goodman et al. demonstrated in a theoretical study how the formation of four different binary complexes lead to four different transition states (denoted as *Type I E*/*Z* and *Type II E*/*Z*), which dictate the yield and selectivity of the transfer hydrogenation.[21] In our recent work on binary TRIP/imine complexes we were able to experimentally show the coexistence of the four core structures (*Type I/II E* and *Type I/II Z*) that were predicted by calculations (Figure 1c).[22] The nomenclature of the four core structures was adapted to the transition states by Goodman.

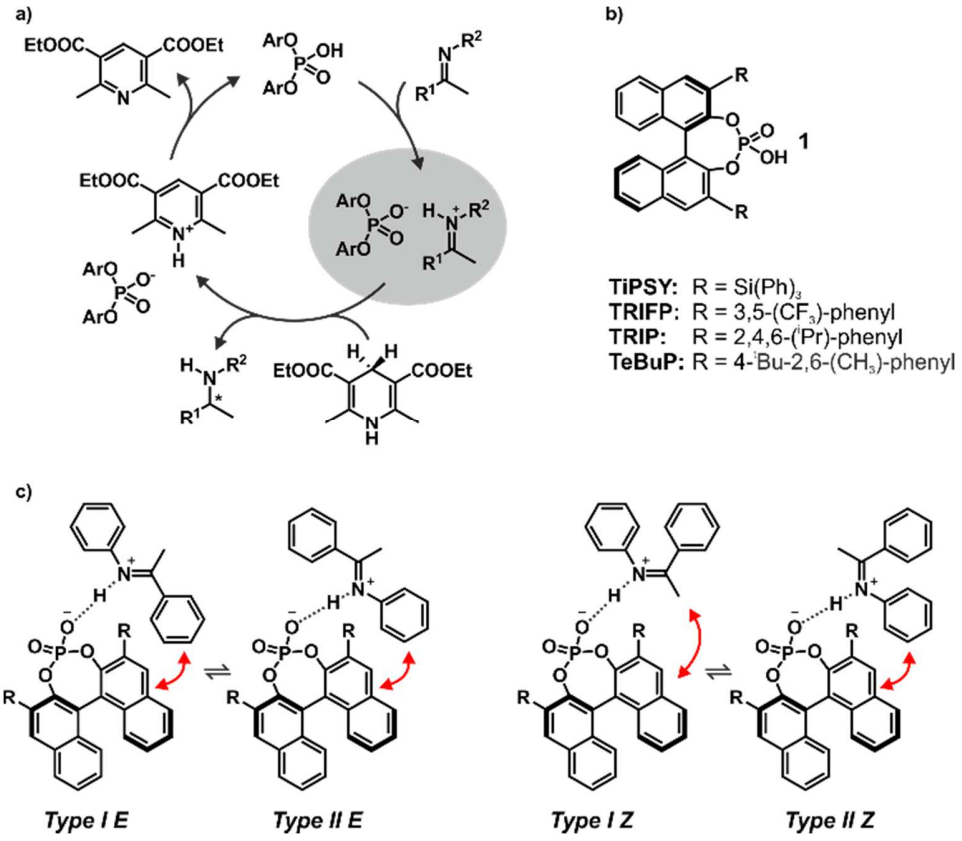

Figure 1. a) Catalytic cycle of the transfer hydrogenation of imines with a chiral phosphoric acid catalyst and a Hantzsch ester as reducing agent. The binary complexed highlighted in grey is the focus of this work; b) Brønsted acid catalysts with different 3,3' groups; c) The four core structures of the binary complex identified in our previous work.[22] The red arrows mark some of the identified interactions.

Furthermore, we conducted an in depth investigation of the hydrogen bond of TRIP/imine complexes with a detailed coupling constant analysis and resulting hydrogen bond geometries.[23] In addition, we recently developed the DTS-hv (Decrypting Transition States by light) method to experimentally identify the transition state situation of TRIP/imine complexes for the enantioselective transfer hydrogenation.[24] With this technique we could identify the competition of two *Z*-imine containing complexes as deciding factor for the resulting enantiomeric excess of the reaction. We demonstrated that the hydrogen bond in the transition state (ternary complex) for *Z*-configured imines is stronger than that of *E*-imines, which is already visible in the binary complex.[23] For a series of TRIP complexes with different imines our investigations showed an invariance of the general structures and structural features,[22] but no research was done regarding the structural variations for different 3,3'-substituents. The strong influence of the 3,3'-substituents on yield and enantioselectivity is readily visible in all reported reactions with BINOL derived CPAs. Substituted phenyl moieties are generally favoured, while extending the aromatic system to naphthyl or 4-biphenyl groups shows a negative impact on yield and enantiomeric excess for the investigated transfer hydrogenation of imines.

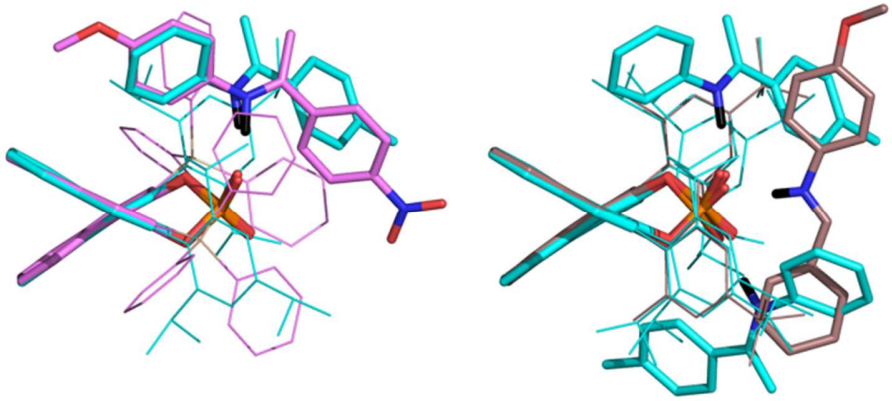

Figure 2. a) Structure similarity of a crystal structure of a TiPSY/imine complex[6] (pink) and structure *Type II E* of a TRIP/imine complex identified in our previous work[22] (cyan); b) structure deviation of the crystal structure of a TeBuP/imine complex[25] (brown) vs both *Type II E* (cyan above) and *Type I E* (cyan below). The imine shows an intermediate position of *Type I E* and *Type II E*.

To our knowledge, the only experimental information on the structures of BINOL derived CPAs/imine complexes other than our TRIP/imine investigations were provided from the groups of MacMillan[6] and Schneider[25] in the form of crystal structures. The structure of MacMillan consists of a TiPSY/imine complex and is in good agreement with core structure

Type II E that was experimentally identified in TRIP/imine complexes in our group (Figure 2a). The crystal structure of Schneider consists of a TeBuP ((*R*)-3,3'-bis(4-tertbutyl)-(2,6-dimethylphenyl))-1,1'-binaphthyl-2,2′-diyl hydrogenphosphate)/imine. Here, the imine exhibits an intermediate position of structures *Type I E* and *Type II E* probably due to the crystallization of a dimeric complex (Figure 2b). However, no experimental data is available on the influence of different 3,3' substituents on the complex structure in solution. Our recent investigations on binary CPA/imine complexes in the transfer hydrogenation were used as an experimental basis for this publication. The extensive knowledge about structures, hydrogen bonds and even transition state combinations opens up a unique possibility to elucidate a potential correlation between experimentally determined ground state parameters of the binary complexes and enantioselectivities in a given mechanistic pathway.Therefore, in this report we investigate the chiral phosphoric acids TiPSY and TRIFP in binary complexes with imines by means of NMR spectroscopy, supplemented by theoretical calculations. The complex structures as well as hydrogen bond strengths and geometries are determined and compared to TRIP/imine complexes and the reported crystal structures.

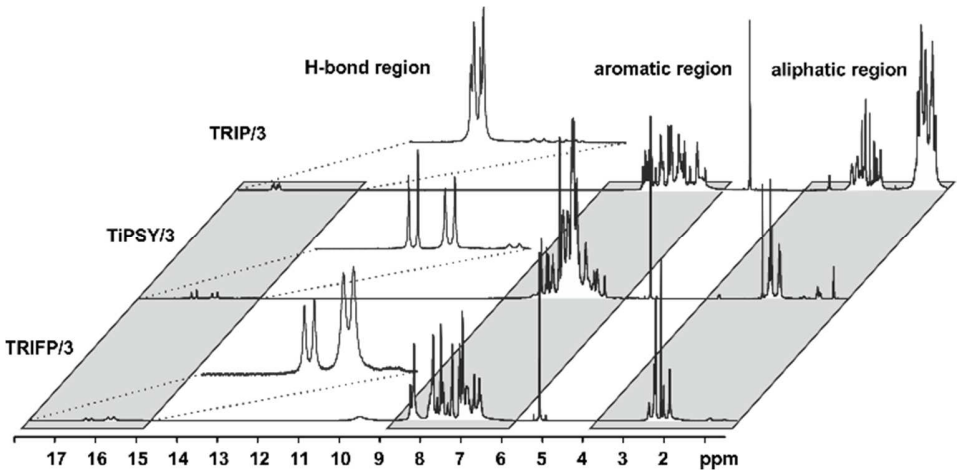

Figure 3. Comparison of the ^{1}H spectra of complexes between catalysts TRIP, TiPSY and TRIFP and imine **3** at 180 K in CD_2Cl_2; in all cases the strong hydrogen bonds allow for an in depth NMR spectroscopic analysis; the increased linewidths of TRIFP/imine complexes and the chemical shift overlap of key signals, especially in the aromatic region, excluded them for the structural investigations via NOE analysis.

The influence of the different 3,3' substituents of BINOL derived CPAs on general complex structure as well as hydrogen bond distances and geometries is experimentally and theoretically described. The resulting contributions to reactivity and selectivity of the catalysts in the transfer hydrogenation reaction are discussed.

4.3 Results and Discussion

4.3.1 Investigated systems and their NMR properties

In order to investigate the influence of different 3,3' substituents of CPAs on the complex structures of CPA/imine complexes, we studied three of the main CPAs catalysts used in synthesis (for structures see Figure 1b, for ^{1}H spectra Figure 3). The triphenylsilyl groups of TiPSY produced significantly higher signal overlap in our NMR spectroscopic investigations than the previously determined TRIP/imine complexes, but still allowed for structural investigations via NOE analysis. For CPA/imine complexes of TRIFP, a lack of NMR signal splitting regarding key signals involved in catalyst/imine interaction in both aromatic and aliphatic regions prevented a structural investigation. In addition, NMR signals in TRIFP/imine complexes experienced a significant line broadening when compared to TiPSY/imine and TRIP/imine complexes (Figure 3). In addition to our NOE investigations we performed a detailed hydrogen bond analysis of several TiPSY/imine and TRIFP/imine complexes, because of the high sensitivity of these NMR parameters ($^{1}J_{NH}$, $^{2h}J_{PH}$ and $^{3h}J_{PN}$ coupling constants) to structural changes, as demonstrated in our previous work.[23] Here, the good signal splitting in the H-bond region, allowed for the investigation of imine complexes with both catalysts TiPSY and TRIFP (Figure 3).

Structural investigations of imines **1**, **13**, **14** and **15** and their respective complexes with TiPSY were performed in CD_2Cl_2 at 180 K, as this solvent showed the highest signal dispersion and allowed for an NMR assignment as well as NOE analysis. For the hydrogen bond analysis, binary complexes of TiPSY with imines **1**-**8** (Figure 4a) and TRIFP with imines **1**-**5** were investigated again in CD_2Cl_2. In order to compare hydrogen bond geometry properties between these complexes with data obtained from a previous work,[23] complexes of TRIP and imines **1**-**6** and **9**-**12** were added to the analysis.

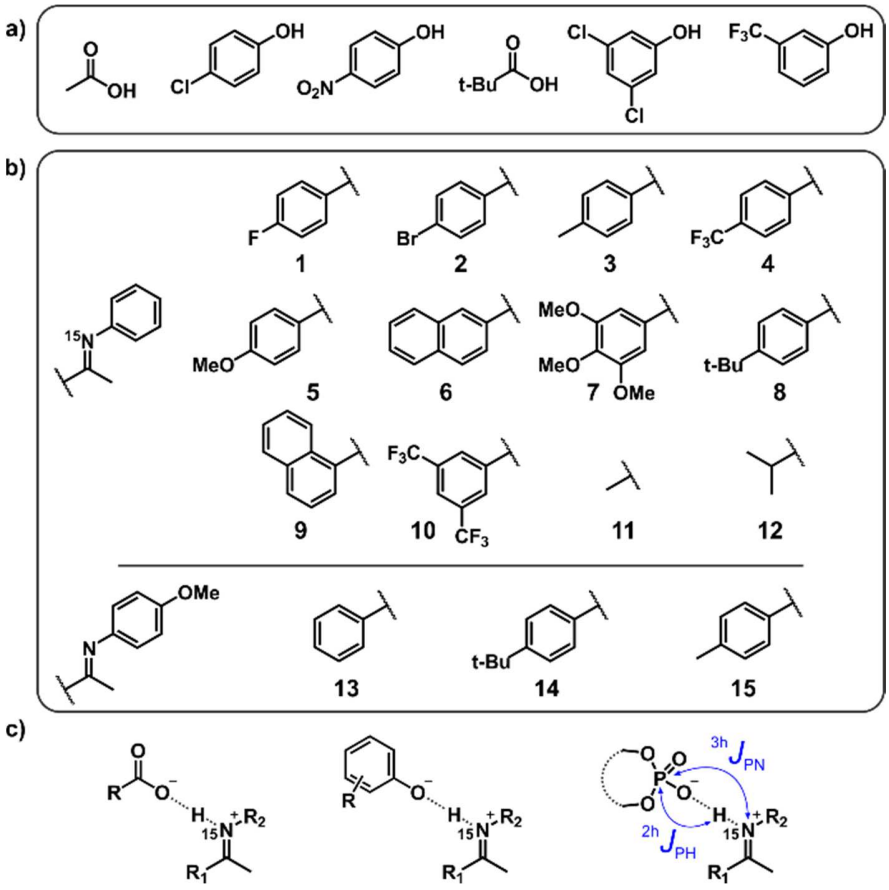

Figure 4. a) Acids and phenol derivatives used in the hydrogen bond analysis; b) a total of twelve ^{15}N-labelled imines (**1**-**12**) were used to provide hydrogen bond distance information from the Steiner-Limbach curve; imines **13**-**15** were used for the NOE analyses; c) hydrogen bonds investigated in the Steiner-Limbach plot and coupling constants analyzed in this work ($^{2h}J_{PH}$ and $^{3h}J_{PN}$).

^{15}N labelling of the imines allowed for ^{15}N chemical shift investigations and detection of $^{2h}J_{PH}$ and $^{3h}J_{PN}$ coupling constants (Figure 4b). In addition to the phosphoric acid catalysts, tetrafluoroboric acid (HBF_4) was used to form predominantly ion paired complexes, whereas acetic acid (AcOH), trimethyl acetic acid (TMA) and various phenols (4-chlorophenol, 4-nitrophenol, 3,5-dichlorphenol, 3-(trifluoromethyl)phenol) were used to form predominantly neutral complexes. As detailed in our previous work, dichloromethane or freonic solvent mixtures[23] were used as solvents to produce small signal linewidths and the highest achievable signal dispersion at low temperatures. Temperatures between 180 K and 130 K were needed to sufficiently slow down the exchange processes in solution.

4.3.2 Theoretical model structures and structure comparison

Our theoretical calculations of TiPSY, TRIFP/**3**,**4**,**5** confirm the general existence of the four core structures (*Type I/II E*/*Z*) as also described for TRIP/imine complexes (for computational details, see Supplementary S80,S81 and Table S9).[22] Each of the *E*- and *Z*-imine complexes features two different orientations of the imine (Figure 5). In the *Type I* orientation, the ketone moiety is located in close proximity to the BINOL backbone of the catalyst. In the *Type II* orientation, the imine is rotated around the hydrogen bond by ~180° and the aniline moiety is located close to the BINOL backbone.

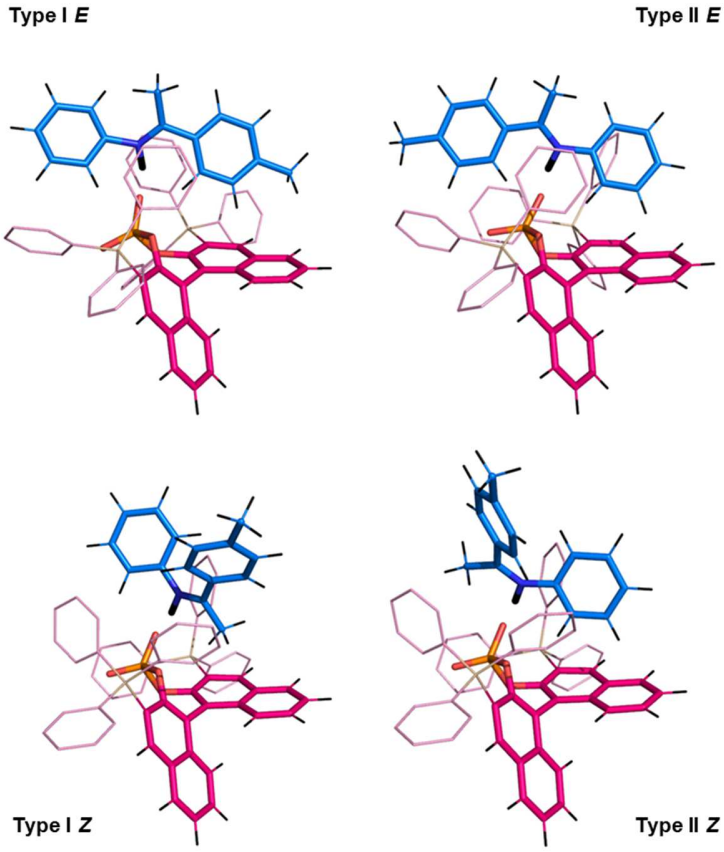

Figure 5. Theoretical calculations of the TiPSY/**3** complex show four core structures, two of which contain the *E* isomer and two structures containing the *Z* isomer of the imine, the imine is rotated by ~180° when comparing structure *Type I* to structures *Type II* for both isomers; Similar core structures were also predicted for binary complexes of TiPSY/**4**,**5** and TRIFP/**3**,**4**,**5**.

Geometrical comparison of the four core structures from the calculation revealed a high degree of invariance in the CPA/imine complexes. As in TRIP/imine complexes[22] the two orientations of the *E* and *Z* imine in TiPSY/**3**-**5** (Figure 5) as well as TRIFP/**3**-**5** binary

complexes are obtained. Furthermore, similar van der Waals interaction types (π- π, CH- π) are clearly recognizable from the structural analysis. As shown in the previous studies,[23] the acidic proton is located closer to the imine in TiPSY and TRIFP binary complexes, which indicates a strong predominant zwitter ionic character. No neutral hydrogen bond complexes could be obtained in the dielectric medium at low temperature. The OHN angles range from 161o to 179°, showing an almost linear bond geometry. The POH angle varies from 110° to 132°, showing a substantial covalent contribution in the hydrogen bond.[26] Furthermore, due to the linearity of the hydrogen bond, the calculated PON angle is similar to the POH angle. Overall, the similarity observed in all three different catalysts driven by the strong hydrogen bond explains the high tolerance towards substrates with different electronic properties, i.e. the activation of different substrates is independent to the substituent pattern of the catalyst. Despite the similar activation mode and high structural conservation, the measured *ee* values and yields seem to be dependent to the 3,3'-substituent present in the catalyst. Therefore we searched for structural differences caused by different 3,3'-substituents.

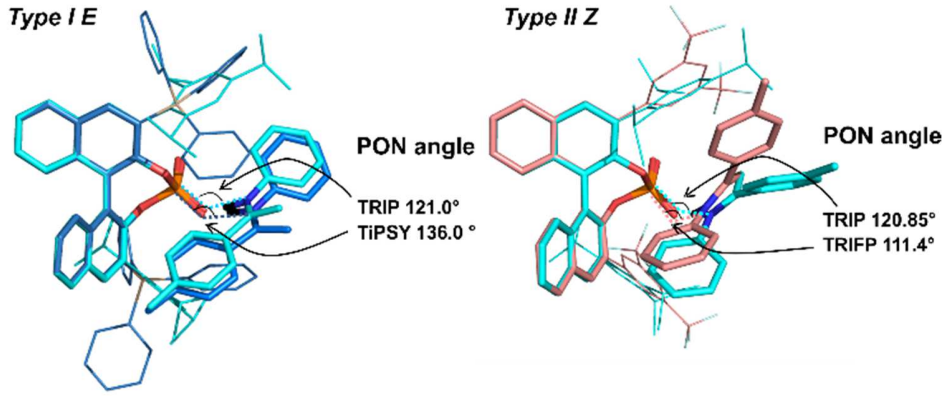

Figure 6. Left side: Superposition of the calculated structure *Type I E* of complex TiPSY/**3** (marine blue) and calculated structure *Type I E* of TRIP/**3** (cyan);[22] right side: Superposition of the *Type II Z* structures of TRIP/**3** (cyan) and TRIFP/**3** (salmon); the main structural deviation between the complexes is a result of the different PON angles.

From the calculation, the only significant difference obtained for the ground state structures are the bending angles (POH, PON, OHN) of the hydrogen bond. This structural variance may be one of the factors attributing to the energetic differences of transition states. However, to establish a correlation between structure and reactivity/stereoselectivity, an experimental validation of the different bending in the predicted CPA/imine complexes is required. Usually, fine parameters, such as bending angles across hydrogen bonds are hardly accessible by experiments. However, our special NMR spectroscopic access to the hydrogen bonds in

CPA/imine complexes combined with an interpretation by theoretical structural analysis should allow for an experimental validation. Therefore, a NMR structure determination of the different conformations and a full characterization of the hydrogen bonds were performed experimentally by NMR spectroscopic methods.

4.3.3 NMR assignment and structure determination of TiPSY/imine complexes

For complexes providing such degree of signal overlap as shown in Figure 3, there are quite a few NMR spectroscopic techniques that are typically used to improve signal dispersion. These are mainly 3D experiments such as 3D-^{15}N NOESY HSQC[27] or 3D ^{13}C NOESY HSQC[28] or pure shift techniques. [29–31] Especially the multidimensional approach[32–34] is broadly applied in biochemistry and requires the use of specific labeling strategies.[35–37] Due to the limited possibilities to include isotope labeling via different synthetic strategies into the catalyst or the imine, the chemical exchange even at low temperatures[22] and the lowered solubility at the required temperatures, all of these more advanced techniques proved to be too insensitive to provide structural information in our case. Instead we focused mainly on the most sensitive one- and two-dimensional NMR methods (^{1}H,^{1}H / ^{1}H,^{13}C 2D spectra for assignments and selective 1D NOESY[38–40]/ 2D NOESY/ ^{1}H,^{19}F HOESY[41,42] spectra for structural investigations).

In TiPSY/imine mixtures (1:1) at 300 K, only one averaged set of NMR ^{1}H signals is visible from the catalyst whereas two sets of signals corresponding to the *E*- and *Z*- isomers of the imine inside the binary complex are observed (similar to the situation in TRIP/imine complexes[22]). The *E*- and *Z*-isomers of the imines were identified from NOESY experiments (Supplementary S1). At 180 K, the ^{1}H signals of the catalyst split into three different sets of signals corresponding to the respective interactions with the *E*-imine (two sets) and with the *Z*-imine (one set) (Supplementary S2,S4,S5). The decrease of temperature is required in order to reduce the effect of conformational averaging and chemical exchange. Since DTS-hv experiments[24] revealed the *Z*-complexes as the reactive species, we paid attention to the variation of the *E*/*Z* imine ratios in the investigated complexes at 180 K. Indeed, varying ratios generally higher than in TRIP/imine complexes were found. In the TiPSY/**1** complex, the *E*/*Z* ratio reached 68:32. For the TiPSY/**13** complex, a 44:56 *E*/*Z* ratio was found, a rare example with higher *Z*-imine concentration. The respective *E*/*Z* ratios found for imines **14** and **15** were 50:50 and 53:47 (see hydrogen bond section for reactivity discussion and Supplementary S3 for data). A complete assignment of the TiPSY/imine complexes was done for imines **1**, **13**,

14 and **15** at 180 K (for spectra and assignment strategies see Supplementary S1-S28). Despite a severe signal overlap in the crowded aromatic region (Supplementary S4, S5), most of the signals were unambiguously assigned.

The assignment of the *E Type* core structures of the TiPSY/imine complexes (*Type I E*, *Type II E*) is shown exemplarily on imine **1**. With the help of ^{19}F spectroscopy the spectral resolution can be vastly improved by reducing the complexity of the obtained spectra.[43–45] Orientation *Type I E* was identified in a 2D ^{1}H ^{19}F HOESY experiment. A total of four HOE cross-peaks were found between the fluorine atom of imine **1** and the BINOL backbone of the catalyst (Figure 7).

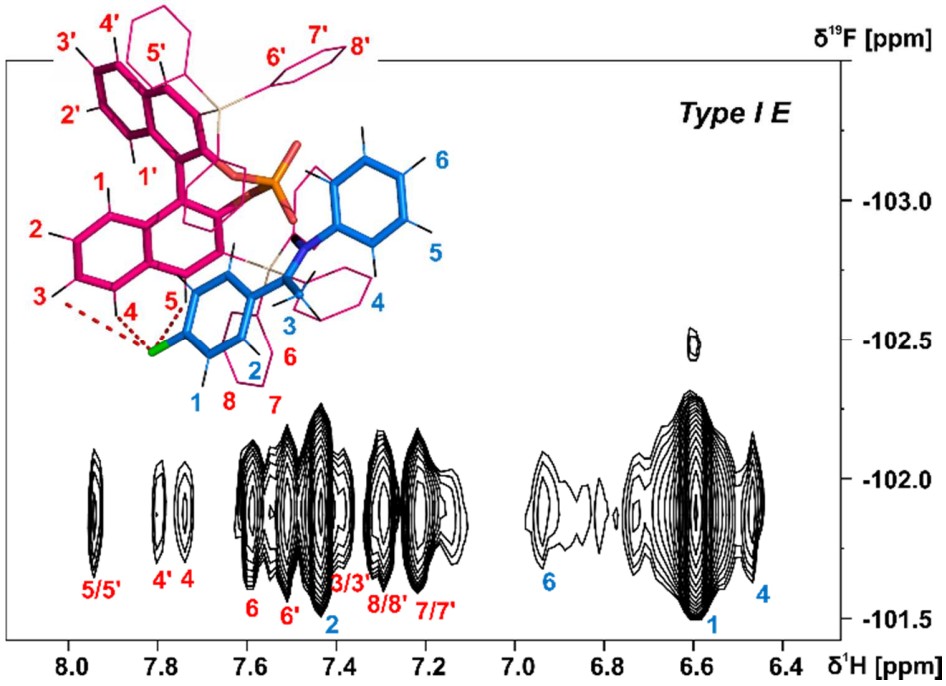

Figure 7. Section of a ^{1}H,^{19}F 2D HOESY spectrum of TiPSY/**1** at 180 K in CD_2Cl_2 at 600 MHz; Red dashed lines correspond to the intermolecular HOEs identifying complex structure *Type I E* (for detailed NMR parameters see Supplementary S14).

The presence of the HOE cross-peaks between imine **1** and the protons 3, 4 and 5 of the TIPSY backbone in combination with the hydrogen bond confirm the existence of the *Type I E* structure. Due to a dissociation, rotation and re-association of the TiPSY/imine complexes (Figure 8), HOEs are also observed between the fluorine atom of **1** and the opposite naphthyl moiety of the catalyst (Figure 7, HOE to proton 4'). This exchange is slow on the NMR timescale compared to the tilting mechanism that leads to an exchange between structures *Type I E* and *Type II* E (Figure 8). A rotation of the *E*-imine inside the complex can be

excluded, since the rotational barrier for this process would be by far too high due to the steric hindrance of imine inside the complex. The same complex structures were identified for imines **14** and **15** (Figures S17 and S19).

Orientation *Type II E* in the TiPSY/**1** complex was identified by using selective 1D NOESY experiments. By selectively exciting the aromatic proton in para position of the aniline moiety of **1**, NOEs to the protons 4' and [5, 5'] of the BINOL backbone of the catalyst were observed (Figure 9). These NOEs in combination with the strong hydrogen bond between catalyst and imine confirm structure *Type II E* in the TiPSY/**1** complex.

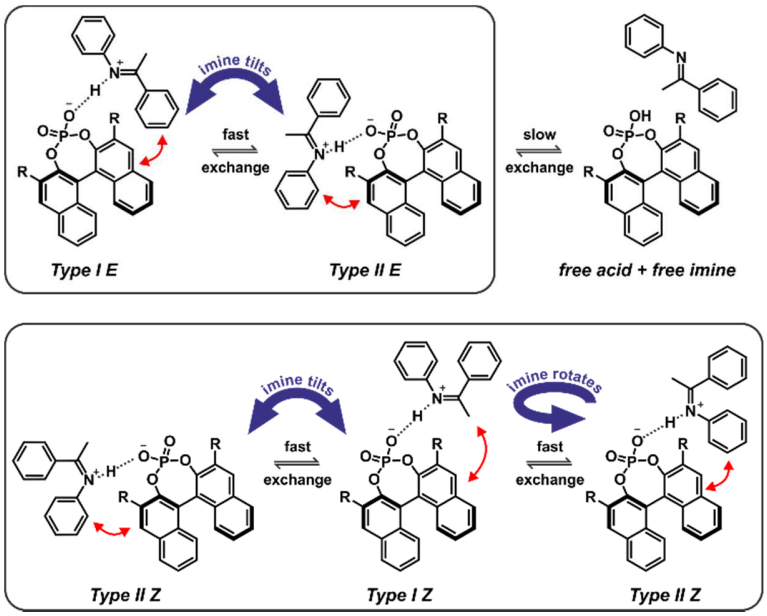

Figure 8. Complex exchange processes in TiPSY/imine complexes; an exchange via tilting of the imine is observed between structures *Type I E* and *Type II E* as well as a disassociation and association process of the TiPSY/*E*-imine complexes; the exchange via tilting is fast on the NMR time-scale and leads to a different interaction pattern for each half of the catalyst; the dissociation and association process is slow on the NMR time-scale and leads to exchange peaks between the catalyst halves; in addition to an exchange via tilting of the imine, the reduced steric hindrance of the *Z*-imine enables an additional fast exchange between structures *Type I Z* and *Type II Z* via rotation, leading to a different signal pattern.

Again, a NOE is observed between the excited proton and the opposite naphthyl moiety of the catalyst backbone due to the described dissociation/association process (Figure 9, NOE to 4).

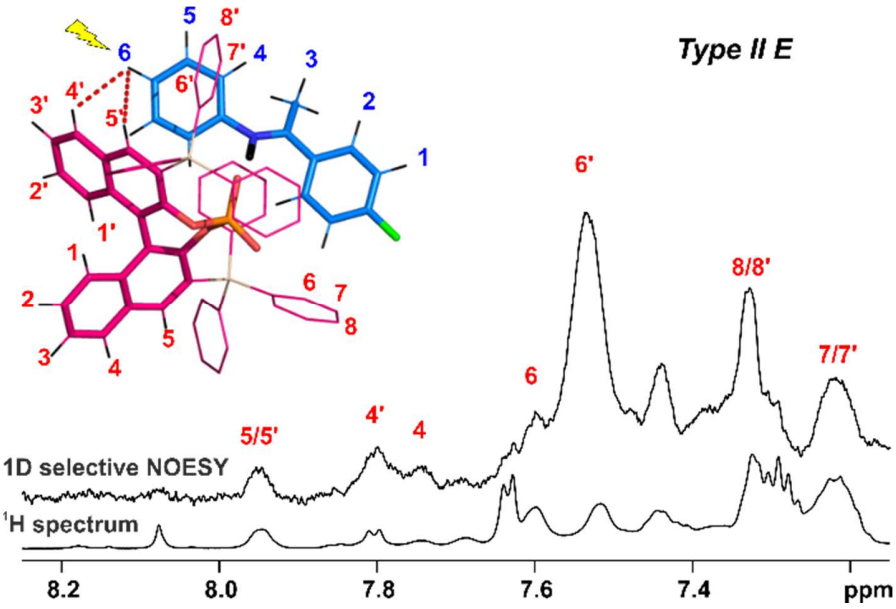

Figure 9. Selective 1D NOESY spectrum (blue) and reference ^{1}H spectrum of complex TiPSY/**1** (red) at 180 K in CD2Cl2 at 600 MHz; highlighted cross-peaks (red dashed lines) correspond to the interaction between the aromatic proton in para position 6 (blue) of **1** and the backbone protons 4' and [5, 5'] of the catalyst (red) (NMR parameters in Supplementary S15); NOE to opposite signal 4 also visible due to dissociation/reassociation of the complex.

This fast exchange on the NMR time scale between structures *Type I E* and *Type II E* is identical to our investigations on TRIP/imine complexes.[22] The interactions of the imine with both naphthyl units of the BINOL backbone of the catalyst described above are in agreement with the tilting process of the *E*-imine inside the complex. Similar NOE patterns for conformations *Type I E* and *Type II E* were observed for TiPSY complexes with the imines **13**, **14** and **15** (Supplementary S16-S20).

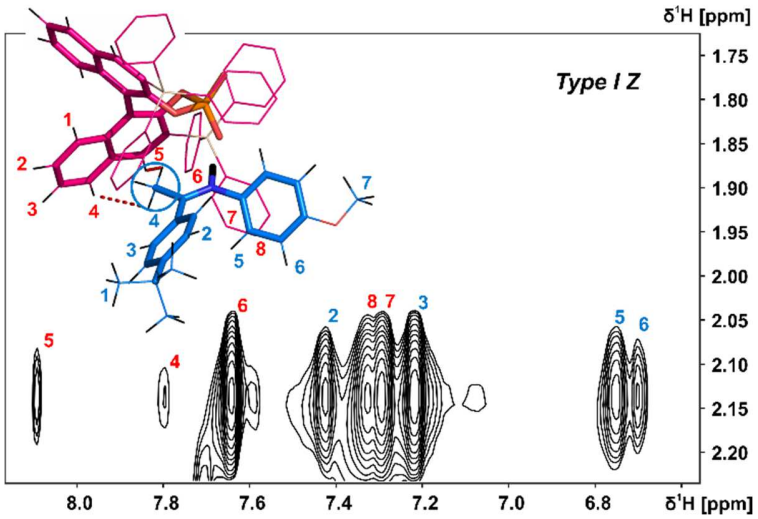

Figure 10. Excerpt of the 2D NOESY spectrum of TiPSY/**14** at 180 K in CD_2Cl_2 at 600 MHz; intermolecular cross-peaks (red numbers) detail the interaction between α methyl group of **14** (blue spin 4) and BINOL backbone of the catalyst (for detailed parameters see Supplementary S25).

In contrast to the TiPSY/*E*-imine structures, only one set of signals is observed for the BINOL backbone of the catalyst in the TiPSY/*Z*-imine complexes. This can be explained by the reduced steric hindrance of the Z-imine enabling an exchange between orientation *Type I Z* and *Type II Z* via rotation of the imine around the hydrogen bond (Figure 8). This exchange pathway in addition to the exchange via tilting of the imine (see TiPSY/*E*-imine), results in only one average set of ^{1}H signals for the BINOL backbone of the catalyst similar to our recent findings on TRIP/*Z*-imine complexes.[22]

Both orientations *Type I Z* and *Type II Z* were detected for the TiPSY/*Z*-imine complexes. Complex TiPSY/14 is used exemplarily for the assignment of *Type I Z* (Figure 10). In the ^{1}H NOESY spectrum, two specific intermolecular NOEs between the alpha methyl group of the imine and the BINOL backbone of the catalyst were found. This interaction, in combination with the strong hydrogen bond between catalyst and imine shows the existence of orientation *Type I Z* in solution. The same NOE pattern can be observed for all other investigated complexes TiPSY/**1**,**13**,**15** (Supplementary S21, S23 and S27).

Orientation *Type II Z* could again be confirmed in selective 1D NOESY spectra, which is exemplarily shown for the TiPSY/**15** complex (Figure 11). By selectively exciting the methoxy group of imine **15**, three intermolecular NOEs were observed to the BINOL backbone of the catalyst (spins 3, 4 and 5). In combination with the strong hydrogen bond between catalyst

and imine, this NOE pattern confirms the existence of orientation *Type II Z* for the TiPSY/**15** complex. This orientation was also confirmed for the other investigated complexes TiPSY/**1**,**13**,**14** (Supplementary figures S22, S24 and S26). An identical NOE pattern was previously observed in TRIP/imine complexes,[22] reinforcing the similarities between the two catalysts regarding the catalyst/substrate interaction.

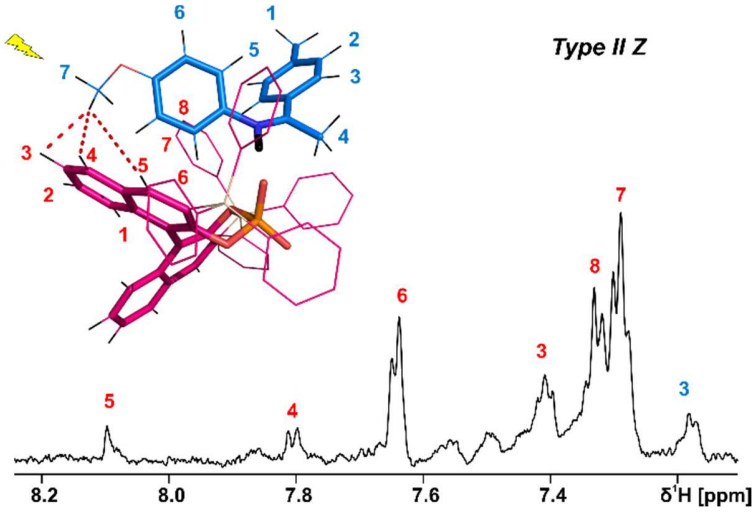

Figure 11. Selective 1D NOESY spectrum of complex TiPSY/**15** at 180 K in CD_2Cl_2 at 600 MHz; intermolecular cross-peaks (red numbers) to show the interaction between the p methoxy group of **15** (NOE 7) and the BINOL backbone of the catalyst (for detailed parameters see Supplementary S27).

Altogether, the four core structures, *Type I E*, *Type II E*, *Type I Z*, *Type II Z* were unambiguously determined by NMR spectroscopic investigations for complexes of TiPSY and imines **1**, **13**, **14** and **15** and approve the theoretically predicted conformational space for TiPSY/imine complexes (Figure 5).

4.3.4 Hydrogen Bond Analysis in TiPSY and TRIFP catalysts and comparison with TRIP

NOE studies are capable of providing principal conformational information (see above) but are weak in addressing subtle structural changes such as small deviations in PON angles as predicted by the theoretical calculations (see Figure 6). Therefore, detailed hydrogen bond investigations were used as a probe to further investigate the influence of the 3,3' substituents of BINOL derived CPAs on the hydrogen bond geometry, i.e. the resulting catalyst/substrate structures. Furthermore, the relative hydrogen bond strengths was investigated in terms of an

internal acidity and their correlation to the reactivity of the complexes.

The Steiner-Limbach correlation curve can be used to characterize hydrogen bonds in phosphoric acid catalyst/imine complexes as recently demonstrated for TRIP/imine complexes.[23] By plotting the ^{1}H chemical shift δ(OHN) of the acidic proton against the ^{15}N chemical shift of the basic nitrogen δ(OHN), a parabolic correlation curve can be fitted to the data (Figure 12 and Tables S1-S6). In order to achieve a sufficient fit, hydrogen bonds in a variety of different strengths are required. All catalyst/imine complexes investigated in this work feature a strong hydrogen bond with ^{1}H chemical shifts ranging from 15 to 19 ppm. For the ^{15}N chemical shifts in this analysis the zero-point was set to 340 ppm to show the deviation of the complexed imines from their neutral form (δ(^{15}N) = ~330 ppm) and range from -90 to -150 ppm. In addition to the strong hydrogen bonds of the Brønsted acid catalyst/imine complexes, several phenol derivatives, organic acids and tetrafluoroboric acid were used in combination with different imines for the data points of weaker hydrogen bonds on the outer parts of the curve. Due to the similarities of a hydrogen bond acceptor and donor pair to a proton-transfer reaction, the obtained correlation curve can be used to determine the valence bond orders p_{OH}^{H} and p_{HN}^{H} as presented in equations (1-4)

$$\delta(O\underline{H}N) = \delta(O\underline{H})^{0} p_{OH}^{H} + \delta(\underline{H}N)^{0} p_{HN}^{H} + 4\,\delta(O\underline{H}N)^{*} p_{OH}^{H}\, p_{HN}^{H} \quad (1)$$

$$\delta(OH\underline{N})_{ref} = \delta(\underline{N})^{0} p_{OH}^{H} + \delta(H\underline{N})^{0} p_{HN}^{H} + 4\,\delta(OH\underline{N})^{*}\, p_{OH}^{H}\, p_{HN}^{H} \quad (2)$$

$$p_{OH}^{H\,\prime} = p_{OH}^{H} - c^{H}\,(p_{OH}^{H}\, p_{HN}^{H})^{f}(p_{OH}^{H} - p_{HN}^{H}) - \mathrm{d}^{H}(p_{OH}^{H}\, p_{HN}^{H})^{g} \quad (3)$$

$$p_{OH}^{H\,\prime} = p_{OH}^{H} - c^{H}\,(p_{OH}^{H}\, p_{HN}^{H})^{f}(p_{OH}^{H} - p_{HN}^{H}) - \mathrm{d}^{H}(p_{OH}^{H}\, p_{HN}^{H})^{g} \quad (4)$$

By varying the correction factors proposed by Limbach and Desinov[46] (Supplementary table S1,S2) the agreement between the Steiner-Limbach curve and the experimental data points can be improved. The empirically determined valence bond orders are used to calculate the corresponding atomic distances (r_{OH}, r_{NH}, r_{NO}) as presented in equations (5-6) (Supplementary Table S5 and S6).

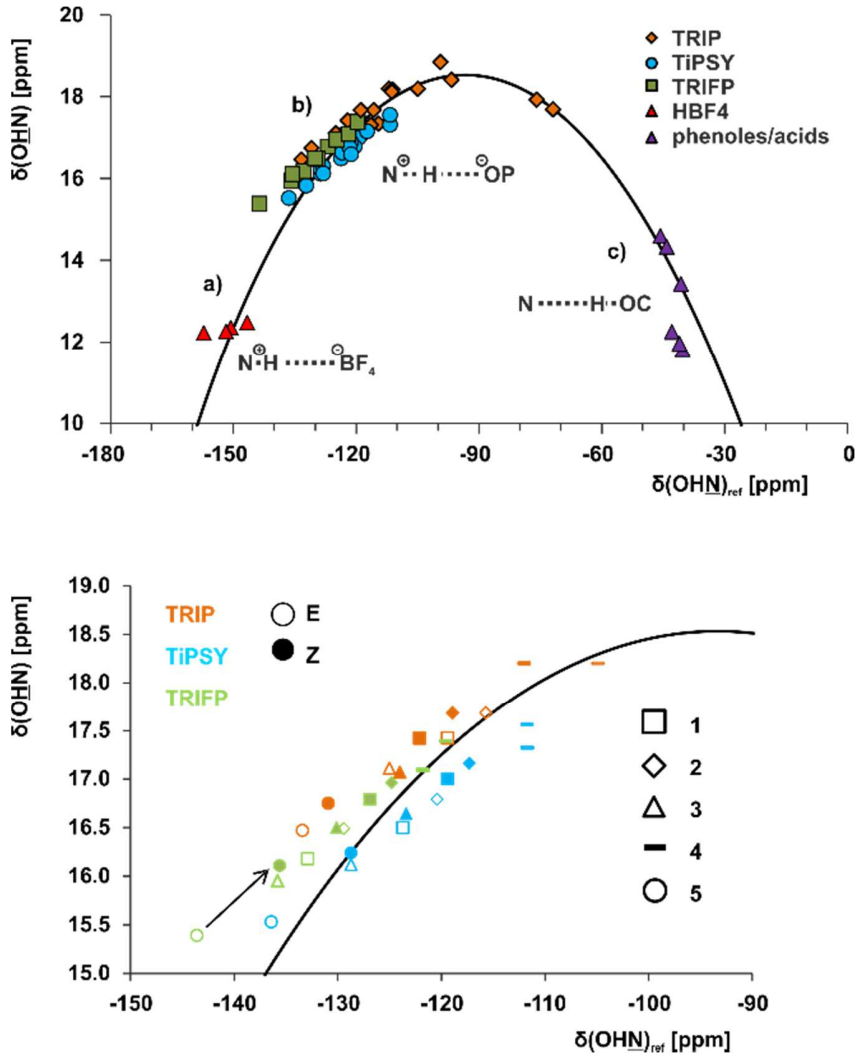

Figure 12. Plot of δ(OHN) against δ(OHN) of the hydrogen bonded complexes; a) HBF_4 with imines **3** and **5** ; b) TiPSY in complex with imines **1**-**8** ; TRIFP catalyst in complex with imines 1-5 ; TRIP catalyst in complex with imines **1**-**6**; **9**-**12**;[23] c) carboxylic acids and phenols with imines **3** and **5**; the ^{15}N chemical shifts of all complexes are referenced to {δ(OHN) = δ(OHN)exp – 340 ppm} (for experimental conditions see Table S3 and S4); lower panel: CPA/imine section of the Steiner-Limbach plot to highlight the difference between *E* and *Z* imines.

All investigated TiPSY and TRIFP complexes show a strong hydrogen bond with a predominantly ion pair character. Significant differences are observed when comparing the catalysts. TiPSY/imine complexes generally feature stronger hydrogen bonds (higher ^1H shift) than TRIFP/imine complexes (Figure 12). When comparing the *E* imine to the *Z* imine, stronger hydrogen bonds are generally found in the catalyst/*Z* imine complexes, as indicated by the low field ^1H shift of the hydrogen atom (Figure 12, lower panel). This difference in

hydrogen bond strength might explain the preference of Z imine transition states, as described in our recent work.[24]

The derived r_{NO} distances in a binary complex are often associated with the hydrogen bond strength and contraction degree of the complex. In general, the r_{NO} distances can be calculated as the sum of the r_{NH} and r_{OH}, when the OHN angle is 180°. However, it should be noticed, small deviation from linearity was predicted from the calculation. Given a range of OHN angles between 161° and 177° for complexes of TRIP, TiPSY or TRIFP with *E*/*Z*-imines **3**, **4**, and **5** the derived r_{NO} distance must be shorter than the sum of r_{NH} and r_{OH}. Therefore, the OHN angles were determined from the calculation and a correction was applied to the derived r_{NO} distances from the Steiner-Limbach analysis (see Supplementary Table S5,S6 and S8 and Figure S78). The bending correction is generally small and amounts to 2-3 pm. All CPA/imine complexes showed adequately short r_{NO} distances (2.49-2.65 Å), which are characteristic for strong hydrogen bond complexes.[26,47,48] The trend in r_{NO} distances of CPA/*E* imine complexes after the angle correction follows the hydrogen bond strength. In contrast, no trend is observed in CPA/*Z* imine complexes (Figure 13).

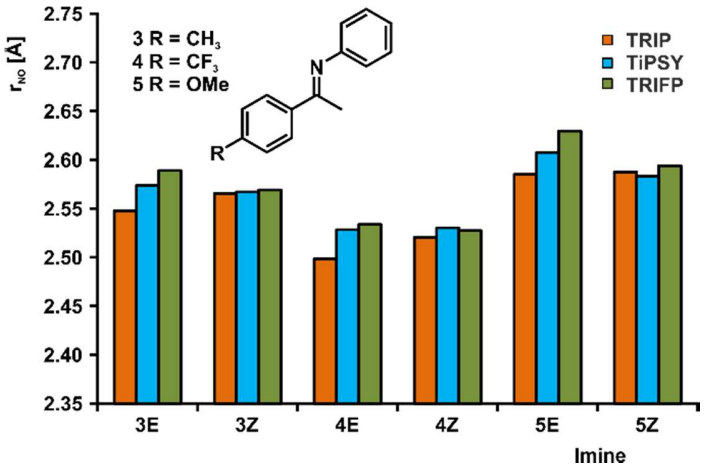

Figure 13. Comparison between catalyst/imine hydrogen bond r_{NO} intermolecular distances obtained from Steiner-Limbach curve for imines **3**-**5**; the calculated OHN angles were used to correct the measured distances.

The internal acidity of the catalysts in their imine complexes can be measured by comparing the determined r_{NO} distances (Figure 13). Longer distances are observed for stronger acids, since a stronger protonation leads to a higher deviation of the proton position from the middle of the bond. This internal acidity shows a different trend for the *E* imine complexes (pKaTRIFP < pKaTiPSY < pKaTRIP) than for the *Z* imine complexes, where similar distances are

observed for every catalyst. The external acidities of TRIFP and TRIP, as described in a scale by O'Donoghue (pKaTRIFP < pKaTRIP),[49] correlate at least in their trend with our internal acidities of the E-imine complexes. However, our calculated external acidity of TiPSY (pKaTRIFP < pKaTRIP < pkATiPSY, see Supplementary S77) shows a deviation to the internal relative acidities of the investigated complexes. Furthermore, the almost identical internal acidities of the *Z* imine complexes show no correlation. This can be explained by the dispersive interactions between catalyst and substrate, which influence the hydrogen bond and thereby the internal acidity.

Previously, a correlation was postulated between the acidity of CPAs and their reactivity.[50] With the internal acidities at hand we tested the relative reactivities of the three catalysts at identical conditions comparable to our NMR investigations and identified TRIP as the most reactive. TRIFP showed a slightly lower reactivity and TiPSY reacted very slowly (for data see Supplementary S79). This lack of correlation to their internal acidities illustrates that there is no direct correlation between acidity and reactivity in the transfer hydrogenation reaction at least for these three catalysts and their pKa range. This further suggests a strong dependence of the reactivity on the isomerization of the imine, as previously reported in our group.[24] In this study, a competition of two *Z* imine transition state complexes was identified as the reactive pathway. The *E*:*Z* ratio of the investigated imines (see above) also shows no correlation with the observed reactivity, indicating that the kinetics of the isomerization contribute significantly to the rate determining step.[24]

The analysis of the $^{1}J_{NH}$ values (see Supplementary Table S3 and S4) further confirmed the internal acidities discussed above on r_{NO} distances. Generally, the same qualitative trend found in the experiments for the scalar coupling constants was obtained from the calculations ($^{1}J_{NH}$ TRIP < $^{1}J_{NH}$ TiPSY < $^{1}J_{NH}$ TRIFP, Supplementary S29 and S30). Similar as in TRIP/imine complexes, the calculated $^{1}J_{NH}$ coupling constants for the TiPSY/imine complexes are in good agreement with the experimental values, which confirm the predominantly ion pair character of the complex. The higher acidity of TRIFP, compared to TiPSY and TRIP, favors a more ion paired character of the hydrogen bond, i.e. a weaker H-bond.

In order to gain further insights into the hydrogen bond situation, $^{2h}J_{PH}$ were measured. A correlation is observed where increasing $^{2h}J_{PH}$ values are associated to decreasing ^{1}H chemical shift values in a linear manner (in contrast to the experiment, the calculations were only able to predict the order of magnitude of the $^{2h}J_{PH}$ scalar coupling, but no correlation with the ^{1}H chemical shifts of the acidic hydrogen was observed). The experimentally observed

linear trend of this correlation remains valid across the investigated catalysts TiPSY, TRIP and TRIFP, with couplings in TRIP complexes being on the lower end and couplings with TRIFP being on the upper end of the detected range. This behavior of decreasing coupling constant value (in absolute value) associated with proton chemical shift increases corresponds to the formation of a stronger hydrogen bond and validates again the discussed internal acidity of the complexes. However, the geometry of the hydrogen bond cannot be obtained by the analysis of $^{2h}J_{PH}$ scalar coupling and its magnitude is not a simple linear function of the P-H-distance and POH angle.

Therefore, $^{3h}J_{PN}$ scalar couplings were measured to investigate the geometry of the CPA/imine complexes. In detail, $^{3h}J_{PN}$ values related to TRIP/imine complex range between 2.0 and 3.2 Hz and $^{3h}J_{PN}$ values from TiPSY/imine complex range between 3.2 and 4.8 Hz (Figure 14).

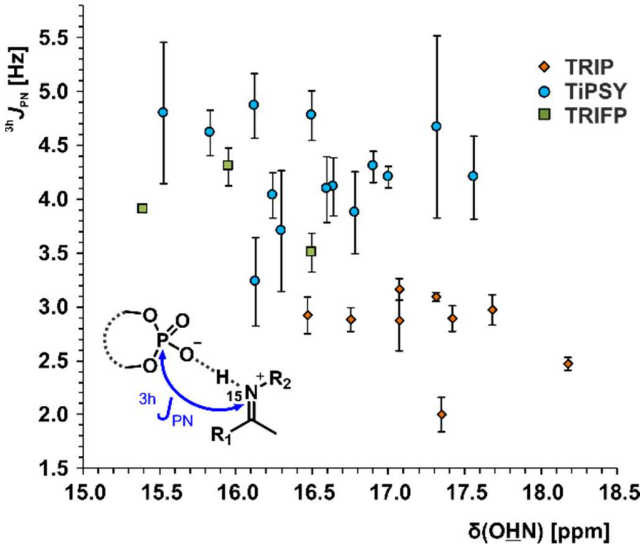

Figure 14. Plot of $^{3h}J_{PN}$ values against δ(OHN); for TiPSY/imine complexes (cyan), TRIFP/imine complexes (green) and TRIP/imine complexes[23] (orange) different absolute values are found and no correlation with the basicity of the imine indicating general structural deviations for the three catalysts is observed.

In comparison to $^{1}J_{NH}$ and $^{2h}J_{PH}$, the $^{3h}J_{PN}$ coupling constants show no trend when plotted against the ^{1}H chemical shift. Instead similar values are found for each individual catalyst, indicating an independence of the basicity of the imine on the measured $^{3h}J_{PN}$ coupling constants. The calculated structures consistently show an almost linear hydrogen bond (OHN angle > 161°), which explains the poor correlation between $^{3h}J_{PN}$ and chemical shift/hydrogen bond strength. Furthermore, the attempt to correlate the $^{3h}J_{PN}$ coupling with the POHN torsional angle in all catalyst/imine binary complexes via the Karplus equation[51,52] was not

successful due to the linearity of the H-bond. Similar $^{3h}J_{PN}$ coupling constants were previously measured and successfully calculated by DFT in intermolecular hydrogen bonds (PO-HN) of proteins and nucleic acids, where a correlation between $^{3h}J_{PN}$ coupling constant and the α(POH) angle as well as the r_{NO} distance was reported.[53,54] The geometric dependency of $^{3h}J_{PN}$ seems to be independent to the nuclei type, which is observed in a comparable system (CO-HN) investigated by Barfield showing a good correlation between $^{3h}J_{CN}$ and α(COH), r_{HO}.[55] In these studies, the hydrogen bond strength, which is indicated by r_{HO} or r_{NO}, determines the "sensitivity" factor for the function $^{3h}J_{XN}$(α (XOH), r_{YO}) (with X=P/C and Y=N,H). In contrast to the previous works, no correlation between hydrogen bond strength (i.e. r_{NO} or r_{HO}) and $^{3h}J_{PN}$ could be obtained, neither from experiment nor theoretical structure analysis in our CPA/imine system. The reason behind this poor correlation lies in the narrow range of the hydrogen bond strength in the investigated CPA/imine complexes, which is demonstrated in the Steiner-Limbach curve. Since the r_{NO}/r_{HO} are quasi constant, the function $^{3h}J_{XN}$(α(XOH), r_{YO}) is reduced to $^{3h}J_{XN}$ (α(XOH)). Indeed, much better correlation between α(POH)/ α(PON) and $^{3h}J_{PN}$ was obtained from the calculation (Figure 15 and Supplementary Table S8). This is in accordance with previous studies of Brüschweiler and Barfield[53,55] which showed larger $^{3h}J_{XN}$ in more linear α(XOH) (X=P/C). The apparent linear dependency of $^{3h}J_{PN}$ to α(POH) in our system owes again to the small variation in the angle (110°-135°).

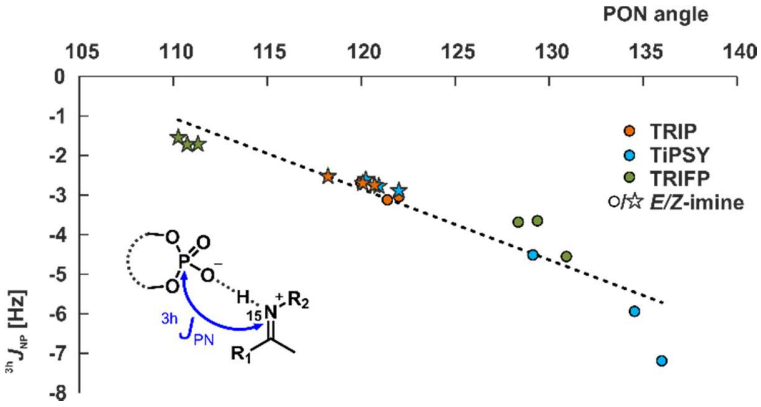

Figure 15. Plot of calculated $^{3h}J_{PN}$ values against the calculated PON angles; the smallest angles are observed for *Z* imine complexes of TRIFP (~110°); compared to TRIFP and TiPSY, there is no significant gap between the *E*- and *Z* isomers of TRIP/imine complexes; the PON angles of binary CPA/imine complexes *Type I/II E* and *Type I/II Z* are Boltzmann averaged.

The measured $^{3h}J_{PN}$ coupling constants show the same trend as the calculated values, but due to the fast exchange of the hydrogen bond protons between both imine isomers, a strong contribution of the opposite isomer is observed in the measured values (see Supplementary

S5,S6).

When comparing the different catalysts, the computed coupling constants and PON angles showed a significant gap between the *E* and *Z* isomers for the complexes of TRIFP and TiPSY. Complexes of TRIP on the other hand do not exhibit such a difference. Moreover, the PON angles of the TRIFP/*Z* imine complexes (~110°) substantially differ from the angles observed for TiPSY and TRIP (~120°). The steric and electronic properties of the imines and 3,3'-substituents of the catalyst (both proximal and distal) seem to be reflected in the different PON-angles found in the binary complexes. Indeed, further analysis of the steric parameters of the catalyst showed that the proximal steric (the rotational barrier of the 3,3'-substituent) correlates with the PON angle in CPA/*E*-imine complexes (Figure 16a). In contrast, the distal parameter (AREA) seems to correlate with the PON angle in CPA/Z-complex (Figure 16b). However, it should be noted that the correlation between the PON-angle in CPA/E-imine complexes and the proximal steric is non-linear. Since both proximal and distal parameters of Goodman were derived substrate independently, the pure steric model cannot account important interactions between substrate and catalyst, such as charge separation in the H-bond assisted ion pair and dispersion. In contrast, the PON angle includes implicitly all effects; steric repulsion, dispersion and electrostatic interactions. Thus, the effect of the proximal functional group in the complex may be minor or dominant, depending on the ratio between the electrostatic/dispersion and the repulsive potentials of the proximal bulk. In particular, the non-linear behavior caused by partial charges and dispersion resurfaces in TiPSY/imine and TRIFP/imine complexes. These catalysts contain functional group other than extended planar aromatic, alkyl groups and non-substituted BINOL-CPA (reference catalyst). In TRIFP/**3***E*, the 3,3'-substituents bears a slightly negative partial charge (-0.063e$^-$), which can attractively interact with the protonated imine 3 (+0.770e-). In contrast, the 3,3'-substituents in TiPSY/**3***E* are positively charged (on average +0.430e$^-$) and repulsively interact with the imine **3***E* (+0.871e-). Both weakly attractive and repulsive forces may trigger the non-linear response, especially when the proximal steric is negligible (rotational barrier TiPSY = 1.35 kcal/mol; TRIFP = 2.02 kcal/mol). Indeed, when the data points corresponding to TiPSY and TRIFP are omitted, a linear correlation is then restored.

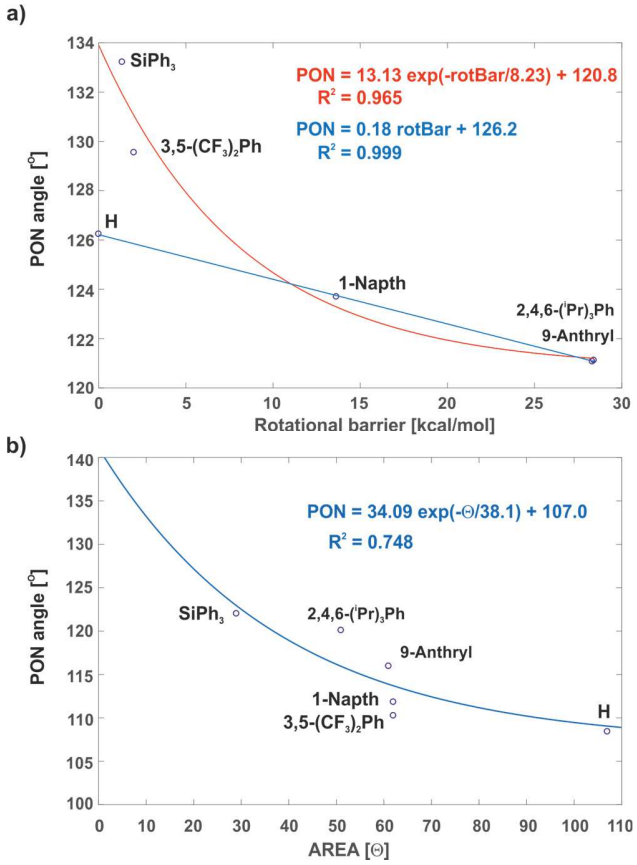

Figure 16. a) Correlation between proximal steric parameter (rotational barrier of the 3,3'-substituent) and PON-angles of CPA/*E*-imine complexes. The computed reference binary complex possesses an average PON-angle of 126.2°, which fits perfectly to y-axes intercept according to the linear fit (126.2°). b) Correlation between distal steric parameter (AREA) and PON-angles of CPA/Z-imine complexes. The asymptotic value for AREA is fixed to 107°, since the unsubstituted reference catalyst must have the least distal steric.

Nevertheless, previous theoretical calculation showed that the two steric descriptors of the catalyst are transmittable to the transition states (the proximal steric was proposed to determine the *Type I*/*Type II* selectivity and the distal steric contributes in the *E*/*Z* selectivity). This indicates that the steric factor is dominant in determining the stereochemical outcome. Therefore, since the PON angle is a conjunct parameter of steric-electronic effects of the catalyst and imines in the ground state, this parameter can be considered as an extension of the pure steric model of the catalyst and might be also transferred similarly to the stereo determining step as the two pure steric properties of the catalyst. Further investigations on the correlation of PON angles and steric descriptors AREA and rotational barrier are underway.

In summary, the hydrogen bond analysis via Steiner-Limbach plot showed different internal acidities when compared to the external ones. Both acidity scales do not exhibit any correlation with the reactivity for the transfer hydrogenation reaction. The PON/POH angle, which correlates with the $^{3h}J_{PN}$ coupling constant, was identified as almost substrate independent, particularly for the *Z* imine complexes (Figure 15). In the case of the reactive *Z*-imine complexes, this parameter is even reflected in the stereoselectivities of the catalysts. Moreover, this geometrical parameter can be correlated with the steric descriptor AREA for the CPA/*Z*-imine complexes and with the rotational barrier for the CPA/*E*-imine complexes (Figure 16).

4.4 Conclusion

A combination of detailed NMR spectroscopic studies and theoretical calculations was used to tackle the influence of different 3,3'-substituents on the structure, the hydrogen bond geometry and the internal acidity of binary imine/chiral phosphoric acid complexes. Theoretical calculations of TiPSY/imine complexes predicted the coexistence of four core structures (*Type I/II E* and *Type I/II Z*) in solution, which was corroborated experimentally for several TiPSY/imine complexes via 1D/2D NOESY/HOESY techniques at 180 K. Together with the previously investigated TRIP/imine structures, this confirmed experimentally the four conformations as the main conformers, even under variation of the 3,3'-substituents. The structures were corroborated by a detailed NMR investigation of the hydrogen bonds of five different imines in complexes with TiPSY and TRIFP in combination with data from the previously reported TRIP/imine complexes. This allowed for the first time to establish an internal acidity scale of CPA/imine complexes. The hydrogen bond distances obtained from a combined Steiner-Limbach plot of TiPSY, TRIFP and TRIP/imine complexes are in good agreement with the calculated values and show generally stronger hydrogen bonds (weaker acidity) for TRIP/imine complexes compared to TiPSY and TRIFP. An analysis of experimentally determined $^{1}J_{NH}$ and $^{2h}J_{PH}$ coupling constants confirmed this pattern. Neither this internal acidity nor calculated external acidities correlate with the observed reactivities in transfer hydrogenation reactions. Thus, at least for complexes with strong hydrogen bonds and in transfer hydrogenation reactions of CPAs the acidity is not the main factor determining reactivity of CPA/imine complexes.

More importantly, the PON angle of the hydrogen bonded complexes was identified as an

structural parameter of the binary complexes in the ground state, that is modulated by the stereoinducing 3,3' substituents and is correlated to the measured $^{3h}J_{PN}$ scalar couplings. Thus, different deviations in the PON angles were calculated for the *E*- and *Z* isomers depending on the 3,3'-substituent. As shown by the DTS-hv method, exclusively Z-transition states are involved in the transfer hydrogenation. For TRIFP/Z imine complexes a lower PON angle (~110°) was obtained than for the Z-isomers of TiPSY/TRIP (~120°) which is reflected in the stereoselectivities of the catalysts. Furthermore, the PON angle of CPA/*Z* complexes is correlated to the established steric parameter AREA, whereas the PON angle of CPA/*E* complexes shows a correlation with the rotational barrier of the 3,3' substituents. Further investigations on the correlation of enantioselectivities and the PON angle are underway.

4.5 Computational Details

Binary complexes consist of TiPSY, TRIP and TRIFP with imines **3**, **4**, **5** were optimized at TPSS-D3/def2-SVP level of theory in continuum of CH_2Cl_2.[54,55] The dielectric constant of the solvents was modified to 16.20 to mimic low temperature NMR measurement. Subsequently all minima were verified by frequency analysis (zero imaginary vibrational mode) and thermochemical corrections were added. Single point calculations at SCS-MP2/CBS level of theory (for extrapolation procedure see SI) were employed on top of the optimized geometry.[56] Software used for the optimization was Gaussian09 D.01.[57] For single points, ORCA 3.0.3 was used.[58]

4.6 Experimental Section

Materials and Synthesis

The chiral phosphoric acids, the solvents and compounds used for the syntheses were purchased from Sigma Aldrich. The deuterated dichloromethane used in the NMR samples was purchased from Deutero and dried over CaH. All investigated imines were synthesized using the same procedure we used previously:[21] Ketone (2-5 mmol) and Aniline/*p*-Anisidine (1.1 eq) were refluxed with molecular sieve (4 Å) in toluene for 20 h. The solvent was removed under reduced pressure and the residue was recrystallized in ethanol. The product was dried under reduced pressure.

Sample preparation

The TiPSY/imine samples were prepared at a 1:1 stoichiometric ratio at 50 mM concentration. Catalyst was weighted directly in in standard 5 mm diameter NMR. The catalyst was dried at 80°C at low pressure during 30 minutes. The imine was dissolved in 600 µL CD_2Cl_2 solvent freshly distillated at the desired concentration. The solution containing the imine was added to the dried catalyst under argon atmosphere. Tetramethylsilane (TMS) was added with a syringe. Between the measurements, the samples were stored at - 80°C in a freezer.

NMR experiments

All experiments were performed at an AVANCE BRUKER 600 MHz spectrometer. TBI-F and TBI-P probes were used, depending on the investigated nuclei. Experiments were carried out at a temperature of 180K in order to stabilize the hydrogen bond formation and to observe hydrogen and nitrogen atoms involved in hydrogen bond. Assignment tables and detailed NMR parameters are detailed in supplementary material. Specific experiments such as HOESY were performed with imine TiPSY/**1** sample containing a fluorine atom in order to collect spin specific information. In order to gain sensitivity to detect intermolecular NOEs, selective 1D NOESY were performed at mixing times ranging from 50 to 300 ms (See supplementary material section for details). NMR Data were processed, integrated and plotted using TopSpin 3.2 software.

4.7 References

[1] T. Akiyama, J. Itoh, K. Yokota, K. Fuchibe, *Angew. Chemie Int. Ed.* **2004**, *43*, 1566–1568.

[2] D. Uraguchi, M. Terada, *J. Am. Chem. Soc.* **2004**, *126*, 5356–5357.

[3] M. Rueping, T. Theissmann, M. Stoeckel, A. P. Antonchick, *Org. Biomol. Chem.* **2011**, *9*, 6844–6850.

[4] Q. Yin, S.-G. Wang, S.-L. You, *Org. Lett.* **2013**, *15*, 2688–2691.

[5] T. Marcelli, P. Hammar, F. Himo, *Chem. - A Eur. J.* **2008**, *14*, 8562–8571.

[6] R. I. Storer, D. E. Carrera, Y. Ni, D. W. C. MacMillan, *J. Am. Chem. Soc.* **2006**, *128*, 84–86.

[7] K. Saito, T. Akiyama, *Chem. Commun.* **2012**, *48*, 4573–4575.

[8] M. Yamanaka, J. Itoh, K. Fuchibe, T. Akiyama, *J. Am. Chem. Soc.* **2007**, *129*, 6756–64.

[9] X. Xu, Y. Qian, L. Yang, W. Hu, *Chem. Commun.* **2010**, *47*, 797–799.

[10] E. P. Ávila, R. M. S. Justo, V. P. Gonçalves, A. A. Pereira, R. Diniz, G. W. Amarante, *J. Org. Chem.* **2015**, *80*, 590–594.

[11] K. Shen, X. Liu, Y. Cai, L. Lin, X. Feng, *Chem. – A Eur. J.* **2009**, *15*, 6008–6014.

[12] C. Gharui, S. Singh, S. C. Pan, *Org. Biomol. Chem.* **2017**, *15*, 7272–7276.

[13] S. Saha, C. Schneider, *Chem. - A Eur. J.* **2015**, *21*, 2348–2352.

[14] S. Hoffmann, A. M. Seayad, B. List, *Angew. Chemie Int. Ed.* **2005**, *44*, 7424–7427.

[15] M. Rueping, E. Sugiono, C. Azap, T. Theissmann, *Org. Lett.* **2005**, *7*, 3781–3783.

[16] S. G. Ouellet, A. M. Walji, D. W. C. Macmillan, *Acc. Chem. Res.* **2007**, *40*, 1327–1339.

[17] C. Min, D. Seidel, *Chem. Soc. Rev.* **2017**, *46*, 5889–5902.

[18] J. P. Reid, J. M. Goodman, *J. Am. Chem. Soc.* **2016**, *138*, 7919–7917.

[19] J. P. Reid, J. M. Goodman, *Chem. - A Eur. J.* **2017**, *23*, 14248–14260.

[20] W. Tang, S. Johnston, J. a Iggo, N. G. Berry, M. Phelan, L. Lian, J. Bacsa, J. Xiao, *Angew. Chem. Int. Ed. Engl.* **2013**, *52*, 1668–1672.

[21] L. Simón, J. M. Goodman, *J. Am. Chem. Soc.* **2008**, *130*, 8741–8747.

[22] J. Greindl, J. Hioe, N. Sorgenfrei, F. Morana, R. M. Gschwind, *J. Am. Chem. Soc.* **2016**, *138*, 15965–15971.

[23] N. Sorgenfrei, J. Hioe, J. Greindl, K. Rothermel, F. Morana, N. Lokesh, R. M. Gschwind, *J. Am. Chem. Soc.* **2016**, *138*, 16345–16354.

[24] P. Renzi, J. Hioe, R. M. Gschwind, *J. Am. Chem. Soc.* **2017**, *139*, 6752-6760

[25] M. Sickert, F. Abels, M. Lang, J. Sieler, C. Birkemeyer, C. Schneider, *Chem. – A Eur. J.* **2010**, *16*, 2806–2818.

[26] T. Steiner, *Angew. Chemie* **2002**, *114*, 50–80.

[27] E. R. P. Zuiderweg, S. W. Fesik, *Biochemistry* **1989**, *28*, 2387–2391.

[28] J. Schleucher, M. Schwendinger, M. Sattler, P. Schmidt, O. Schedletzky, S. J. Glaser, O. W. Sørensen, C. Griesinger, *J. Biomol. NMR* **1994**, *4*, 301–306.

[29] M. Foroozandeh, R. W. Adams, M. Nilsson, G. A. Morris, *J. Am. Chem. Soc.* **2014**, *136*, 11867–11869.

[30] J. Mauhart, S. Glanzer, P. Sakhaii, W. Bermel, K. Zangger, *J. Magn. Reson.* **2015**, *259*, 207–215.

[31] K. Zangger, *Prog. Nucl. Magn. Reson. Spectrosc.* **2015**, *86–87*, 1–20.

[32] D. Uhrín, J. Bramham, S. J. Winder, P. N. Barlow, *J. Biomol. NMR* **2000**, *18*, 253–259.

[33] A. Verma, B. Baishya, *J. Magn. Reson.* **2016**, *266*, 51–58.

[34] S. Akoka, P. Giraudeau, *Magn. Reson. Chem.* **2015**, *53*, 986–994.

[35] R. J. Lichtenecker, N. Coudevylle, R. Konrat, W. Schmid, *ChemBioChem* **2013**, *14*, 818–821.

[36] C. Prasanna, A. Dubey, H. S. Atreya, in *Methods Enzymol.*, Academic Press, **2015**, pp. 167–189.

[37] D. P. Frueh, A. C. Goodrich, S. H. Mishra, S. R. Nichols, *Curr. Opin. Struct. Biol.* **2013**, *23*, 734–739.

[38] H. Kessler, H. Oschkinat, C. Griesinger, W. Bermel, *J. Magn. Reson.* **1986**, *70*, 106–133.

[39] K. Stott, J. Stonehouse, J. Keeler, T.-L. Hwang, A. J. Shaka, *J. Am. Chem. Soc.* **1995**, *117*, 4199–4200.

[40] D. Jeannerat, J. Furrer, *Comb. Chem. High Throughput Screen.* **2012**, *15*, 15–35.

[41] C. Yu, G. C. Levy, *J. Am. Chem. Soc.* **1984**, *106*, 6533–6537.

[42] P. S. Pregosin, P. G. Anil Kumar, I. Fernández, *Chem. Rev.* **2005**, *105*, 2977–2998.

[43] K. Shikii, S. Sakurai, H. Utsumi, H. Seki, M. Tashiro, *Anal. Sci.* **2004**, *20*, 1475–1477.

[44] D. P. Cistola, K. B. Hall, *J. Biomol. NMR* **1995**, *5*, 415–419.

[45] L. Fusaro, E. Locci, A. Lai, M. Luhmer, *J. Phys. Chem. B* **2010**, *114*, 3398–3403.

[46] H.-H. Limbach, M. Pietrzak, S. Sharif, P. M. Tolstoy, I. G. Shenderovich, S. N. Smirnov, N. S. Golubev, G. S. Denisov, *Chem. – A Eur. J.* **2004**, *10*, 5195–5204.

[47] P. A. Frey, S. A. Whitt, J. B. Tobin, *Science (80-.).* **1994**, *264*, 1927–1930.

[48] P. A. Frey, *Magn. Reson. Chem.* **2001**, *39*, 190–198.

[49] S. S. Imides, P. T. Tefddols, P. Christ, A. G. Lindsay, S. S. Vormittag, J. Neudçrfl, A. Berkessel, A. C. O. Donoghue, *Chem. - A Eur. J.* **2011**, *17*, 8524–8528.

[50] K. Kaupmees, N. Tolstoluzhsky, S. Raja, M. Rueping, I. Leito, *Angew. Chemie Int. Ed.* **2013**, *52*, 11569–72.

[51] M. Karplus, *J. Chem. Phys.* **1959**, *30*, 11–15.

[52] G. W. Vuister, A. Bax, *J. Am. Chem. Soc.* **1993**, *115*, 7772–7777.

[53] J. Czernek, R. Brüschweiler, *J. Am. Chem. Soc.* **2001**, *123*, 11079–11080.

[54] M. Mishima, M. Hatanaka, S. Yokoyama, T. Ikegami, M. Wälchli, Y. Ito, M. Shirakawa,

J. Am. Chem. Soc. **2000**, *122*, 5883–5884.

[55] M. Barfield, *J. Am. Chem. Soc.* **2002**, *124*, 4158–4168.

[56] J. M. Tao, J. P. Perdew, V. N. Staroverov, G. E. Scuseria, *Phys. Rev. Lett.* **2003**, *91*, 146401.

[57] S. Grimme, J. Antony, S. Ehrlich, H. Krieg, S. Grimme, J. Antony, S. Ehrlich, H. Krieg, *J. Chem. Phys.* **2010**, *132*, 154104.

[58] S. Grimme, *J. Chem. Phys.* **2003**, *118*, 9095.

[59] M. J. Frisch, G. W. Trucks, H. B. Schlegel, G. E. Scuseria, M. A. Robb, J. R. Cheeseman, G. Scalmani, V. Barone, B. Mennucci, G. A. Petersson, et al., **2009**.

[56] F. Neese, *Comput. Mol. Sci.* **2012**, *2*, 73–78.

4.8 Supporting Information

4.8.1 Experimental data

Deuterated solvents were purchased from Deutero or Sigma Aldrich where dry solvents were essential, CD_2Cl_2 was freshly distilled over CaH_2 and Toluene-d8 was refluxed over Na/Benzophenone under Argon atmosphere. Freon mixtures were prepared from $CDCl_3$ and $SbCl_5/SbF_3$ according to literature procedures and stored in small lecture bottles.[1,2] The catalysts were purchased from Sigma Aldrich or synthesized from the bisphenols according the procedure of Klussmann et al.[3] High resolution mass spectra were measured by the central analytics division in the Institute of Organic Chemistry. Gas chromatography coupled with a mass selective detector was performed on an Agilent 6890N Network GC-System.

4.8.2 Synthesis of Imine Substrates

The imines were prepared as described in literature.[4–7] The toluene was used either in p.A. quality or was dried by refluxing over sodium. The ^{15}N-enriched aniline for the presented syntheses below, was purchased from Euriso-top GmbH.

4.8.3 Sample preparation

Preparation of binary complexes in CD_2Cl_2

The catalyst was dried for 30 min at 150°C under reduced pressure. Ketimine and catalyst were directly weighed into a 5 mm NMR tube under an inert argon atmosphere. CD_2Cl_2 (0.6 ml) and 1.0 ml of tetramethylsilane atmosphere were added to the tube. The sample was stored in an -80°C freezer. A 1:1 ratio of catalyst/ketimine was used for all samples. A concentration 25 mmol or 50 mmol/L was used for all samples, depending on solubility at low temperatures.

Preparation of binary complexes in freonic solvent mixtures

The catalyst was dried for 30 min at 150°C under reduced pressure. Ketimine and catalyst were directly weighed into a heavy wall NMR tube equipped with a J. Young valve under an inert argon atmosphere. 1.0 ml of tetramethylsilane atmosphere were added and the sample was connected to a vacuum line. The NMR tube was evacuated and cooled down to 77 K. The freonic solvent mixture was condensed through column filled with P_2O_5 and KOH into the NMR-tube.

4.8.4 Spectrometer data

NMR experiments were performed on Bruker Avance III HD 400 MHz spectrometer, equipped with 5 mm BBO BB-1H/D probe head with Z-Gradients and a Bruker Avance III HD 600 MHz spectrometer, equipped with a 5 mm TBI 1H/19. Temperature was controlled in the VT-experiments by BVT 3000 and BVTE 3900. For NMR measurements employing standard NMR solvents 5 mm NMR tubes were used, if not other noted. For samples in freonic mixtures as solvents, 5 mm heavy wall (1.4 mm wall thickness) NMR tubes equipped with J. Young valves from Wilmad were used. NMR Data were processed, evaluated and plotted with TopSpin 3.2 software. Further plotting of the spectra was performed with Corel Draw X14 – X17 software. ^{1}H, ^{13}C chemical shifts were referenced to TMS or the respective solvent signals. The heteronuclei ^{15}N, ^{19}F and were referenced, employing $\nu(X) = \nu(TMS) \times \Xi\delta_{reference} / 100$ % according to Harris et al.[8] The following frequency ratios and reference compounds were used: Ξ (^{15}N) = 10.132912 (lq. NH_3) and Ξ (^{19}F) = 94.094011 (CCl_3F)

4.8.5 Pulse programs

All pulse programs used are standard Bruker NMR pulse programs.

4.8.6 Acquisition Parameters

^{1}H NMR: Pulse program: zg; Relaxation delay = 2 – 3 s, Acquisition time = 2.48 s, SW = 22.0 ppm, TD = 64k, NS = 8 – 64; zg30; Relaxation delay = 2 s, Acquisition time = 2.48 s, SW = 22.0 ppm, TD = 64k, NS = 8 – 64;

2D-^{1}H,^{1}H NOESY: Pulse program: noesygpph; Relaxation delay = 5 - 8 s, NS = 8-32, mixing time (D8) = 300.00 ms; TD = 4096; increments = 512 - 1k;

2D-^{1}H,^{1}H COSY: Pulse program: cosygpqf; Relaxation delay = 5 - 8 s, NS = 8-32, TD = 4096; increments = 512 - 1k;

^{13}C NMR: Pulse program: zgpg30; Relaxation delay = 2.00 s, Acquisition time = 0.80 s, SW = 270.0 ppm, TD = 64k, NS = 1k – 2k;

2D-^{1}H,^{13}C HSQC: Pulse program: hsqcedetgpsisp2.3; Relaxation delay = 4 - 8 s, NS = 8-32, $^{1}J_{XH}$ = 145 Hz; TD = 4096; increments = 512 - 1k;

2D-^{1}H,^{13}C HMBC: Pulse program: hmbcgplpndqf; Relaxation delay = 4 - 8 s, NS = 8-32, $^{1}J_{XH}$ = 145 Hz, J_{XH}(long range) = 10 Hz; TD = 4096; increments = 512 - 1k;

^{15}N NMR: Pulse program: zg; Relaxation delay = 10.00 s, Acquisition time = 0.54 s, SW = 502.8 ppm, TD = 32k, NS = 256 – 2048;

2D-^{1}H,^{15}N HMBC: Pulse program: inv4gplrndqf; Relaxation delay = 5 - 8 s, NS = 16-32, delay for evolution of long range couplings (D6) = 20.00 ms; TD = 4096; increments = 128 - 512;

^{19}F-NMR: Pulse program: zg30; Relaxation delay = 2 – 3 s, Acquisition time = 11.60 s, SW = 10.0 ppm, TD = 128k, NS = 8 – 64;

2D-^{1}H,^{19}F HOESY: Pulse program: hoesyph; Relaxation delay = 5 - 8 s, NS = 16-32, mixing time (D8) = 500.00 ms; TD = 4096; increments = 1k;

Selective 1D-^{1}H,^{1}H NOESY: Pulse program: selnogp; Relaxation delay = 5 - 8 s, NS = 128-2k, mixing time (D8) = 25 – 1000 ms (150 – 200 ms and NS = 1k-2k for structure identification); TD = 64k; 180° shaped pulse = 50 – 150 ms, shape = Gauss 180.

4.8.7 S1. Identification of *E*- and *Z*-imines inside the complex

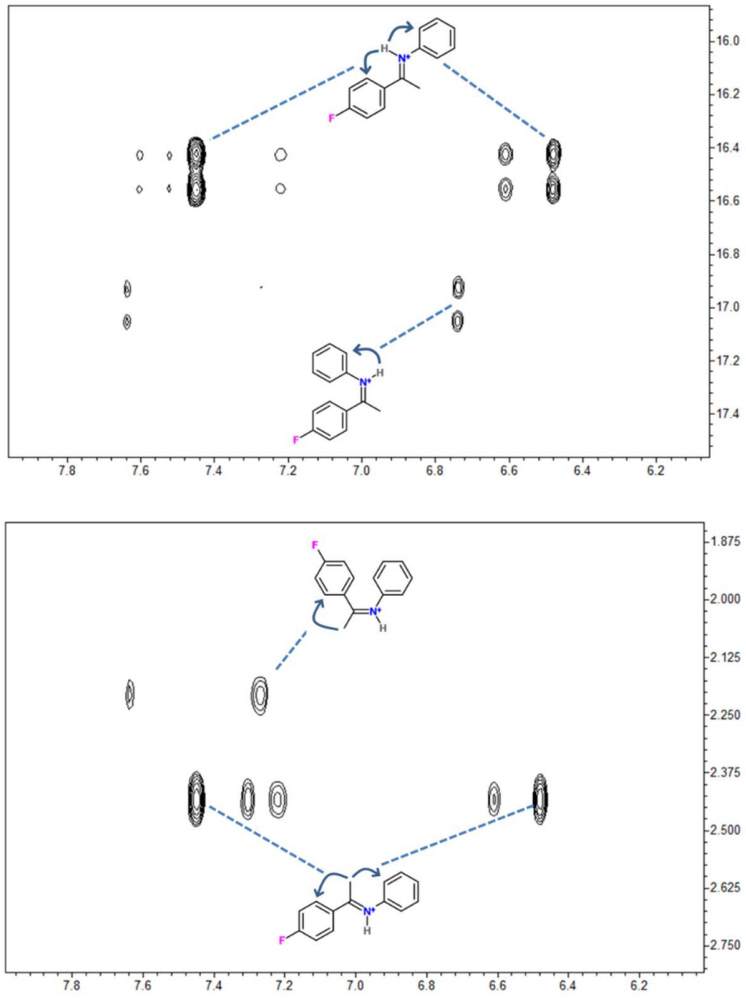

Figure S1: Selected areas from a NOESY experiment allowing identification of *E*- and *Z*-isomers in complex with TiPSY. The aromatic/H-bond section is shown in the upper panel and the aromatic/methyl section is shown in the lower panel. Similar patterns can be observed for the other TiPSY/imine complexes. The two intense *E*-imine cross-peaks from respectively the H-bond proton and α-methyl proton toward the same two aromatic protons. On the other hand only one intense cross peak can be observed for the *Z*-imine towards two different aromatic protons.

NMR Parameters: mixing time 300 ms, Time domain: 2k x 256, recycling delay: 2s, Number of scans: 8. Experiment time: 2h50min.

4.8.8 S2. Intermolecular scalar coupling through hydrogen bonding

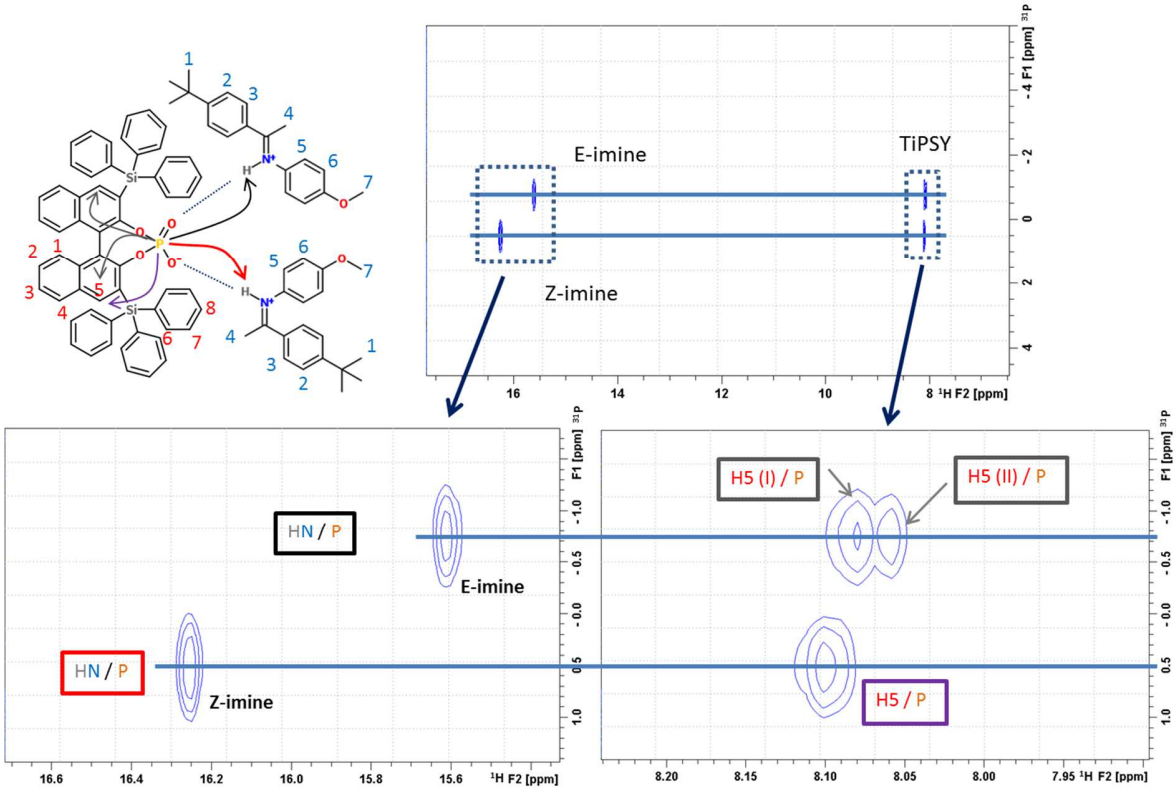

Figure S2. ^{1}H-^{31}P HMBC spectrum; multiple bond correlation signals between ^{1}H and ^{31}P were detected. By knowing the ^{1}H chemical shift involved in hydrogen bonding in each of the *E*- and *Z*-imine forms, ^{31}P assignment for TiPSY in both complexes with *E*- and *Z*- imine becomes accessible (upper panel). Moreover, intramolecular $^{5}J_{HP}$ allow detection of two separated spins (noted H5 (I) and H5 (II)) in the TiPSY/*E*-imine complex corresponding to each side of the catalyst. One internal H5 proton is also detected corresponding to the TiPSY/*Z*-imine complex (lower panel). This was used as a starting point for TiPSY assignment in *E*-imine complex (two sets of signals) and *Z*-imine complex (one set of signals).

NMR parameters: Pulse sequence: hmbcgpndqf, Long range coupling constant 20 Hz, Time domain: 4k x 32 points, Spectral window 22 x 11 ppm, ^{1}H offset frequency: 10 ppm, ^{31}P offset frequency: -0.5 ppm, Recycling delay: 2s, Number of scans: 256. Experiment time: 5h.

4.8.9 S3. *E*:*Z* ratios in investigated TiPSY/imine complexes

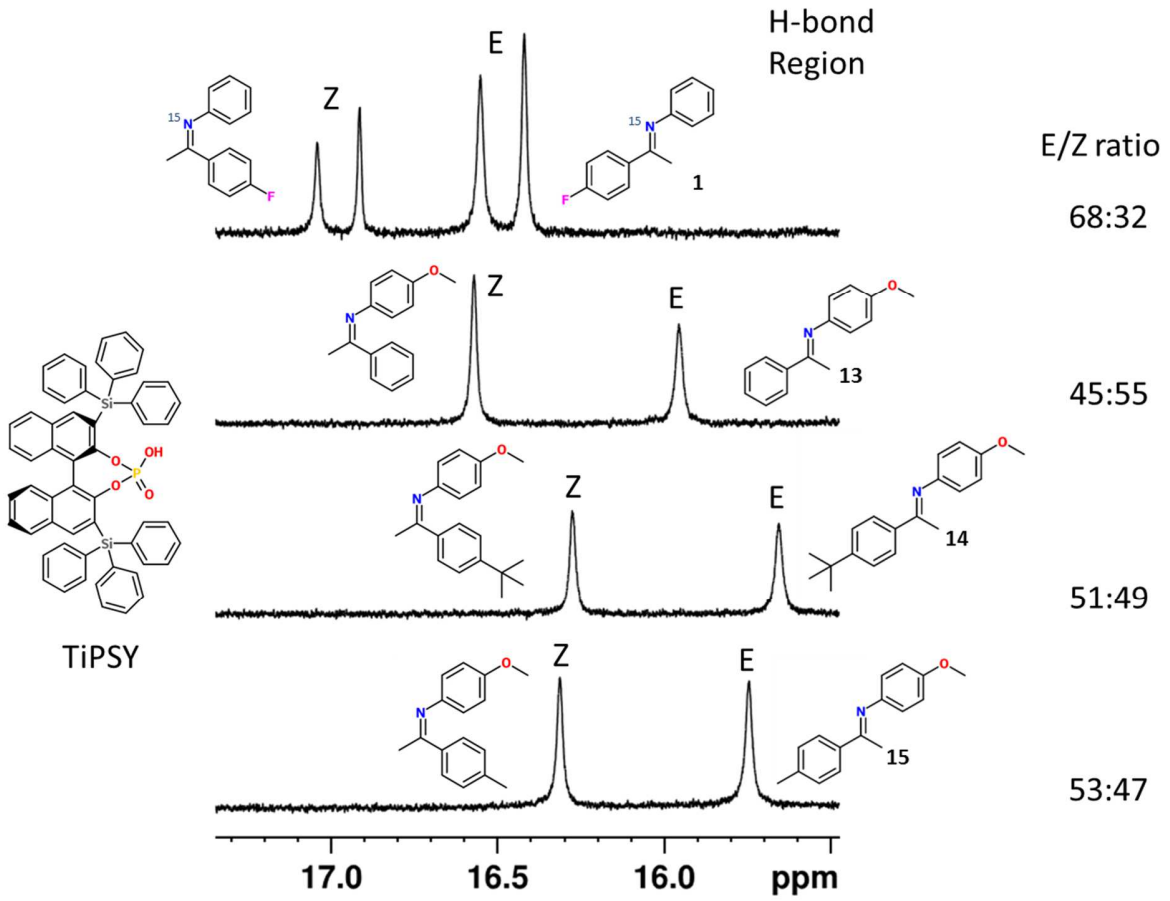

Figure S3. Observed *E:Z* ratios for the investigated TiPSY/imine complexes. The highest amount of the *Z*-isomer was found for imine **14**.

4.8.10 S4. Highlighted ^{1}H ^{13}C HSQC aromatic region of *E*-/*Z*-imine/TiPSY complex

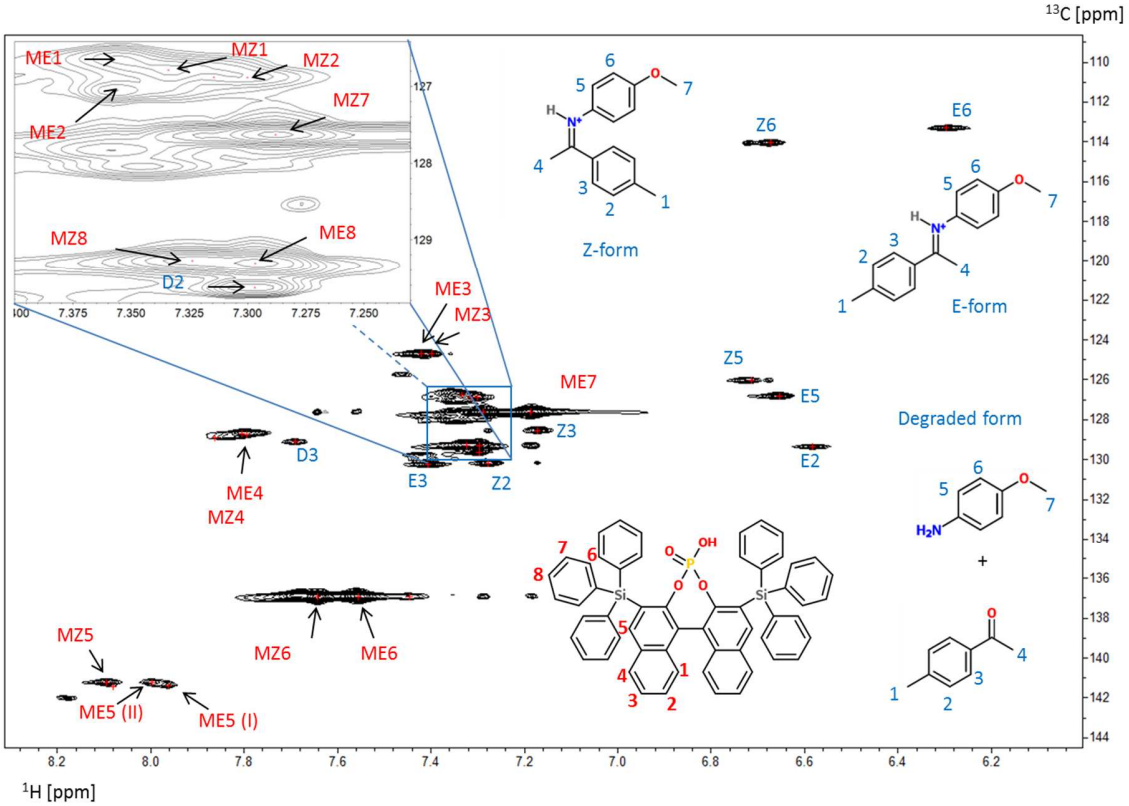

Figure S4. HSQC spectrum using a folded indirect ^{13}C dimension of only 35 ppm spectral window [145,110] ppm. TiPSY/imine **15** is shown exemplarily. Despite a very crowded aromatic region (see magnified area), all aromatic protons from catalyst (red) and imine (sky blue) were identified with their corresponding carbon atoms. Only proton 5 and 6 from the degraded imine form were missing, probably due to a broadening effect of interaction of this form with the TiPSY catalyst.

NMR parameters: Pulse sequence: hsqcetgspi, Coupling constant 145 Hz, Time domain: 4k x 512 points, Spectral window 22 x 35 ppm, ^{1}H offset frequency: 9 ppm, ^{13}C offset frequency 127.5 ppm, Recycling delay: 2s, Number of scans: 32. Experiment time: 10h.

4.8.11 S5. Highlighted ^{1}H ^{13}C HSQC / HMBC aromatic region around TiPSY catalyst signals in complex with *E/Z* imine

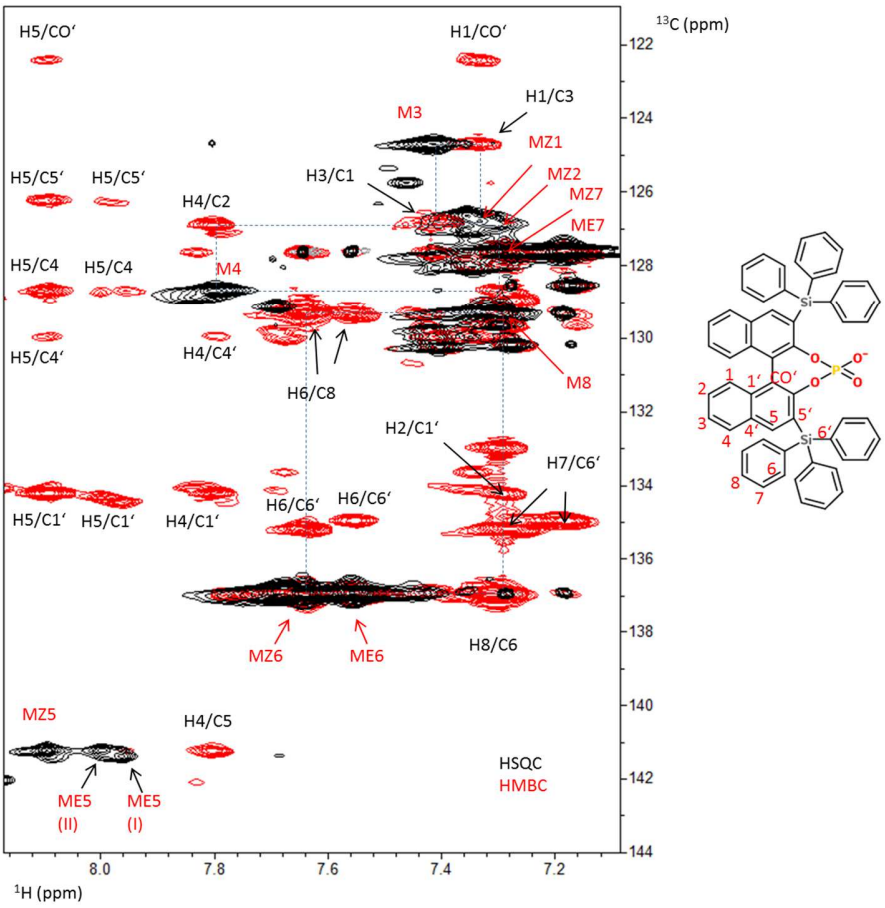

Figure S5. Comparison between HSQC and HMBC which was used for the detection of several catalyst spins (H5-C1', H5-C4', H5-C5', H5-CO', H1-CO', H5-C1', H4-C1' and H2-C1'). Moreover, using a 10 Hz coupling constant, several $^{3h}J_{HC}$ were found inside aromatic rings (H3-C1, H1-C3, H2-C4, H2-C2, H4-C5, H5-C4). As a result, through the detection of ^{1}H and ^{13}C in HSQC and HMBC, all spins are connected and therefore a sequential assignment was obtained in both *E*- and *Z*-imine complexes.

NMR parameters: pulse sequence: hmbcgpndqf ; Coupling constant 145 Hz; J(XH) long range: 10 Hz ;Time domain: 4k x 512 points; spectral window 22 x 75 ppm, ^{1}H offset frequency: 9 ppm, 13C offset frequency 147.5 ppm, recycling delay: 2s, Number of scans: 32; Experiment time: 10h10min.

4.8.12 Assignment of the ^{1}H and ^{13}C chemical shifts

S6. Complex (TiPSY/1E)

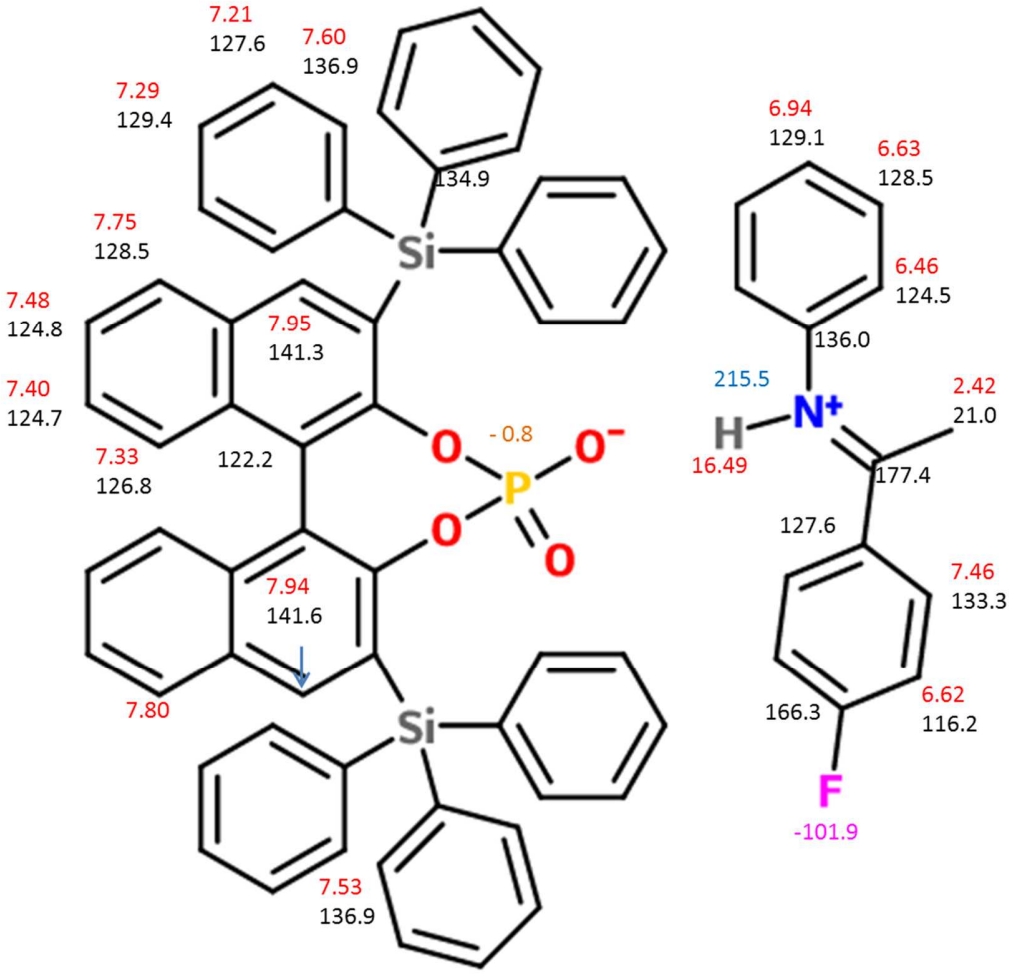

S7. Complex (TiPSY/1Z)

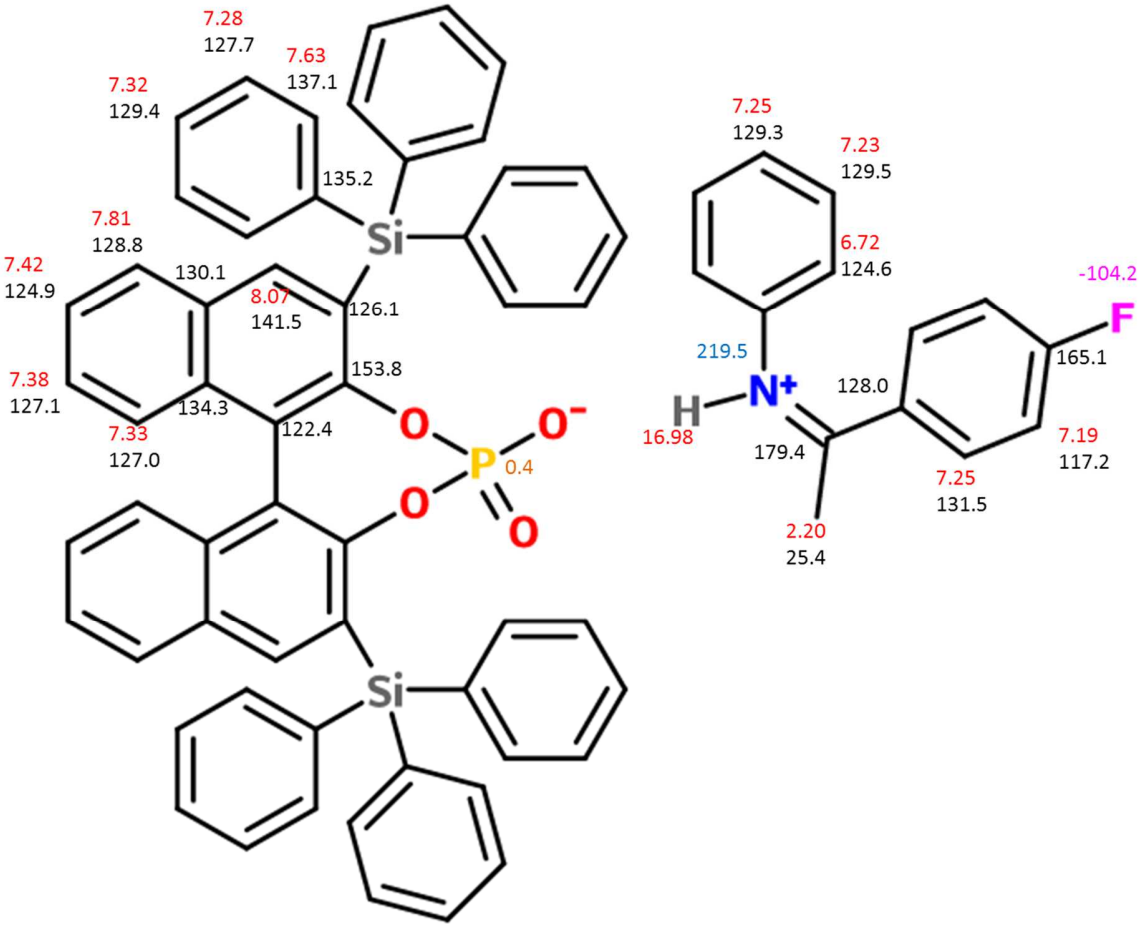

S8. Complex (TiPSY/13E)

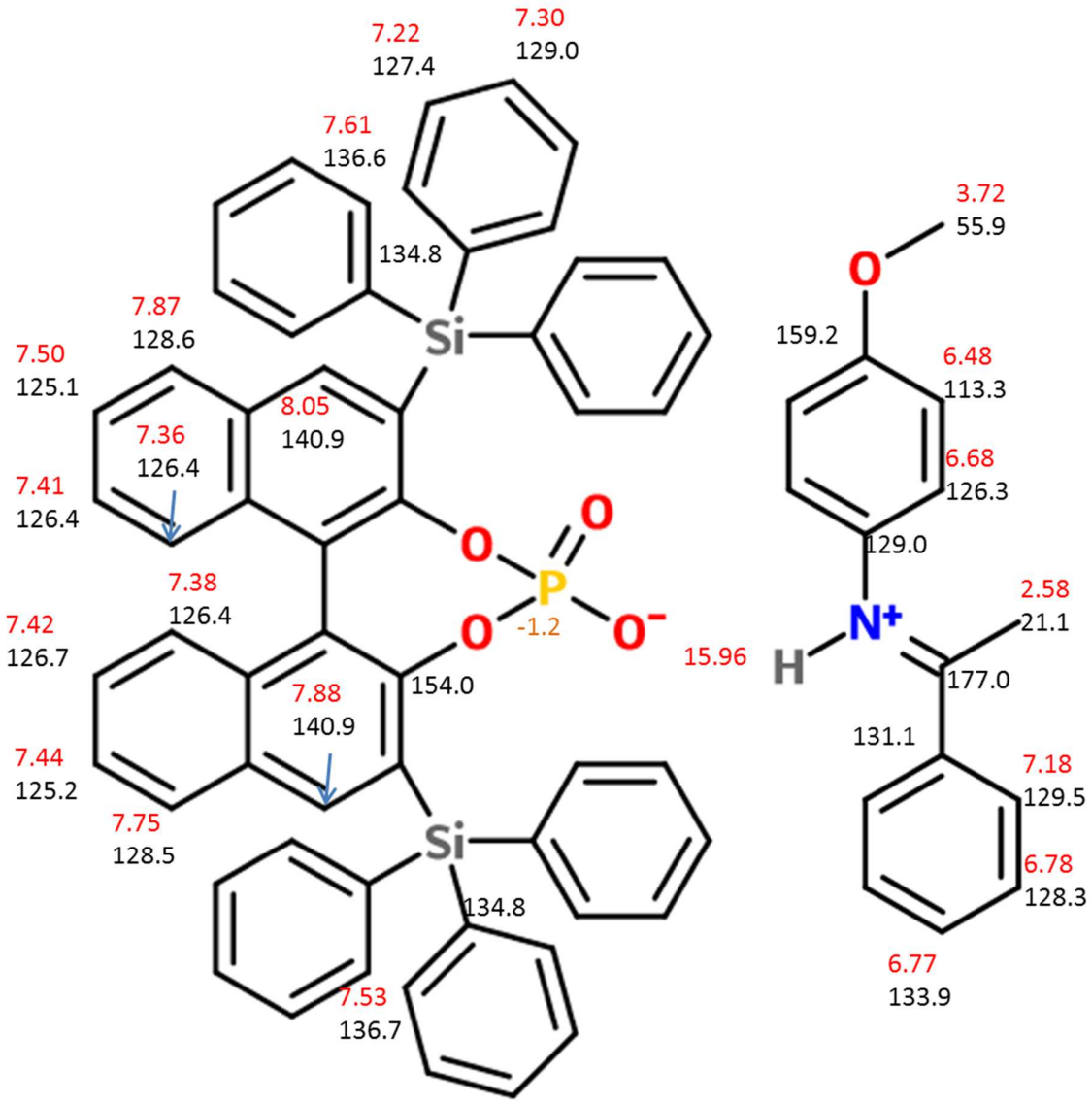

Remark: due to overlap between proton signals in the aromatic imine keto moiety (6.77; 6.78 and 7.18 ppm) and intense TiPSY side-chain signal at 7.22 ppm, the *Type I E*-imine orientation in TiPSY/**13** was not unambiguously assigned.

S9. Complex (TiPSY/13Z)

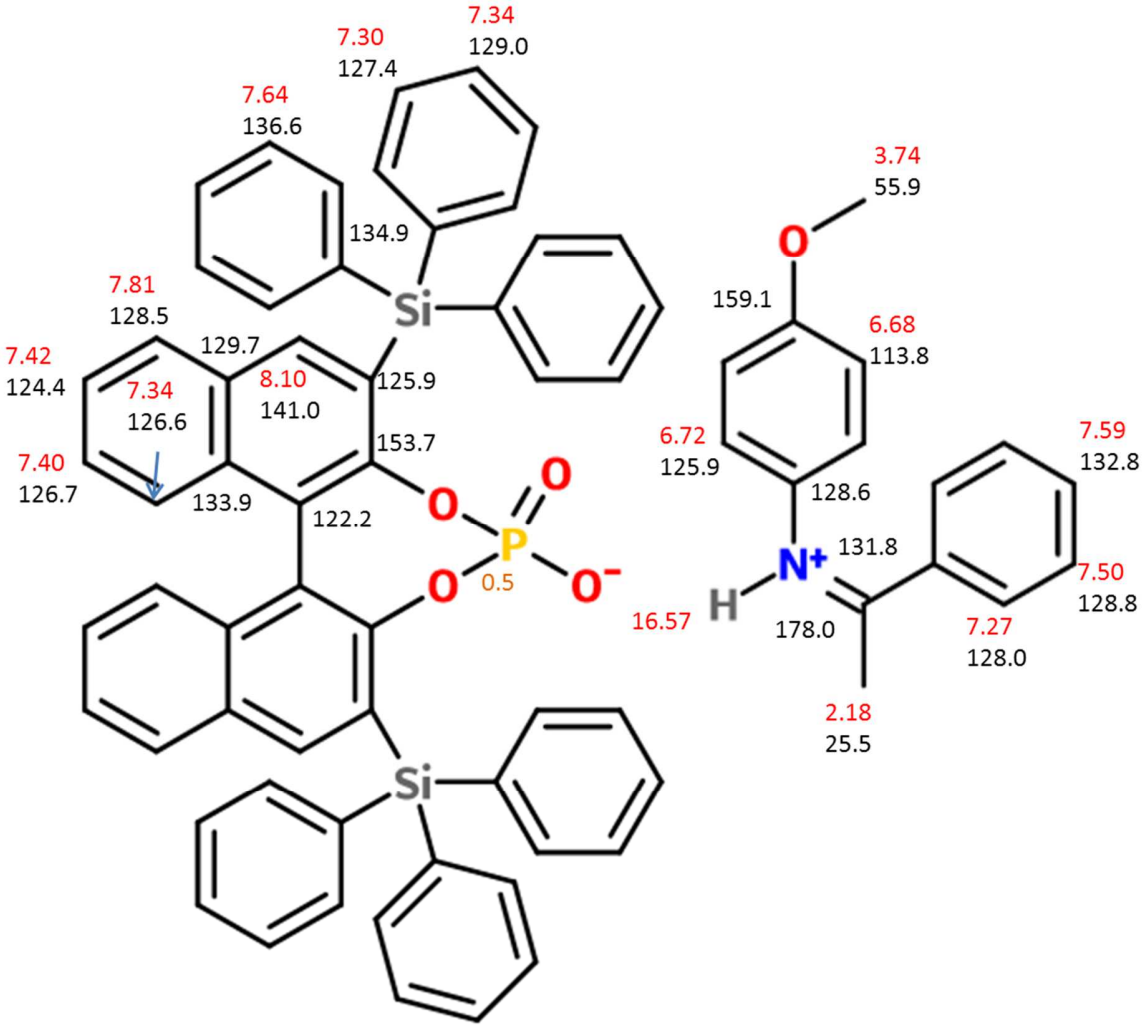

S10. Complex (TiPSY/14E)

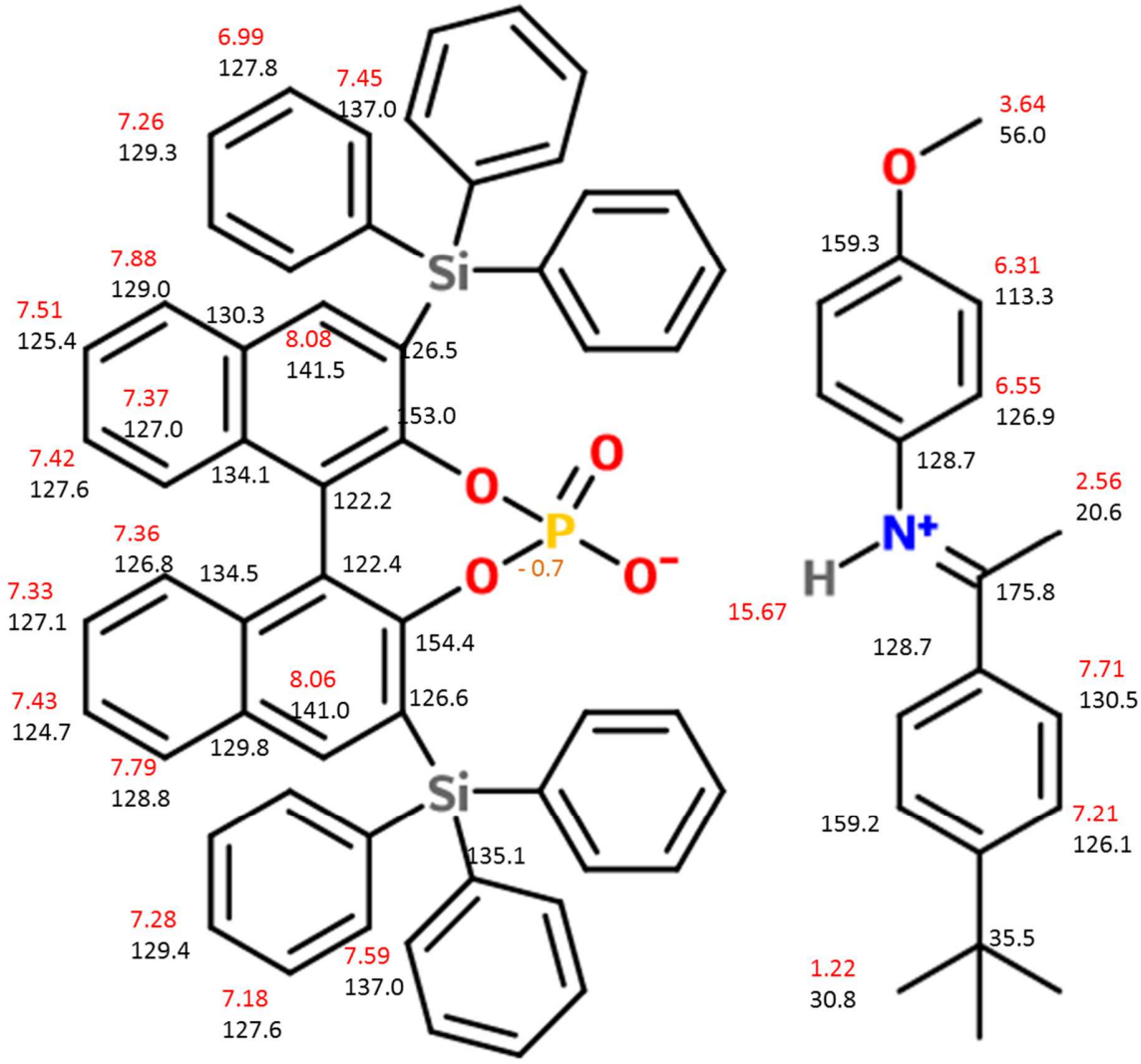

S11. Complex (TiPSY/14Z)

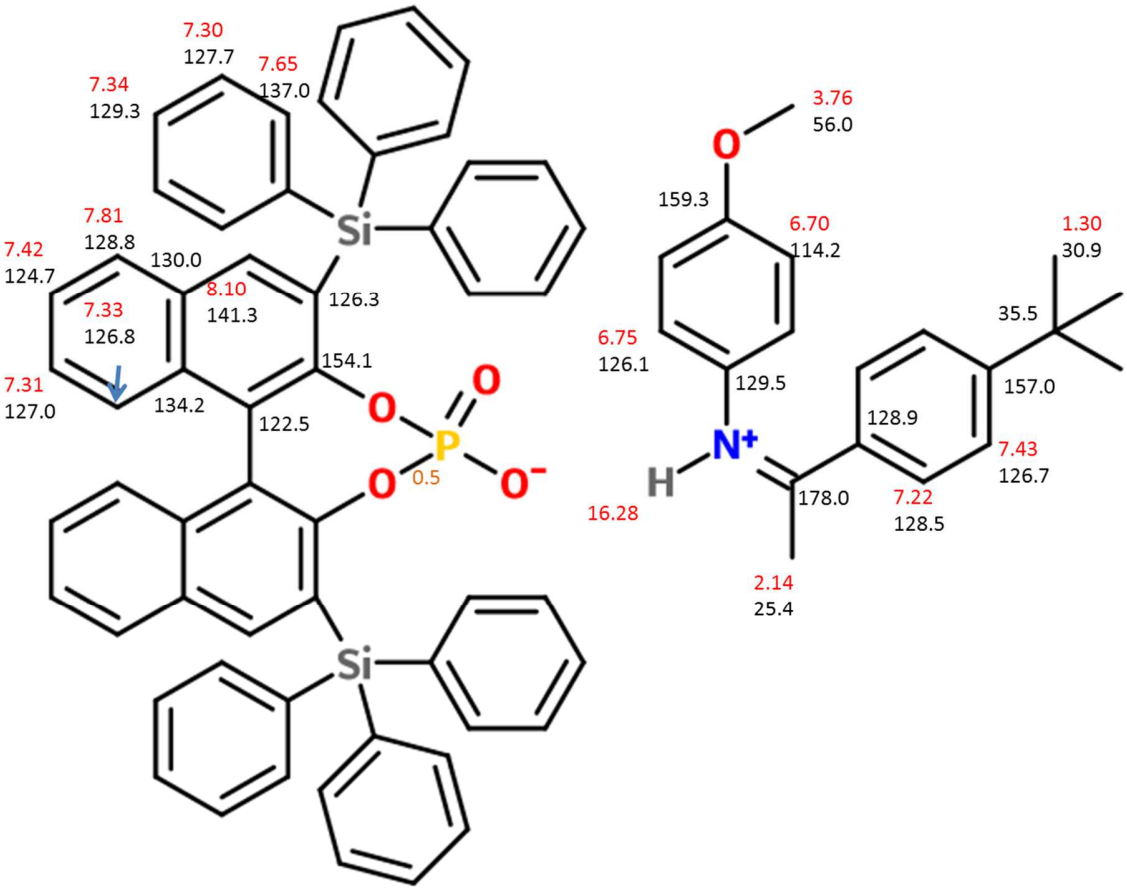

S12. Complex (TiPSY/15E)

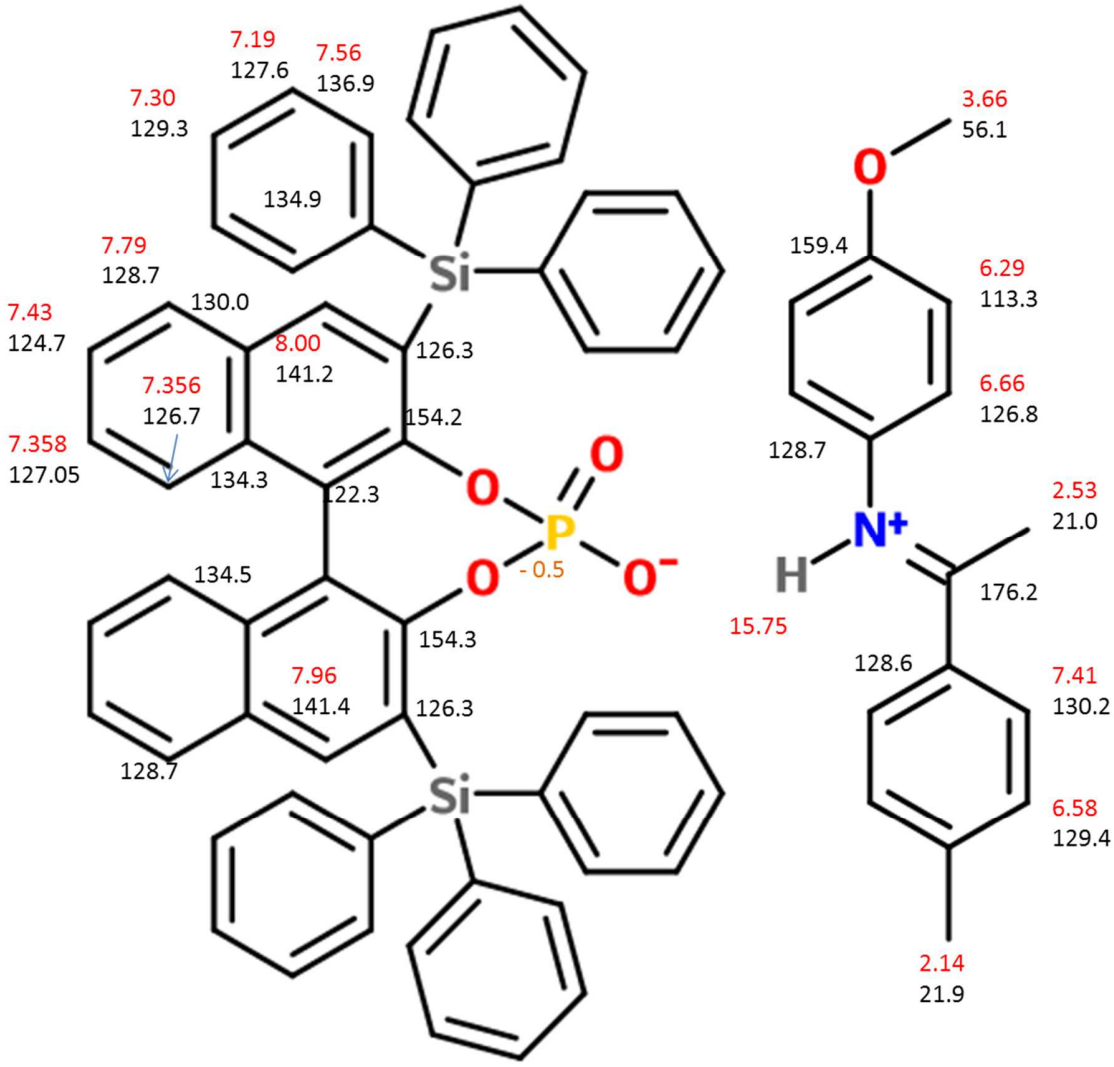

S13. Complex (TiPSY/15Z)

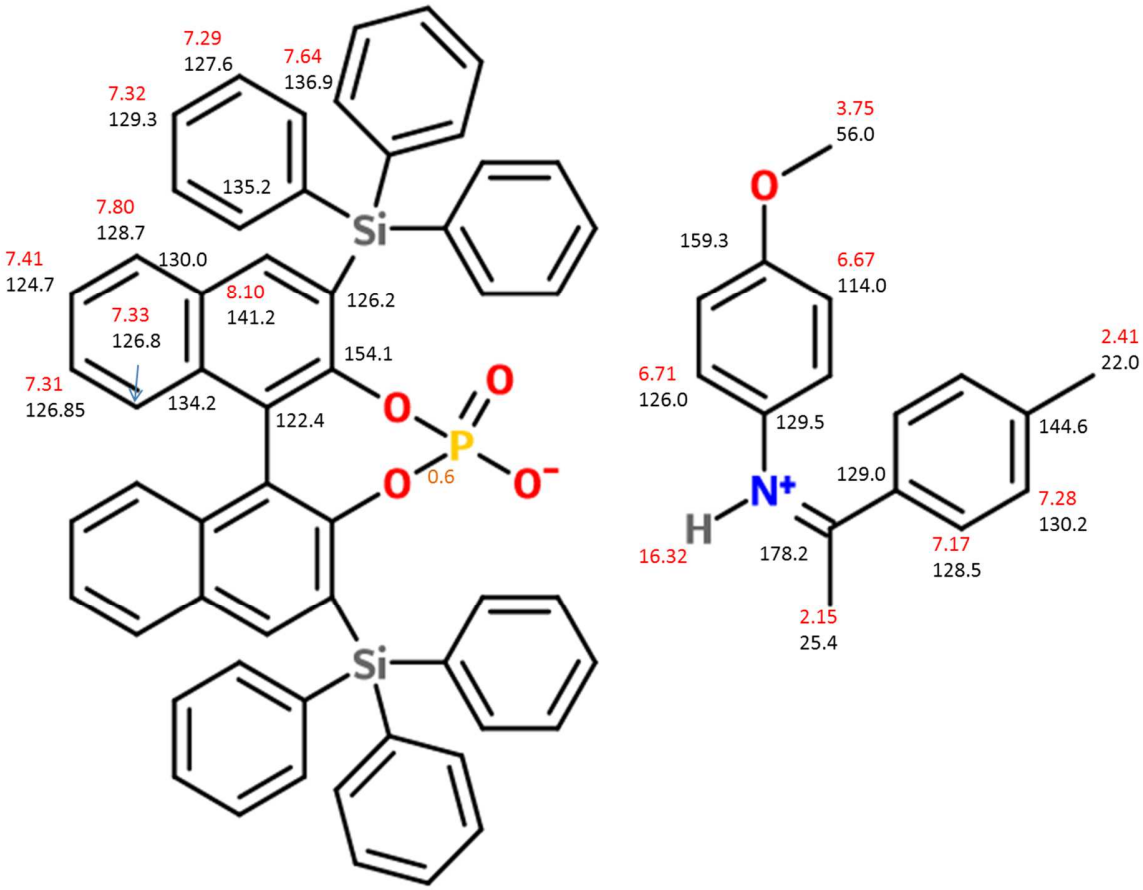

4.8.13 Structure identification of all TiPSY/E-imine complexes

S14. *Type I* TiPSY/1E Complex

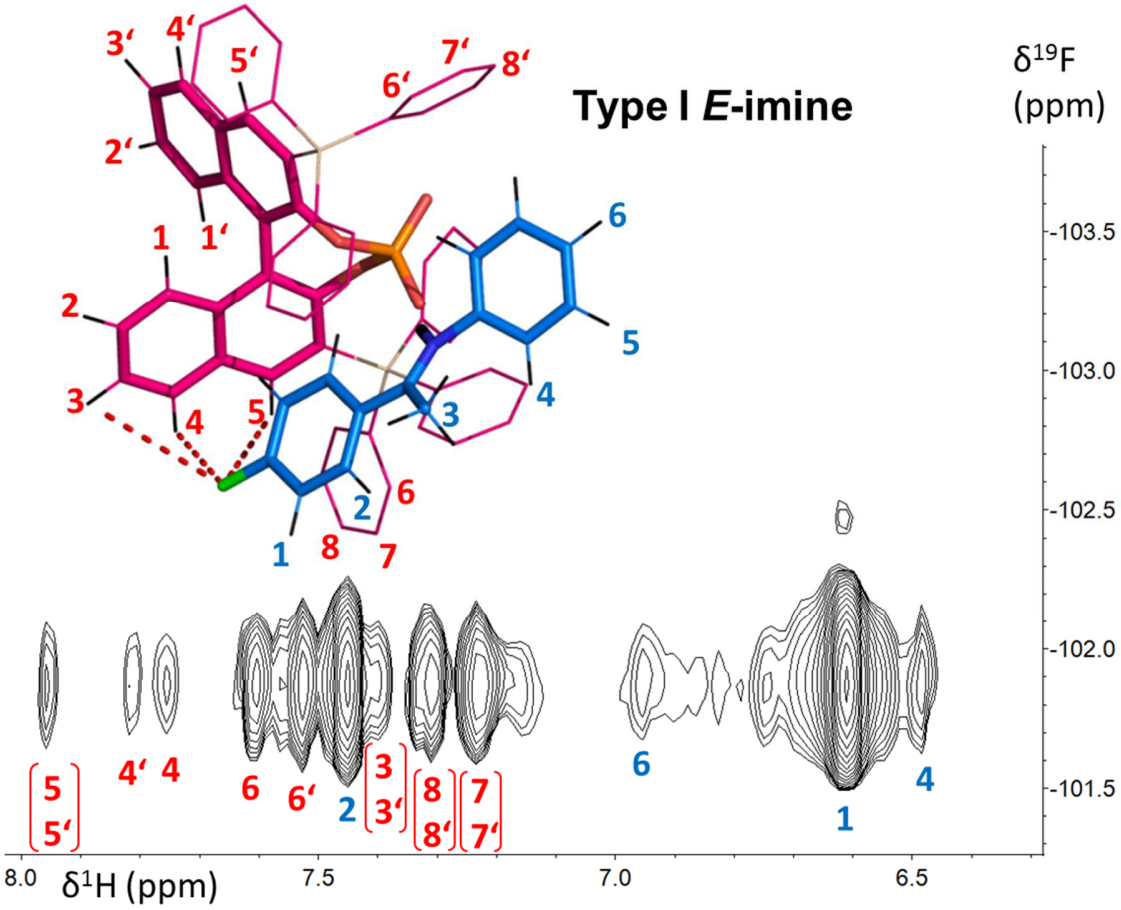

Experiment parameters: Pulse sequence: hoesyph, Mixing time 300 ms, Time domain: 4k x 32 points, Spectral window 26 x 6 ppm, ^{1}H offset frequency: 10 ppm, ^{19}F offset frequency -103 ppm, Recycling delay: 2s, Number of scans: 32. Experiment time: 1h24min.

S15. *Type II* TiPSY/1E Complex

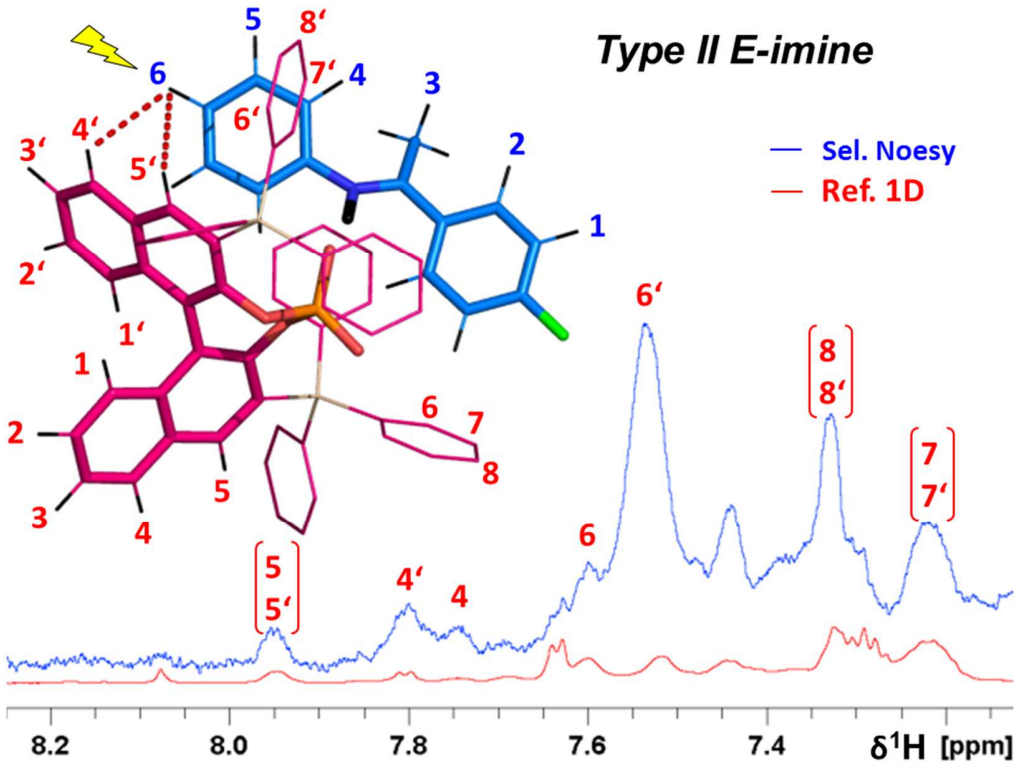

Experiment parameters: Pulse sequence: selnogp, Mixing time 100 ms, Selective 180° Gaussian pulse at 6.94 ppm: 49 ms using Topspin shape tool. Time domain: 64k points, Spectral window 22 ppm, ^{1}H offset frequency: 10 ppm, Recycling delay: 4s, Number of scans: 1k. Experiment time: 1h54min.

S16. *Type II* TiPSY/13E Complex

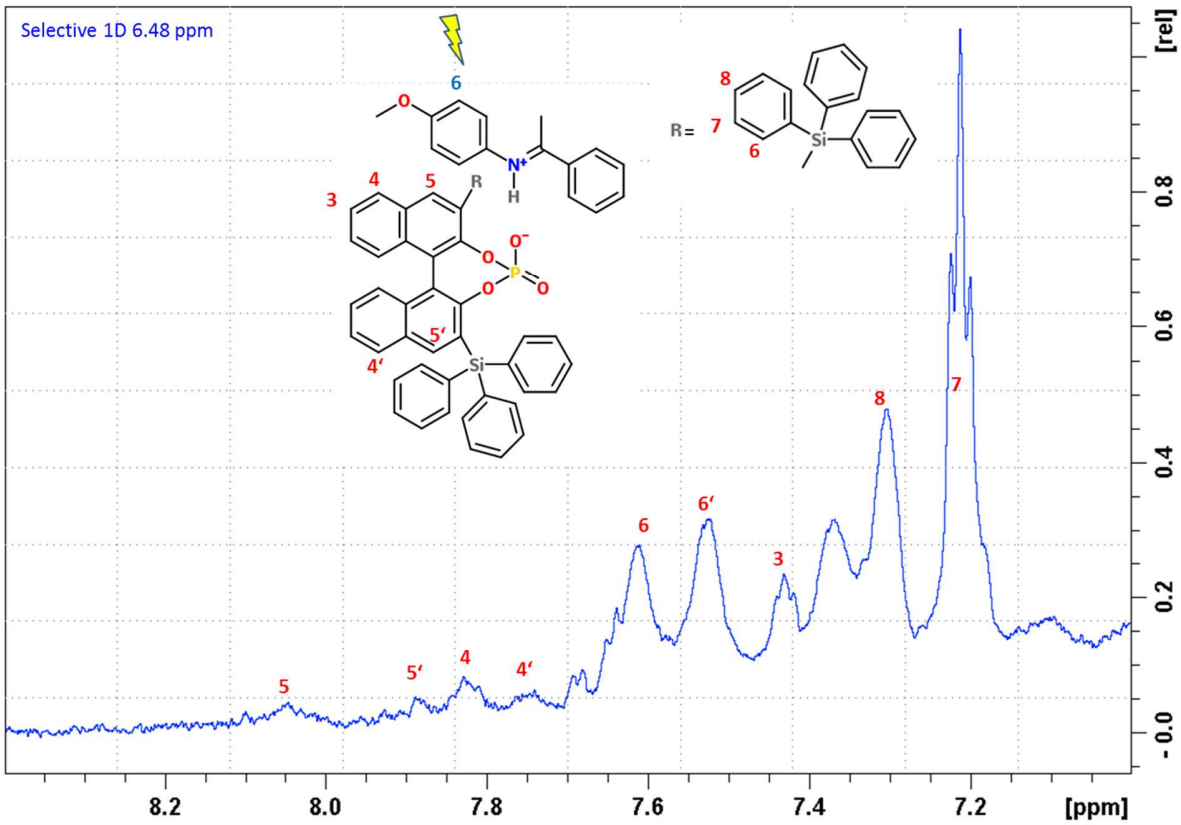

From imine **13**, five NOEs to the catalyst backbone signals were observed (spins 3, 4, 4', 5 and 5').

Experiment parameters: Pulse sequence: selnogp, Mixing time 100 ms, Selective 180° Gaussian pulse at 6.48 ppm: 19 ms using Topspin shape tool. Time domain: 64k points, Spectral window 22 ppm, ^{1}H offset frequency: 10 ppm, Recycling delay: 4s, Number of scans: 1k. Experiment time: 1h54min.

S17. *Type I* TiPSY/14E Complex

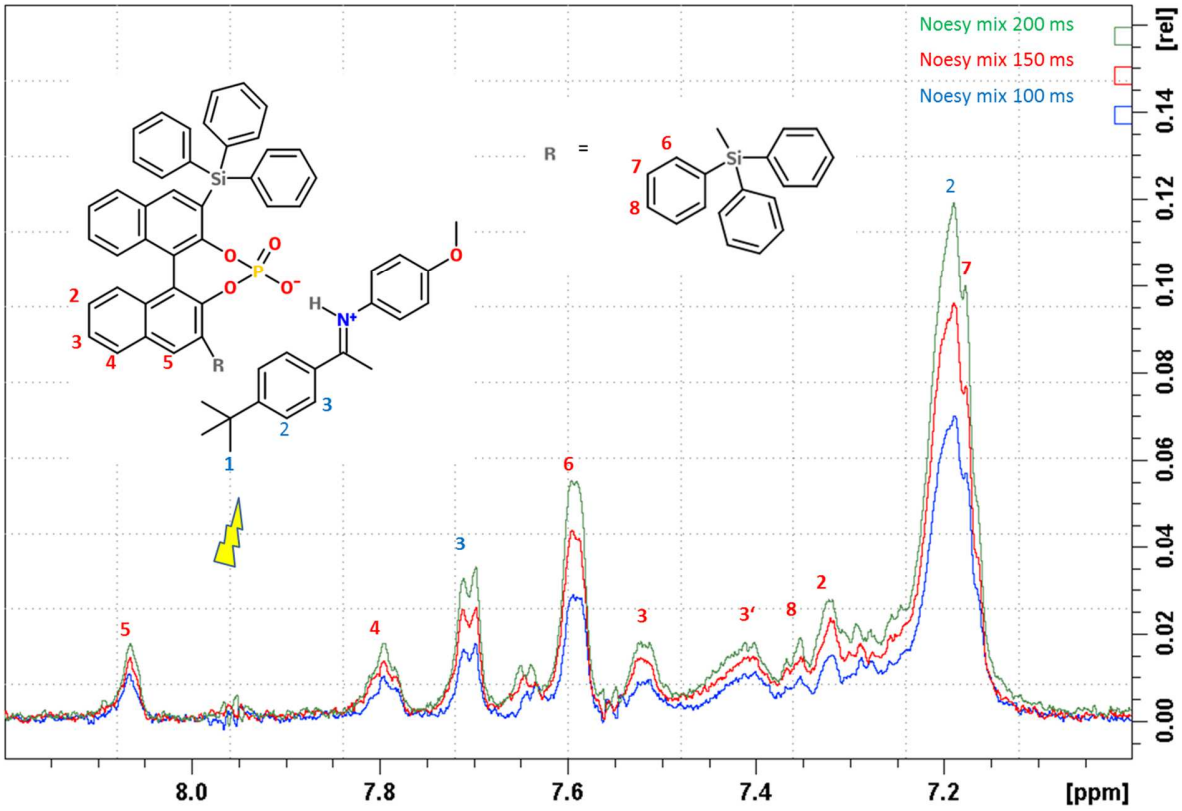

Experiment parameters: Pulse sequence: selnogp, mixing time 100 - 300 ms, Selective 180° Gaussian pulse at 1.22 ppm: 72 ms using Topspin shape tool. Time domain: 64k points, Spectral window 22 ppm, ^{1}H offset frequency: 10 ppm, Recycling delay: 4s, Number of scans: 1k. Experiment time: 1h54min.

S18. *Type II* TiPSY/14E Complex

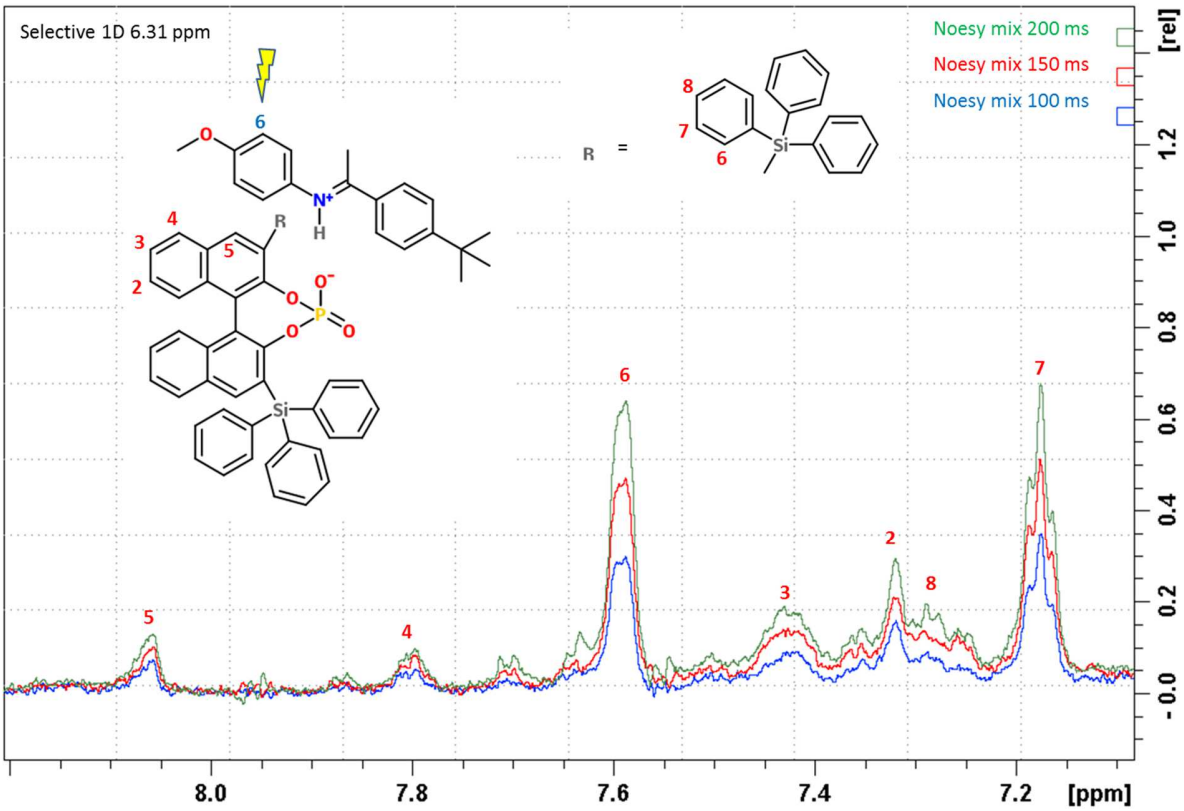

From imine **14**, four specific intermolecular NOE with TiPSY backbone were detected (spins 2, 3, 4 and 5).

Experiment parameters: Pulse sequence: selnogp, Mixing time 100; 150; 200 ms, Selective 180° Gaussian pulse at 6.31 ppm: 20 ms using Topspin shape tool. Time domain: 64k points, Spectral window 22 ppm, ^{1}H offset frequency: 10 ppm, Recycling delay: 5s, Number of scans: 1k. Experiment time: 1h54min.

S19. *Types I - II* TiPSY/15E Complex

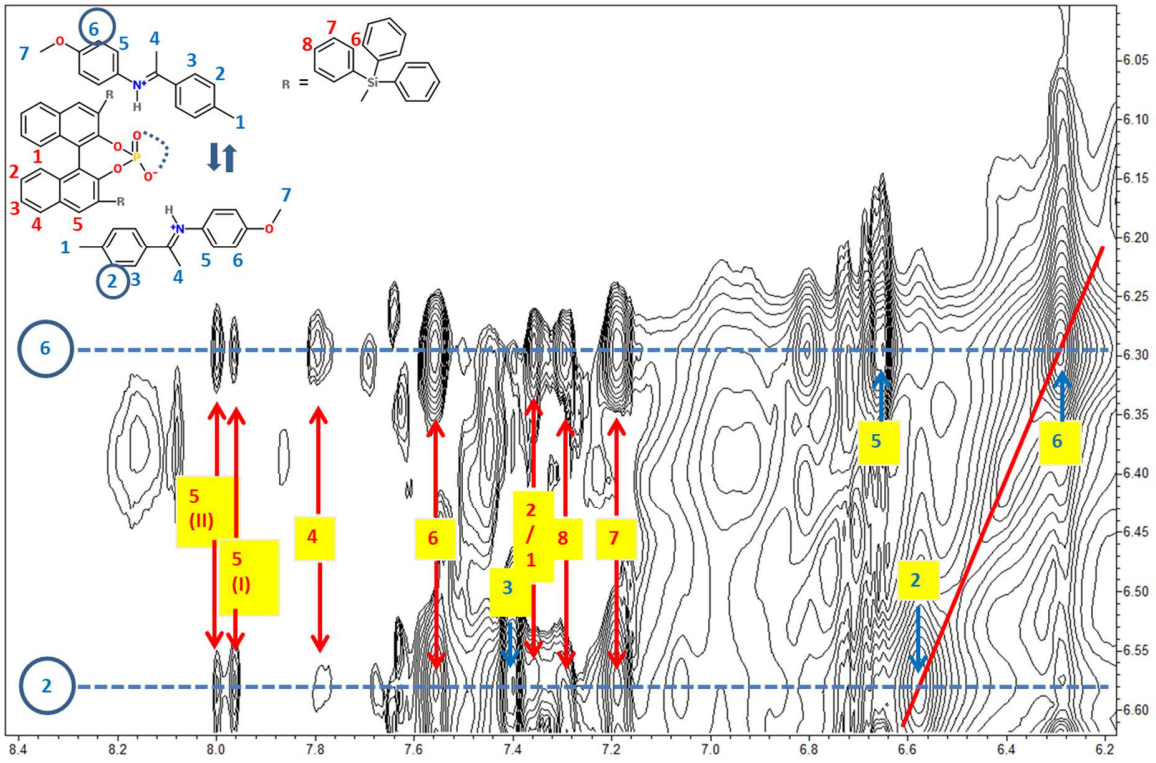

With imine **15**, from two different examples, intermolecular NOEs were found to TiPSY backbone signals (spins 1 or 2 in overlap, 3, 4, 5 and 5'). Here both patterns between *Type I* and *Type II* can be directly compared.

Experiment parameters: Pulse sequence: noesygpphpp, Mixing time 200 ms, Time domain: 8k x 512 points, Spectral window 34 x 11.5 ppm (folded indirect dimension) ^{1}H offset frequency: 3.75 ppm, Recycling delay: 2s, Number of scans: 32. Experiment time: 11h12min.

S20. *Type II* TiPSY/15E Complex

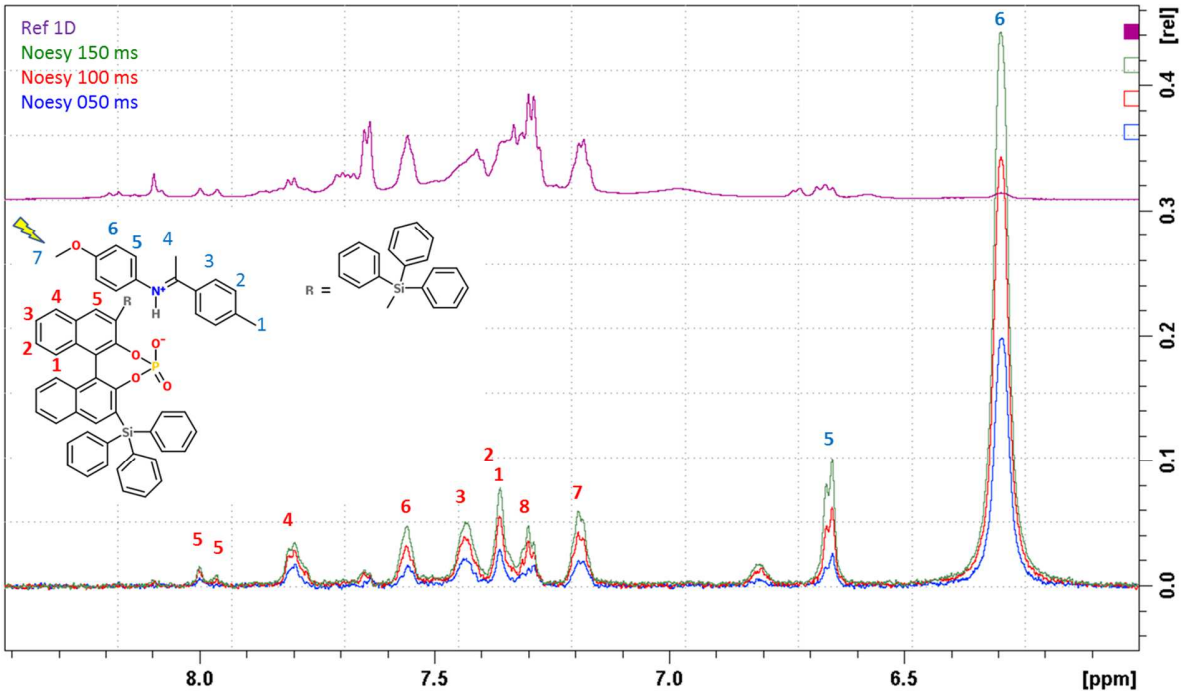

With the imine **15**, from two different examples, intermolecular NOEs were found with TiPSY backbone signals (spins 1 or 2 in overlap, 3, 4, 5 and 5'). The same pattern is found with a selective excitation on the methoxy group.

Experiment parameters: Pulse sequence: selnogp. Mixing time 50 - 150 ms. Selective 180° Gaussian pulse at 3.66 ppm: 78 ms using Topspin shape tool. Time domain: 64k points. Spectral window 22 ppm. ^{1}H offset frequency: 9 ppm. Recycling delay: 4s. Number of scans: 1k. Experiment time: 1h54min.

4.8.14 Structure identification of all TiPSY/*Z*-imine complexes

S21. *Type I* TiPSY/1Z Complex

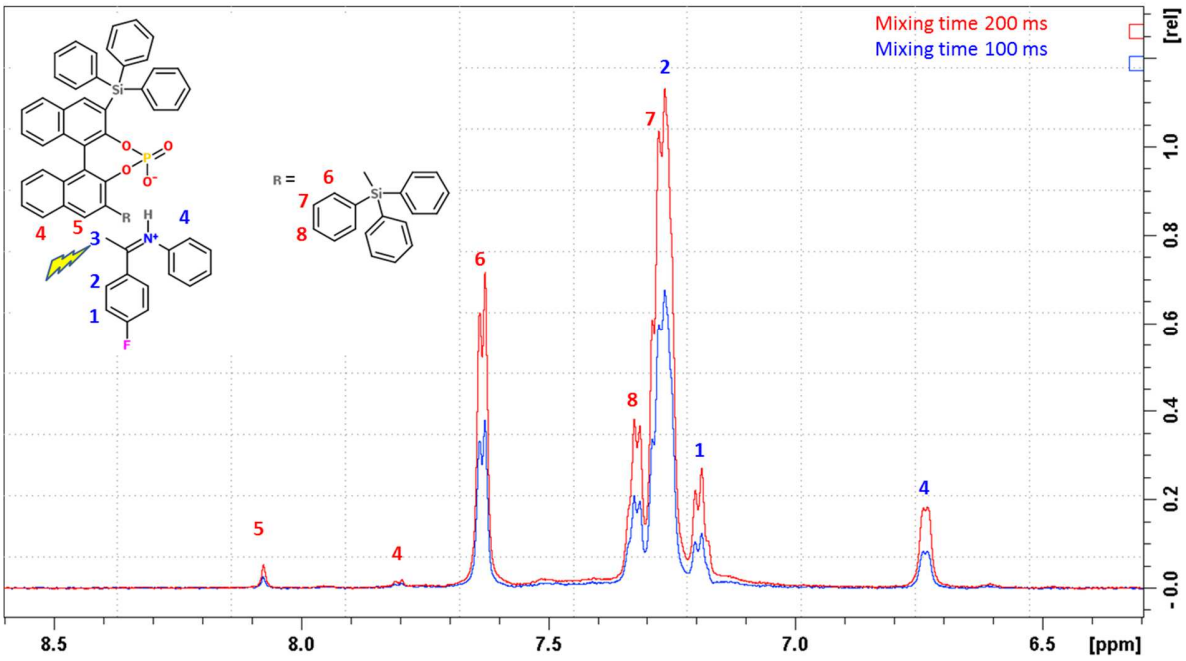

Experiment parameters: Pulse sequence: selnogp. mixing time 100 - 200 ms. Selective 180° Gaussian pulse at 3.66 ppm: 38 ms using Topspin shape tool. Time domain: 64k points. Spectral window 22 ppm. ^{1}H offset frequency: 10 ppm. Recycling delay: 4s. Number of scans: 1k. Experiment time: 1h55min.

S22. *Type II* TiPSY/1Z Complex

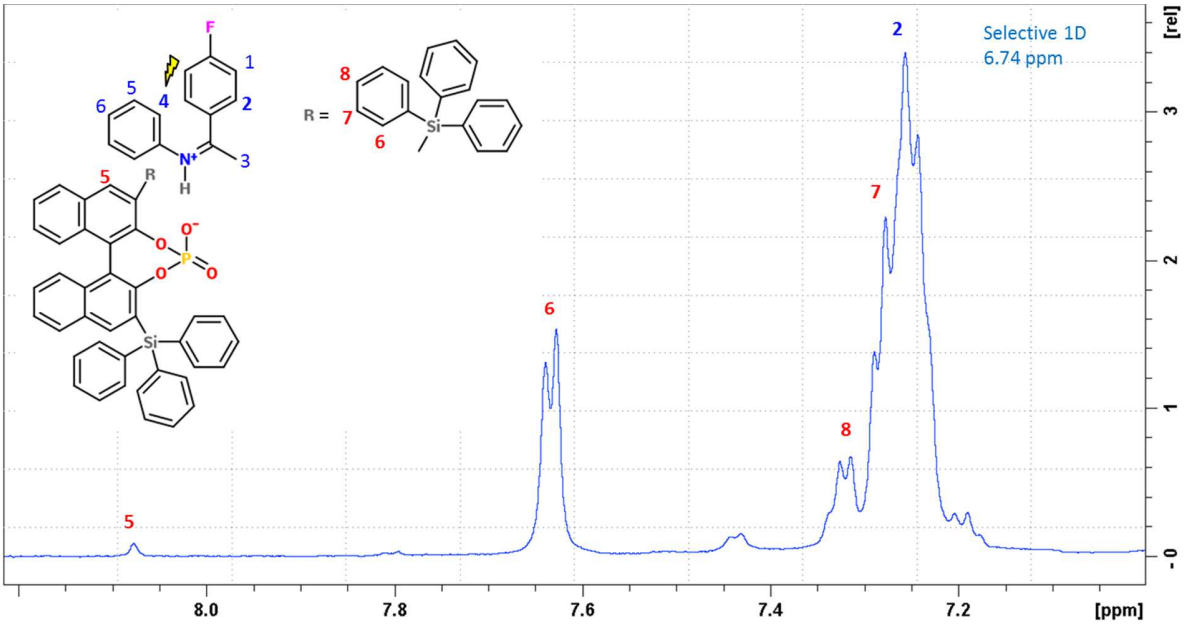

Experiment parameters: Pulse sequence: selnogp, mixing time 150 ms, Selective 180° Gaussian pulse at 6.74 ppm: 45 ms using Topspin shape tool. Time domain: 64k points, Spectral window 22 ppm, ^{1}H offset frequency: 10 ppm, Recycling delay: 4s, Number of scans: 1k. Experiment time: 1h55min.

S23. *Type I* TiPSY/13Z Complex

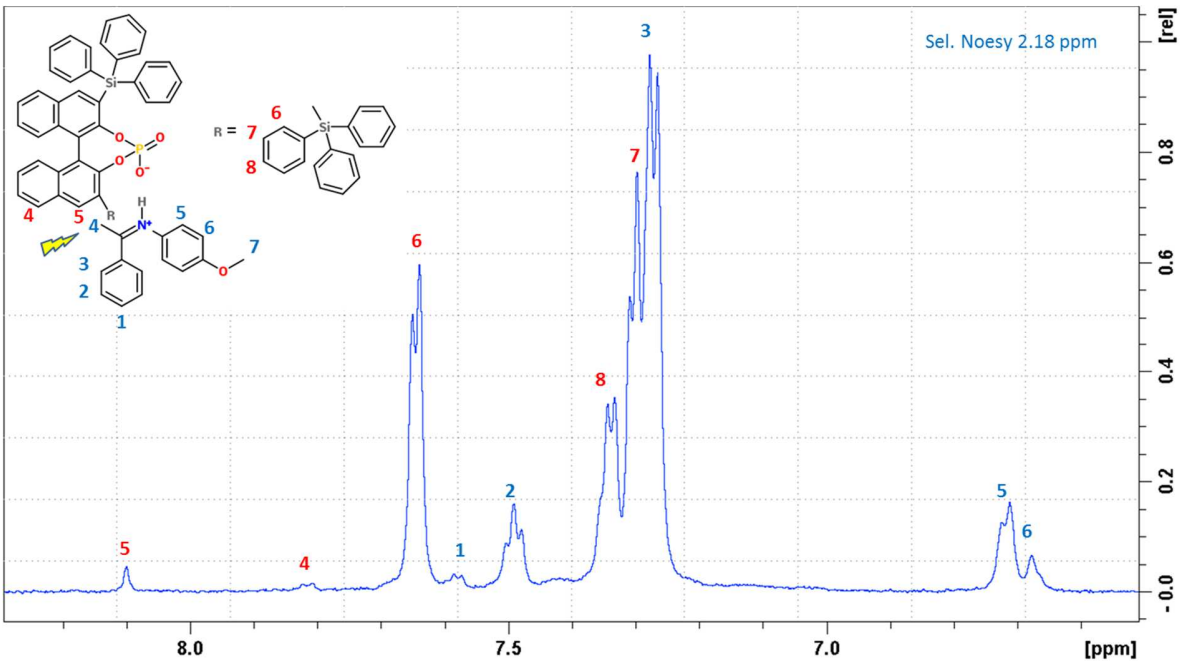

Experiment parameters: Pulse sequence: selnogp, mixing time 200 ms, Selective 180° Gaussian pulse at 2.18 ppm: 89 ms using Topspin shape tool. Time domain: 64k points, Spectral window 22 ppm, ^{1}H offset frequency: 10 ppm, Recycling delay: 4s, Number of scans: 1k. Experiment time: 1h56min.

S24. *Type II* TiPSY/14E-Z Complexes

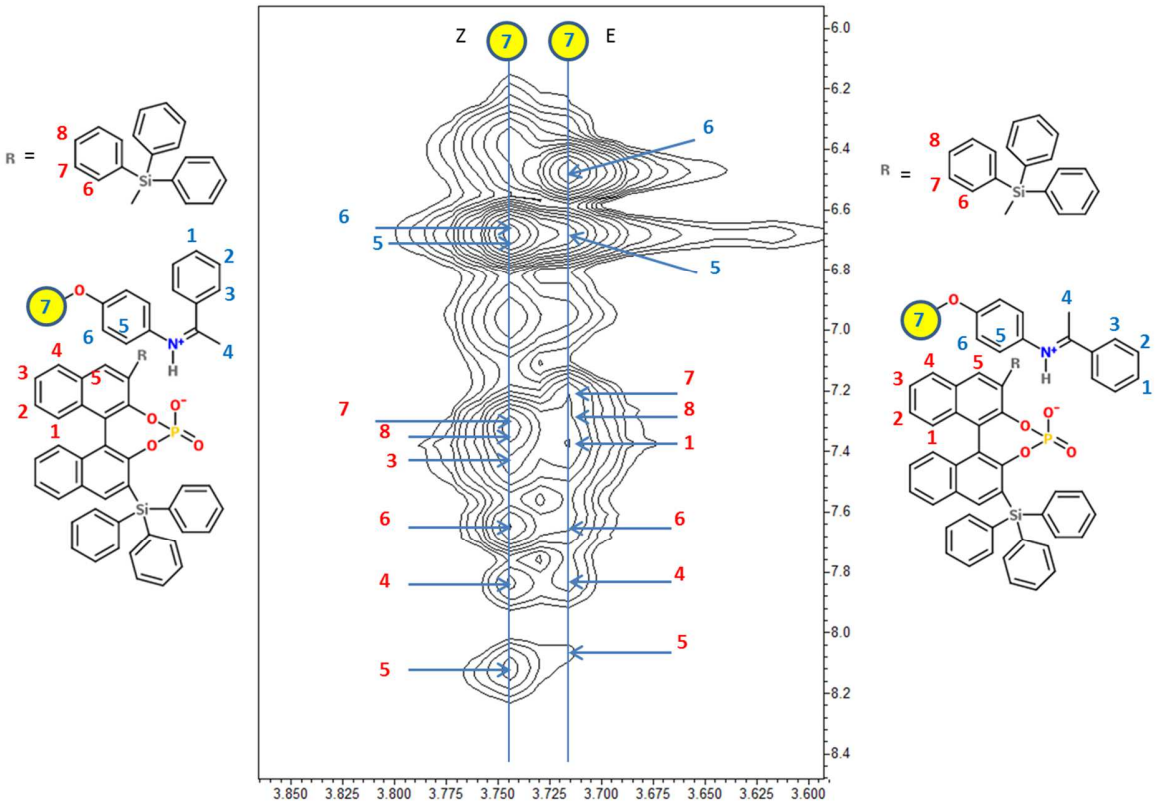

Pulse sequence: noesygpphpp, mixing time 500 ms, Time domain: 4k x 256 points, Spectral window 29 x 13 ppm (folded indirect dimension) ^{1}H offset frequency: 5.5 ppm, Recycling delay: 2s, Number of scans: 32. Experiment time: 6h4min.

S25. *Type I* TiPSY/14Z Complex

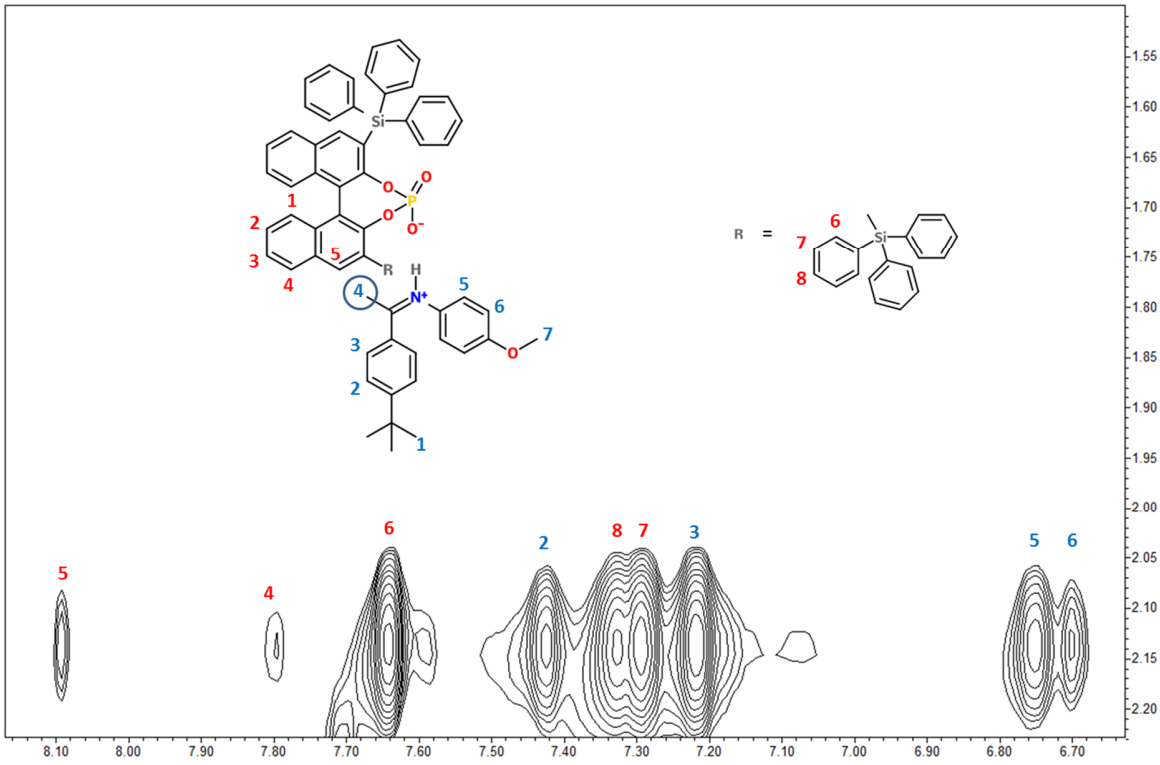

Experiment parameters: Pulse sequence: noesygpphpp, Mixing time 300 ms, Time domain: 4k x 512 points, Spectral window 22 x 22 ppm ^{1}H offset frequency: 10 ppm, Recycling delay: 2s, Number of scans: 40. Experiment time: 11h12min.

S26. *Type II* TiPSY/14Z Complex

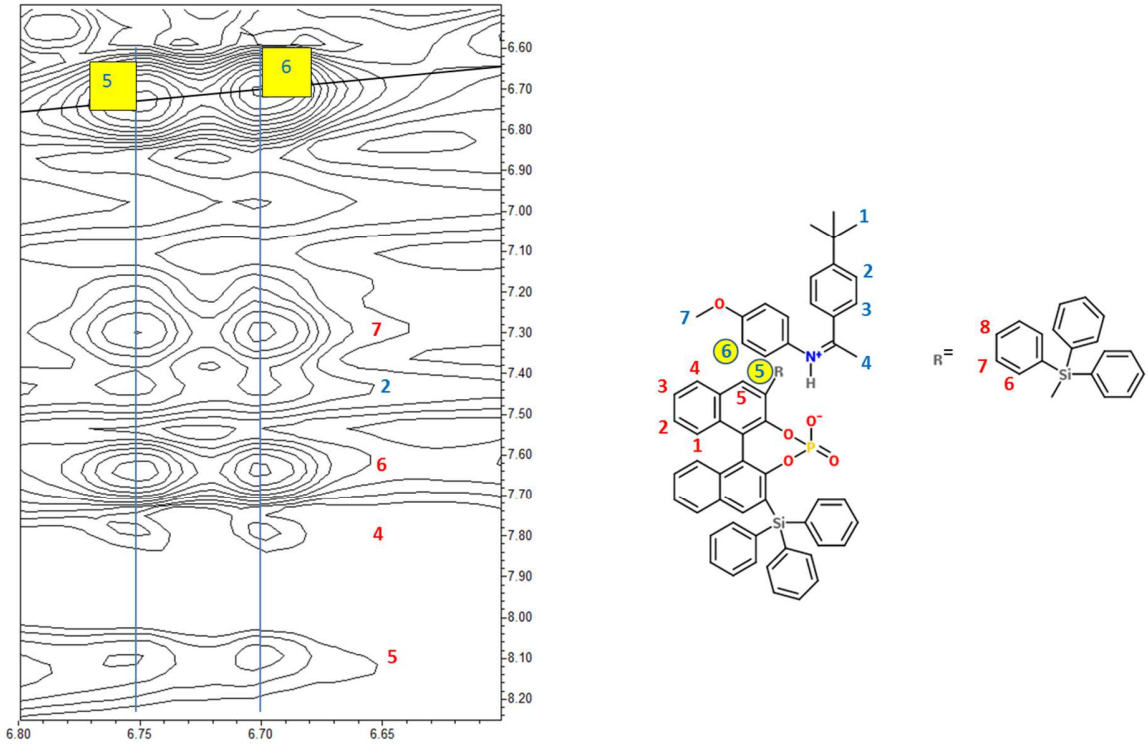

Experiment parameters: Pulse sequence: noesygpphpp, Mixing time 300 ms, Time domain: 4k x 512 points, Spectral window 22 x 22 ppm ^{1}H offset frequency: 10 ppm, Recycling delay: 2s, Number of scans: 40. Experiment time: 11h12min.

S27. *Type I* TiPSY/15E-Z Complexes

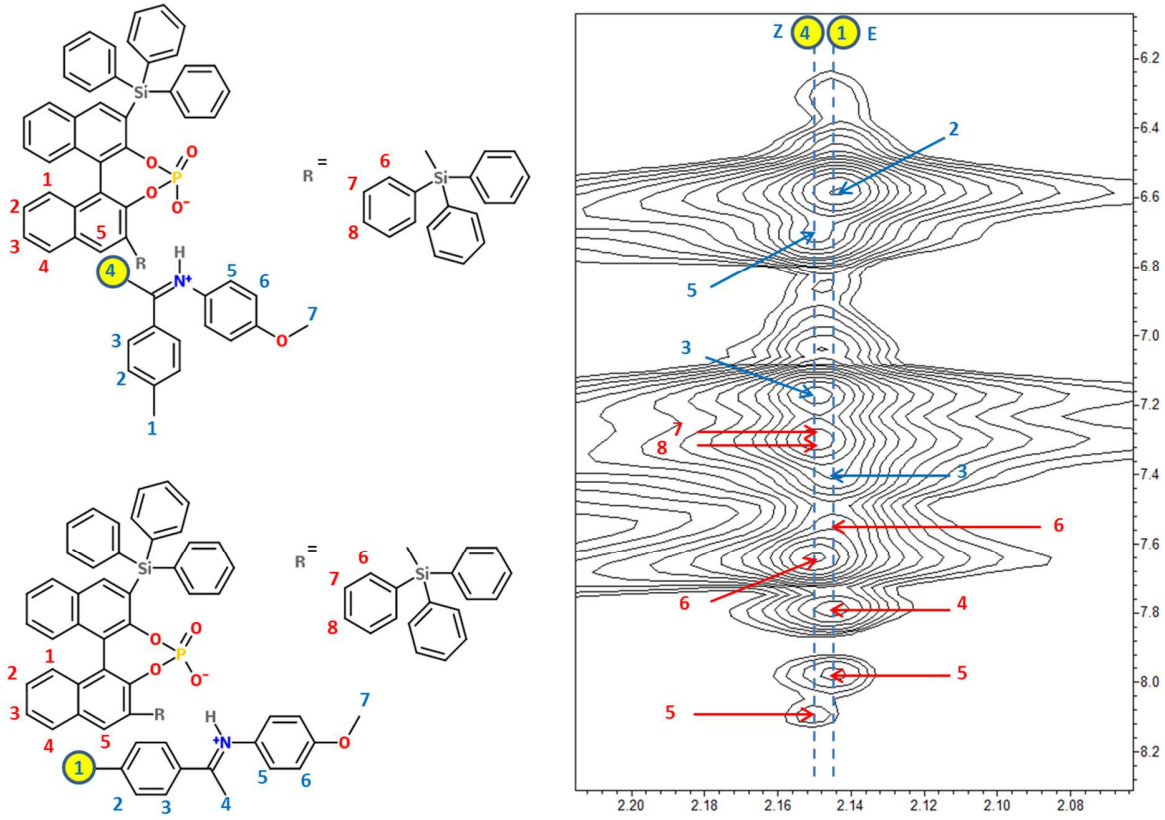

Experiment parameters: Pulse sequence: noesygpphpp, Mixing time 200 ms, Time domain: 4k x 512 points, Spectral window 22 x 22 ppm ^{1}H offset frequency: 9 ppm, Recycling delay: 2s, Number of scans: 32. Experiment time: 10h56min.

S28. *Type II* TiPSY/15Z Complex

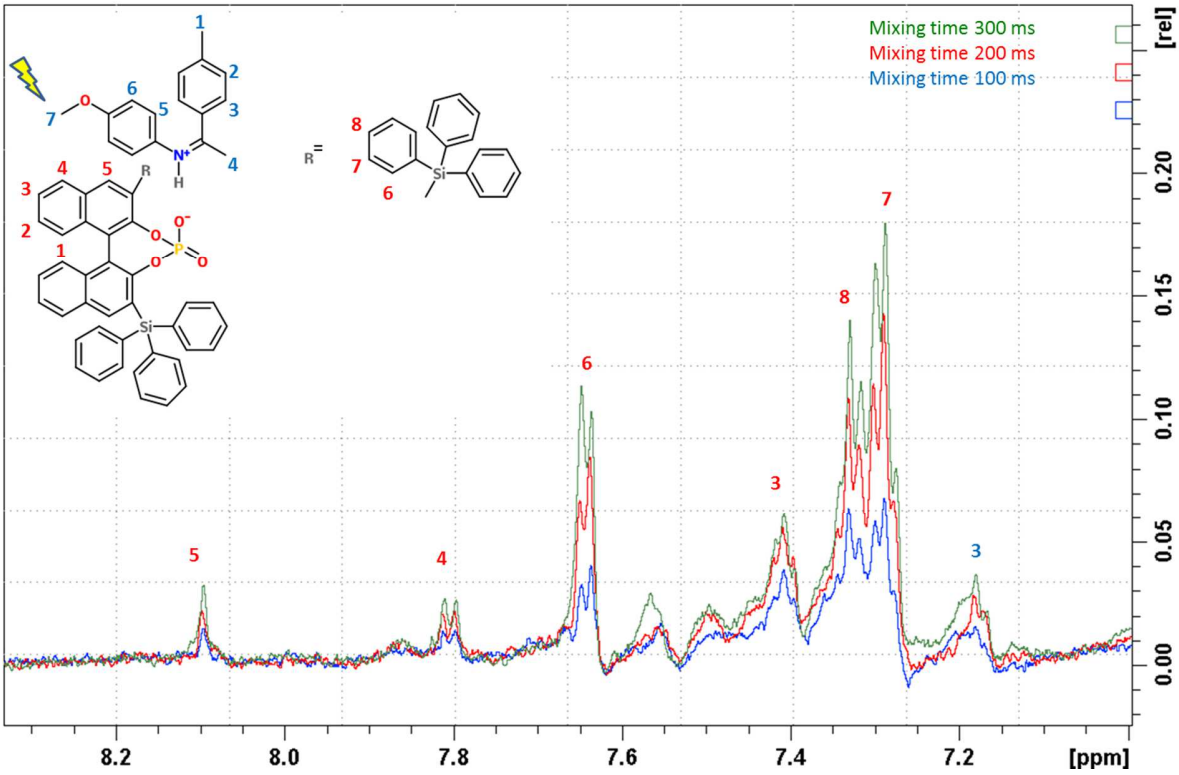

Experiment parameters: Pulse sequence: selnogpzs, Mixing time 100, 200 and 300 ms, Selective 180° Gaussian pulse at 3.75 ppm: 69 ms using Topspin shape tool. Time domain: 24k points, Spectral window 22 ppm, ^{1}H offset frequency: 9 ppm, Recycling delay: 8s, Number of scans: 768. Experiment time: 1h57min.

4.8.15 S29. Steiner-Limbach curve: $^{1}J_{HN}$ against δ_{OHN} in hydrogen bonding

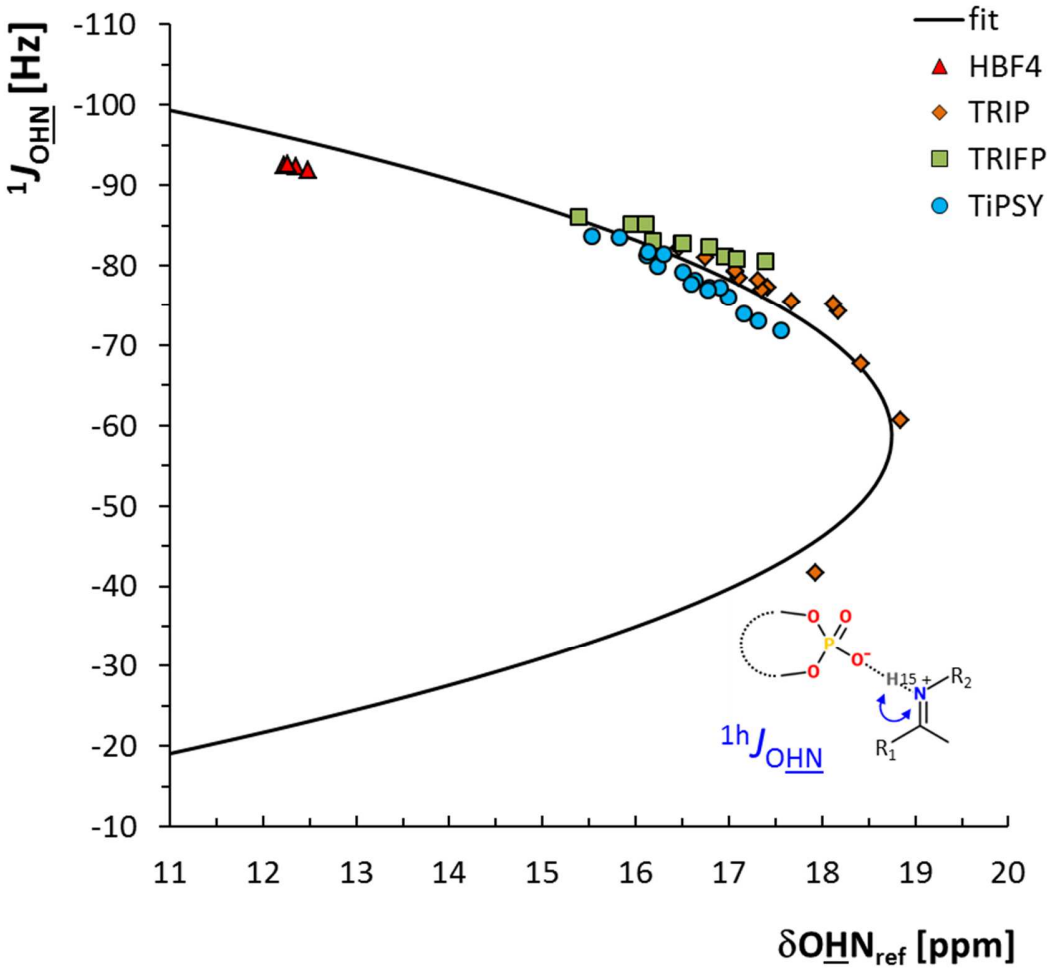

Figure S29. Plot of $^{1h}J_{\underline{HN}}$ values against δ(O<u>H</u>N). Experimental δ(O<u>H</u>N)/$^{1h}J_{\underline{HN}}$ pair values derived from TiPSY/imine complexes (cyan), pair values from TRIFP/imine complexes (green) and TRIP/imine complexes (orange)

Measurements of scalar couplings $^{1h}J_{NH}$ in CPA/imine complexes were also performed. As previously shown,[9] chemical shift and scalar coupling are related to one another according to the following equation (1):

$$^{1}J_{(O\underline{HN})} = {}^{1}J_{(\underline{HN})^{\circ}} * p_{HN}^{H} - 8 * {}^{1}J_{(O\underline{HN})^{*}} * \left(p_{OH}^{H}\right)^{2} * p_{HN}^{H}$$

(1)

Three clusters appeared corresponding to each of the three investigated catalysts. The complexes formed with TRIP have overall higher ^{1}H chemical shift values [16.5; 18.5 ppm] compared to the complexes formed with TiPSY and TRIFP. This indicates formation of a stronger hydrogen bond. Differences in ^{1}H chemicals shifts between TRIFP and TiPSY are smaller. Still, higher ^{1}H shifts values were found for complexes involving TiPSY versus complexes involving TRIFP. On the other hand, the separation between TiPSY and TRIFP clusters is mainly due to the $^{1h}J_{NH}$ values. Consistently higher $^{1h}J_{NH}$ values (smaller in absolute values) were obtained with TiPSY complexes versus TRIFP. Overall, experimental data points corresponding to TiPSY complexes are closer to the focus of the parabolic curve than the experimental data from TRIFP complexes. Since the focus of the curve (right side of the plot) corresponds to the shortest hydrogen bond, complexes formed with TiPSY are overall slightly stronger than complexes formed with TRIFP. This result confirms the previous one obtained with the Steiner-Limbach curve using the ^{15}N chemical shift.

4.8.16 S30. Measured $^1J_{HN}$ coupling constant from 1-5 imines in complex with TRIP, TiPSY and TRIFP

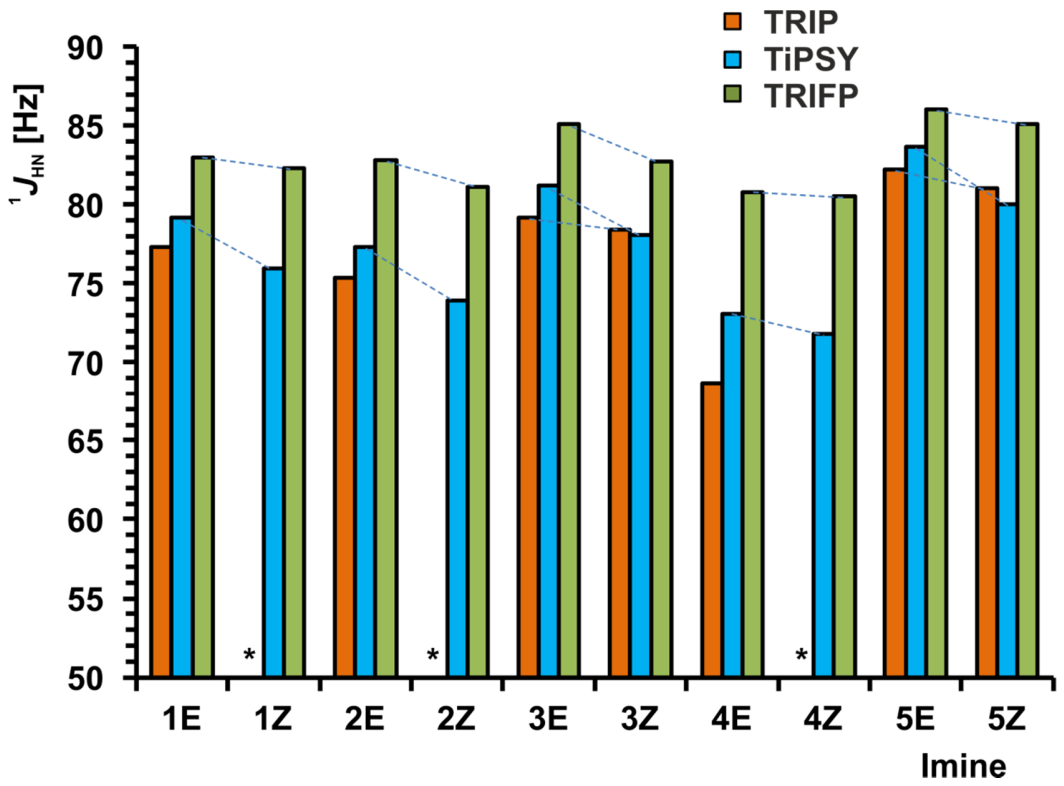

Figure S30. Comparison between experimental catalyst/imine $^1J_{OHN}$ coupling constant. Dotted lines show the difference between *E* and *Z*-isomers. The following trend is observed regarding $^1J_{OHN}$ values: $^1J_{OHN}$ TRIP < $^1J_{OHN}$ TIPSY < $^1J_{OHN}$ TRIFP. Missing values in TRIP Z-imine complexes are marked by an asterisk.

4.8.17 S31. Measured $^{2h}J_{HP}$ coupling constant vs. $\delta_{O\underline{H}N}$ chemical shifts in CPA/imine complexes

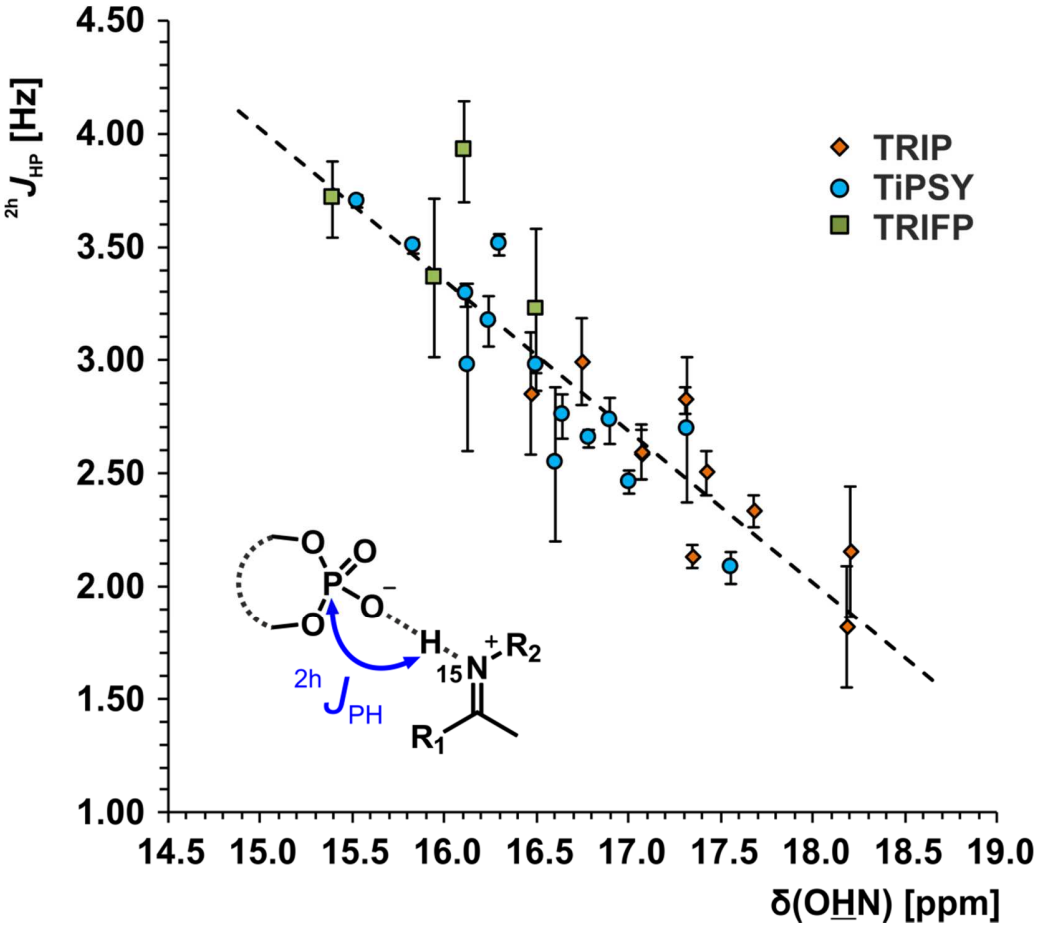

Figure S31. Plot of $^{2h}J_{PH}$ values against $\delta_{(O\underline{H}N)}$. The linear trendline (black) is derived from experimental $\delta_{(O\underline{H}N)}$ / $^{2h}J_{PH}$ pair values from TiPSY/imine complexes (cyan). Pair values from TRIFP/imine complexes (green) and TRIP/imine complexes (orange) follow a similar pattern

4.8.18 Qualitative detection and quantitative determination of $^{2h}J_{PH}$ and $^{3h}J_{PN}$ scalar couplings

Both qualitative detection and quantitative determination of $^{2h}J_{PH}$ and $^{3h}J_{PN}$ regarding TRIP/imine complexes were obtained in our group.[4] The method was explained in details in the supplementary materials. The same method is applied here for the TiPSY/imine and TRIP/imine complexes. It takes advantage of the magnetization transfer between the nuclei involved in the hydrogen bridges detected in the correlation experiments. The $^{2h}J_{PH}$ couplings between the transferred proton in the iminium ion and the ^{31}P nucleus in the phosphate ion were measured qualitatively by mono and two dimensional ^{1}H, ^{31}P-HMBC experiments. First, this illustrates again that both isomers form a contact ion pair (CIP) with the phosphate anion.[10] Second, this indicates a covalent character of the formed hydrogen bond in the catalyst substrate complex.[11] It is well known that protons which are involved in a hydrogen bond experience, beside an increase of their isotropic chemical shift (low-field shift),[12] an enlargement of their chemical shift anisotropy (CSA) as well.[13,14] Several NMR experimental studies on trans hydrogen bond scalar coupling in bio macromolecules suggest that theoretically the magnetization transfer between both the involved nuclei can be mediated instead of a Fermi contact interaction (scalar coupling)[12] by a relaxation interference of the ^{1}H CSA and the ^{1}H-X dipole interaction (whereas X is the acceptor atom).[11,15–17] To ensure that the measured magnetization transfer between ^{1}H and ^{31}P is caused mainly by scalar coupling between^{1}H and ^{31}P and is not mediated by a cross correlation between ^{1}H-CSA and ^{1}H-^{31}P dipole interaction, modified 1D ^{1}H-^{31}P-HMBC experiments developed by Löhr et al. were employed.[11,18] The 1D HMBC experiments clearly show that scalar coupling is decisive for magnetization transfer in the HMBC experiments. In the R-TRIP/**5** complex, the NH protons of both configurationally isomers show a correlation with the ^{31}P nucleus in the 1D-^{1}H,^{31}P-HMBC spectrum (Figure S34). The relaxation interference mechanism contributes only by a small extent and is therefore a negligible factor (for the pulse sequences, see Figure S32).

4.8.19 S32. Modified 1D-^{1}H,^{31}P-HMBC pulse sequence for $^{2h}J_{HP}$ detection

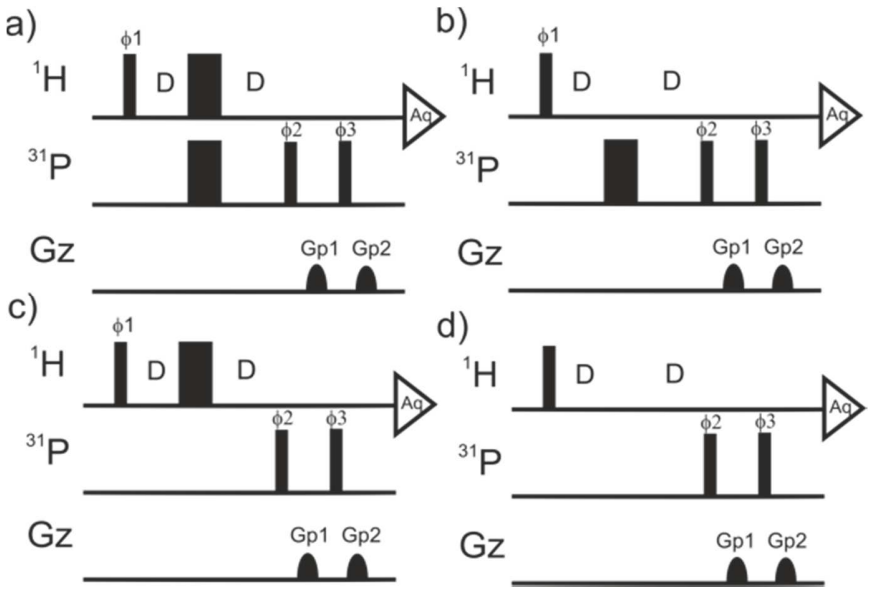

Figure S32. Modified 1D-^{1}H,^{31}P-HMBCs developed by Löhr *et al.*[11,18,19] a) Polarization transfer is mediated only by scalar coupling b) and c) Polarization transfer is mediated by ^{1}H-CSA and ^{1}H- ^{31}P-DD cross relaxation. d) Polarization transfer is mediated by the sum of scalar coupling and the ^{1}H-CSA and ^{1}H-^{31}P-DD cross relaxation. Thin and wide bars indicate 90° and 180° pulses. All phases are x, unless otherwise specified. Pulse phases: f1 = x, x, -x, -x; f2 = x, -x; f3 = 4 (x), 4(-x). Gradient strength [G/cm]: Gp1 = 22.28; Gp2 = -13.26.

4.8.20 S33. 3D-HNPO pulse sequence adapted from 3D-HNCO for $^{3h}J_{PN}$ detection

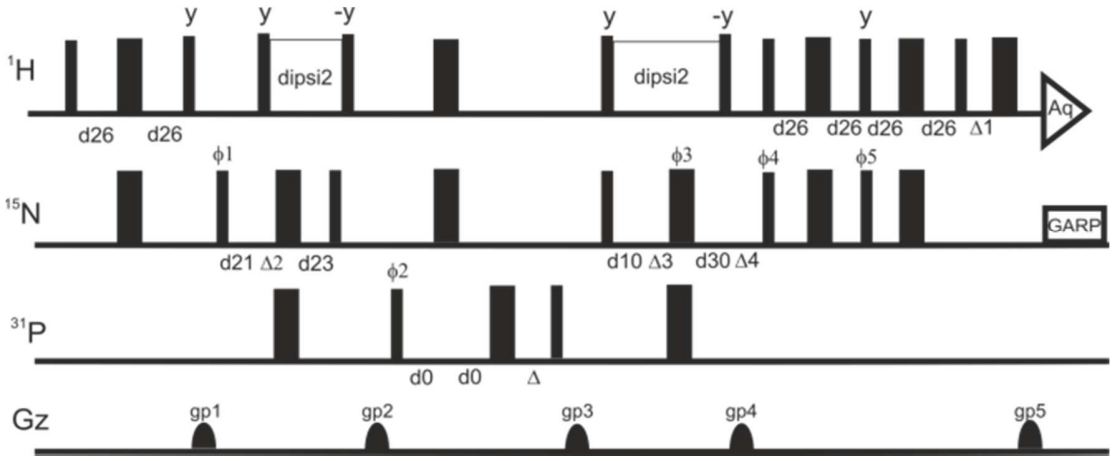

Figure S33. HNPO pulse sequence for detection of $^{h3}J_{PN}$ couplings, based on the HNCO sequence of Cordier et al. (Bruker pulse catalog: *hncogphb3d*).[18–20] Thin and wide bars indicate 90° and 180° pulses. All pulses have the phase x, unless other noted. Pulse phases: f1 = 8 (x), 8 (-x); f2 = x, -x; f3 = 4 (x), 4(-x); f4 = x, x, -x, -x; f5 = -y, -y, y, y; Delays: d0 = incremented delay in F1; d10 = incremented delay in F2(^{15}N); d30 = decremented delay in F2(^{15}N); d21 = ½ $^1J_{NH}$; d26 = ¼ $^1J_{NH}$. Gradient strength [G/cm]: gp1 = 33.41; gp2 = -22.28; gp3 = 5.57; gp4 = 44.56; gp5 = 4.51. Acquisition modes for 3D measurements: States-TPPI in F1(^{31}P), Echo-Antiecho in F2(^{15}N), DQD in F3(^{1}H).

In order to determine the $^{3h}J_{PN}$ coupling constants qualitatively, 3D-HNPO spectra were measured (Figures S33 and S37). The two signals obtained in the cube of the 3D-HNPO of (R)-TRIP/**5** complex correlate all three nuclei involved in the hydrogen-bond to each other and the two spin-triples are unambiguously assigned. Therefore, a coupling across the hydrogen-bond between the ^{31}P nuclei of the catalyst and the ^{15}N nuclei of the substrate could be verified. The resulting 2D-^{1}H,^{15}N and 2D-^{1}H,^{31}P planes of the 3D HNPO spectrum of R-TRIP/**5** complex are shown in Figure S37.

4.8.21 Detection of $^{2h}J_{HP}$ scalar couplings

4.8.21.1 S34. Detection of $^{2h}J_{HP}$ scalar coupling in TRIP/5 complex

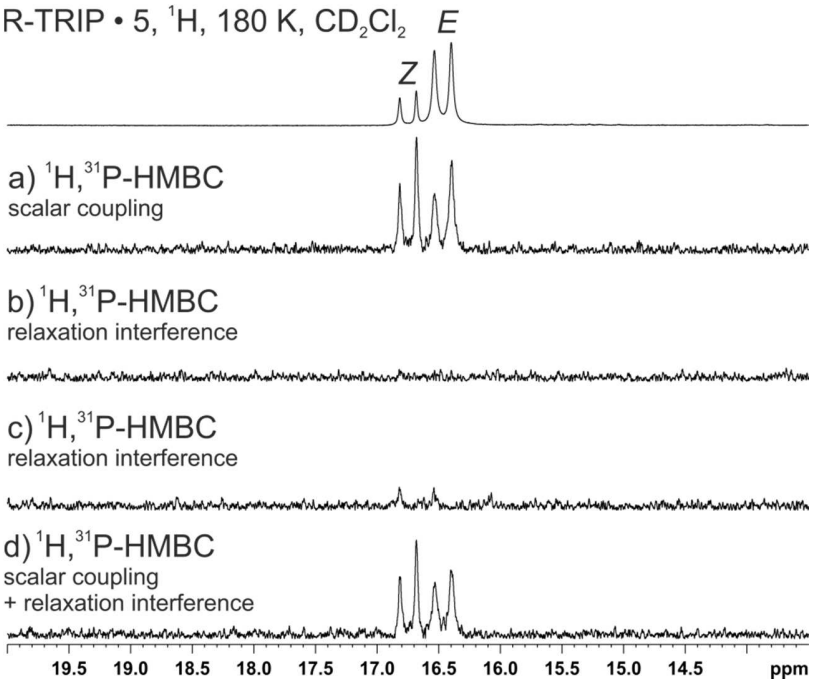

Figure S34. ^{1}H and 1D-^{1}H,^{31}P-HMBC spectra of a mixture of R-TRIP/**5** in CD_2Cl_2 at 180 K. a) Experiment was performed with exclusive detection of scalar coupling and the NH protons of both isomers give rise to a signal b) and c) Only cross relaxation between ^{1}H-CSA and ^{1}H^{31}P-DD contributes to polarization transfer d) Both scalar coupling and relaxation interference contribute to the polarization transfer. All HMBC experiments were performed with 128 ns transients, a transfer delay D of 12.68 ms, an acquisition time of 2.73 s and a interscan delay of 1 s. The ^{1}H spectrum was scaled individually.

S35. Detection of $^{2h}J_{HP}$ scalar coupling in TRIFP/3 complex

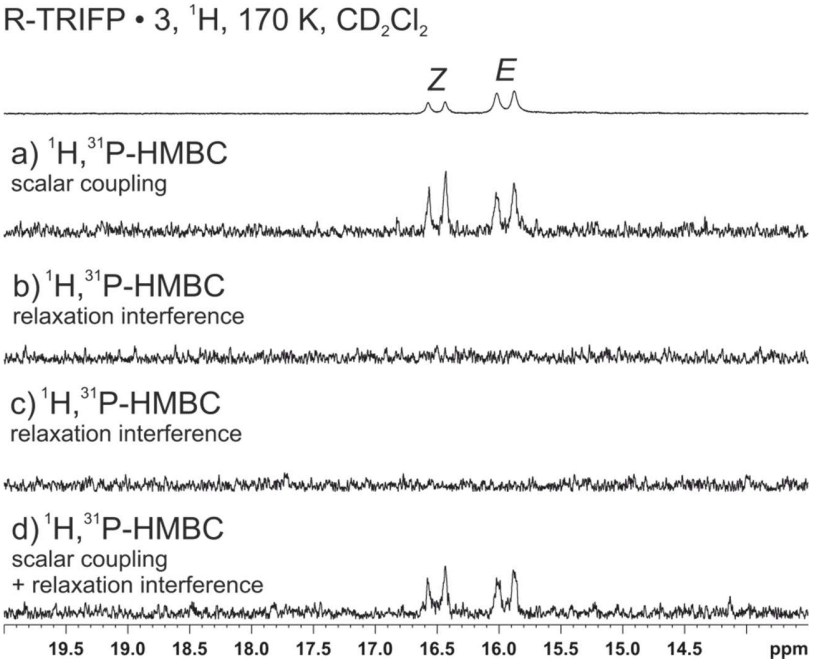

Figure S35. ^{1}H and 1D-^{1}H,^{31}P-HMBC spectra of a mixture of R-TRIP/3 in CD_2Cl_2 at 170 K. a) Experiment was performed with exclusive detection of scalar coupling and the NH protons of both isomers give rise to a signal b) and c) Only cross relaxation between ^{1}H-CSA and ^{1}H^{31}P-DD contributes to polarization transfer d) Both scalar coupling and relaxation interference contribute to the polarization transfer. All HMBC experiments were performed with 512 transients, a transfer delay D of 12.69 ms, an acquisition time of 2.73 s and a interscan delay of 1 s. The ^{1}H spectrum was scaled individually.

S36. Detection of $^{2h}J_{HP}$ scalar coupling in TiPSY/1 complex

R-TiPSY • **1**, ^{1}H, 180K, CD_2Cl_2

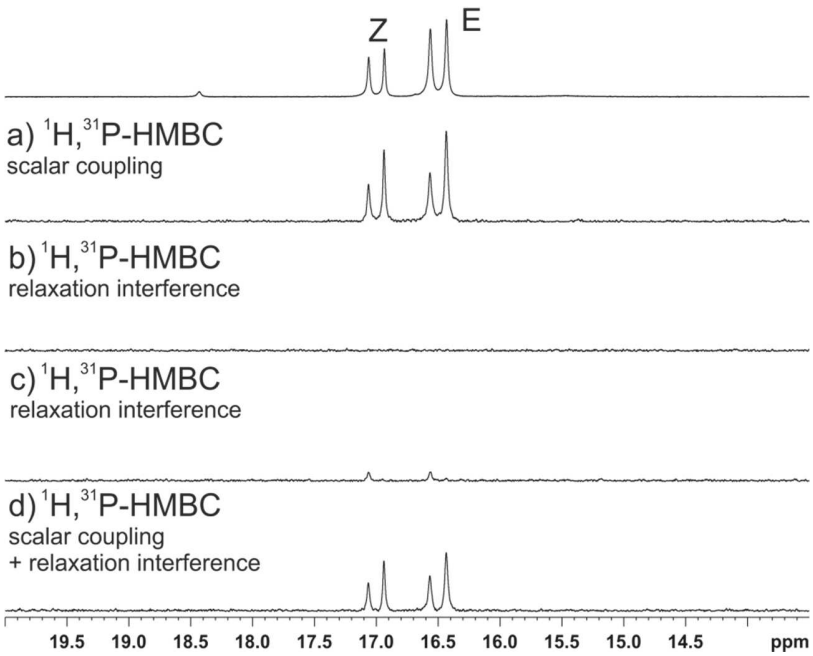

Figure S36. ^{1}H and 1D-^{1}H,^{31}P-HMBC spectra of a mixture of *R*-TiPSY/1 in CD_2Cl_2 at 180 K. a) Experiment was performed with exclusive detection of scalar coupling and the NH protons of both isomers give rise to a signal b) and c) Only cross relaxation between ^{1}H-CSA and ^{1}H^{31}P-DD contributes to polarization transfer. All HMBC experiments were performed with 128 transients, a transfer delay D of 12.69 ms, an acquisition time of 0.30 s and a interscan delay of 4 s. The ^{1}H spectrum was scaled individually.

4.8.22 Detection of $^{3h}J_{PN}$ scalar couplings

S37. Detection of $^{3h}J_{PN}$ scalar coupling in TRIP/5 complex

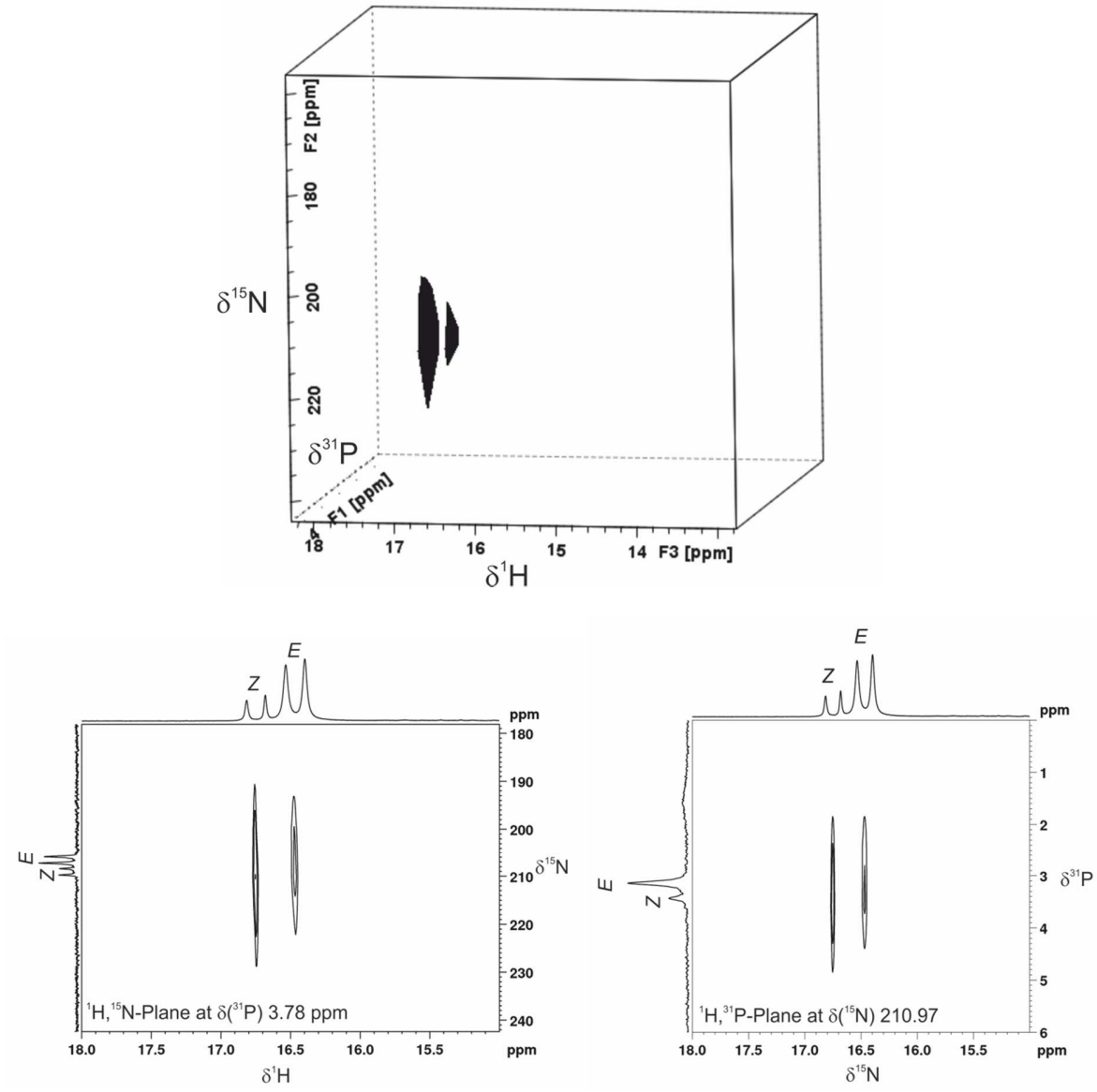

Figure S37. 2D Planes of the 3D HNPO of *R*-TRIP/5 in CD_2Cl_2 at 180 K.

4.8.23 S38. Spin-Echo pulse sequence for the determination of $^{2h}J_{HP}$ coupling constants

For the quantification of the $^{2h}J_{P,H}$ and $^{3h}J_{P,H}$ coupling constants, spin echo difference experiments and 1D-HNPO difference experiments were employed, methods which were applied by Federwisch *et al.* on the artificial acylguanidine receptor systems before (Figures S38 and S39).[18,19]

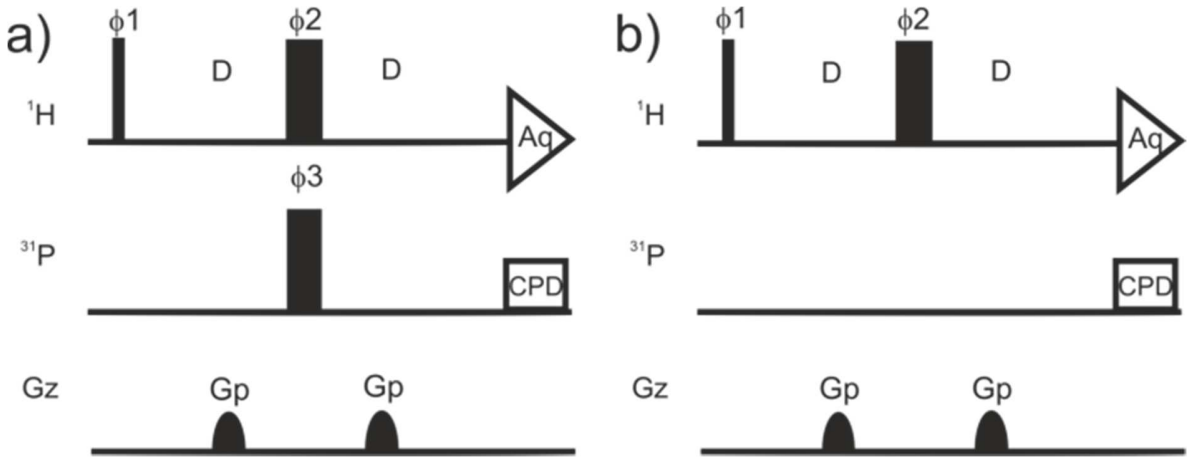

Figure S38. Spin Echo pulse sequence for determination of $^{2h}J_{PH}$ coupling constants.[18,19] The image is adapted from references.[18,19] Thin and wide bars indicate 90° and 180° pulses. f1= x,x –x,-x,y,y,-y-y; f2 = y, -y, y, -y, x, -x, x, -x; f3 = x, -x, x, -x, y, -y, y, -y; Gp [G/cm] = 5.57

4.8.24 S39. 1D-HSQC pulse sequences for the determination of the $^{3h}J_{PN}$ coupling constants

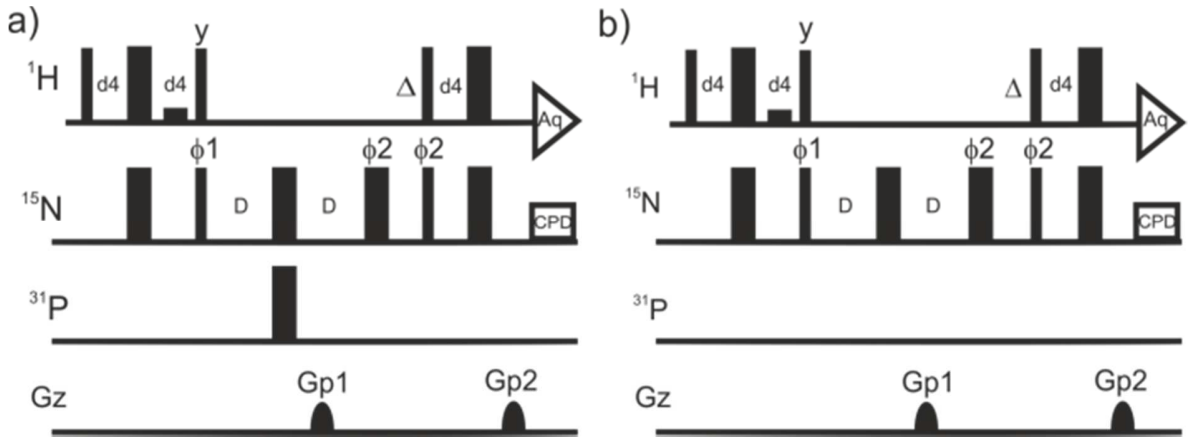

Figure S39. 1D-HSQC pulse sequences for determining the $^{3h}J_{PN}$ coupling constants.[18,19] a) The 180° pulse leads to development of scalar coupling between ^{31}P and ^{15}N and therefore a decrease of the measured signal intensity. b) The 180° pulse on ^{31}P is omitted and the scalar coupling between ^{15}N and ^{31}P is refocused. Thin and wide bars indicate 90° and 180° pulses. All pulse phases are x, unless otherwise specified. Pulse phases: f1 = x, -x; f2 = x, x, -x, -x. Gradient strength [G/cm]: Gp1 = 44.56; Gp2 = 4.51.

4.8.25 S40. Equations used for $^{2h}J_{HP}$ and $^{3h}J_{PN}$ determination from experimental data

Applying a 180° pulse on ^{31}P in the center of spin echo period leads to development of coupling between ^{1}H and ^{31}P and to reduced signal intensity (Equation (2)). Hence the measured signal intensity I_{co} is proportional to $e^{-(2D/T2)} \cos(2D\pi\ ^{ah}J_{PX})$.[18,19,21,22] Leaving out the 180° pulse on ^{31}P during the two pulse sequence results in refocussing of scalar coupling and the signal intensity I_{dec} is only proportional to $e^{-2D/T2}$.[18,19,21,22] Both expressions are summarized, to obtain a coupling constant dependent equation for the attenuation factor (Equations (4-6)), from which $^{2h}J_{PH}$ and $^{3h}J_{PN}$ are derived.[18,19,21,22]

$$I_{CO} = \exp\left(\frac{-2D}{T_2}\right)\cos\left(2D\ \pi\ {}^{ah}J_{PX}\right) \quad (2)$$

$$I_{dec} = \exp\left(\frac{-2D}{T_2}\right) \quad (3)$$

$$\frac{I_{dec} - I_{CO}}{I_{dec}} = 1 - \cos\left(2D\ \pi\ {}^{ah}J_{PX}\right) \quad (4)$$

$${}^{ah}J_{PX} = \frac{\arccos\left(1 - \frac{I_{dec} - I_{CO}}{I_{dec}}\right)}{2D\ \pi} \quad (5)$$

$${}^{ah}J_{PX} = \frac{\arccos\left(\frac{I_{CO}}{I_{dec}}\right)}{2D\ \pi} \quad (6)$$

Figure S40. The equations above (2) and (3) are general expressions for the intensities of the coupled I_{co} and decoupled I_{dec} spectra. (4) is an expression for the attenuation factor and its dependency on the trans hydrogen bond scalar coupling constant $^{ah}J_{PX}$.[18,19,21,22]. Coupling constant $^{ah}J_{PX}$ is extracted from equation (4) into (5) and further simplified in equation (6).

The measured absolute intensities ($^{2h}J_{PH}$) and integrals ($^{3h}J_{PN}$) for each individual delay **D** are listed below.

4.8.26 $^{2h}J_{PH}$ measured attenuations from CPA/imine complexes

S41. *R*-TRIP/1

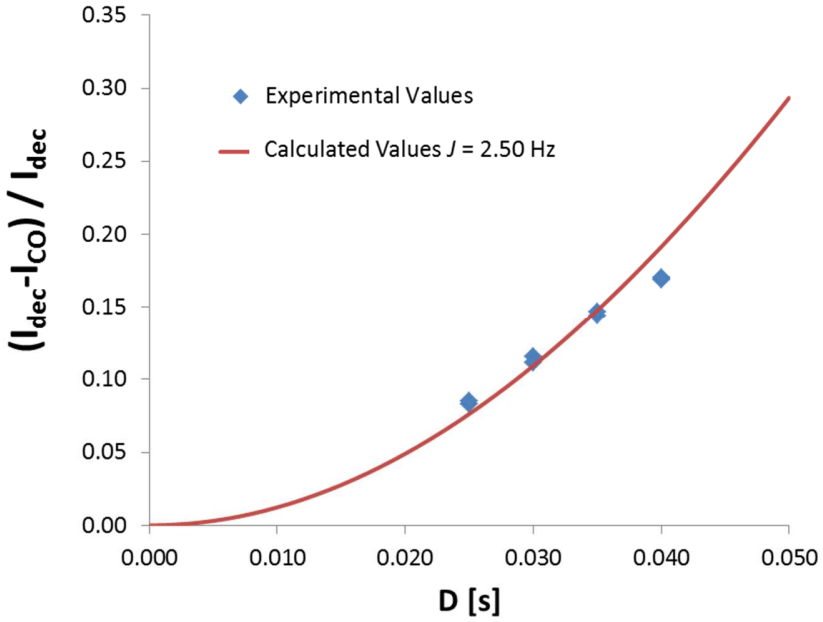

$^{2h}J_{PH}$ Attenuation of *R*-TRIP/1

D[s]		I_{co} [abs]	I_{dec} [abs]	$^{2h}J_{PH}$ [Hz]	$(I_{dec}-I_{co})/I_{dec}$
E/Z	0.025	1412142	1539977	2.61	0.083
	0.025	2330718	2546381	2.64	0.085
	0.030	1058914	1197552	2.58	0.116
	0.030	1872330	2107142	2.53	0.111
	0.035	692911	809663	2.47	0.144
	0.035	1297707	1520186	2.49	0.146
	0.040	452719	544445	2.34	0.168
	0.040	898991	1083317	2.36	0.170

Fit	±
2.50	0.10

S42. *R*-TRIP/2

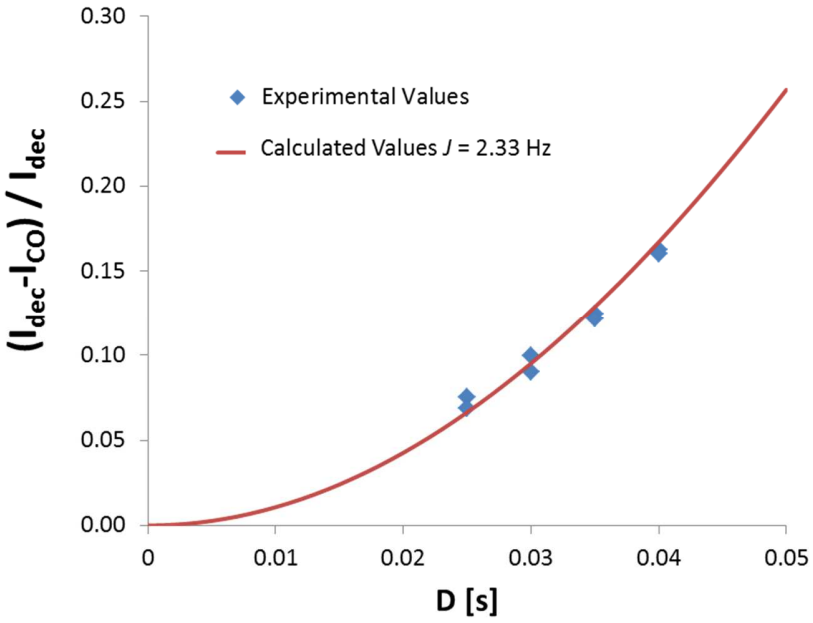

$^{2h}J_{PH}$ Attenuation of *R*-TRIP/2

D[s]		I_{co} [abs]	I_{dec} [abs]	$^{2h}J_{PH}$ [Hz]	$(I_{dec}-I_{co})/I_{dec}$
E/Z	0.025	607105	656503	2.49	0.075
	0.025	964068	1035393	2.38	0.069
	0.030	359275	398931	2.39	0.099
	0.030	610280	670766	2.27	0.090
	0.035	210773	240821	2.30	0.125
	0.035	380331	433097	2.27	0.122
	0.040	121142	144624	2.30	0.162
	0.040	234086	278674	2.28	0.160

Fit	±
2.33	0.07

S43. *R*-TRIP/3

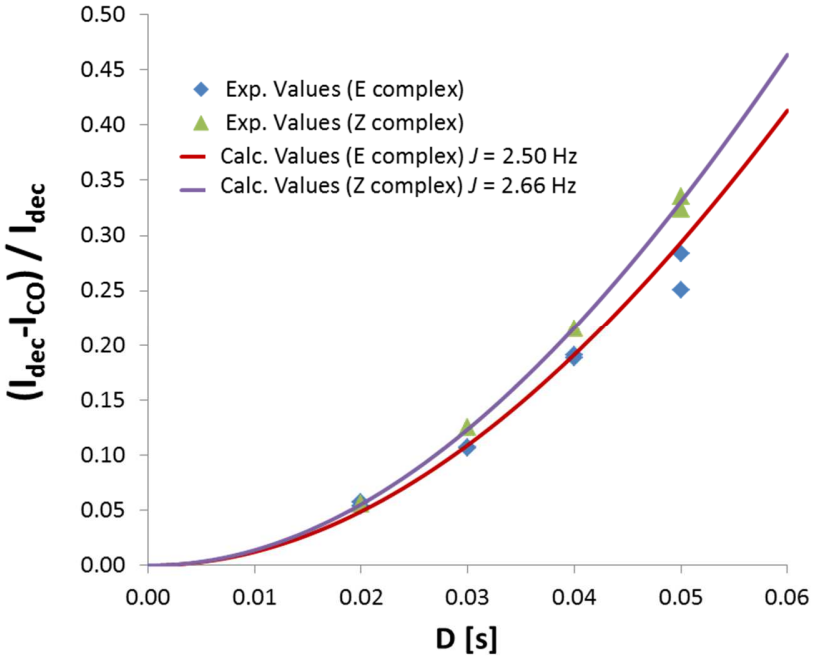
0.50
0.45
0.40
0.35
0.30
0.25
0.20
0.15
0.10
0.05
0.00
0.00
0.01
0.02
0.03
0.04
0.05
0.06
D [s]
(Idec-ICO) / Idec
Exp. Values (E complex)
Exp. Values (Z complex)
Calc. Values (E complex) J = 2.50 Hz
Calc. Values (Z complex) J = 2.66 Hz

D[s]		I_{co} [abs]	I_{dec} [abs]	$^{2h}J_{PH}$ [Hz]	$(I_{dec}-I_{co})/I_{dec}$
E	0.02	666101	704073	2.63	0.054
	0.02	948083	1005884	2.71	0.057
	0.03	490385	549078	2.48	0.107
	0.03	765762	857191	2.47	0.107
	0.04	646971	799277	2.50	0.191
	0.04	1119535	1378734	2.48	0.188
	0.05	225019	314266	2.46	0.284
	0.05	418306	558076	2.30	0.250
Z	0.02	834900	883784	2.66	0.055
	0.02	1362257	1441933	2.66	0.055
	0.03	860790	983529	2.68	0.125
	0.03	1652811	1889930	2.69	0.125
	0.04	1594589	2031017	2.66	0.215
	0.04	3616995	4607243	2.66	0.215
	0.05	684056	1028707	2.68	0.335
	0.05	1876457	2775716	2.64	0.324

	Fit	±
E	2.50	0.12
Z	2.66	0.02

S44. *R*-TRIP/4

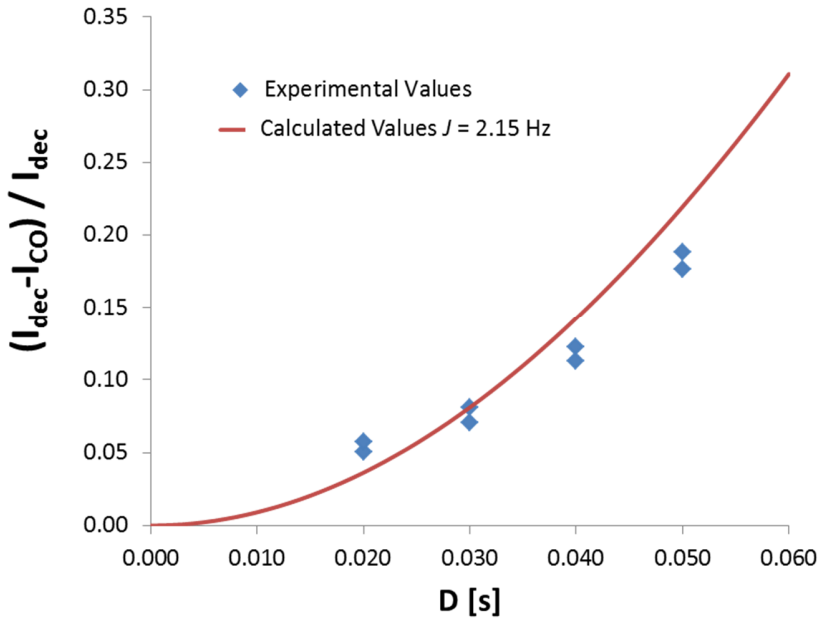

$^{2h}J_{PH}$ Attenuation of *R*-TRIP/4

D[s]		I_{co} [abs]	I_{dec} [abs]	$^{2h}J_{PH}$ [Hz]	$(I_{dec}-I_{co})/I_{dec}$
E/Z	0.020	965083	1016359	2.54	0.050
	0.020	1370330	1453895	2.71	0.057
	0.030	349745	380432	2.15	0.081
	0.030	573736	617203	2.00	0.070
	0.040	260665	297031	1.99	0.122
	0.040	483289	544502	1.90	0.112
	0.050	96332	116983	1.92	0.177
	0.050	207877	256028	1.98	0.188

Fit	±
2.15	0.29

S45. *R*-TRIP/5

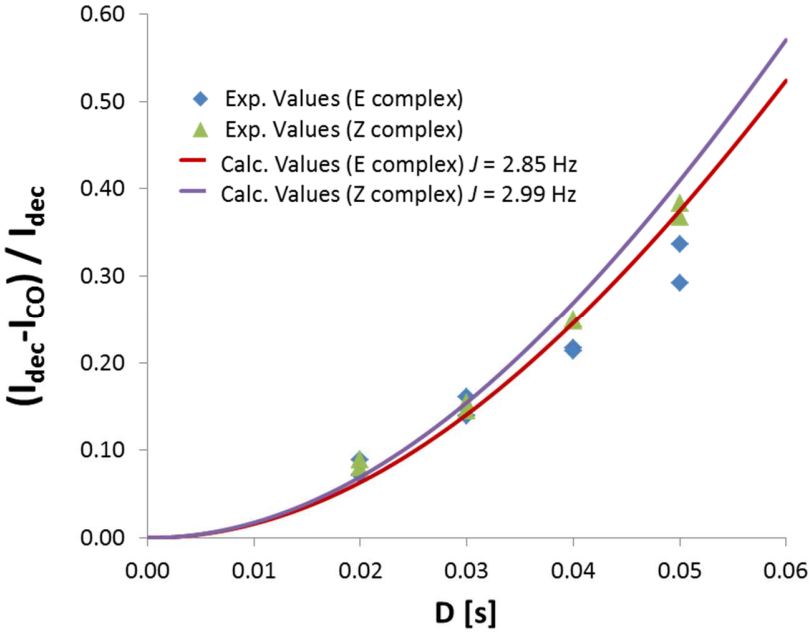
0.60
0.50
0.40
0.30
0.20
0.10
0.00
0.00
0.01
0.02
0.03
0.04
0.05
0.06
D [s]
(Idec-ICO) / Idec
Exp. Values (E complex)
Exp. Values (Z complex)
Calc. Values (E complex) J = 2.85 Hz
Calc. Values (Z complex) J = 2.99 Hz

D[s]		I_{co} [abs]	I_{dec} [abs]	$^{2h}J_{PH}$ [Hz]	$(I_{dec}-I_{co})/I_{dec}$
E	0.02	285017	313012	3.39	0.089
	0.02	413255	445395	3.04	0.072
	0.03	107315	127798	3.05	0.160
	0.03	177044	205574	2.83	0.139
	0.04	33739	43064	2.67	0.217
	0.04	60428	76809	2.65	0.213
	0.05	9470	13371	2.49	0.292
	0.05	17538	26425	2.69	0.336
Z	0.02	302130	328407	3.20	0.080
	0.02	513165	563613	3.39	0.090
	0.03	196318	229629	2.89	0.145
	0.03	392174	463530	2.98	0.154
	0.04	97022	128961	2.86	0.248
	0.04	234836	313188	2.88	0.250
	0.05	41947	67956	2.88	0.383
	0.05	122748	194053	2.82	0.367

	Fit	±
E	2.85	0.29
Z	2.99	0.20

S46. *R*-TRIP/9

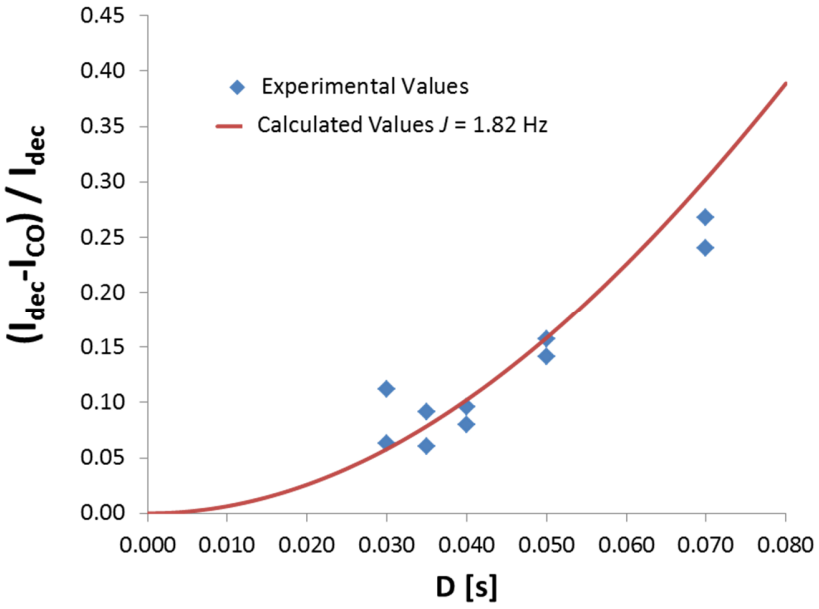

$^{2h}J_{PH}$ Attenuation of *R*-TRIP/9

D[s]		I_{co} [abs]	I_{dec} [abs]	$^{2h}J_{PH}$ [Hz]	$(I_{dec}-I_{co})/I_{dec}$
Z	0.030	3315308	3731718	2.53	0.112
	0.030	3952066	4219802	1.90	0.063
	0.035	2933694	3229334	1.96	0.092
	0.035	3216122	3423745	1.59	0.061
	0.040	3723118	4118155	1.76	0.096
	0.040	3932813	4273242	1.60	0.080
	0.050	1878215	2229088	1.81	0.157
	0.050	2042217	2377479	1.71	0.141
	0.070	407305	556201	1.70	0.268
	0.070	469877	618711	1.61	0.241

Fit	±
1.82	0.27

S47. *R*-TRIP/11

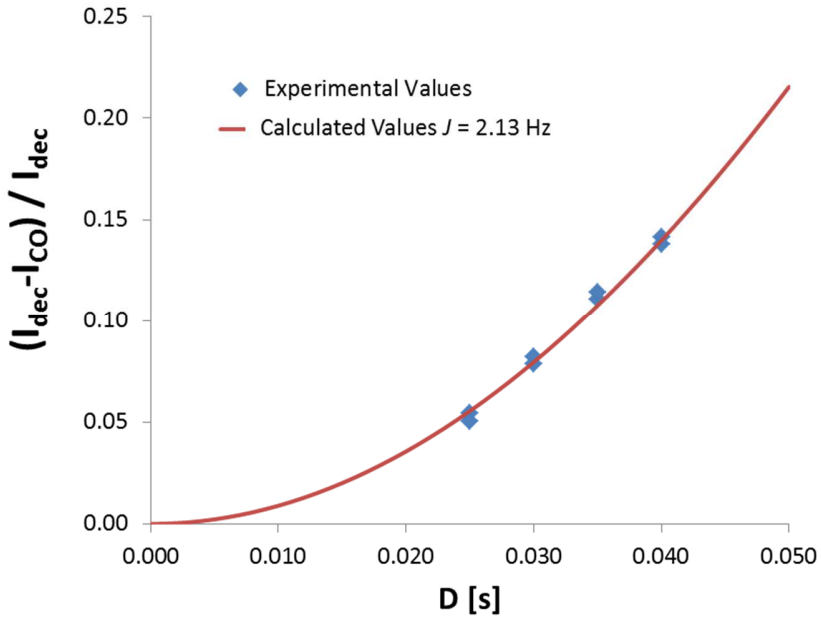

$^{2h}J_{PH}$ Attenuation of *R*-TRIP/11

D[s]	I_{co} [abs]	I_{dec} [abs]	$^{2h}J_{PH}$ [Hz]	$(I_{dec}-I_{co})/I_{dec}$
0.025	775434	820090	2.11	0.054
0.025	912204	960647	2.03	0.050
0.030	554835	602280	2.12	0.079
0.030	665524	724877	2.16	0.082
0.035	391190	439797	2.16	0.111
0.035	475487	536762	2.19	0.114
0.040	273016	316750	2.12	0.138
0.040	342671	398969	2.14	0.141

Fit	±
2.13	0.05

S48. *R*-TRIP/12

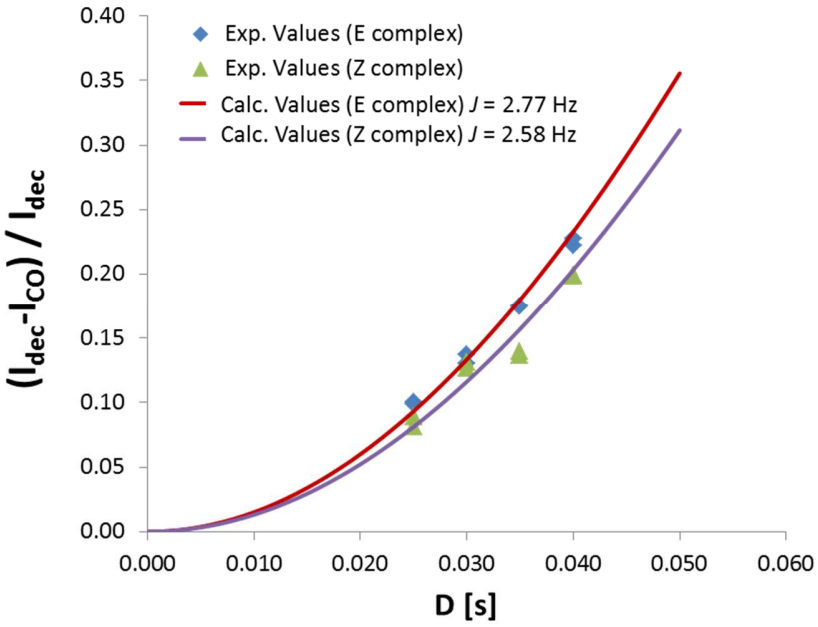
Exp. Values (E complex)
Exp. Values (Z complex)
Calc. Values (E complex) J = 2.77 Hz
Calc. Values (Z complex) J = 2.58 Hz
(Idec-ICO) / Idec
D [s]
0.40
0.35
0.30
0.25
0.20
0.15
0.10
0.05
0.00
0.000
0.010
0.020
0.030
0.040
0.050
0.060

D[s]		I_{co} [abs]	I_{dec} [abs]	$^{2h}J_{PH}$ [Hz]	$(I_{dec}-I_{co})/I_{dec}$
E	0.035	1216421	1474483	2.73	0.175
	0.035	1969510	2385655	2.73	0.174
	0.040	930536	1195842	2.70	0.222
	0.040	1572898	2035990	2.74	0.227
	0.030	1625362	1869287	2.74	0.130
	0.030	2496631	2894329	2.81	0.137
	0.025	1650429	1833873	2.87	0.100
	0.025	2442804	2709466	2.85	0.098
Z	0.035	189324	219160	2.40	0.136
	0.035	285801	332039	2.43	0.139
	0.040	134102	167533	2.56	0.200
	0.040	209894	261932	2.55	0.199
	0.030	264190	304120	2.75	0.131
	0.030	382870	438302	2.70	0.126
	0.025	292024	320459	2.70	0.089
	0.025	409170	445220	2.58	0.081

	Fit	±
E	2.77	0.06
Z	2.58	0.13

S49. *R*-TRIFP/3

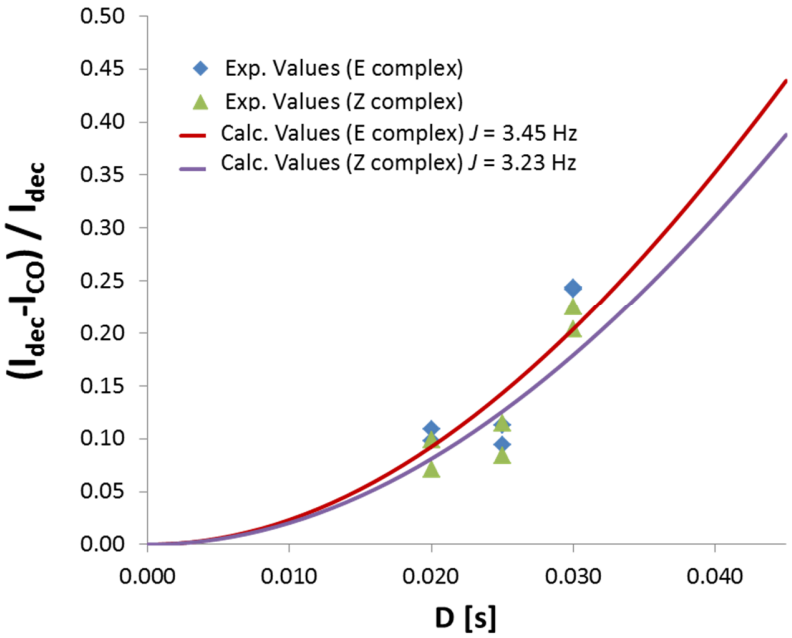
0.50
0.45
0.40
0.35
0.30
0.25
0.20
0.15
0.10
0.05
0.00
0.000
0.010
0.020
0.030
0.040
D [s]
(Idec-ICO) / Idec
Exp. Values (E complex)
Exp. Values (Z complex)
Calc. Values (E complex) J = 3.45 Hz
Calc. Values (Z complex) J = 3.23 Hz

D[s]		I_{co} [abs]	I_{dec} [abs]	$^{2h}J_{PH}$ [Hz]	$(I_{dec}-I_{co})/I_{dec}$
E	0.030	11811	15579	3.77	0.242
E	0.030	19050	25180	3.78	0.243
E	0.020	38717	42917	3.55	0.098
E	0.020	49144	55179	3.76	0.109
E	0.025	19939	22014	2.79	0.094
E	0.025	27489	30980	3.05	0.113
Z	0.030	15853	19903	3.44	0.203
Z	0.030	27226	35149	3.63	0.225
Z	0.020	49889	53677	3.01	0.071
Z	0.020	68193	75660	3.57	0.099
Z	0.025	24050	26264	2.63	0.084
Z	0.025	36299	40989	3.08	0.114

	Fit	±
E	3.45	0.43
Z	3.23	0.39

S50. *R*-TRIFP/5

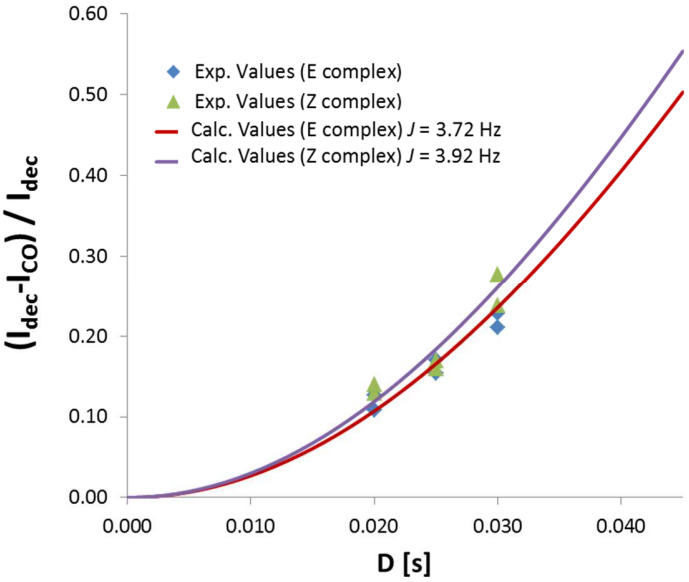

D[s]		I_{co} [abs]	I_{dec} [abs]	$^{2h}J_{PH}$ [Hz]	$(I_{dec}-I_{co})/I_{dec}$
E	0.030	88242	111750	3.50	0.210
	0.030	53652	69508	3.66	0.228
	0.025	126875	152948	3.77	0.170
	0.025	192144	227118	3.58	0.154
	0.020	145622	163384	3.75	0.109
	0.020	204787	234405	4.04	0.126
Z	0.030	6083	7975	3.73	0.237
	0.030	11024	15251	4.05	0.277
	0.025	17131	20373	3.64	0.159
	0.025	27837	33507	3.76	0.169
	0.020	21261	24412	4.09	0.129
	0.020	33441	38873	4.26	0.140

	Fit	±
E	3.72	0.19
Z	3.92	0.24

S51. *R*-TiPSY/1

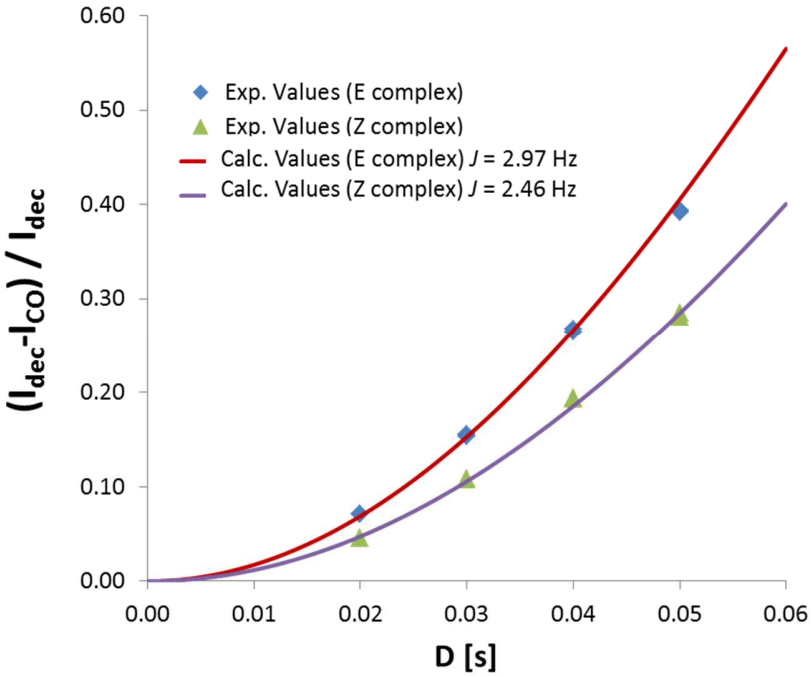
0.60
0.50
0.40
0.30
0.20
0.10
0.00
0.00
0.01
0.02
0.03
0.04
0.05
0.06
D [s]
(Idec-ICO) / Idec
Exp. Values (E complex)
Exp. Values (Z complex)
Calc. Values (E complex) J = 2.97 Hz
Calc. Values (Z complex) J = 2.46 Hz

D[s]		I_{co} [abs]	I_{dec} [abs]	$^{2h}J_{PH}$ [Hz]	$(I_{dec}-I_{co})/I_{dec}$
E	0.02	1002276	1078913	3.02	0.071
	0.02	1582339	1703373	3.02	0.071
	0.03	2721414	3212757	2.97	0.153
	0.03	4918965	5820503	2.99	0.155
	0.04	1170278	1590327	2.96	0.264
	0.04	2400846	3275711	2.98	0.267
	0.05	476256	783439	2.92	0.392
	0.05	1097076	1809137	2.93	0.394
Z	0.02	861880	902487	2.40	0.045
	0.02	1525895	1597538	2.39	0.045
	0.03	2939832	3293495	2.48	0.107
	0.03	6160007	6906070	2.49	0.108
	0.04	1608952	1992666	2.51	0.193
	0.04	4006271	4969963	2.52	0.194
	0.05	856974	1198656	2.46	0.285
	0.05	2527759	3514091	2.44	0.281

	Fit	±
E	2.97	0.04
Z	2.46	0.05

S52. *R*-TiPSY/3

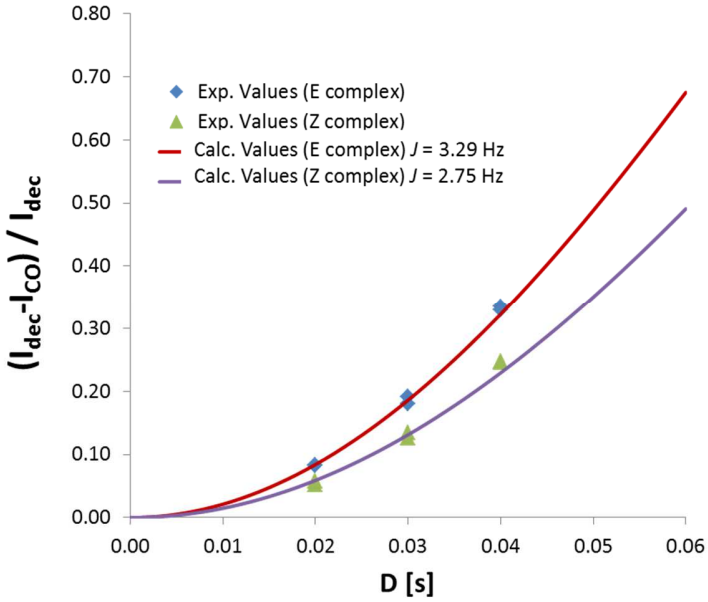

	D[s]	I_{co} [abs]	I_{dec} [abs]	$^{2h}J_{PH}$ [Hz]	$(I_{dec}-I_{co})/I_{dec}$
E	0.02	654107	712947	3.26	0.083
	0.02	1120832	1221209	3.25	0.082
	0.03	218701	270707	3.34	0.192
	0.03	452953	552350	3.23	0.180
	0.04	69952	105312	3.36	0.336
	0.04	169934	253393	3.33	0.329
Z	0.02	1945673	2053458	2.59	0.052
	0.02	4267833	4529324	2.72	0.058
	0.03	1082311	1250315	2.78	0.134
	0.03	2947337	3369936	2.69	0.125
	0.04	566127	752192	2.86	0.247
	0.04	1895039	2514229	2.85	0.246

	Fit	±
E	3.29	0.05
Z	2.75	0.10

S53. *R*-TiPSY/4

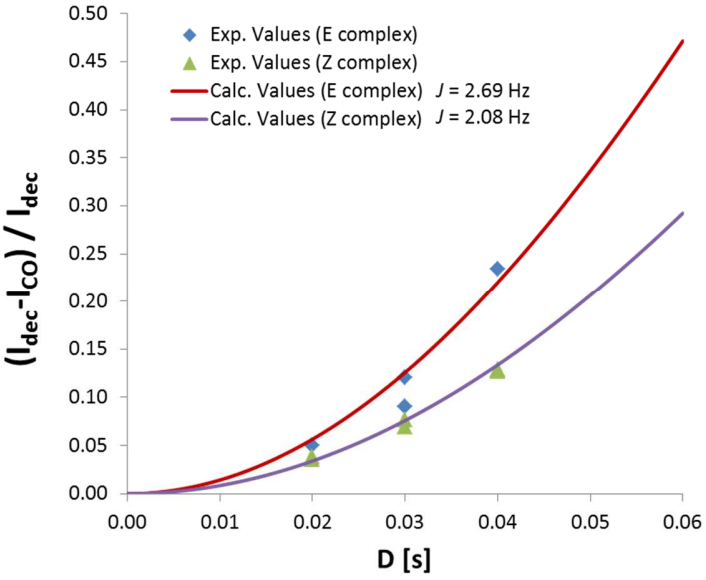

D[s]		I_{co} [abs]	I_{dec} [abs]	$^{2h}J_{PH}$ [Hz]	$(I_{dec}-I_{co})/I_{dec}$
E	0.02	385680	405907	2.52	0.050
	0.02	617648	628953	-	-
	0.03	119275	135652	2.63	0.121
	0.03	218464	240172	2.27	0.090
	0.04	32076	41888	2.78	0.234
	0.04	67786	81217	-	-
Z	0.02	1479253	1538106	2.21	0.038
	0.02	2956441	3066386	2.14	0.036
	0.03	891944	965530	2.08	0.076
	0.03	2170216	2331692	1.99	0.069
	0.04	522679	600251	2.05	0.129
	0.04	1498409	1716109	2.03	0.127

	Fit	±
E	2.69	0.32
Z	2.08	0.07

S54. *R*-TiPSY/5

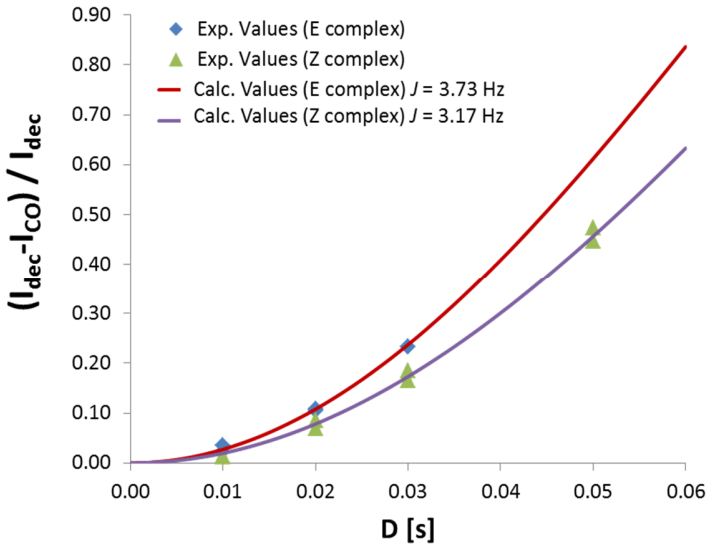

	D[s]	I_{co} [abs]	I_{dec} [abs]	$^{2h}J_{PH}$ [Hz]	$(I_{dec}-I_{co})/I_{dec}$
E	0.02	386103	430845	3.66	0.104
	0.02	174632	196023	3.75	0.109
	0.03	113468	147888	3.69	0.233
	0.03	39423	51386	3.69	0.233
	0.01	185974	190253	3.38	0.022
	0.01	138428	143408	4.21	0.035
Z	0.02	1597354	1716619	2.98	0.069
	0.02	443607	484899	3.31	0.085
	0.03	987802	1184222	3.10	0.166
	0.03	187074	229538	3.28	0.185
	0.05	307114	554502	3.13	0.446
	0.05	28472	54126	3.24	0.474
	0.01	708681	717275	2.47	0.012
	0.01	407168	412997	2.68	0.014

	Fit	±
E	3.73	0.04
Z	3.17	0.12

S55. *R*-TiPSY/6

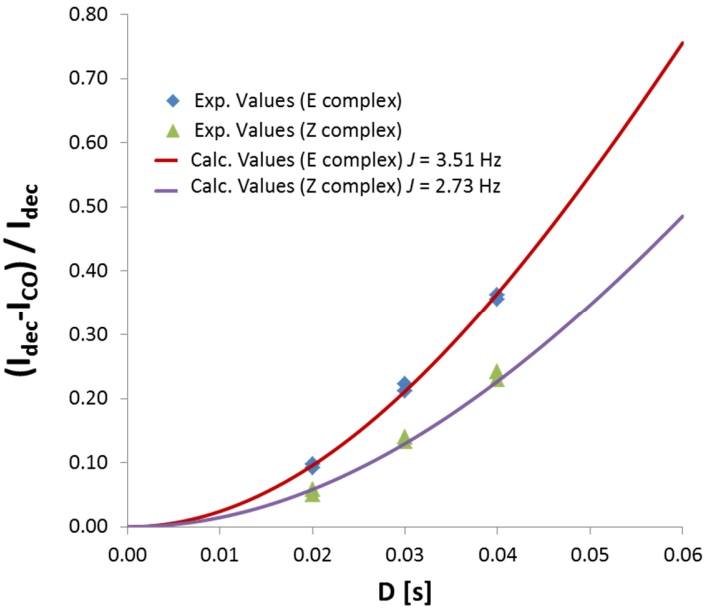

D[s]		I_{co} [abs]	I_{dec} [abs]	$^{2h}J_{PH}$ [Hz]	$(I_{dec}-I_{co})/I_{dec}$
E	0.02	549785	609635	3.56	0.098
	0.02	965872	1063734	3.44	0.092
	0.03	164585	211555	3.60	0.222
	0.03	351329	445367	3.51	0.211
	0.04	46281	72557	3.50	0.362
	0.04	118273	183472	3.46	0.355
Z	0.02	1175667	1247399	2.71	0.058
	0.02	2761496	2906166	2.52	0.050
	0.03	583650	678165	2.83	0.139
	0.03	1754826	2022302	2.76	0.132
	0.04	282068	371853	2.82	0.241
	0.04	1079673	1401306	2.75	0.230

	Fit	±
E	3.51	0.06
Z	2.73	0.11

S56. *R*-TiPSY/7

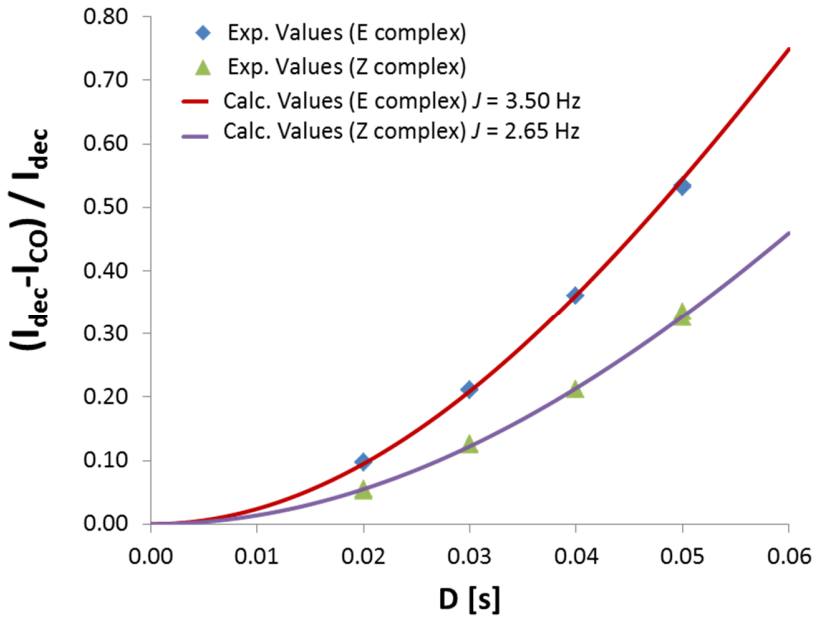
0.80
0.70
0.60
0.50
0.40
0.30
0.20
0.10
0.00
0.00
0.01
0.02
0.03
0.04
0.05
0.06
D [s]
(Idec-ICO) / Idec
Exp. Values (E complex)
Exp. Values (Z complex)
Calc. Values (E complex) J = 3.50 Hz
Calc. Values (Z complex) J = 2.65 Hz

D[s]		I_{co} [abs]	I_{dec} [abs]	$^{2h}J_{PH}$ [Hz]	$(I_{dec}-I_{co})/I_{dec}$
E	0.02	2888053	3198870	3.54	0.097
	0.02	4824730	5338785	3.52	0.096
	0.03	1375187	1742690	3.51	0.211
	0.03	2692556	3413081	3.51	0.211
	0.04	605314	945990	3.49	0.360
	0.04	1381508	2159425	3.49	0.360
	0.05	236286	504473	3.45	0.532
	0.05	621629	1335725	3.46	0.535
Z	0.02	440455	466380	2.67	0.056
	0.02	832174	877785	2.58	0.052
	0.03	207786	237830	2.70	0.126
	0.03	478419	546433	2.68	0.124
	0.04	93538	118759	2.64	0.212
	0.04	262815	333432	2.64	0.212
	0.05	39514	59453	2.69	0.335
	0.05	136712	202650	2.64	0.325

	Fit	±
E	3.50	0.03
Z	2.65	0.04

S57. *R*-TiPSY/8

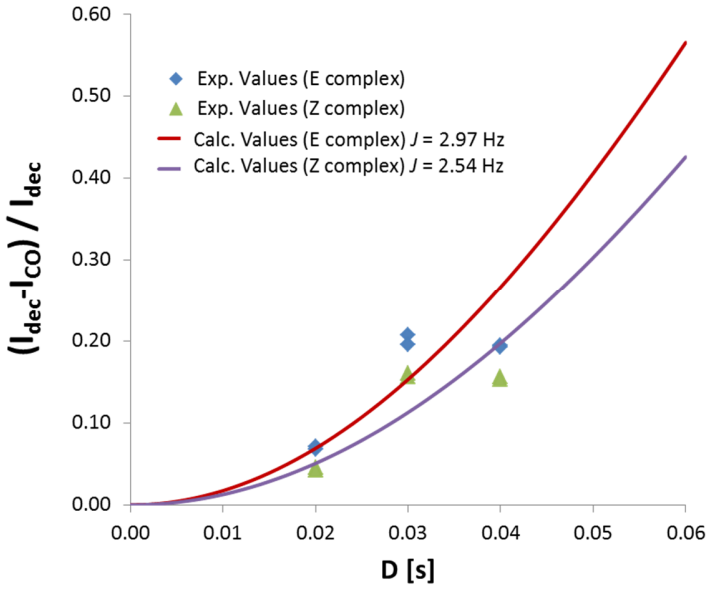

D[s]		I_{co} [abs]	I_{dec} [abs]	$^{2h}J_{PH}$ [Hz]	$(I_{dec}-I_{co})/I_{dec}$
E	0.02	653640	701021	2.94	0.068
	0.02	1041647	1121095	3.01	0.071
	0.03	225245	284210	3.48	0.207
	0.03	423752	526748	3.37	0.196
	0.04	228974	284219	2.52	0.194
	0.04	426240	527864	2.51	0.193
Z	0.02	1671305	1751673	2.42	0.046
	0.02	3691295	3852524	2.31	0.042
	0.03	873092	1039387	3.04	0.160
	0.03	2401793	2845908	3.00	0.156
	0.04	876245	1038750	2.26	0.156
	0.04	2408573	2845080	2.23	0.153

	Fit	±
E	2.97	0.41
Z	2.54	0.38

4.8.27 $^{3h}J_{PN}$ measured attenuations from CPA/imine complexes

S58. *R*-TRIP/1

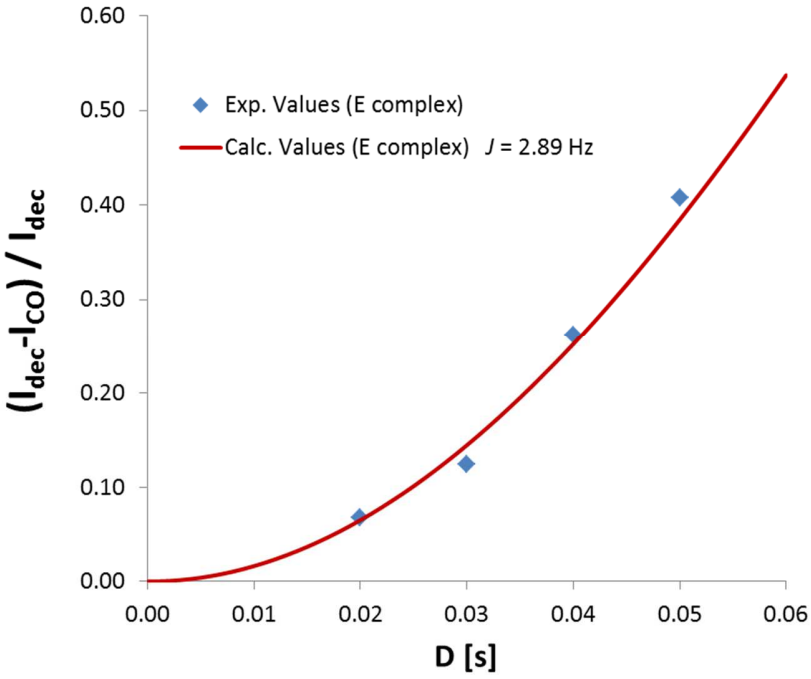

$^{3h}J_{PN}$ Attenuation of *R*-TRIP/1

D[s]		I_{co} [rel]	I_{dec} [rel]	$^{3h}J_{PN}$ [Hz]	$(I_{dec}-I_{co})/I_{dec}$
E	0.02	93.21	100	2.95	0.068
	0.03	87.52	100	2.68	0.125
	0.04	73.81	100	2.95	0.262
	0.05	59.27	100	2.98	0.407

	Fit	±
E	2.89	0.14

S59. *R*-TRIP/2

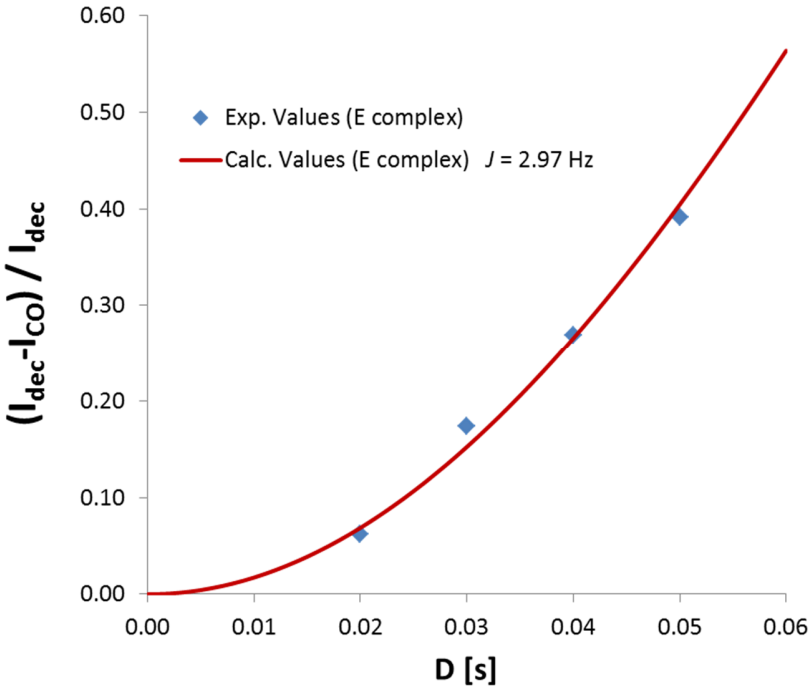

$^{3h}J_{PN}$ Attenuation of *R*-TRIP/2

D[s]		I_{co} [rel]	I_{dec} [rel]	$^{3h}J_{PN}$ [Hz]	$(I_{dec}-I_{co})/I_{dec}$
E	0.02	93.84	100	2.81	0.062
	0.03	82.56	100	3.18	0.174
	0.04	73.06	100	2.99	0.269
	0.05	60.89	100	2.92	0.391

	Fit	±
E	2.97	0.16

S60. *R*-TRIP/3

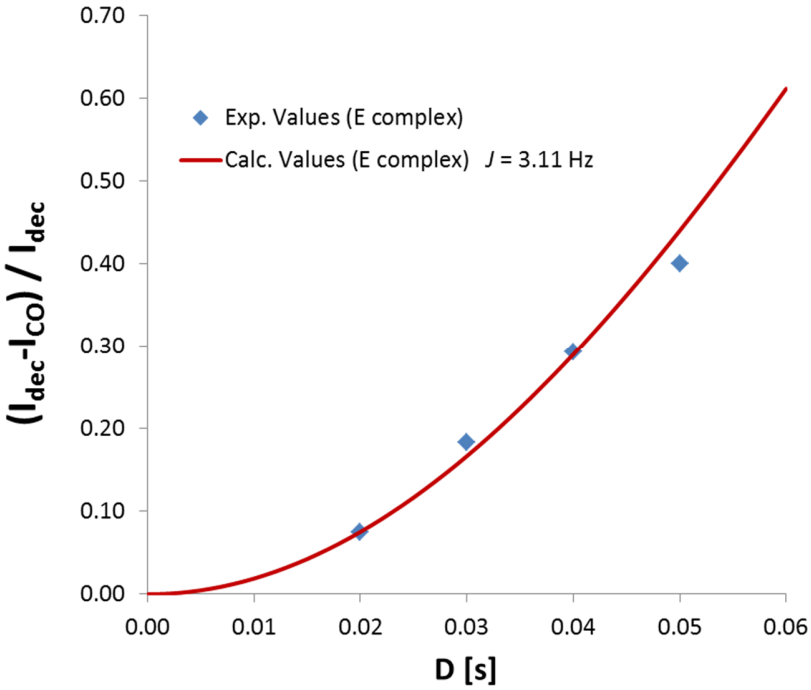

D[s]		Ico [rel]	Idec [rel]	$^{3h}J_{PN}$ [Hz]	(Idec-Ico)/Idec
E	0.02	100	108.14	3.11	0.075
E	0.03	100	122.38	3.26	0.183
E	0.04	100	141.38	3.12	0.293
E	0.05	100	166.92	2.96	0.401

	Fit	±
E	3.11	0.12

S61. *R*-TRIP/5

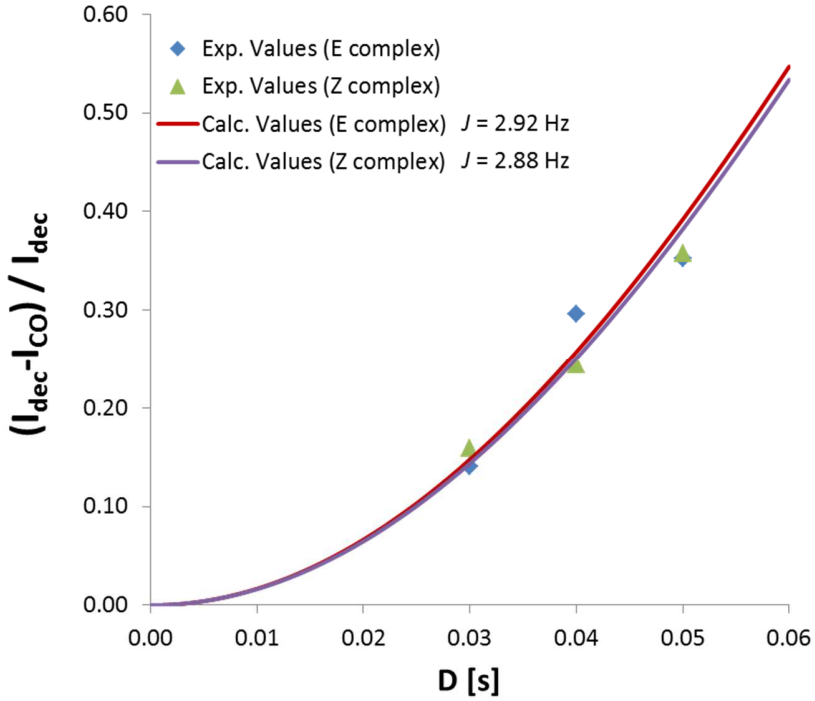

D[s]		I_{co} [rel]	I_{dec} [rel]	$^{3h}J_{PN}$ [Hz]	$(I_{dec}-I_{co})/I_{dec}$
E	0.03	75.41	87.75	2.85	0.141
	0.04	43.66	62.07	3.15	0.297
	0.05	31.93	49.33	2.76	0.353
Z	0.03	84.08	100	3.03	0.159
	0.04	75.65	100	2.84	0.244
	0.05	64.21	100	2.78	0.358

	Fit	±
E	2.92	0.20
Z	2.88	0.13

S62. *R*-TRIP/9

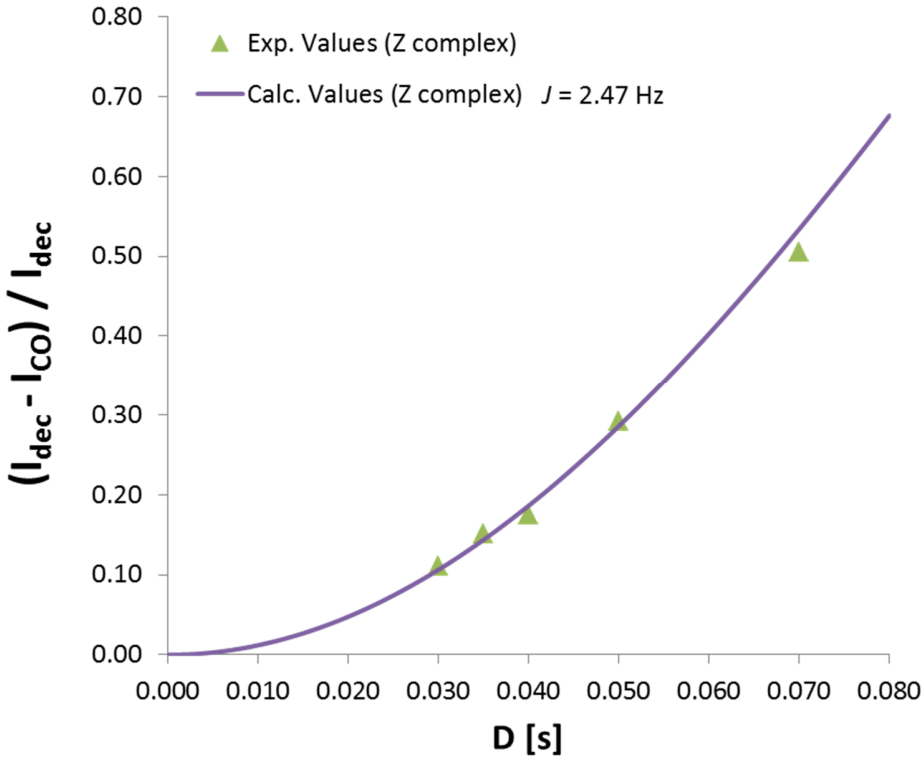

$^{3h}J_{PN}$ Attenuation of *R*-TRIP/9

	D[s]	I_{co} [rel]	I_{dec} [rel]	$^{3h}J_{PN}$ [Hz]	$(I_{dec}-I_{co})/I_{dec}$
Z1/Z2	0.030	88.86	100	2.53	0.111
	0.035	84.90	100	2.53	0.151
	0.040	82.47	100	2.39	0.175
	0.050	70.79	100	2.50	0.292
	0.070	49.47	100	2.39	0.505

	Fit	±
Z	2.47	0.07

S63. *R*-TRIP/11

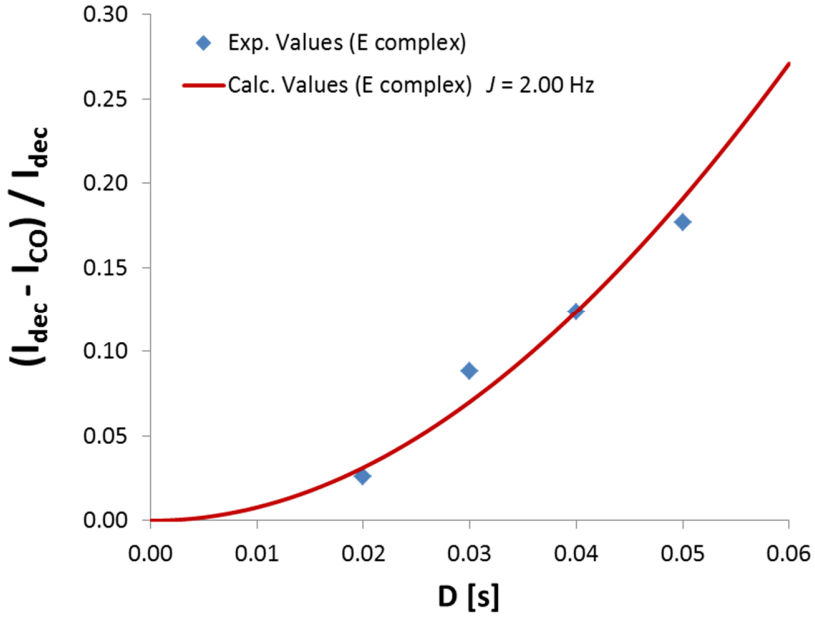

$^{3h}J_{PN}$ Attenuation of *R*-TRIP/11

D[s]		I_{co} [rel]	I_{dec} [rel]	$^{3h}J_{PN}$ [Hz]	$(I_{dec}-I_{co})/I_{dec}$
E/Z	0.02	97.42	100	1.81	0.026
	0.03	91.15	100	2.25	0.088
	0.04	87.63	100	2.00	0.124
	0.05	82.34	100	1.92	0.177

	Fit	±
E/Z	2.00	0.19

S64. *R*-TRIP·12

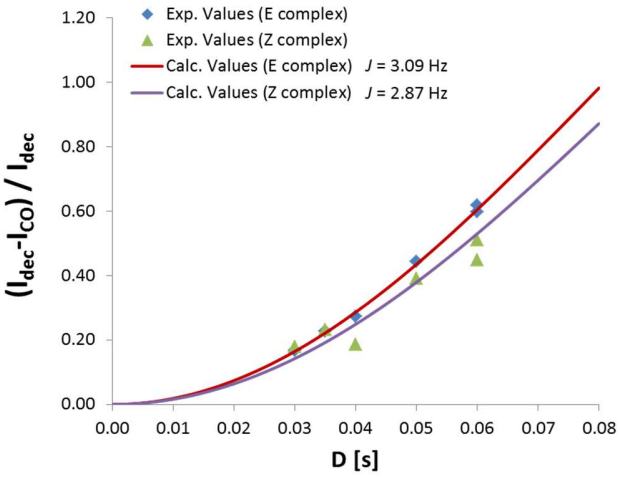

$^{3h}J_{PN}$ Attenuation of *R*-TRIP/12

D[s]		I_{co} [rel]	I_{dec} [rel]	$^{3h}J_{PN}$ [Hz]	$(I_{dec}-I_{co})/I_{dec}$
E	0.05	55.73	100	3.12	0.443
	0.04	72.74	100	3.01	0.273
	0.03	83.17	100	3.12	0.168
	0.06	38.25	100	3.13	0.618
	0.06	40.30	100	3.07	0.597
	0.035	77.28	100	3.13	0.227
Z	0.05	9.31	15.30	2.92	0.392
	0.04	13.92	17.08	2.46	0.185
	0.03	15.42	18.80	3.23	0.180
	0.06	6.20	12.68	2.81	0.511
	0.06	7.57	13.72	2.62	0.448
	0.035	14.59	19.02	3.17	0.233

	Fit	±
E	3.09	0.05
Z	2.87	0.30

S65. *R*-TRIFP/3

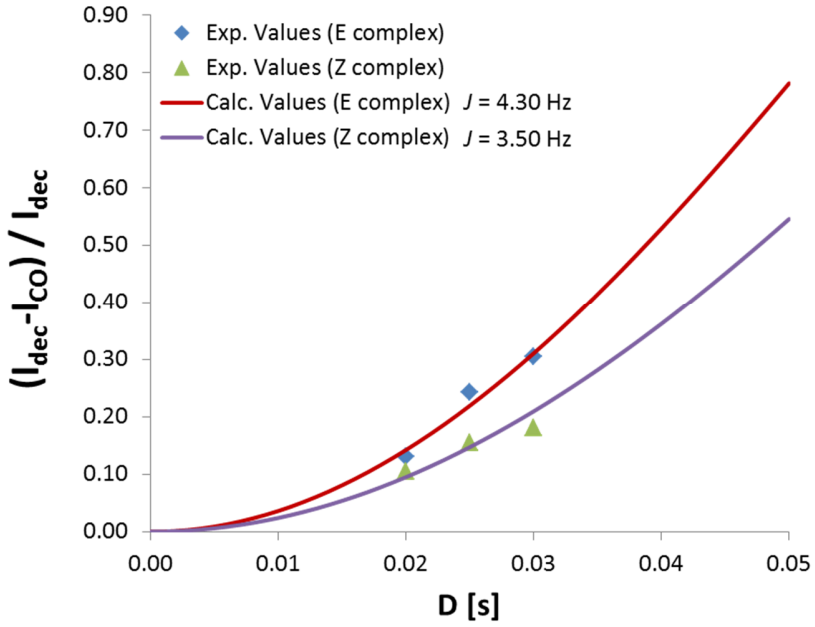

$^{3h}J_{PN}$ Attenuation of *R*-TRIFP/3

D[s]		I_{co} [rel]	I_{dec} [rel]	$^{3h}J_{PN}$ [Hz]	$(I_{dec}-I_{co})/I_{dec}$
E	0.03	62.81	90.45	4.26	0.306
	0.02	99.18	113.99	4.10	0.130
	0.03	85.50	112.85	4.53	0.242
Z	0.03	81.90	100	3.24	0.181
	0.02	89.57	100	3.67	0.104
	0.03	84.58	100	3.58	0.154

	Fit	±
E	4.30	0.21
Z	3.50	0.22

S66. *R*-TRIFP/5

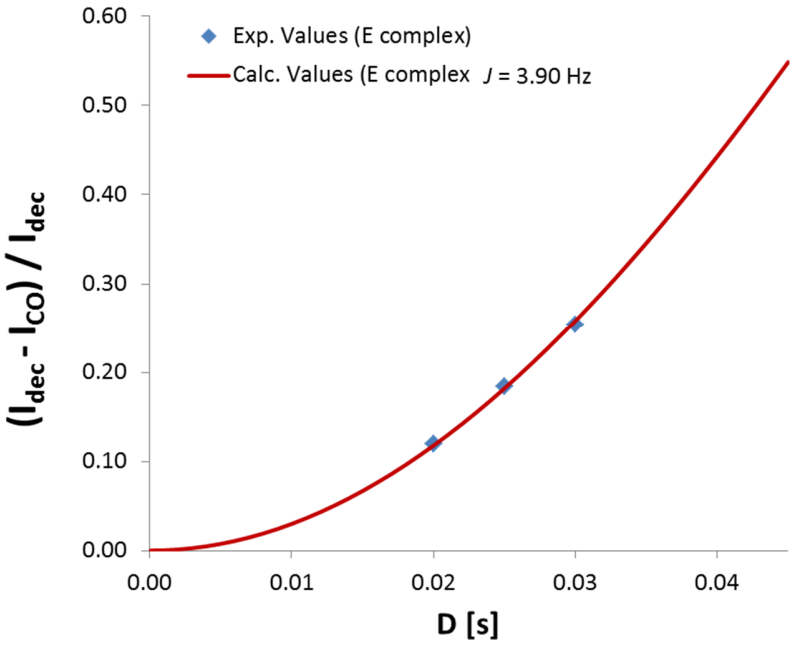

$^{3h}J_{PN}$ Attenuation of *R*-TRIFP/5

D[s]		I_{co} [rel]	I_{dec} [rel]	$^{3h}J_{PN}$ [Hz]	$(I_{dec}-I_{co})/I_{dec}$
E	0.02	88.10	100	3.92	0.119
	0.025	81.60	100	3.92	0.184
	0.03	74.64	100	3.86	0.254

	Fit	±
E	3.90	0.03

S67. *R*-TiPSY/1

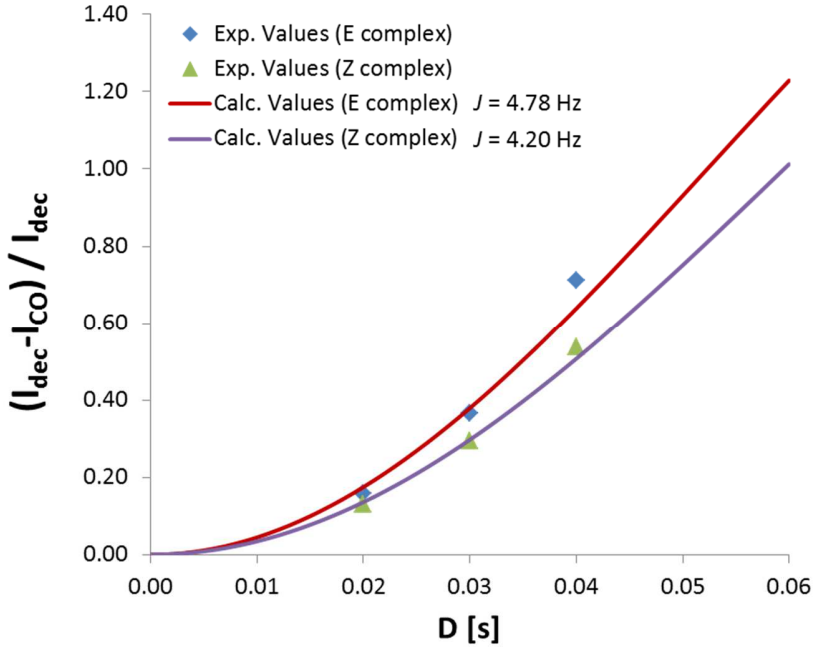

$^{3h}J_{PN}$ Attenuation of *R*-TiPSY/1

D[s]		I_{co} [rel]	I_{dec} [rel]	$^{3h}J_{PN}$ [Hz]	$(I_{dec}-I_{co})/I_{dec}$
E	0.02	84.10	100.02	4.55	0.159
	0.03	43.53	68.62	4.69	0.366
	0.04	31.61	109.65	5.09	0.712
Z	0.02	100.00	114.85	4.09	0.129
	0.03	70.67	100.00	4.17	0.293
	0.04	100.00	216.68	4.34	0.538

	Fit	±
E	4.78	0.28
Z	4.20	0.13

S68. *R*-TiPSY/3

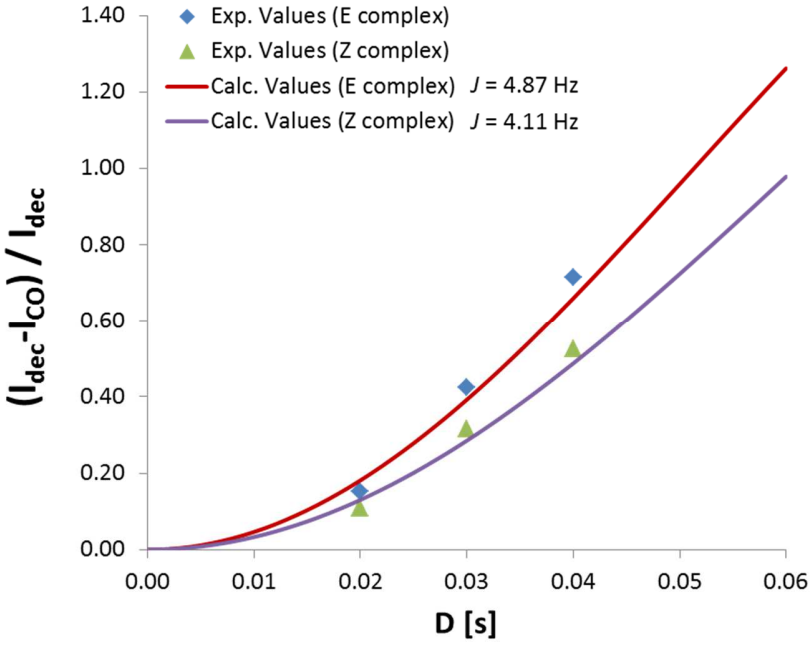

D[s]		I_{co} [rel]	I_{dec} [rel]	$^{3h}J_{PN}$ [Hz]	$(I_{dec}-I_{co})/I_{dec}$
E	0.02	19.28	22.74	4.45	0.152
	0.03	8.65	15.03	5.08	0.424
	0.04	2.04	7.13	5.10	0.714
Z	0.02	89.24	100.00	3.73	0.108
	0.03	68.41	100.00	4.34	0.316
	0.04	47.51	100.00	4.28	0.525

	Fit	±
E	4.87	0.37
Z	4.11	0.34

S69. *R*-TiPSY/4

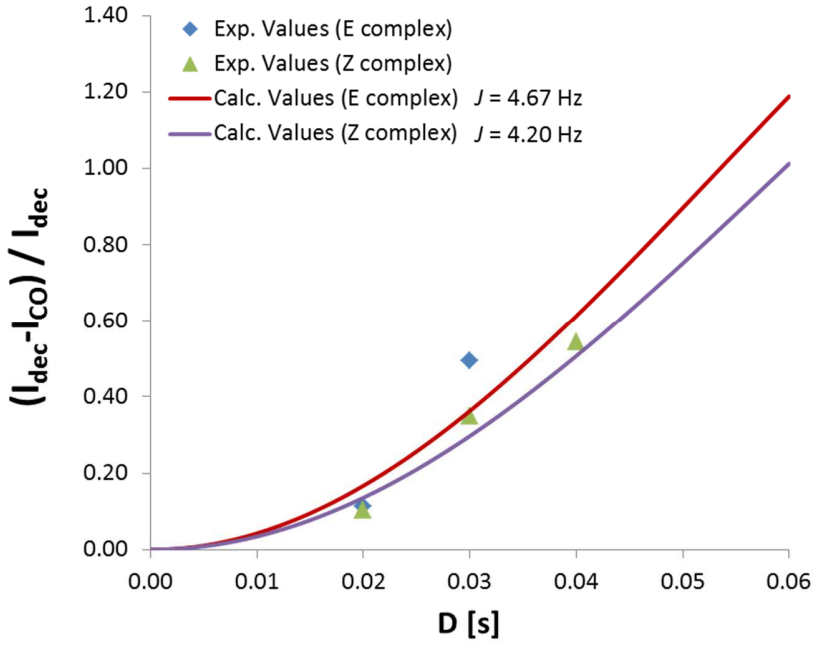

$^{3h}J_{PN}$ Attenuation of *R*-TiPSY/4

D[s]		I_{co} [rel]	I_{dec} [rel]	$^{3h}J_{PN}$ [Hz]	$(I_{dec}-I_{co})/I_{dec}$
E	0.02	16.27	18.35	3.83	0.113
	0.03	8.27	16.36	5.52	0.494
Z	0.02	89.59	100	3.66	0.104
	0.03	65.16	100	4.57	0.348
	0.04	45.72	100	4.36	0.543

	Fit	±
E	4.67	1.20
Z	4.20	0.47

S70. *R*-TiPSY/5

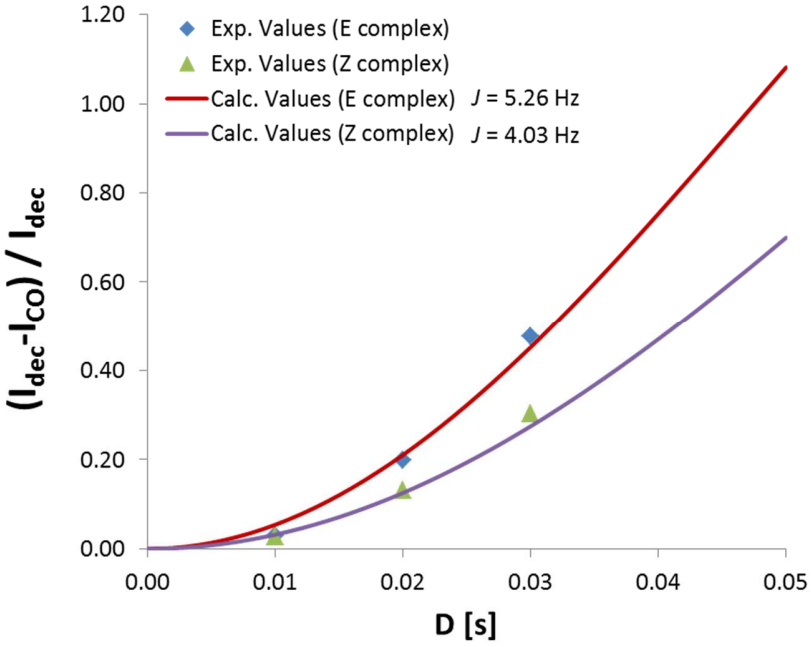

D[s]		I_{co} [rel]	I_{dec} [rel]	$^{3h}J_{PN}$ [Hz]	$(I_{dec}-I_{co})/I_{dec}$
E	0.02	15.97	19.92	5.10	0.198
	0.03	4.98	9.53	5.42	0.477
	0.01	18.35	18.91	3.88	0.030
Z	0.02	86.94	100	4.11	0.131
	0.03	69.77	100	4.24	0.302
	0.01	97.26	100	3.73	0.027

	Fit	±
E	5.26	0.22
Z	4.03	0.26

S71. *R*-TiPSY/6

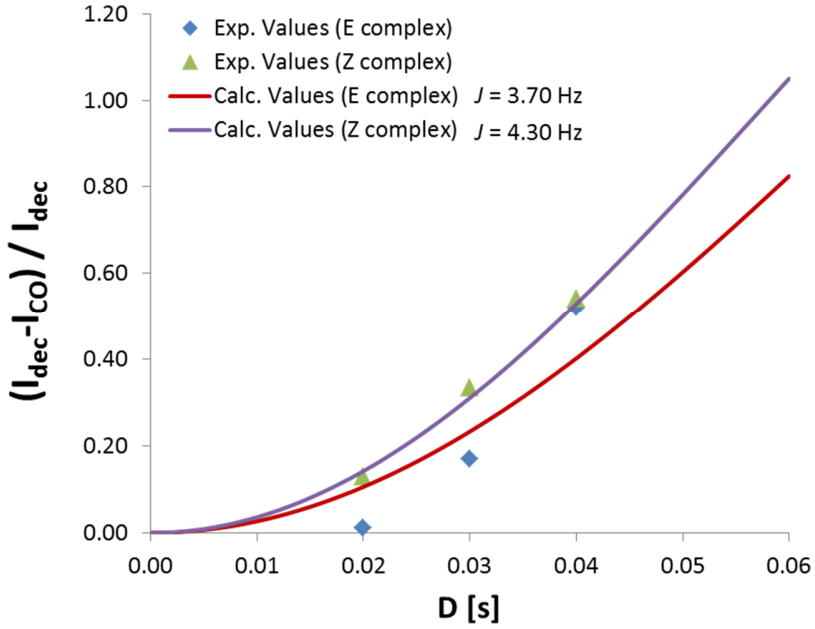

$^{3h}J_{PN}$ Attenuation of *R*-TiPSY/6

D[s]		I_{co} [rel]	I_{dec} [rel]	$^{3h}J_{PN}$ [Hz]	$(I_{dec}-I_{co})/I_{dec}$
E	0.02	3.57	3.61	1.22	0.012
	0.03	8.08	9.74	3.14	0.170
	0.04	1.83	3.82	4.26	0.521
Z	0.02	87.09	100	4.09	0.129
	0.03	66.74	100	4.46	0.333
	0.04	45.93	100	4.35	0.541

	Fit	±
E	3.70	0.80
Z	4.30	0.20

S72. *R*-TiPSY/7

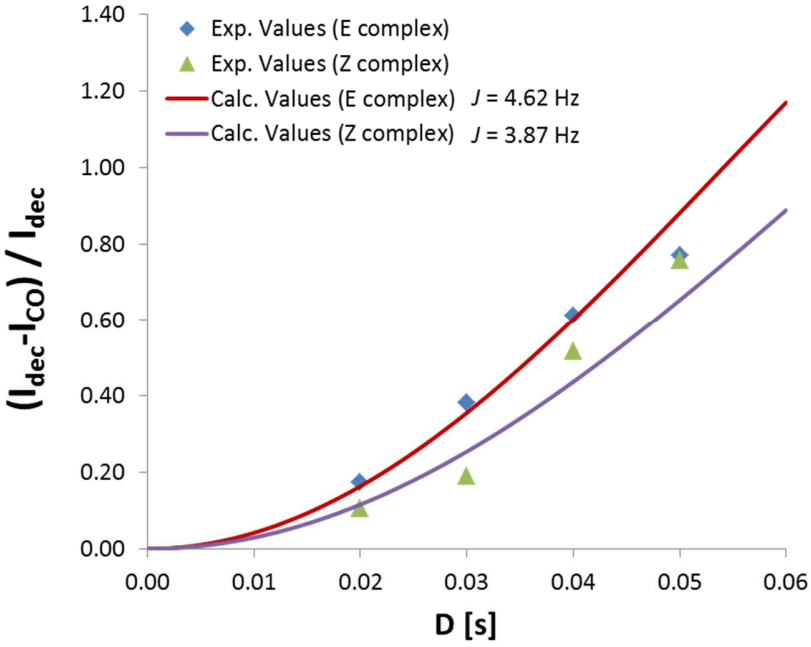

$^{3h}J_{PN}$ Attenuation of *R*-TiPSY/7

D[s]		I_{co} [rel]	I_{dec} [rel]	$^{3h}J_{PN}$ [Hz]	$(I_{dec}-I_{co})/I_{dec}$
E	0.02	82.69	100	4.75	0.173
	0.03	61.68	100	4.81	0.383
	0.04	38.83	100	4.66	0.612
	0.05	22.97	100	4.26	0.770
Z	0.02	36.41	40.74	3.70	0.106
	0.03	128.45	158.41	3.32	0.189
	0.04	88.02	181.75	4.24	0.516
	0.05	80.37	330.39	4.22	0.757

	Fit	±
E	4.62	0.25
Z	3.87	0.44

S73. *R*-TiPSY/8

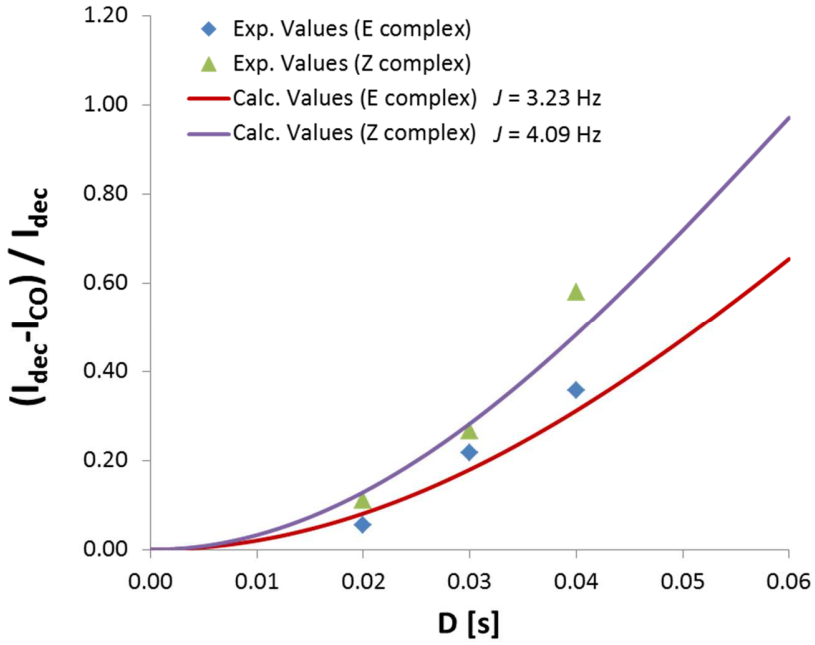

$^{3h}J_{PN}$ Attenuation of *R*-TiPSY/8

D[s]		I_{co} [rel]	I_{dec} [rel]	$^{3h}J_{PN}$ [Hz]	$(I_{dec}-I_{co})/I_{dec}$
E	0.02	18.46	19.53	2.65	0.055
	0.03	15.72	20.09	3.57	0.218
	0.04	9.97	15.49	3.47	0.356
Z	0.02	88.88	100	3.79	0.111
	0.03	73.30	100	3.97	0.267
	0.04	42.12	100	4.52	0.579

	Fit	±
E	3.23	0.50
Z	4.09	0.38

4.8.28 Model comparison: TiPSY/3 vs. TRIP/3 complex

S74. *Type II E*

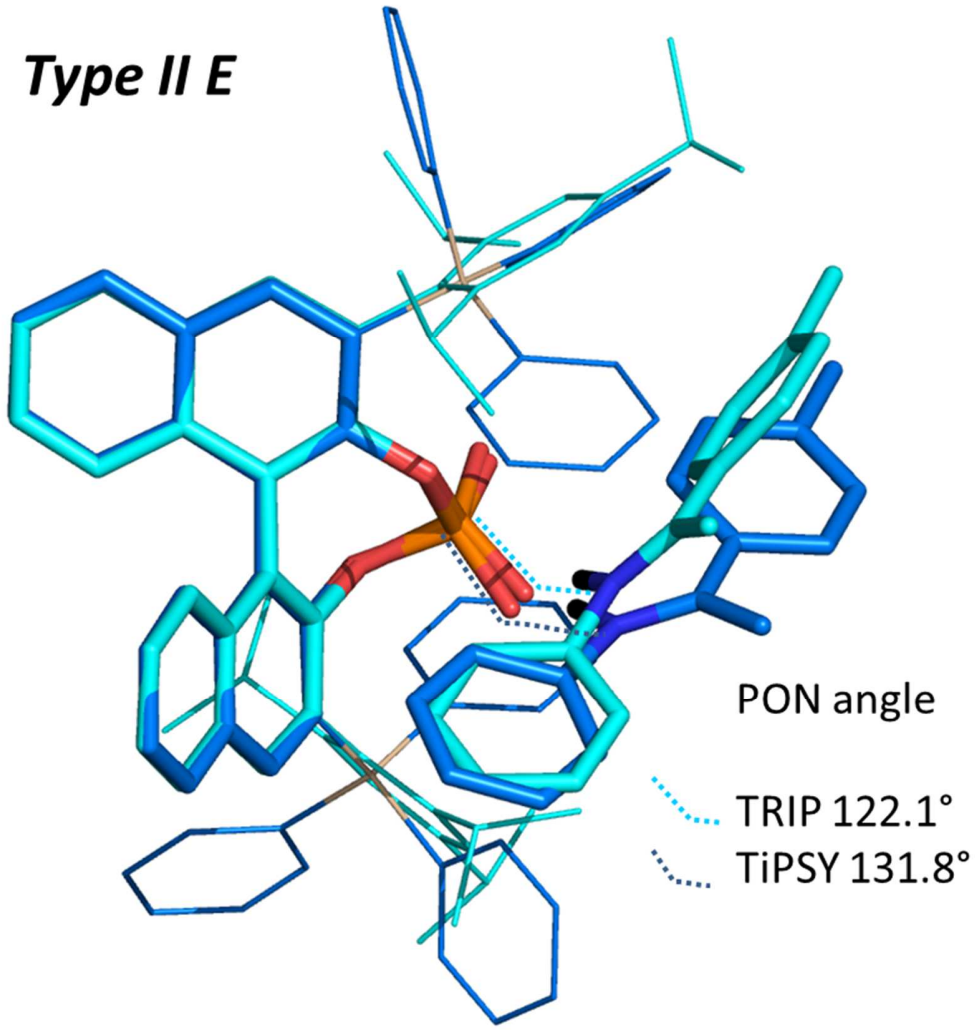

Superposition of the calculated structure *Type II E*- of complex TiPSY/**3** (marine blue) and calculated structure *Type II E* of TRIP/**3** (cyan).

S75. *Type I Z*

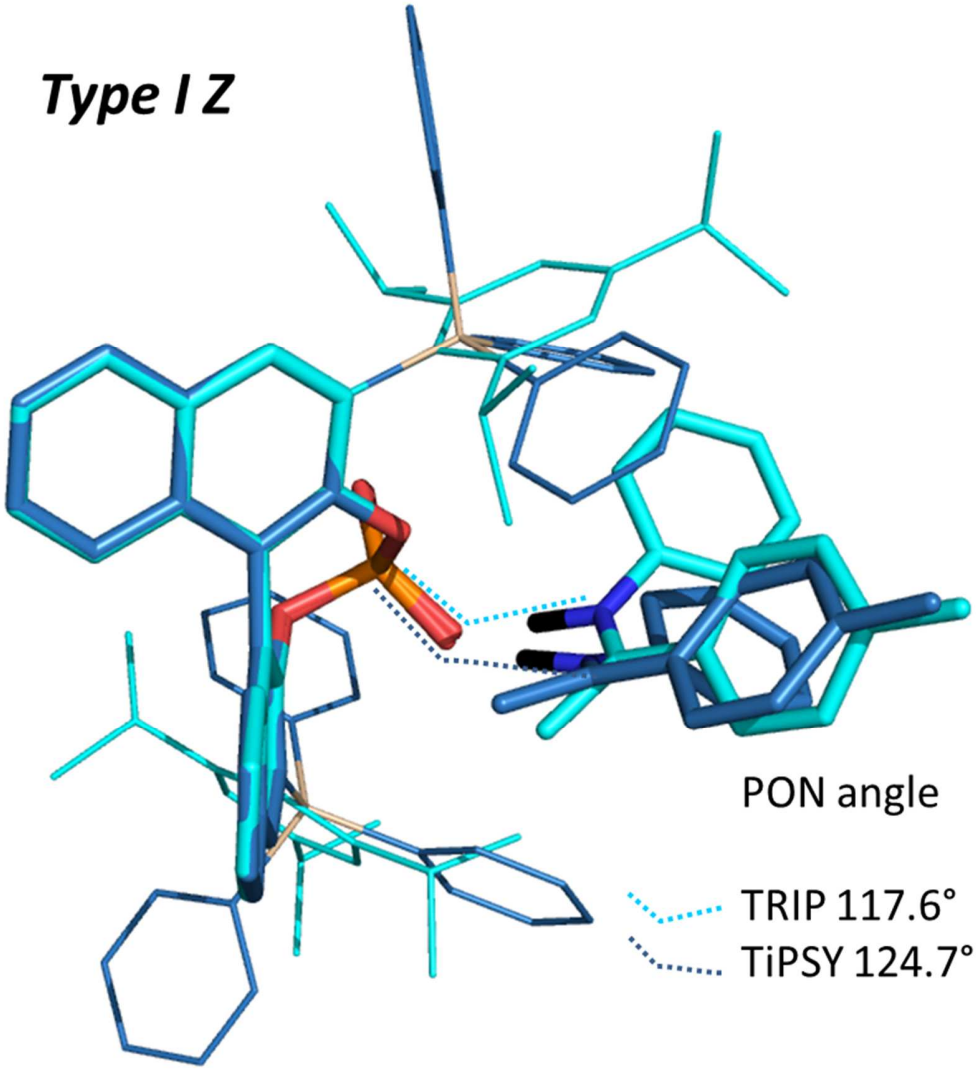

Superposition of the calculated structure *Type I Z*- of complex TiPSY/**3** (marine blue) and calculated structure *Type I Z* of TRIP/**3** (cyan).

S76. *Type II Z*

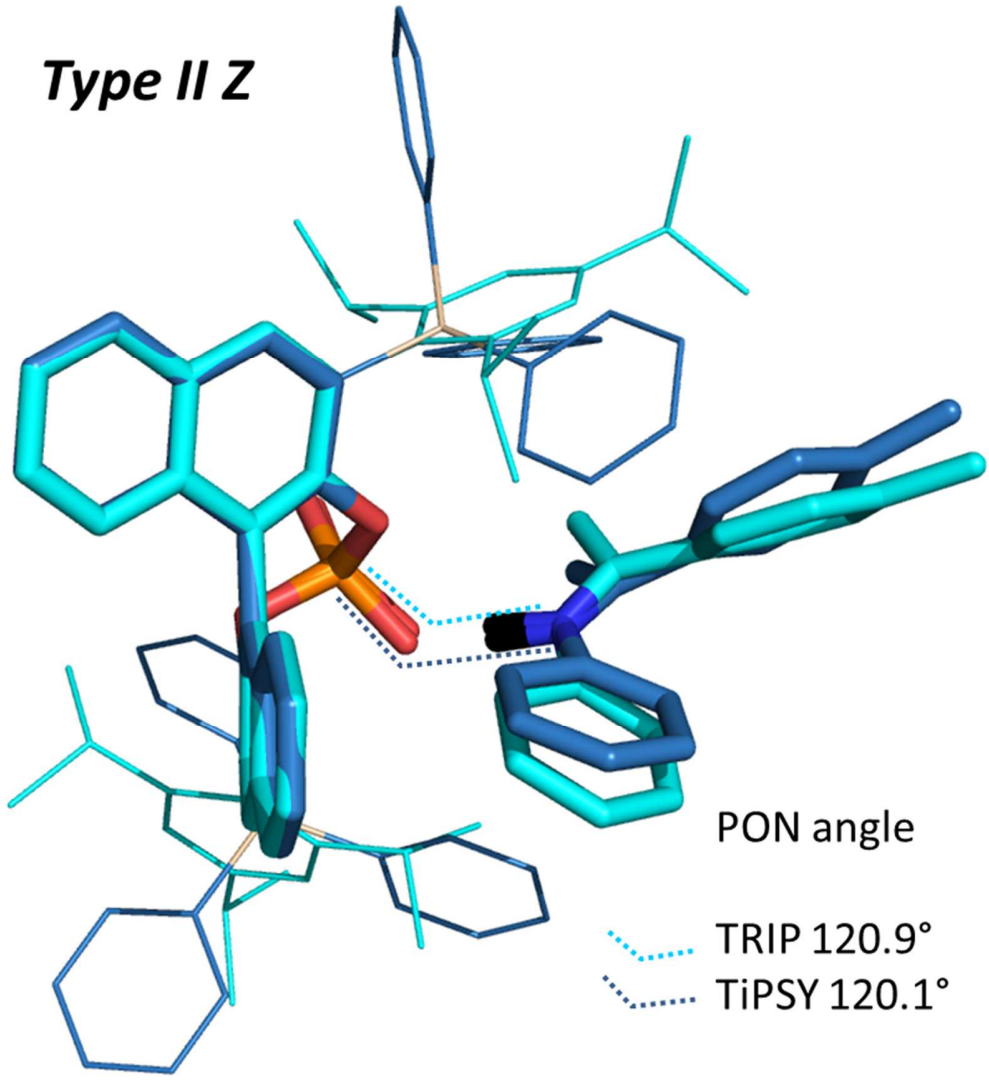

Superposition of the calculated structure *Type II Z*- of complex TiPSY/**3** (marine blue) and calculated structure *Type II Z* of TRIP/**3** (cyan).

4.8.29 Table S1. NMR parameters used for the hydrogen-bond correlations

Systems	δ(N)° ppm	δ(HN)° ppm	δ(OHN)* ppm	δ(OH)° ppm	δ(HN)° ppm	δ(OHN)* ppm
pyridine–HA[9] in CDF_3/CDF_2Cl	0	126	-4	2	7	20
collidine–HA[9] in CDF_3/CDF_2Cl	0	126	-8	2	7	20
Solid collidine–HA[4]	0	126	0	-3	7	20
Imine/TRIP[9]	0	-170	-6	2	6	16
Imine/TiPSY, imine/TRIFP and Imine/TRIP	0	-170	-6	2	6	16

NMR parameters are used in the equations below (7)-(8) to calculate the Steiner-Limbach curve coordinates without correction factors.

$$\delta(OHN) = \delta(OH)^{0} p_{OH}^{H} + \delta(HN)^{0} p_{HN}^{H} + 4\,\delta(OHN)^{*} p_{OH}^{H}\, p_{HN}^{H} \quad (7)$$

$$\delta(OHN)_{ref} = \delta(N)^{0} p_{OH}^{H} + \delta(HN)^{0} p_{HN}^{H} + 4\,\delta(OHN)^{*} p_{OH}^{H}\, p_{HN}^{H} \quad (8)$$

4.8.30 Table S2. Parameters of the geometric hydrogen-bond correlations

Systems	b_{OH} [Å]	r°_{OH} [Å]	b_{HN} [Å]	r°_{NH} [Å]	f	g	c^H	d^H
Weak and medium strong OHN bonds[9]	0.371	0.942	0.385	0.992	0	0	0	0
pyridine–HA and collidine-HA[9] in CDF_3/CDF_2Cl	0.371	0.942	0.385	0.992	5	2	360	0.7
pyridine–HA and collidine-HA solid[4]	0.371	0.942	0.385	0.992	5	2	360	0.7
Imine/TRIP catalyst[12]	0.371	0.942	0.385	0.992	8	2	360	0.3
Imine/TiPSY, imine/TRIFP and Imine/TRIP	0.371	0.942	0.385	0.992	8	2	360	0.35

Adjusting the d^H factor in equations (9)-(10) drastically improves the fitting by modulating the curve amplitude.

$$p_{OH}^{H\,'} = p_{OH}^{H} - c^H\,(p_{OH}^{H}\,p_{HN}^{H})^{f}(p_{OH}^{H} - p_{HN}^{H}) - \mathrm{d}^H(p_{OH}^{H}\,p_{HN}^{H})^{g} \quad (9)$$

$$p_{HN}^{H\,'} = p_{HN}^{H} + c^H\,(p_{OH}^{H}\,p_{HN}^{H})^{f}(p_{OH}^{H} - p_{HN}^{H}) - \mathrm{d}^H(p_{OH}^{H}\,p_{HN}^{H})^{g} \quad (10)$$

This d^H factor was described as isotope sensitive and requires to be empirically determined.[9] Depending on the system studied, d^H factors typically range between 0 (maximum amplitude without attenuation) and 0.7 (reduced amplitude). In our system, a 0.35 factor was used to optimize the curve trajectory for the CPA/imine complexes. Parameters c^H, f and g did not provide a significant improvement while fitting and were not modified in accordance with our previous work (Supplementary table S2).[4,9]

Distance parameters are used to retrieve r_{OH} and r_{NH} atomic distances from derived bond order according to the equations:

$$p_{OH}^{H} = exp\left\{\frac{-(r_{OH} - r^{\circ}_{OH})}{b_{OH}}\right\} (5) \quad ; \quad p_{NH}^{H} = exp\left\{\frac{-(r_{NH} - r^{\circ}_{NH})}{b_{NH}}\right\} (6)$$

Table S3. Steiner-Limbach correlation curve data points: HBF_4, TRIP and TRIFP complexes

NMR parameters (δ^1H, $\delta^{15}N$, $^1J_{HN}$, $^{2h}J_{HP}$, $^{3h}J_{PN}$) of HBF_4/imine, *R*-TRIP/imine and *R*-TRIFP/imine complexes in CD_2Cl_2.

Complex	δ ^{1}H [ppm]	δ ^{15}N [ppm]	$^1J_{NH}$ [Hz]	$^{2h}J_{HP}$ [Hz]	$^{3h}J_{PN}$ [Hz]	Solvent	T [K]	Ref.
HBF_4/**3***E*	12.35	189.4	92.3	---	---	CD_2Cl_2	180	TMS
HBF_4/**3***Z*	12.48	193.4	91.9	---	---	CD_2Cl_2	180	TMS
HBF_4/**5***E*	12.23	182.8	92.5	---	---	CD_2Cl_2	180	TMS
HBF_4/**5***Z*	12.26	188.2	92.6	---	---	CD_2Cl_2	180	TMS
R-TRIP/**1**E	17.42	220.6	77.3	2.50 ± 0.10	2.89 ± 0.14	CD_2Cl_2	180	TMS
R-TRIP/**1***Z*	17.42	217.9	n.d.			CD_2Cl_2	180	TMS
R-TRIP/**2***E*	17.68	224.3	75.4	2.33 ± 0.07	2.97 ± 0.16	CD_2Cl_2	180	TMS
R-TRIP/**2***Z*	17.68	221.1	n.d.			CD_2Cl_2	180	TMS
R-TRIP/**3***E*	17.07	216.0	79.2	2.50 ± 0.12	3.11 ± 0.12	CD_2Cl_2	180	$CHDCl_2$
R-TRIP/**3***Z*	17.11	215.0	78.4	2.66 ± 0.02		CD_2C_{l2}	180	$CHDCl_2$
R-TRIP/**4***E*	18.20	235.1	68.7	2.15 ± 0.29	n.d.	CD_2Cl_2	180	TMS
R-TRIP/**4***Z*	18.20	228.0	n.d.			CD_2Cl_2	180	TMS
R-TRIP/**5***E*	16.47	206.6	82.2	2.85 ± 0.27	2.92 ± 0.20	CD_2Cl_2	180	TMS
R-TRIP/**5***Z*	16.75	209.1	81.0	2.99 ± 0.19	2.88 ± 0.13	CD_2Cl_2	180	TMS
R-TRIP/**9**E	18.42	243.3	67.7	n.d.	n.d.	CD_2Cl_2	180	TMS
R-TRIP/**9**Z1	18.18	228.9	74.3	1.82 ± 0.27	2.47 ± 0.07	CD_2Cl_2	180	TMS
R-TRIP/**9**Z2	18.13	228.7	75.2			CD_2Cl_2	180	TMS
R-TRIP/**10***E*	17.70	268.1	n.d.	n.d	n.d.	CD_2Cl_2	180	TMS
R-TRIP/**10***E*	17.93	264.1	41.7	n.d	n.d.	CD_2Cl_2	170	TMS
R-TRIP/**10***Z*	18.85	240.6	60.6	n.d	n.d.	CD_2Cl_2	180	TMS
R-TRIP/**11**	17.35	225.5	77.0	2.13 ± 0.05	2.00 ± 0.19	CD_2Cl_2	200	TMS
R-TRIP/**12***E*	17.31	223.6	78.1	2.77 ± 0.06	3.09 ± 0.05	CD_2Cl_2	180	TMS
R-TRIP/**12***Z*	17.07	221.7	79.3	2.58 ± 0.13	2.87 ± 0.30	CD_2Cl_2	180	TMS
R-TRIFP/**1***E*	16.18	207.1	83.0	n.d.	n.d.	CD_2Cl_2	170	TMS

Complex	δ ^{1}H	δ ^{15}N	$^{1}J_{NH}$	$^{2h}J_{HP}$	$^{3h}J_{PN}$	Solvent	T [K]	Ref.
R-TRIFP/**1***Z*	16.79	213.1	82.3	n.d.	n.d.	CD_2Cl_2	170	TMS
R-TRIFP/**2***E*	16.49	210.6	82.8	n.d.	n.d.	CD_2Cl_2	170	TMS
R-TRIFP/**2***Z*	16.96	215.2	81.1	n.d.	n.d.	CD_2Cl_2	170	TMS
R-TRIFP/**3***E*	15.95	204.2	85.1	3.45 ± 0.43	4.30 ± 0.21	CD_2Cl_2	170	TMS
R-TRIFP/**3**Z	16.50	209.9	82.7	3.23 ±0.39	3.50 ± 0.22	CD_2Cl_2	170	TMS
R-TRIFP/**4***E*	17.09	218.2	80.8	n.d.	n.d.	CD_2Cl_2	170	TMS
R-TRIFP/**4***Z*	17.39	220.4	80.5	n.d.	n.d.	CD_2Cl_2	170	TMS
R-TRIFP/ **5***E*	15.39	196.4	86.0	3.72 ± 0.19	3.90 ± 0.03	CD_2Cl_2	170	TMS
R-TRIFP/**5***Z*	16.11	204.4	85.1	3.92 ± 0.24	n.d.	CD_2Cl_2	170	TMS

4.8.31 Table S4. Steiner-Limbach correlation curve data points: TiPSY and acids and phenols

NMR parameters (δ^{1}H, δ^{15}N, $^{1}J_{HN}$, $^{2h}J_{HP}$, $^{3h}J_{PN}$) of TiPSY/imine complexes in CD_2Cl_2, and ^{1}H, ^{15}N chemical shifts of acids and phenol/imine complexes.

Complex	δ ^{1}H [ppm]	δ ^{15}N [ppm]	$^{1}J_{NH}$ [Hz]	$^{2h}J_{HP}$ [Hz]	$^{3h}J_{PN}$ [Hz]	Solvent	T [K]	Ref.
R-TiPSY/**1**E	16.50	216.3	79.2	2.97 ± 0.04	4.78 ± 0.28	CD_2Cl_2	180	TMS
R-TiPSY/**1**Z	17.00	220.6	76.0	2.46 ± 0.05	4.20 ± 0.13	CD_2cl_2	180	TMS
R-TiPSY/**2**E	16.79	219.6	77.3	n.d.	n.d.	CD_2Cl_2	180	TMS
R-TiPSY/**2**Z	17.16	222.7	73.9	n.d.	n.d.	CD_2Cl_2	180	TMS
R-TiPSY/**3**E	16.12	211.3	81.2	3.29 ± 0.05	4.87 ± 0.37	CD_2Cl_2	180	TMS
R-TiPSY/**3**Z	16.64	216.6	78.1	2.75 ± 0.10	4.11 ± 0.34	CD_2Cl_2	180	TMS
R-TiPSY/**4**E	17.32	228.3	73.1	2.69 ± 0.32	4.67 ± 1.20	CD_2Cl_2	180	TMS
R-TiPSY/**4**Z	17.56	228.3	71.8	2.08 ± 0.07	4.20 ± 0.47	CD_2Cl_2	180	TMS

Complex	δ ^{1}H	δ ^{15}N	$^{1}J_{NH}$	$^{2h}J_{HP}$	$^{3h}J_{PN}$	Solvent	T [K]	Ref.
R-TiPSY/**5**E	15.53	203.6	83.7	3.73 ± 0.04	5.26 ± 0.22	CD_2Cl_2	179/ 170	TMS
R-TiPSY/**5**Z	16.24	211.3	80.0	3.17 ± 0.12	4.03 ± 0.26	CD_2Cl_2	179/ 170	TMS
R-TiPSY/**6**E	16.30	212.0	81.4	3.51 ± 0.05	3.70 ± 0.80	CD_2Cl_2	180	TMS
R-TiPSY/**6**Z	16.90	218.8	77.2	2.73 ± 0.10	4.30 ± 0.20	CD_2Cl_2	180	TMS
R-TiPSY/**7**E	15.83	207.8	83.5	3.50 ± 0.03	4.62 ± 0.25	CD_2Cl_2	190/ 180	TMS
R-TiPSY/**7**Z	16.78	218.3	77.0	2.65 ± 0.04	3.87 ± 0.44	CD_2Cl_2	190/ 180	TMS
R-TiPSY/**8**E	16.13	212.0	81.7	2.97 ± 0.41	3.23 ± 0.41	CD_2Cl_2	180	TMS
R-TiPSY/**8**Z	16.60	218.8	77.7	2.54 ± 0.38	4.09 ± 0.31	CD_2Cl_2	180	TMS
4-NO2-Phenol/**3**	13.43	299.3	n.d.	---	---	$CDCl_2F$	130	TMS
4-Cl-Phenol /**5**	11.81	299.7	n.d.	---	---	$CDCl_2F$	130	TMS
3,5-Cl-Phenol/**5**	12.25	297.1	n.d.	---	---	$CDCl_2F$	130	TMS
3-CF3-Phenol/**5**	11.96	299.0	n.d	---	---	$CDCl_2F$	130	TMS
Acetic Acid/**5**	14.60	294.3	n.d.	---	---	$CDCl_2F$	130	TMS
TMA/**5**	14.34	295.8	n.d	---	---	$CDCl_2F$	130	TMS

4.8.32 Table S5. Hydrogen bond distance determination from bond order derived from Steiner-Limbach curve: HBF_4, TRIP and TRIFP complexes

Respective bond orders ρ_{OH} and ρ_{OH}, $q_1 = \frac{r_{NH} - r_{OH}}{2}$, q_2, r_{NH} and r_{OH} obtained from HBF_4/imine, TRIP/imine and TRIFP/imine complexes.

Complex	ρ_{OH}	ρ_{NH}	q_1	q_2 or (r_{NO}) [Å]	r_{NH} [Å]	r_{OH} [Å]	Solvent	T [K]
HBF_4/**3***E*	0.12 ± 0.01	0.87 ± 0.01	-0.34 ± 0.01	2.77 ± 0.01	1.05 ± 0.01	1.72 ± 0.02	CD_2Cl_2	180
HBF_4/**3***Z*	0.14 ± 0.02	0.85 ± 0.02	-0.32 ± 0.02	2.74 ± 0.03	1.05 ± 0.01	1.68 ± 0.03	CD_2Cl_2	180
HBF_4/**5***E*	0.10 ± 0.03	0.89 ± 0.03	-0.38 ± 0.05	2.84 ± 0.07	1.04 ± 0.02	1.80 ± 0.08	CD_2Cl_2	180
HBF_4/**5***Z*	0.12 ± 0.01	0.87 ± 0.01	-0.35 ± 0.02	2.78 ± 0.02	1.04 ± 0.01	1.74 ± 0.02	CD_2Cl_2	180
R-TRIP/**1**E	0.30 ± 0.01	0.67 ± 0.01	-0.12 ± 0.01	2.54 ± 0.01	1.15 ± 0.01	1.39 ± 0.01	CD_2Cl_2	180
R-TRIP/**1***Z*	0.29 ± 0.02	0.68 ± 0.02	-0.13 ± 0.02	2.54 ± 0.02	1.14 ± 0.02	1.40 ± 0.02	CD_2Cl_2	180
R-TRIP/**2***E*	0.32 ± 0.01	0.65 ± 0.01	-0.11 ± 0.01	2.53 ± 0.01	1.16 ± 0.01	1.37 ± 0.01	CD_2Cl_2	180
R-TRIP/**2***Z*	0.31 ± 0.02	0.66 ± 0.02	-0.11 ± 0.02	2.53 ± 0.02	1.15 ± 0.02	1.38 ± 0.02	CD_2Cl_2	180
R-TRIP/**3***E*	0.27 ± 0.02	0.70 ± 0.02	-0.15 ± 0.02	2.55 ± 0.01	1.13 ± 0.01	1.42 ± 0.02	CD_2Cl_2	180
R-TRIP/**3***Z*	0.27 ± 0.02	0.70 ± 0.02	-0.15 ± 0.02	2.56 ± 0.02	1.13 ± 0.02	1.42 ± 0.02	CD_2Cl_2	180
R-TRIP/**4***E*	0.37 ± 0.02	0.59 ± 0.02	-0.06 ± 0.02	2.51 ± 0.01	1.19 ± 0.01	1.31 ± 0.02	CD_2Cl_2	180
R-TRIP/**4***Z*	0.35 ± 0.02	0.61 ± 0.03	-0.08 ± 0.02	2.51 ± 0.02	1.18 ± 0.02	1.33 ± 0.02	CD_2Cl_2	180
R-TRIP/**5***E*	0.23 ± 0.03	0.74 ± 0.03	-0.19 ± 0.03	2.59 ± 0.03	1.11 ± 0.02	1.48 ± 0.04	CD_2Cl_2	180
R-TRIP/**5***Z*	0.25 ± 0.03	0.73 ± 0.03	-0.17 ± 0.03	2.58 ± 0.03	1.12 ± 0.02	1.46 ± 0.04	CD_2Cl_2	180
R-TRIP/**9**E	0.41 ± 0.02	0.55 ± 0.02	-0.03 ± 0.02	2.50 ± 0.01	1.22 ± 0.02	1.28 ± 0.02	CD_2Cl_2	180
R-TRIP/**9**Z1	0.35 ± 0.02	0.61 ± 0.02	-0.08 ± 0.02	2.51 ± 0.01	1.18 ± 0.02	1.33 ± 0.02	CD_2Cl_2	180
R-TRIP/**9**Z2	0.35 ± 0.02	0.62 ± 0.02	-0.08 ± 0.02	2.51 ± 0.01	1.18 ± 0.02	1.34 ± 0.02	CD_2Cl_2	180
R-TRIP/**10***E*	0.57 ± 0.01	0.39 ± 0.01	0.10 ± 0.01	2.51 ± 0.01	1.35 ± 0.01	1.15 ± 0.01	CD_2Cl_2	180
R-TRIP/**10***E*	0.55 ± 0.01	0.41 ± 0.01	0.08 ± 0.01	2.50 ± 0.01	1.33 ± 0.01	1.17 ± 0.01	CD_2Cl_2	170
R-TRIP/**10***Z*	0.42 ± 0.03	0.54 ± 0.03	-0.01 ± 0.02	2.50 ± 0.01	1.23 ± 0.02	1.26 ± 0.03	CD_2Cl_2	180
R-TRIP/**11**	0.31 ± 0.02	0.66 ± 0.02	-0.11 ± 0.02	2.53 ± 0.02	1.15 ± 0.02	1.38 ± 0.02	CD_2Cl_2	200
R-TRIP/**12***E*	0.30 ± 0.02	0.67 ± 0.02	-0.12 ± 0.02	2.54 ± 0.01	1.15 ± 0.02	1.39 ± 0.02	CD_2Cl_2	180
R-TRIP/**12***Z*	0.29 ± 0.02	0.68 ± 0.02	-0.13 ± 0.02	2.54 ± 0.02	1.14 ± 0.02	1.40 ± 0.02	CD_2Cl_2	180
R-TRIFP/**1***E*	0.23 ± 0.02	0.75 ± 0.02	-0.19 ± 0.02	2.59 ± 0.02	1.10 ± 0.02	1.49 ± 0.03	CD_2Cl_2	170
R-TRIFP/**1***Z*	0.26 ± 0.02	0.71 ± 0.02	-0.16 ± 0.02	2.57 ± 0.02	1.12 ± 0.01	1.44 ± 0.02	CD_2Cl_2	170
R-TRIFP/**2***E*	0.25 ± 0.02	0.73 ± 0.02	-0.17 ± 0.02	2.58 ± 0.02	1.11 ± 0.01	1.46 ± 0.02	CD_2Cl_2	170
R-TRIFP/**2***Z*	0.27 ± 0.02	0.70 ± 0.02	-0.15 ± 0.02	2.56 ± 0.01	1.13 ± 0.01	1.43 ± 0.02	CD_2Cl_2	170
R-TRIFP/**3***E*	0.22 ± 0.02	0.76 ± 0.03	-0.21 ± 0.03	2.61 ± 0.03	1.10 ± 0.02	1.51 ± 0.03	CD_2Cl_2	170
R-TRIFP/**3**Z	0.24 ± 0.02	0.73 ± 0.02	-0.18 ± 0.02	2.58 ± 0.02	1.11 ± 0.02	1.47 ± 0.02	CD_2Cl_2	170
R-TRIFP/**4***E*	0.28 ± 0.01	0.69 ± 0.01	-0.14 ± 0.01	2.55 ± 0.01	1.14 ± 0.01	1.41 ± 0.01	CD_2Cl_2	170
R-TRIFP/**4***Z*	0.30 ± 0.01	0.67 ± 0.01	-0.13 ± 0.01	2.54 ± 0.01	1.14 ± 0.01	1.39 ± 0.01	CD_2Cl_2	170
R-TRIFP/**5***E*	0.19 ± 0.03	0.80 ± 0.04	-0.25 ± 0.04	2.65 ± 0.05	1.08 ± 0.02	1.57 ± 0.06	CD_2Cl_2	170
R-TRIFP/**5***Z*	0.22 ± 0.03	0.76 ± 0.03	-0.20 ± 0.03	2.60 ± 0.03	1.10 ± 0.02	1.50 ± 0.04	CD_2Cl_2	170

4.8.33 Table S6. Hydrogen bond distance determination from bond order derived from Steiner-Limbach curve: TiPSY, acid and phenol complexes

Respective bond orders ρ_{OH} and ρ_{OH}, $q_1 = \frac{r_{NH} - r_{OH}}{2}$, q_2, r_{NH} and r_{OH} obtained from TiPSY/imine and acid and phenol/imine complexes.

Complex	ρ_{OH}	ρ_{NH}	q_1	q_2 (r_{NO}) [Å]	r_{NH} [Å]	r_{OH} [Å]	Solvent	T [K]
R-TiPSY/**1**E	0.26 ± 0.02	0.71 ± 0.02	-0.16 ± 0.02	2.56 ± 0.02	1.12 ± 0.02	1.44 ± 0.02	CD_2Cl_2	180
R-TiPSY/**1**Z	0.29 ± 0.02	0.68 ± 0.02	-0.13 ± 0.02	2.55 ± 0.02	1.14 ± 0.02	1.41 ± 0.02	CD_2cl_2	180
R-TiPSY/**2**E	0.28 ± 0.02	0.69 ± 0.02	-0.14 ± 0.02	2.55 ± 0.02	1.13 ± 0.02	1.42 ± 0.02	CD_2Cl_2	180
R-TiPSY/**2**Z	0.30 ± 0.02	0.67 ± 0.02	-0.13 ± 0.02	2.54 ± 0.02	1.14 ± 0.02	1.40 ± 0.02	CD_2Cl_2	180
R-TiPSY/**3**E	0.24 ± 0.01	0.74 ± 0.01	-0.18 ± 0.01	2.58 ± 0.01	1.11 ± 0.01	1.47 ± 0.01	CD_2Cl_2	180
R-TiPSY/**3**Z	0.27 ± 0.02	0.71 ± 0.02	-0.15 ± 0.02	2.56 ± 0.01	1.13 ± 0.01	1.43 ± 0.02	CD_2Cl_2	180
R-TiPSY/**4**E	0.31 ± 0.03	0.65 ± 0.03	-0.11 ± 0.03	2.53 ± 0.02	1.16 ± 0.02	1.37 ± 0.03	CD_2Cl_2	180
R-TiPSY/**4**Z	0.32 ± 0.02	0.64 ± 0.02	-0.10 ± 0.02	2.52 ± 0.02	1.16 ± 0.02	1.36 ± 0.03	CD_2Cl_2	180
R-TiPSY/**5**E	0.21 ± 0.02	0.77 ± 0.02	-0.22 ± 0.02	2.62 ± 0.02	1.09 ± 0.01	1.53 ± 0.02	CD_2Cl_2	179/ 170
R-TiPSY/**5**Z	0.24 ± 0.01	0.73 ± 0.01	-0.18 ± 0.01	2.58 ± 0.01	1.11 ± 0.01	1.47 ± 0.01	CD_2Cl_2	179/ 170
R-TiPSY/**6**E	0.25 ± 0.01	0.73 ± 0.01	-0.17 ± 0.01	2.58 ± 0.01	1.11 ± 0.01	1.46 ± 0.01	CD_2Cl_2	180
R-TiPSY/**6**Z	0.28 ± 0.02	0.69 ± 0.02	-0.14 ± 0.02	2.55 ± 0.01	1.13 ± 0.01	1.42 ± 0.02	CD_2Cl_2	180
R-TiPSY/**7**E	0.22 ± 0.01	0.75 ± 0.01	-0.20 ± 0.01	2.60 ± 0.01	1.10 ± 0.01	1.50 ± 0.01	CD_2Cl_2	190/ 180
R-TiPSY/**7**Z	0.27 ± 0.02	0.70 ± 0.02	-0.15 ± 0.02	2.55 ± 0.02	1.13 ± 0.01	1.42 ± 0.02	CD_2Cl_2	190/ 180
R-TiPSY/**8**E	0.24 ± 0.01	0.73 ± 0.02	-0.18 ± 0.02	2.58 ± 0.01	1.11 ± 0.01	1.47 ± 0.02	CD_2Cl_2	180
R-TiPSY/**8**Z	0.27 ± 0.02	0.70 ± 0.02	-0.15 ± 0.02	2.56 ± 0.02	1.13 ± 0.02	1.43 ± 0.03	CD_2Cl_2	180
4-NO2-Phenol/**3**	0.76 ± 0.01	0.22 ± 0.01	0.27 ± 0.01	2.62 ± 0.01	1.58 ± 0.01	1.04 ± 0.01	$CDCl_2F$	130
4-Cl-Phenol /**5**	0.79 ± 0.03	0.20 ± 0.03	0.30 ± 0.03	2.65 ± 0.04	1.62 ± 0.05	1.03 ± 0.02	$CDCl_2F$	130
3,5-Cl-Phenol/**5**	0.77 ± 0.03	0.21 ± 0.03	0.28 ± 0.04	2.64 ± 0.04	1.60 ± 0.05	1.04 ± 0.02	$CDCl_2F$	130
3-CF3-Phenol/**5**	0.78 ± 0.03	0.20 ± 0.03	0.29 ± 0.03	2.65 ± 0.04	1.62 ± 0.05	1.03 ± 0.02	$CDCl_2F$	130
Acetic Acid/**5**	0.73 ± 0.01	0.25 ± 0.01	0.23 ± 0.01	2.59 ± 0.01	1.53 ± 0.02	1.06 ± 0.01	$CDCl_2F$	130
TMA/**5**	0.74 ± 0.01	0.24 ± 0.01	0.24 ± 0.01	2.60 ± 0.01	1.54 ± 0.02	1.06 ± 0.01	$CDCl_2F$	130

4.8.34 S77, Calculation of pKa values

An acidity scale with pKA values of different Brønsted acid catalysts, including TRIP and TRIFP was published by O'Donoghue in 2011.[23] To our knowledge, there is no such scale including the three catalysts TRIP TRIFP and TiPSY. Therefore, relative pKa values in DMSO of TRIP, TRIFP and TiPSY for an external acidity scale were calculated at DG_{298} SCS-MP2/CBS//TPSS-D3/def2-SVP level of theory using eq S1 and S2.

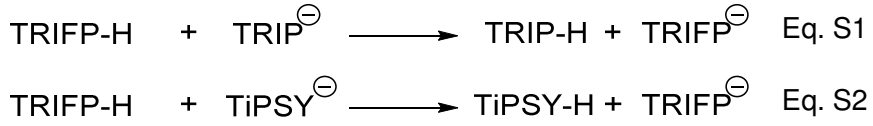

Table S7. Experimental[23] and calculated relative pKa values of the CPAs

	pKa_{calc}	pKa_{exp}
TRIFP	0.0	0
TRIP	+0.78	+1.59
TiPSY	+5.60	n.a.

The calculations show the highest pKa value for TRIFP followed by TRIP, as measured in the experiment. A much lower pKa value is found for TiPSY. The trend of the external acidity predicted in the calculations does not correlate with the internal acidity scale obtained from the Steiner-Limbach analysis (pKa(TRIFP) < pKa(TiPSY)< pKa(TRIP)). This demonstrates that other interactions (dispersion, steric, and electrostatic) significantly contribute in the internal scale. Overall both external and internal acidity scales do not correlate well with the reactivity (see kinetic measurement).

4.8.35 S78, Measured r_{NO} distances and angle correction from Steiner-Limbach analysis.

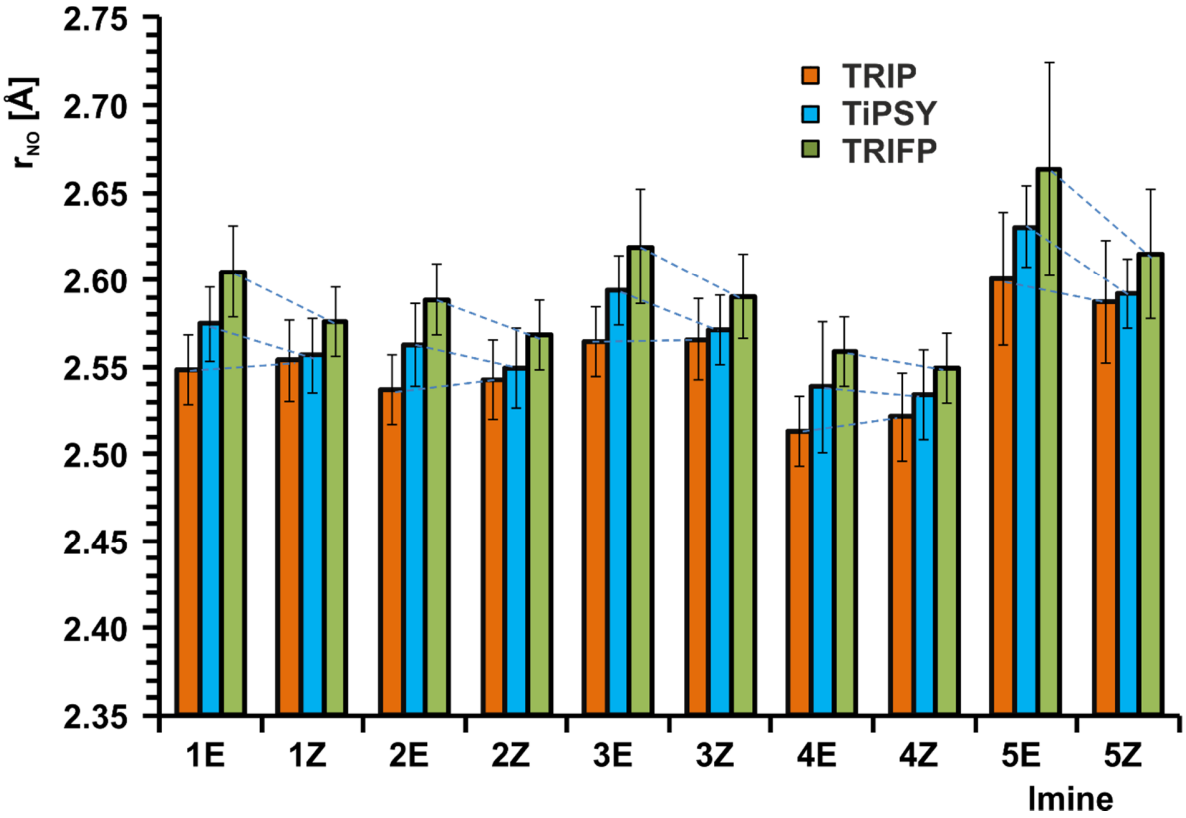

Comparison of the r_{NO} distances of the hydrogen bonds of different catalyst/imine complexes. Without corrected angles, the same trend is found for *E*-imines and *Z*-imines: the shortest distances are found in TRIP/imine complexes, followed by TiPSY/imine complexes and TRIFP/imine complexes. This intrinsic acidity scale of the catalysts shows a different trend than the calculated external acidity scale and the reported acidity scale of O'Donoghue.[23] After correcting the measured distances with the calculated OHN angles, the trend is preserved of the *E*-imines, whereas similar distances are found for the *Z*-imine complexes.

The angle correction was done by using the law of cosine, with θ being the calculated OHN angle in the binary complex.

$$r_{NO} = \sqrt{r_{NH}^2 + r_{OH}^2 - 2r_{NH}r_{OH}\cos\theta} \qquad \text{Eq. S3}$$

Table S8. Calculated PON and OHN angles in the hydrogen bond of binary complex CPA/imine.

TRIP	OHN [deg]	PON [deg]
3E	166.9	122.0
3Z	177.7	120.7
4E	167.6	121.4
4Z	177.6	118.2
5E	167.3	120.0
5Z	178.9	120.1
TRIFP		
3E	162.4	128.4
3Z	165.2	111.3
4E	163.7	130.9
4Z	164.8	110.7
5E	161.5	129.4
5Z	165.4	110.3
TiPSY		
3E	165.5	134.5
3Z	173.2	120.2
4E	169.7	136.0
4Z	174.0	120.9
5E	164.7	129.1
5Z	170.4	122.0

4.8.36 S79, Reaction kinetics of the transfer hydrogenation by NMR

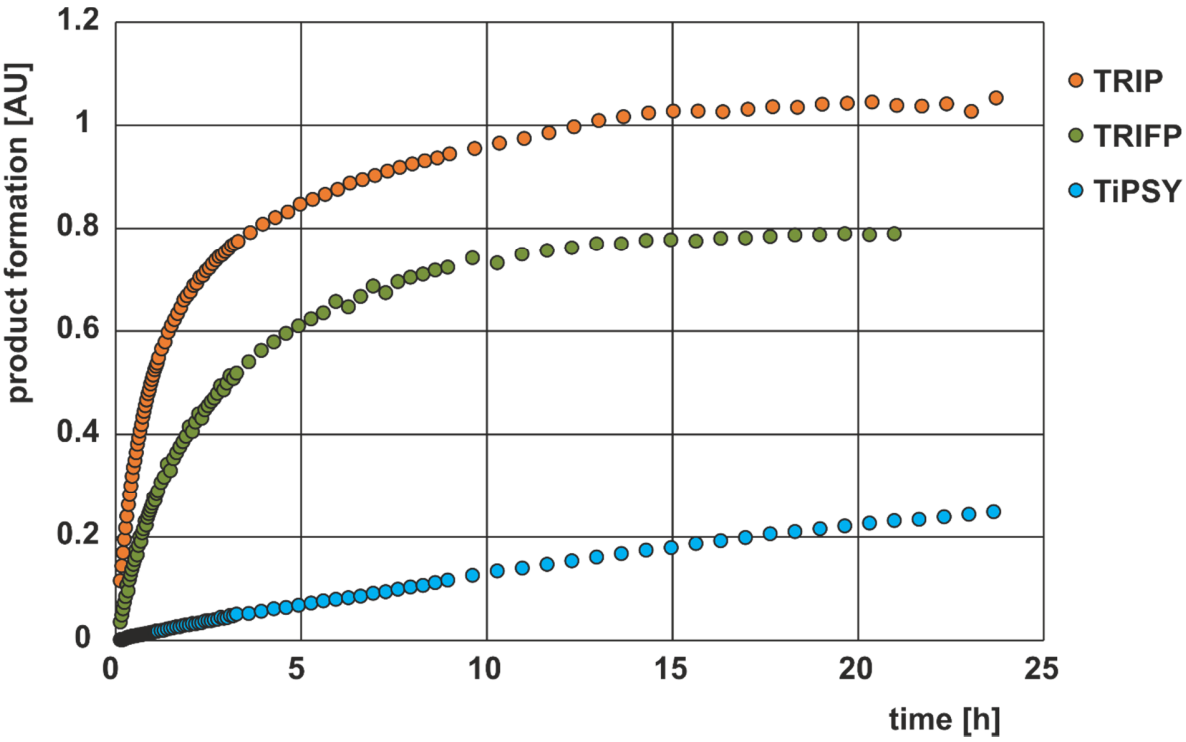

NMR kinetics of the reactions of catalysts TRIP, TRIFP and TiPSY with imine **3**. The reaction was performed with a 0.1 molar solution of **3** with 1.4 equivalents of diethyl 1,4-dihydro-2,6-dimethyl-3,5-pyridinedicarboxylate and 1 mol% of catalysts at 313.15 K in 0.5 ml deuterated dichloromethane. The imine was prepared as described in the experimental section and catalysts and Hantzsch ester were purchased from Sigma Aldrich. To compare the intensities of the spectra, the intensity of the alpha-methyl group of the imine in the first spectrum was used to calibrate the intensities of the alpha-methyl groups of the products. For this reaction higher yields and enantiomeric excesses are reported in toluene as a solvent. Since structure determination and hydrogen bond analyses in this paper were done in dichloromethane, this solvent was also used for the reaction kinetics.

The fastest reaction is observed with TRIP, followed by TRIFP. Catalyst TiPSY shows only a slow product formation, which might be explained by the reaction conditions. Furthermore, the enantioselective preparation of amines was reported by reductive amination instead of transfer hydrogenation by MacMillan.[24] No correlation can be found between the intrinsic acidity of the catalysts and the reactivity, since a higher intrinsic acidity was found for TiPSY/imine complexes than for TRIFP/imine complexes.

4.8.37 Table S9. Experimental vs. Calculated $^{3h}J_{PN}$ in the hydrogen bond of binary complex CPA/imine

	$^{3h}J_{PN}$ [Hz] calc.	$^{3h}J_{PN}$ [Hz] exp.	PON [°]	ee exp.
TRIP				
3*E*	-3.04	3.11	122.0	
3*Z*	-2.75	3.11	120.7	
4*E*	-3.12	n.d.	121.4	
4*Z*	-2.53	n.d.	118.2	
5*E*	-2.68	2.92	120.0	
5*Z*	-2.68	2.88	120.1	86
TRIFP				
3*E*	-3.68	4.30	128.4	
3*Z*	-1.71	3.50	111.3	
4*E*	-4.55	n.d.	130.9	
4*Z*	-1.72	n.d.	110.7	
5*E*	-3.65	3.90	129.4	
5*Z*	-1.53	n.d.	110.3	74
TiPSY				
3*E*	-5.94	4.87	134.5	
3*Z*	-2.61	4.11	120.2	
4*E*	-7.19	4.67	136.0	
4*Z*	-2.77	4.20	120.9	
5*E*	-4.51	4.80	129.1	
5*Z*	-2.86	4.03	122.0	91

4.8.38 Table S10. Boltzmann averaged G_{180} SCS-MP2/CBS of the binary complexes

	G_{180} SCS-MP2/CBS
TiPSY/3 *E*	-4007.805891
TiPSY/4 *E*	-4305.365048
TiPSY/5 *E*	-4082.937481
TiPSY/3 *Z*	-4007.800767
TiPSY/4 *Z*	-4305.357848
TiPSY/5 *Z*	-4082.930539
TRIFP/3 *E*	-3852.151708
TRIFP/4 *E*	-4149.707746
TRIFP/5 *E*	-3927.286595
TRIFP/3 *Z*	-3852.154565
TRIFP/4 *Z*	-4149.713579
TRIFP/5 *Z*	-3927.285321
TRIP/3 *E*	-3210.8455623
TRIP/4 *E*	-3537.8889684
TRIP/5 *E*	-3285.9694768
TRIP/3 *Z*	-3123.5210663
TRIP/4 *Z*	-3508.3975724
TRIP/5 *Z*	-3285.9655149

4.8.39 S80 Computational details

Binary complexes consist of TiPSY, TRIP and TRIFP with imines **3**, **4**, **5** were optimized at TPSS-D3/def2-SVP level of theory in continuum of CH_2Cl_2.[25,26] The dielectric constant of the solvents was modified to 16.20 to mimic low temperature NMR measurement. Subsequently all minima were verified by frequency analysis (zero imaginary vibrational mode) and thermochemical corrections were added. Single point calculations at SCS-MP2/CBS level of theory (for extrapolation procedure see SI) were employed on top of the optimized geometry[27] Software used for the optimization was Gaussian09 D.01.[28] For single points, ORCA 3.0.3 was used.[29] For the basis set extrapolation procedure Eq.1-3 were used with the basis set def2-SVP and def2-TZVP (X=2,3). α=10.39, β=2.40.

$$E_{\mathrm{SCF}}^{X} = E_{\mathrm{SCF}}^{\infty} + Ae^{-\alpha\sqrt{X}} \quad \text{Eq. 1}$$

$$E_{\mathrm{corr,MP2}}^{\infty} = \frac{X^{\beta}E_{\mathrm{corr,MP2}}^{X} - (X-1)^{\beta}E_{\mathrm{corr,MP2}}^{X-1}}{X^{\beta} - (X-1)^{\beta}} \quad \text{Eq. 2}$$

$$E_{\mathrm{MP2}}^{\infty} = E_{\mathrm{SCF}}^{\infty} + E_{\mathrm{corr,MP2}}^{\infty} \quad \text{Eq. 3}$$

4.8.40 References

[1] J. Siegel, F. Anet, *J. Org. Chem.* **1988**, *9*, 2629–2630.

[2] I. G. Shenderovich, A. P. Burtsev, G. S. Denisov, N. S. Golubev, H.-H. Limbach, *Magn. Reson. Chem.* **2001**, *39*, S91–S99.

[3] M. Klussmann, L. Ratjen, S. Hoffmann, V. Wakchaure, R. Goddard, B. List, *Synlett* **2010**, *2010*, 2189–2192.

[4] N. Sorgenfrei, J. Hioe, J. Greindl, K. Rothermel, F. Morana, N. Lokesh, R. M. Gschwind, *J. Am. Chem. Soc.* **2016**, *138*, 16345–16354.

[5] J. Greindl, J. Hioe, N. Sorgenfrei, F. D. Morana, R. M. Gschwind, *J. Am. Chem. Soc.* **2016**, *49*, 15965–15971.

[6] F. Aznar, C. Valde, *J. Am. Chem. Soc.* **2009**, *131*, 4031–4041.

[7] Y. Schramm, F. Barrios-Landeros, A. Pfaltz, *Chem. Sci.* **2013**, *4*, 2760–2766.

[8] R. K. Harris, E. D. Becker, S. M. Cabral de Menezes, R. Goodfellow, P. Granger, *Magn. Reson. Chem.* **2002**, *40*, 489–505.

[9] H.-H. Limbach, M. Pietrzak, S. Sharif, P. M. Tolstoy, I. G. Shenderovich, S. N. Smirnov, N. S. Golubev, G. S. Denisov, *Chem. – A Eur. J.* **2004**, *10*, 5195–5204.

[10] K. M. Anderson, A. Esadze, M. Manoharan, R. Brüschweiler, D. G. Gorenstein, J. Iwahara, *J. Am. Chem. Soc.* **2013**, *135*, 3613–3619.

[11] F. Löhr, S. G. Mayhew, H. Rüterjans, *J. Am. Chem. Soc.* **2000**, *122*, 9289–9295.

[12] A. J. Dingley, F. Cordier, S. Grzesiek, *Concepts Magn. Reson.* **2001**, *13*, 103–127.

[13] B. Berglund, R. W. Vaughan, *J. Chem. Phys.* **1980**, *73*, 2037–2043.

[14] N. Tjandra, A. Bax, *J. Am. Chem. Soc.* **1997**, *119*, 8076–8082.

[15] A. J. Dingley, S. Grzesiek, *J. Am. Chem. Soc.* **1998**, *120*, 8293–8297.

[16] K. Pervushin, A. Ono, C. Fernández, T. Szyperski, M. Kainosho, K. Wüthrich, *Proc. Natl. Acad. Sci. U. S. A.* **1998**, *95*, 14147–51.

[17] M. Mishima, M. Hatanaka, S. Yokoyama, T. Ikegami, M. Wälchli, Y. Ito, M. Shirakawa, *J. Am. Chem. Soc.* **2000**, *122*, 5883–5884.

[18] G. Federwisch, R. Kleinmaier, D. Drettwan, R. M. Gschwind, *J. Am. Chem. Soc.* **2008**, *130*, 16846–16847.

[19] G. Federwisch, *Diss. Univ. Regensbg.* **2008**.

[20] F. Cordier, S. Grzesiek, *J. Am. Chem. Soc.* **1999**, *121*, 1601–1602.

[21] P. R. Blake, B. Lee, M. F. Summers, M. W. W. Adams, J.-B. Park, Z. H. Zhou, A. Bax, *J. Biomol. NMR* **1992**, *2*, 527–533.

[22] G. W. Vuister, A. C. Wang, A. Bax, *J. Am. Chem. Soc.* **1993**, *115*, 5334–5335.

[23] S. S. Imides, P. T. Tefddols, P. Christ, A. G. Lindsay, S. S. Vormittag, J. Neudçrfl, A. Berkessel, A. C. O. Donoghue, *Chem. - A Eur. J.* **2011**, *17*, 8524–8528.

[24] R. I. Storer, D. E. Carrera, Y. Ni, D. W. C. MacMillan, *J. Am. Chem. Soc.* **2006**, *128*, 84–86.

[25] J. M. Tao, J. P. Perdew, V. N. Staroverov, G. E. Scuseria, *Phys. Rev. Lett.* **2003**, *91*, 146401.

[26] S. Grimme, J. Antony, S. Ehrlich, H. Krieg, S. Grimme, J. Antony, S. Ehrlich, H. Krieg, *J. Chem. Phys.* **2010**, *132*, 154104.

[27] S. Grimme, *J. Chem. Phys.* **2003**, *118*, 9095.

[28] M. J. Frisch, G. W. Trucks, H. B. Schlegel, G. E. Scuseria, M. A. Robb, J. R. Cheeseman, G. Scalmani, V. Barone, B. Mennucci, G. A. Petersson, et al., **2009**.

[29] F. Neese, *Comput. Mol. Sci.* **2012**, *2*, 73–78.

5 Mechanistic investigations on the solvothermal synthesis of quinoline derivatives

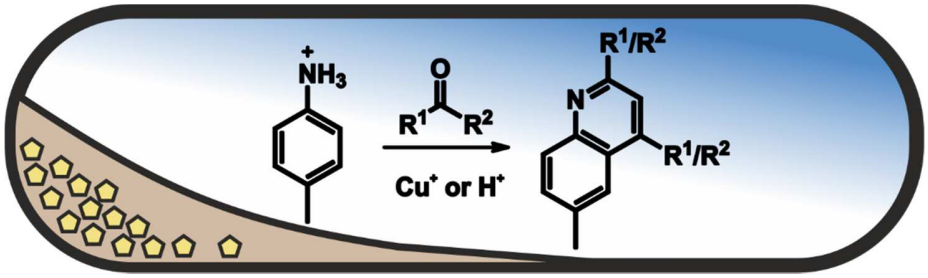

a) Determination of the crystal structures and fluorescence analyses of the copper *catena*-cuprates(I) described in this chapter were done by Max Vilsmeier; b) Preparation of the catena compounds was done by Max Vilsmeier and Christoph Meier; c) Extraction and purification of the quinolone derivatives, as well as mechanistic investigations and NMR analyses were done by Julian Greindl.

5.1 Introduction

Solvothermal synthesis has been successfully used in nanochemistry for the preparation of a variety of compounds. By enabling the control over physical properties of products through variation of reaction conditions, complex nanostructures such as ultralight metal coordination networks, morphologically controlled titanium oxide nanoparticls or chemically synthesized carbon nanosheets have been successfully realized.

In the working group of Prof. Pfitzner, Max Vilsmeier used solvothermal synthesis to prepare cuprate(I) structures (R^1_∞*catena*[Cu_xHal_y]), which consist of repeating copper-halide clusters and organic molecules (see Figure 1 for an example).

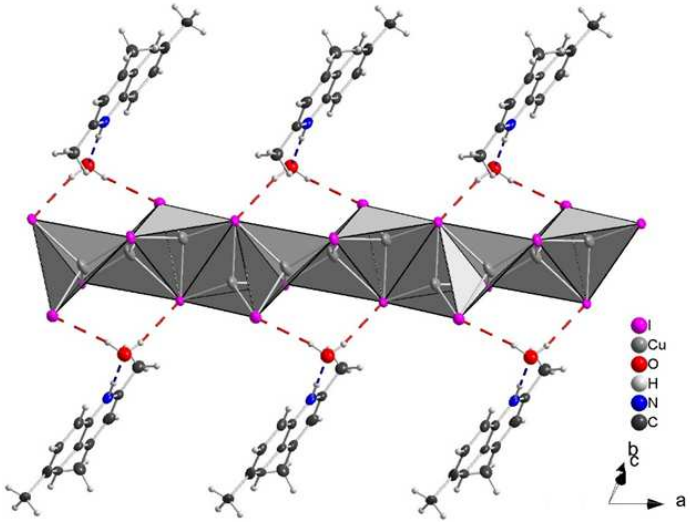

Figure 1. 2,4,6-Trimethylchinolinium H_2O $^1_\infty$*catena*[Cu_2I_3], consisting of edge and face connected [CuI_3] tetrahedrons, resulting in a zigzag chain. Water atoms connect the chinolinium cations to the $[Cu_2I_3]^-$ polyanion via hydrogen bonding (dotted lines).

In this compound the copper-halide clusters are built by [CuX_3] tetrahedrons that are connected via common faces and edge connected. Water molecules are incorporated in the structure of the chain and form hydrogen bonds to the halide atoms at the terminal edges of the [CuX_3] clusters and to protonated nitrogen atoms of the organic compounds. In the reaction of *p*-toluidine and copper halides dissolved in different ketones, X-ray single crystal diffraction experiments revealed the formation of aromatic heterocycles and their implementation in the observed copper(I)-halide chains. These cuprates(I) show fluorescence under UV-light at low temperatures in a variety of colors, depending on the coordination of the Cu(I) ions and the used halides and ketones (Figure 2).

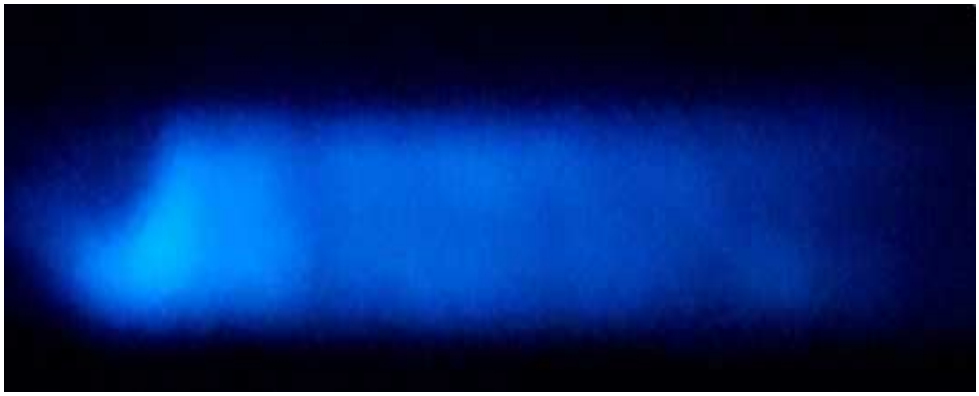

Figure 2. Blue fluorescence of the copper catena $(C_7H_{10}N)(H_2O)_{1/2}\,{}^{2}_{\infty}[CuCl_2]$ observed at 77K under UV light.

The heterocycles incorporated in the cuprate(I)structures are quinolone derivatives, which are formed during the solvothermal preparation of the catena are the focus of the work presented here (Figure 3).

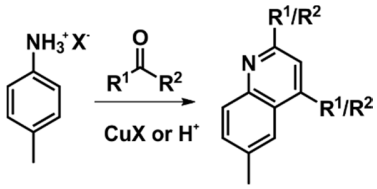

Figure 3. General scheme of the solvothermal reaction of *p*-toluidine and ketones with copper(I) halides or acids as catalyst.

The mechanism for the solvothermal synthesis of quinoline derivatives was investigated and the substrate scope of the reaction was tested. The prepared products, as well as the proposed mechanism, were analyzed with NMR spectroscopic methods in order to confirm the mechanism of the solvothermal synthesis for various substrates.

5.2 Mechanism of the reaction

A similar reaction for the formation of 2,4-dimethylquinoline was reported by Vaughan in 1948. Acetone-anil (2,2,4-trimethyl-1,2-dihydroquinoline) is prepared from acetone and aniline as a precursor and added to a mixture of sodium metal and a small quantity of copper powder in aniline. The mixture is refluxed at 230 °C until the evolution of methane ceases and the product is purified by distillation with an altogether yield of up to 61% (Figure 4). The high temperature is needed for the electrocyclization of the heterocycle.

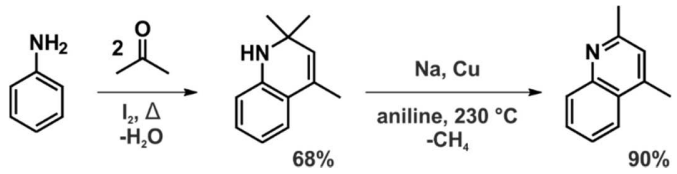

Figure 4. Acetone-anil is prepared from aniline and acetone and added to a solution of sodium metal and copper powder to form 2,4-dimethylquinoline. The evolution of methane gas can be observed in the last reaction step.

For the solvothermal synthesis of quinoline derivatives, acetone and the halide salt of the protonated aniline analogue *p*-toluidine were used as starting material to form 2,4,6-trimethylquinoline. The reaction is a one-pot synthesis that takes place in an ampule over six days at 140 °C. Copper(I) halides were used for the preparation of cuprate(I)structures, but are not necessary for the formation of the quinoline derivative. The same organic product is formed in the absence of copper(I) halides, but a lower conversion is observed.

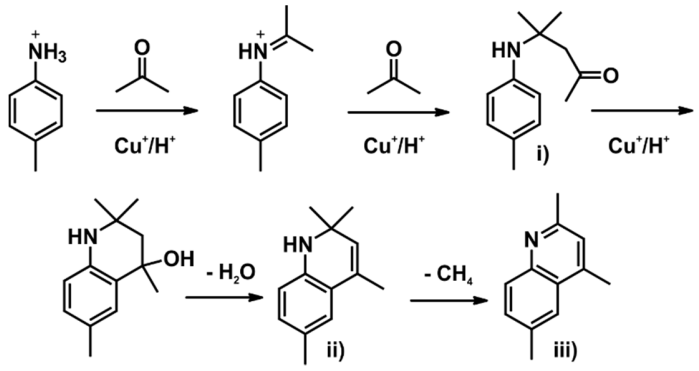

Figure 5. Proposed mechanism of the formation of 2,4,6-trimethylquinoline based on the work of Vaughan; i) an acetone-anil is formed in a Mannich-type reaction; ii) electronic ring closure leads to the formation of a heterocycle; iii) elimination of methane leads to aromatization of the heterocycle.

In accordance to the work of Vaughan, our proposed mechanism consists of the same reaction steps; i) a Mannich-type reaction of *p*-toluidine and two acetone molecules; ii) the

annulation of the molecule via electronic ring closing, which generally requires temperatures of around 250 °C. iii) the elimination of methane via concerted proton-electron transfer and subsequent aromatization of the heterocycle (Figure 5).

Several approaches were used to confirm the proposed mechanism of the solvothermal synthesis of quinoline derivatives. By varying the ketone used in the reaction, different side products were proposed and investigated by NMR spectroscopic methods (Figure 6).

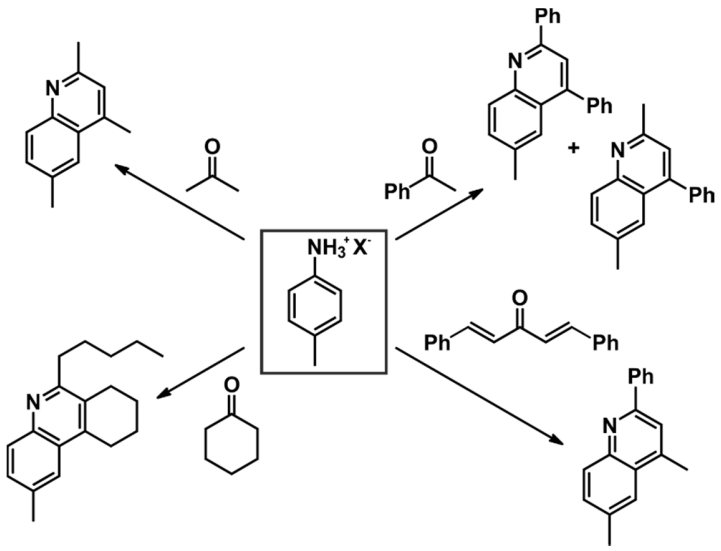

Figure 6. Overview of the investigated reactions. Different ketones were used as starting materials in combination with *p*-toluidine to form quinoline derivatives.

Acetophenone as starting material

The evolution of methane gas during the preparation of 2,4,6-trimethylquinoline could not be proven, since the opening of the ampule leads to a sudden degassing of the sample. In order to confirm the elimination in the final step of the reaction, acetone was replaced with acetophenone and the residual solvent mixture in the ampoule was investigated. Thus the final elimination step leads to either the evolution of methane gas, or the formation of benzene. An NMR analysis of the crude reaction mixture in $CDCl_3$ shows the formation of benzene with a ^{1}H chemical shift of 7.36 ppm and a ^{13}C chemical shift of 128.4 ppm (Figure 7).

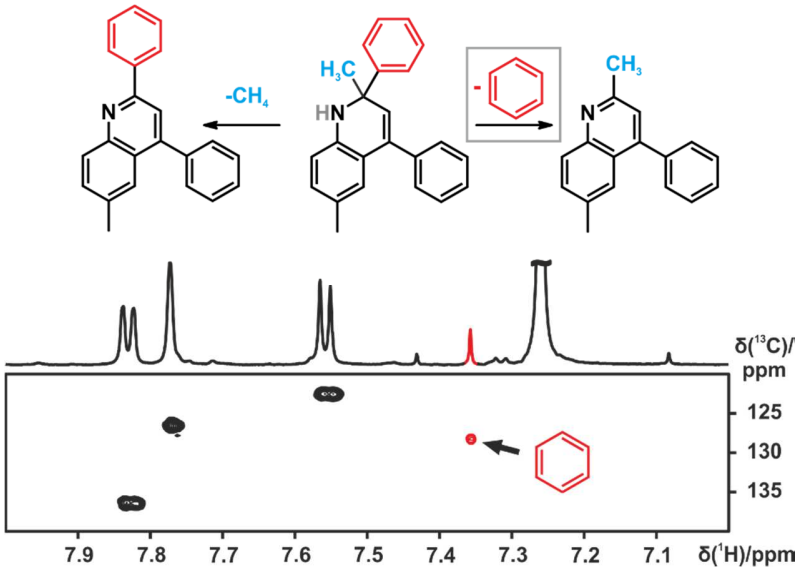

Figure 7. a) The final reaction step leads to the elimination of either methane or benzene. b) Section of an $^{1}H,^{13}C$ HSQC spectrum of the crude product mixture which shows the formation of benzene during the reaction, proving the elimination step.

Despite the observed formation of benzene, no product was identified in the crude reaction mixture. Purification of the proposed products 2,6-dimethyl-4-phenylquinoline and 6-methyl-2,4-diphenylquinoline was not successful in the course of the thesis.

Cyclohexane as starting material

In addition to acetophenone, cyclohexanone was used as the ketone for the reaction to prepare 2-methyl-6-pentyl-7,8,9,10-tetrahydrophenanthridine. When using cyclohexane, no elimination can be observed at the final step of the mechanism. After the Mannich-type reaction and the subsequent ring closure of the heterocycle, the cleavage of the C-C bond via concerted proton-electron transfer leads to a ring opening of a cyclohexane moiety (Figure 8).

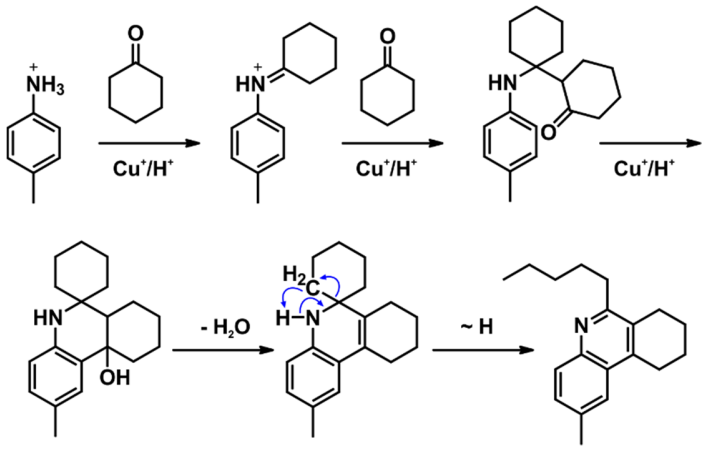

Figure 8. Mechanism of the reaction of *p*-toluidine with cyclohexanone. The final step of the reaction leads to the formation of a saturated pentane moiety by ring opening of the cyclohexane moiety.

In this ring opening, a pentane moiety is formed. The ^{1}H and ^{13}C chemical shifts of the prepared quinoline derivate were unambiguously assigned (see experimental section).

Dibenzalacetone as starting material

The quinoline derivative 4,6-dimethyl-2-phenylquinoline was prepared by using dibenzalacetone as starting material and acetone as solvent and was confirmed by the crystal structure shown in Figure 9.

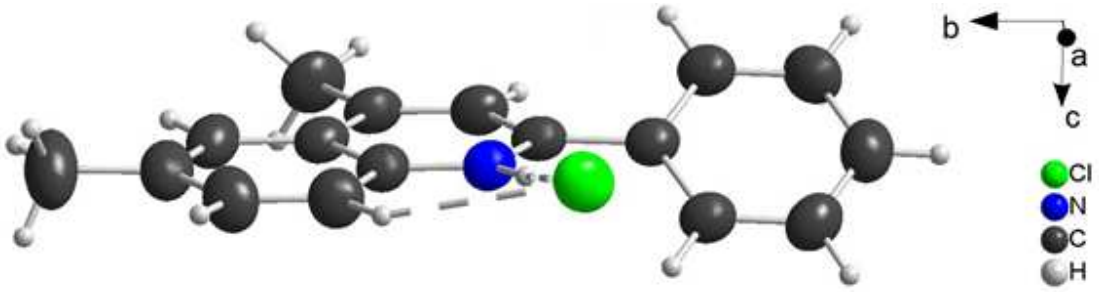

Figure 9. Crystal structure of 4,6-dimethyl-2-phenylquinoline, identified by Max Vilsmeier. The chloride salt of the protonated product is shown.

Dibenzalacetone can dissociate to acetone and benzaldehyde. After the condensation reaction of *p*-toluidine and benzaldehyde, the Mannich type reaction step takes place with acetone. After the electrocyclization, no C-C bond is cleaved in the last step of the reaction, but the formation of hydrogen gas takes place instead (Figure 10).

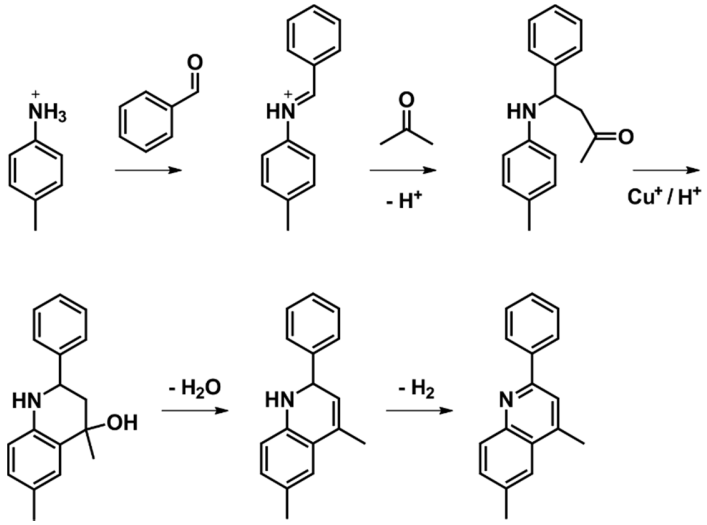

Figure 10. Mechanism of the reaction of *p*-toluidine with dibenzalacetone. The final step of the reaction leads to the formation of a hydrogen gas. The product was identified by single crystal X-ray crystallography.

The product was only confirmed by the crystal structure, since the purification was not possible during the thesis.

5.3 Conclusion and Outlook

By preparing different quinoline derivatives and analyzing the products by NMR spectroscopy and X-ray crystallography, a proposed mechanism of Vaughan from 1948 was confirmed for the newly developed solvothermal synthesis of this substrate class. In the last step of the preparation of 2,4,6-trimethylquinoline, a methyl group is eliminated in the form of methane gas to form the product. By varying the ketone used in the preparation, several products and side-products of the reaction were identified in order to confirm the mechanism and explore the substrate scope of the reaction. Depending on the used ketone, the formation of benzene or hydrogen gas instead of methane can be observed at the last reaction step.

The next step for this solvothermal synthesis is the optimization of reaction conditions and the purification of the product. Initial findings by Max Vilsmeier show the formation of the organic compounds in the absence of copper halides, which can simplify the purification of the product considerably. The substrate scope can be expanded even further by varying the aniline moiety of the reaction and testing additional ketones.

5.4 Experimental section

A general procedure was used for the synthesis of the quinoline derivatives. All solvents were bought from Sigma Aldrich and used without further purification. The solvothermal synthesis was performed over six days at 140 °C in an evacuated quartz ampoule. The crude reaction mixture was filtered and washed with ethylacetate. The residue was mixed with 100 ml water and KOH was added until the mixture was basic. The aqueous phase was extracted with 3x50 ml toluene. The organic phase was dried over $MgSO_4$ and removed under vacuum to yield the solid product. The purification of several products was not achieved during the thesis, due to problems during the crystallization of the product or low yields. The NMR assignment of the products was done by standard 1D and 2D ^{1}H and ^{13}C spectroscopic methods (^{1}H,^{13}C-HSQC, ^{1}H, ^{13}C-HMBC, ^{1}H, ^{1}H-COSY, ^{1}H, ^{1}H-NOESY). ^{1}H chemical shifts are shown in black, ^{13}C chemical shifts are labeled green. The yields of the syntheses were not determined in the course of the thesis, but showed a significant variance depending on the starting materials and the used conditions. Optimization of reaction conditions is the next step for the synthesis of the quinoline derivatives.

2,4,6-Trimethylquinoline

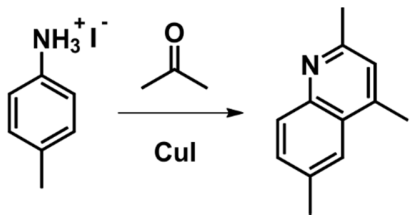

The compound 2,4,6-Trimethylchinolinium H_2O $^1_\infty catena[Cu_2I_3]$ was synthesized from *p*-toluidine hydroiodide (1 eq) and CuI in acetone. Red crystals were formed after cooling of the sample. The compound crystallizes triclinic with the space group *P*-1. See table 1 for additional crystallographic data.

Table 1 Structure and refinement of 2,4,6-Trimethylchinolinium H_2O $^1_\infty catena[Cu_2I_3]$

Compound	$C_{12}H_{16}NO$ $^1_\infty catena[Cu_2I_3]$
Formular weight / gmol^{-1}	698.04
Temperature / K	123.0(1)
Space group	*P*-1 (Nr. 2)
a/ Å	8.4213(6)
b/ Å	10.5622(9)
c/ Å	10.784(1)
α/ °	84.967(7)
β/ °	69.870(7)
γ/ °	75.833(7)
V/ Å^3, *Z*	873.2(1), 2
Diffractometer	Agilent Technologies SuperMova
Density ρ_{calc} / gcm^{-3}	2.655
Absorption coeff. *μ*/ mm^{-1}	7730
Extinction	0.0029(8)
Radiation, *λ*/ Å	MoKα (*λ* = 0.71073)
Reflections collected	11.348
Independent reflections [R_{int}]	11348 [R_{int} = 0.0640, R_{sigma} = 0.0687]
Data/restraints/parameters	11348/0/179
GooF	0.993

R-indexes [*I*≥ 2σ *(I)*]	R_1 = 0.0576, wR_2 = 0.1478
R- indexes [all data]	R_1 = 0.0772, wR_2 = 0.1646
$\Delta\rho_{min}$, $\Delta\rho_{max}$ / eÅ^{-3}	2.23/-1.61
BASF	0.4693

The product was purified as described above.

NMR assignment:

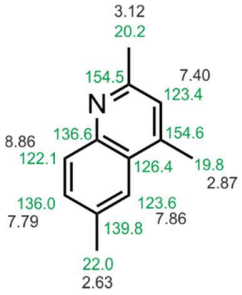

^{1}H-NMR (400.1 MHz, $CDCl_3$) δ_H = 17.89 (bs, 1H), 8.86 (d, 1H, $^3J_{HH}$ = 8.7 Hz), 7.86 (bs, 1H), 7.79 (dd, 1H, $^3J_{HH}$ = 8.7 Hz, $^4J_{HH}$ = 1.6 Hz), 7.40 (s, 1H), 3.12 (s, 3H), 2.87 (s, 3H), 2.63 (s, 3H)

^{13}C- NMR {^{1}H} (100.6 MHz, $CDCl_3$): δ_C = 154.5 (q), 154.4 (q), 139.8 (q), 136.6 (q), 136.0 (t), 126.4 (t), 123.6 (t), 123.4 (t), 122.1 (t), 22.0 (p), 20.2 (p), 19.8 (p)

Reaction of *p*-toluidine and acetophenone

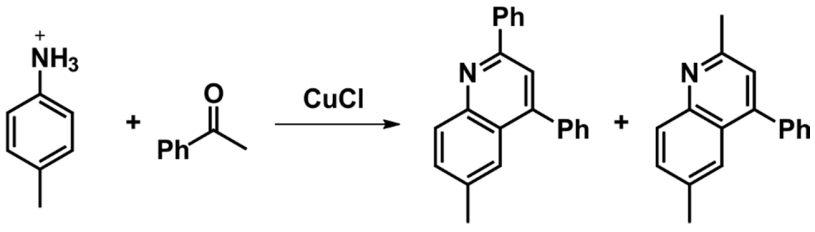

For the solvothermal synthesis of 2,6-dimethyl-4-phenylquinoline and 6-methyl-2,4-diphenylquinoline *p*-Toluidine hydrochloride and CuCl were mixed with acetophenone (1 eq). The crude mixture showed the formation of benzene as a side-product, but the proposed products could not be purified in the course of the thesis.

4,6-dimethyl-2-phenylquinoline hydrochloride

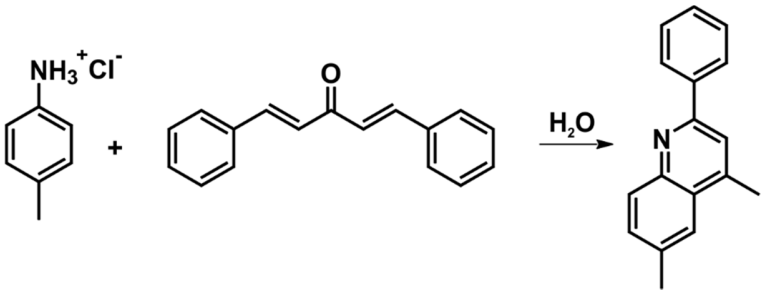

The compound 4,6-dimethyl-2-phenylquinoline hydrochloride was synthesized from *p*-toluidine hydrochloride and dibenzalacetone (1 eq) in acetone and a drop of water. The reaction mixture was cooled down to 0 °C and the formed colorless crystals analyzed. The compound crystallizes monoclinc with the space group *C2/c*. See table 2 for additional crystallographic data.

Table 2 Structure and refinement of 4,6-dimethyl-2-phenylquinoline hydrochloride

Compound	$C_{17}H_{16}ClN$
Formular weight / gmol^{-1}	269.76
Temperature / K	293(2)
Space group	*C*2/*c* (Nr. 15)
a/ Å	13.8502(2)
b/ Å	14.1604(3)
c/ Å	14.1866(2)
β/ °	97.877(2)
V/ Å^3, *Z*	2756.09(8), 8
Diffractometer	Agilent Technologies Gemini R Ultra
Density ρ_{calc} / gcm^{-3}	1.300
Absorption coeff. μ/ mm^{-1}	2.308
Radiation, λ/ Å	CuKα (λ = 1.54184)
Reflections collected	5906
Independent reflections [R_{int}]	2415 [R_{int} = 0.0159, R_{sigma} = 0.0155]
Data/restraints/parameters	2415/0/236
GooF	1.036

R-indexes [*I*≥ 2σ *(I)*]	R_1 = 0.0326, wR_2 = 0.0904
R- indexes [all data]	R_1 = 0.0368, wR_2 = 0.0931
$\Delta\rho_{min}$, $\Delta\rho_{max}$ / eÅ^{-3}	0.18/-0.14

The product was not purified in the course of the thesis.

2-Methyl-6-pentyl-7,8,9,10-tetrahydrophenanthridine

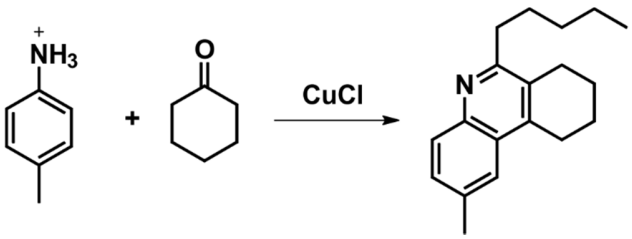

p-Toluidine hydrochloride and a drop of water were mixed with cyclohexanone (1 eq). The product was prepared in a solvothermal synthesis and purified as described above.

NMR assignment:

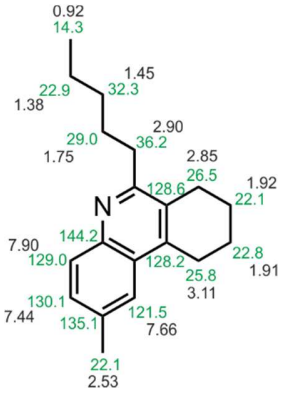

^{1}H-NMR (400.1 MHz, $CDCl_3$) δ_H = 7.90 (bs, 1H), 7.66 (s, 1H), 7.44 (d, 1H, $^{3}J_{HH}$ = 8.5 Hz), 3.11 (m, 2H), 2.90 (m, 2H), 2.85, (2H, m), 2.53, (s, 3H), 1.92 (m, 2H), 1.91 (m, 2H), 1.75 (m, 2H), 1.45, (m, 2H), 1,38 (m, 2H), 0.92 (t, 3H, $^{3}J_{HH}$ = 7.2 Hz).

^{13}C-NMR (100.6 MHz, $CDCl_3$): δ_C = 144.2, 135.1, 130.1, 129.0, 128.6, 128.2, 121.5, 36.2, 32.3, 29.0, 26.5, 25.8, 22.9, 22.8, 22.1, 22.1, 14.3.

5.5 References

[1] D. Banerjee, S. J. Kim, L. A. Borkowski, W. Xu, J. B. Parise, *Cryst. Growth Des*. **2010**, *10*, 709–715.

[2] R. X. Æ. Jian, K. Shang, *J. Mater. Sci*. **2007**, *42*, 6583–6589.

[3] M. Choucair, P. Thordarson, J. A. Stride, *Nat. Nanotechnol*. **2009**, *4*, 30–33.

[4] W. R. Vaughan, *Org. Synth*. **1948**, *28*, 49–51.

[5] D. Craig, *J. Am. Chem. Soc*. **1938**, *60*, 1458–1465.

[6] R. H. Reitsema, *Chem. Rev*. **1948**, *43*, 43–68.

6 Conclusion

The main focus of this thesis were NMR spectroscopic investigations in Brønsted acid catalysis, especially analyses regarding the binary complexes of BINOL derived chiral phosphoric acids and imine substrates. The structures of these complexes, as well as the hydrogen bond that is formed between the phosphoric acid and the substrate, were extensively studied in order to investigate the reasons for the enantioselectivity of this catalyst class, the great substrate scope, and the ever increasing number of reactions that can be catalyzed by chiral phosphoric acids. Despite the growing importance of Brønsted acid catalysis, surprisingly little is known about the intermediates and activation modes of the reactions. Thus, the objective of this work was to give deeper insight into catalyst/substrate interactions and therefore improve the selection process of known chiral phosphoric acid catalysts as well as aid the way to a more focused development process of knew catalysts.

The structures of binary catalyst/imine complexes are examined in the second chapter. With the help of low temperature measurements, four coexisting complex structures and their complex exchange pathways were identified. For the first time, the structures of complexes containing the *Z*-isomer of the imine were experimentally investigated. The main interaction point in each complex is the strong hydrogen bond, which acts as an anchor between catalyst and imine. In addition to a complete assignment of imine substrates and the BINOL backbone of the catalyst by standard 1D and 2D NMR methods (^{1}H, ^{13}C, ^{15}N, ^{31}P, ^{19}F, ^{1}H,^{1}H COSY, ^{1}H,^{13}C HSQC, ^{1}H,^{13}C HMBC), 2D ^{1}H,^{1}H NOESY, 2D ^{1}H,^{19}F NOESY and selective 1D NOESY spectra were used to identify additional interactions and the resulting complexes. By rotating or tilting the imine around the hydrogen bond anchor and by dissociation and association processes, the different complex structures can be interconverted. Some of these exchange pathways are fast on the NMR timescale and lead to averaged sets of signals, while others show signal splitting at low temperatures. The exchange via rotation was only found in the two structures containing the *Z*-isomer of the imine. Due to the greater steric hindrance of the *E*-imine, the two structures containing this isomer exhibit an exchange via tilting only. An additional slow exchange via dissociation and association is observed between the *E*-isomer of the imine in solution and inside the complex. These findings explains the observed signal patterns in the investigated complexes. The four core structures were identified for several imines in complex with the catalyst TRIP and are supported by theoretical calculations. This invariance of the identified structures across a variety of imines gives a reason for the great substrate scope of chiral phosphoric acids: The strength of the hydrogen bond outweighs

smaller interaction patterns and enables a high tolerance for different functional groups of the imine substrates.

The focus of the third chapter is the hydrogen bond of Brønsted acid catalyst/imine complexes. The chiral phosphoric acid catalyst TRIP was investigated in combination with several ^{15}N labelled imines with varying functional groups. By labelling the imine substrates with the NMR active isotope ^{15}N, a number of parameters become accessible by NMR spectroscopy, which were used to analyze hydrogen bond characteristics. The ^{15}N chemical shift of the imine can be used as a probe for the degree of protonation of the substrate, which is indicated by an increasing high field shift. By correlating the ^{15}N chemical shift of the substrate to the ^{1}H chemical shift of the hydrogen bond proton, a Steiner-Limbach curve was created, which identifies the formed bonds as strong, low-barrier hydrogen bonds. In addition to chemical shifts, a number of coupling constants involved in the hydrogen bond were measured. The $^{1}J_{NH}$ coupling between the nitrogen of the substrate and the hydrogen bond proton increases with the degree of protonation. The $^{2h}J_{PH}$ coupling between the hydrogen bond proton and the phosphorous of the Brønsted acid catalyst shows a dependence on the geometry of the hydrogen bond. By utilizing 3D NMR spectroscopic techniques, the $^{3h}J_{NP}$ coupling constants across the hydrogen bonds were measured and compared. For all investigated imines, an invariance of the mainly linear hydrogen bonds was observed with the main variation being the position of the hydrogen bond proton depending on the basicity of the substrate. In all but one case, predominantly ionic catalyst/imine complexes were found. This further constitutes the strength of the hydrogen bond and its function as an anchor between catalyst and substrate. All measurements are supported by theoretical calculations, in which a good agreement of the calculated gas phase structures to the observed chemical shifts was found.

The fourth chapter of the thesis focusses on the influence of the 3,3'-substituents of BINOL derived chiral phosphoric acids on complex structures and hydrogen bond geometries. With a combination of experimental data and theoretical calculations, the structures of several TiPSY/imine complexes was determined and compared to our previously reported structures of TRIP/imine complexes and known crystal structures of chiral phosphoric acid/imine complexes. The structure determination of the TiPSY/imine complexes revealed the existence of the four core structures that were identified for the TRIP/imine complexes, with only a slight variations in hydrogen bond angles. The sensitivity of the hydrogen bond to structural changes was then used to identify the differences of TRIP/imine, TiPSY/imine and TRIFP/imine complexes. The main disparity was found for the measured $^{3h}J_{PN}$ coupling constants, which

are correlated to the PON angle of the hydrogen bond. This angle determines the position of the imine in relation to the catalyst in all four core structures, without fundamentally changing the observed interactions between catalyst and substrate. The findings presented here indicate a dependence of the observed enantiomeric excesses on the hydrogen bond angle, whereas other parameters, such as acidity of the catalyst or hydrogen bond distance show no noticeable correlation.

In conclusion, with the help of NMR spectroscopic investigations, we were able to identify the coexistence of four core structures of several binary chiral phosphoric acid/imine complexes in solution and illustrated their complex exchange pathways. In addition to two catalyst/*E*-imine complexes, two structures containing the *Z*-isomer of the imine substrate were identified and experimentally investigated for the very first time. An invariance of the four core structures was found for several investigated imine substrates and for the catalysts TRIP and TiPSY. The strong hydrogen bond that is part of every complex outclasses other intermolecular interaction and gives an explanation for the immense substrate scope of chiral phosphoric acid catalyzed reactions. These hydrogen bonds were extensively studied by NMR spectroscopic methods and described as strong, low-barrier hydrogen bonds. For the investigated catalyst/imine complexes of TRIP, TiPSY and TRIFP, mainly changes for the hydrogen bond geometries were observed, which in turn lead to slight structural variations for the binary complexes, without altering the main interaction patterns. The investigated binary complexes are intermediates and act as precursors for the transition states of the Brønsted acid catalyzed transfer hydrogenation of imines. Theoretical calculations predict the formation of a ternary complex after the addition of the reducing agent. The investigation of these ternary complexes is part of a future study based on the results presented in this thesis.

In the fifth chapter, the mechanism of the solvothermal synthesis of quinoline derivatives was investigated. These derivatives were initially identified by Max Vilsmeier as side products in the preparation of *catena*-copper(I) chains. A mechanism was proposed on the basis of a similar reaction reported by Vaughan in 1948. By varying the used ketone educts and analyzing the products and side-products of the reaction by X-ray single crystal crystallography and NMR spectroscopy, the proposed mechanism was confirmed for a variety of quinoline derivatives.

7 Abbreviation Register

1D	one dimensional
2D	two dimensional
3D	three dimensional
AcOH	acetic acid
APCI	atmospheric pressure chemical ionization
Å	ångström
1,1'-BINOL	1,1'-bi-2-naphtol
BF	basic transmitter frequency
Boc_2O	di-*tert*-butyldicarbonate
Boc	*tert*-butyloxycarbonyl
OP	transmitter frequency offset
bs	broad signal
COSY	correlation spectroscopy
cm	centimeter
°C	degree celsius
CSA	chemical shift anisotropy
D	delay
δ	chemical shift
DCA	dichloroacetic acid
DCM	dichloromethane
DD	dipolar dipolar
DFT	density functional theory
DMSO	dimethyl sulfoxide
DPP	diphenyl phosphate

DS	dummy scans
EI	electron impact
ESI	electron spray ionization
EV	electron volt
GPCRs	G-protein coupled receptors
GC-MS	gas chromatography – mass spectrometry
g	gram
h	hour(s)
HMBC	heteronuclear multiple bond correlation
HMQC	heteronuclear multiple quantum correlation
HSQC	heteronuclear single quantum coherence
HR-MS	high resolution mass spectrometry
*i*Pr	isopropyl
K	kelvin
LUMO	lowest unoccupied molecular orbital
MCA	chloro acetic acid
mg	milligram
mL	milliliter
mmol	millimole
mM	millimolar
MS	molecular sieves
n.d.	not determined
NMR	nuclear magnetic resonance
NOE	nuclear overhauser effect
NOESY	nuclear overhauser enhancement spectroscopy
NS	number of scans

p.A.	per analysis
pm	picometer
ppm	part per million
r.t.	room temperature
RT	retention time
SW	spectral width
µL	microliter
µmol	micromole
FID	free induction decay
TD	size of FID
TEA	triethylamine
TFA	trifluoro acetic acid
THF	tetrahydrofurane
TLC	thin layer chromatography
TMA	trimethyl acetic acid
TMS	tetramethylsilane
(*R*)- TiPSY	3,3′-Bis(triphenylsilyl)-1,1′-binaphthyl-2,2′-diylhydrogenphosphate
(*R*)- TRIP	3,3′-Bis(2,4,6-triisopropylphenyl)-1,1′-binaphthyl-2,2′-diylhydrogenphosphate
(*R*)- TRIFP	3,3’-Bis(3,5-trifluoromethylphenyl)-1,1’-binaphtyl-2,2’-diylhydrogenphosphate